TAMPEREEN TEKNILLINEN YLIOPISTO
TAMPERE UNIVERSITY OF TECHNOLOGY

Mikko Rantala

Heat Transfer Phenomena in Float Glass Heat Treatment Processes

Julkaisu 1355 • Publication 1355

Tampere 2015

Tampereen teknillinen yliopisto. Julkaisu 1355
Tampere University of Technology. Publication 1355

Mikko Rantala

Heat Transfer Phenomena in Float Glass Heat Treatment Processes

Thesis for the degree of Doctor of Science in Technology to be presented with due permission for public examination and criticism in Konetalo Building, Auditorium K1702, at Tampere University of Technology, on the 26th of November 2015, at 12 noon.

Tampereen teknillinen yliopisto - Tampere University of Technology
Tampere 2015

ISBN 978-952-15-3646-5 (ISBN)
ISBN 978-952-15-3692-2 (PDF)
ISSN 1459-2045

ABSTRACT

Glass tempering is a process in which the strength of float glass is improved with heat treatment. In a tempering furnace glass is on top of rotating ceramic rollers. In the process glass plates are heated with thermal radiation and forced convection up to about 640°C and then cooled by air jets at a cooling rate depending on the glass thickness. The residual stress, i.e., tempering level depends on the cooling speed. In order to solve glass temperatures during a tempering process, the problem is to find solving method for radiation heat flux, convection heat transfer coefficients and contact heat transfer coefficient. The aim of the heat-soak process for tempered glass is to eliminate glasses at risk of spontaneous breakage. In the process glasses are heated up to 290˚C by hot air flowing in a channel between them. The problem is to find solving methods for glass and air temperatures which depend on the stream-wise coordinate and time.

A method for solving radiation heat flux from a tubular resistor to a plate under it was developed.

The radiative properties of clear and low emissivity coated soda-lime glass were shown and thermal radiation in a plate glass was described. A new method for solving net radiation heat transfer between a clear plate glass and diffuse surroundings was developed. In the method the radiation between glass volume elements is ignored and integration over hemisphere is covered by using the mean reflectivity of glass surface and the mean propagation angle at which radiation travels in glass. The use of the method is limited to glass temperatures below 700°C. The method was also adapted to coated glass. The method was used to show the effect of the radiation wavelength, glass thickness and low emissivity coating to plate glass radiation properties. The results of the method were compared against results in the literature. The method gave the same results. In the simplest version of the new method only the first internal reflection from glass-air interface was considered, and even then the accuracy was high.

The development of an air jet was introduced with equations. The momentum of the jet was solved experimentally and the results were compared against calculated ones. Local convection heat transfer coefficients on a flat surface under a sonic velocity air jet alike in glass tempering furnace were solved experimentally by using a constant heat flux plate. The effect of discharging pressure, orifice diameter and nozzle-to-plate distance to heat transfer was studied. The literature correlations were used and new experiments were made to research heat transfer under an impinging incompressible jet. It was observed that when the momentum of a jet and nozzle to plate distance are equal, then heat transfer is quite equal, even if the nozzle diameter and discharging pressure varied.

Heat transfer under an array of air jets alike in glass tempering chiller was studied experimentally and with a literature correlation. In the experiment three different jet arrays were used in which only the nozzle diameter varied. The heat transfer of each jet array was found to be quite equal when the fan power needed to create jets was the same. The heat transfer coefficients given by the correlation corresponded well to the ones given by new measurements. Measured heat transfer coefficients were 11 to 14 % higher than the predicted ones, and the change in the overpressure changed the measured heat transfer coefficients in the same relation as it changed the measured ones.

The contact heat transfer between glass and rollers was studied. The following estimate for effective contact heat transfer coefficient of glass on top of ceramic rollers in tempering furnace was found: $1 \leq \bar{h}_{ct} L_{rp} \leq 3$ W/(mK).

The methods for solving heat transfer between glass and air flowing in a narrow channel between glasses were presented for both turbulent and laminar flow. The method for solving heat transfer in a heat soak furnace was developed. In the heat soak furnace studied the flow was found to be turbulent, but also laminar flow could occur during the final stages of the heating due to increasing air

temperature, i.e., decreasing Reynolds number. Theoretically predicted and measured temperatures were found to be in reasonable agreement. An extended method for furnace designer and operator for solving heat transfer in a heat soak furnace was developed with witch was found that in a very narrow channel the heating time increased dramatically because the air temperature at the end of such a channel was almost as low as glass temperature, i.e., heat from the air was already transferred to glass. The heating time also increased with the glass flow-wise length and thickness, although the total mass of the glass loading remained the same.

PREFACE

I have been dealing with heat transfer in glass heat treatment machines since I started my master thesis in 1997. After graduating, I continued my work in Tampere University of Technology. Since 2005 I have worked in Glaston Finland Oy (former Tamglass Engineering Oy) manufacturing glass heat treatment machines in which glass is tempered, bended, laminated or otherwise processed. The primary aim of my work has been to develop the glass heat treatment machines and increase heat transfer know-how in the company. During the years I have solved many kinds of practical problems relating to heat transfer, designed heat treatment processes, created heat transfer modelling codes, and so on. The success in applying heat transfer theories into practice when a new machine is under development has required experimental tests in a laboratory and with a ready-made machine to verify the accuracy of theoretical results. The solution methods which I have used for solving heat transfer problems are based on literature, experiments, self-written equations and solution codes. In addition to pure heat transfer problems, I have worked with many other topics relating to heat treated plate glass. Since 2009 I have handled the patent matters of the company together with my R&D work.

Now the selected portion of the work done during years 1997-2012 is compiled and edited as to thesis.

I wish to express great gratitude to Professor Reijo Karvinen for his advices, support and interest regarding the thesis.

Thanks also go to my colleagues during my years in Tampere University of Technology, and to present colleagues in Glaston Finland Oy. Special thanks to M.Sc. Tarmo Pesonen and M.Sc. Jukka Vehmas.

Finally, I want to thank my dear wife Tuija, my dear son Eemeli and my dear daughter Emma.

Mikko Rantala

Tampere, November 2015

NOMENCLATURE

Latin symbols

A	surface area, [m^2]; absorptance, [-]
a	hemispherical total absorption, [W/m^2]
$a_{\Delta\lambda}$	hemispherical wavelength band absorption, [W/m^2]
$a(\lambda)$	hemispherical spectral absorption, [$W/(m^2\mu m)$]
Bi	Biot number, [-]
c, c_0	speed of light, speed of light in vacuum, [m/s]
c_f	friction factor, [-]
c_p	specific heat, [J/(kgK)]
C_1, C_2, C_3	constants for Planck function and Wien's displacement law, see Sec. 8.2
C_v, C_a	coefficients for true velocity and contraction at vena contracta, [-]
C_D	discharge coefficient, $C_D = C_v C_a$, [-]
d, D	diameter, [m]; optical distortion and optical power in Sec. 5.6, [1/m]
d_h	hydraulic diameter, [m]
$e(T)$	emissive power, [W/m^2]
$e(\lambda,T)$	hemispherical spectral emissive power, [$W/(m^2\mu m)$]
E	emittance, [-]; elastic modulus, [Pa]; energy, [J]; integral function in Eq. (10.1)
F	force, [N]; focal length in Sec. 5.6, [m]
F_{i-j}	view factor, [-]
Fo	Fourier number, [-]
$F_b(\lambda_1,\lambda_2,T)$	fraction of blackbody emissive power lying in spectral region λ_1 to λ_2
g	gravity, [m/s^2]
G_n	eigenfunction
h	local convection heat transfer coefficient, [$W/(m^2K)$]; Planck's const. in pg. 44
$\bar{h}$	surface averaged or mean convection heat transfer coefficient, [$W/(m^2K)$]
H	distance from nozzle inlet to surface, [m]
H	half-width of air channel in Chap. 15, [m]
$i(T)$	intensity of radiation, [$W/(m^2\,sr)$]
$i(\lambda,T)$	spectral intensity of radiation, [$W/(m^2\mu m\,sr)$]
I	electric current, [A]
I, I_0	modified Bessel functions, [-]
J	momentum, [N]
k	thermal conductivity, [W/(mK)]
k	Boltzmann constant in pg. 44; surface roughness in pg. 53
L	glass thickness, length, [m]
L_{sq}, L_{tr}	distance between nozzles, see Figure 12.14, [m]
m	mass, [kg]
$\dot{m}$	mass flow rate, [kg/s]; In Chap. 15 $\dot{m} = u_{m0}\rho_0 H$, [kg/(sm)]
M	molar mass, [kg/mol]
n	refractive index, [-]; (n means normal in figures in Sec. 8.3.2)
Nu	Nusselt number, $Nu = hD/k$, (D = orifice diameter), [-]
p	absolute pressure, [Pa]
Δp	pressure difference, overpressure, [Pa]
P	periphery of channel, [m]
P_{fan}	fan power, [W]
Pr	Prandtl number $Pr = c_p\mu/k$, [-]
q	heat flux, [W/m^2]

Q	rate of heat flow, [W]
r	radial coordinate, [m]
R	radius, [m]; reflectance, [-]; reflection function in Sec. 10.1
Re	Reynolds number, $Re = u\rho D/\mu = 4\dot{m}/(\pi D\mu)$, [-]
R_u	ideal gas constant, R_u = 8.314 [J/(kgmol)]
S	glass thickness in Chap. 13, glass half-thickness in Chap. 15, [m]
S	net radiation source term inside glass, $S = \partial q_r/\partial x$, [W/m^3]
$S_{xi\text{-}xj}$, $S_{i,l}$, $S_{i,u}$	net radiation source term in a glass layer, [W/m^2]
S_1, S_2	dimensions in Figure 8.7 and Figure 8.8, [m]
t, Δt	time, time-step, [s]; (t means tangent in figures in Sec. 8.3.2)
T	temperature, [K]; transmittance, [-]
u	velocity, [m/s]
U	voltage, [V]; heat-transmission value, [W/(m^{2}K)]
$\dot{V}$	volume flow rate, [m^3/s]
W	roller wave distortion in Sec. 5.6, [m]
x, y, z	Cartesian coordinates, [m]
Δx	length-step or thickness step, [m]
x^*	non-dimensional distance of channel, $x^* = kx/(\rho c_p H^2 u_m)$
Y_v	dimension in Figure 8.6, [m]

Greek symbols

α	absorptivity, [-]; or angle in Figure 8.6
α	coefficient of linear expansion in Eq. (4.1), [μ/°C]
β	angle in Figure 8.5
γ	isentropic constant (for air γ = 1.4), [-]; angle in Figure 8.5
δ	jet radius (see pg. 86), [m]; height of air gap, [m]
ε	emissivity, [-]
η	non-dimensional time, $\eta = ht/(\rho c_p S)$; variable in Sec. 10.1
η	fan efficiency in Eq. (12.19)
θ	polar angle (measured from normal of the surface)
θ, θ'	propagation angle of radiation, in air θ and glass θ'
θ	non-dimensional glass temperature
κ	absorption coefficient, [cm^{-1}]
λ, λ'	wavelength, in air λ and glass λ', [m]
λ_n	eigenvalue
μ	dynamic viscosity, [kg/m s]; direction cosine, $\mu = \cos\theta'$ in Sec. 10.1
υ	propagation speed of radiation in Chap. 9 and 10, [m/s]
ν	frequency in Chaps. 9 and 10, [s^{-1}]
ν	Poisson's ratio in Chaps. 4 and 13, [-]
ϑ	non-dimensional air temperature
ξ	non-dimensional distance in Eqs. (15.3) and (15.4), $\xi = hx/(\dot{m} c_p)$
ξ	dummy non-dimensional distance in Eqs. (15.8) and (15.9)
ρ	density, [kg/m^3]; or reflectivity, [-]
σ	Stefan-Bolzmann constant, σ = 5.6703×10^{-8} W/(m^{2}K^4)
σ_{zz}, σ_{yy}	stress, [Pa]
τ	transmissivity, $\tau = (1-\rho)$, [-]; thickness transmittance, $\tau = e^{-\kappa(\lambda)L/\cos\theta'}$ in Sec. 9.3
τ, τ_L	optical depth τ and optical thickness τ_L in Sec. 10.1
φ	circumferential angle
ψ'	effective directional transmittance, see Eq. (9.16)

ψ'_m	effective transmittance, see Eq. (9.20)
Ω	solid angle, [sr]
ω	rotation speed, [r/s]

Subscripts

a	air
b, B	blackbody radiation
c	convection, critical, channel
cal	calculated
ct	contact heat transfer
d,D	diameter
e	electric, exit
eff	effective
f	free area (nozzle area)
fw	furnace wall
gg	gas-gap
H	refers to radiation from heater
l	lower surface, local in Chap. 13
L	thickness, losses
m	mean
me	medium
mea	measured
min	minimum
n	normal, *(θ = 0)*
o	opaque
p	plate, point
r	roller, resistor, radiation
rp	roller pitch
s	solid surface, surroundings
sp	solid spot
tot	total
u	upper surface
v	frequency
vc	vena contracta
w	wall
λ	spectral, i.e. ,wavelength dependent
0	initial
∞	ambient air, surrounding surfaces
$\perp$	radiation polarized perpendicularly to plane of incidence
$\Uparrow$	radiation polarized parallel to plane of incidence

Superscripts

p+1	refers to future after time step Δt
—	line above symbol refers to mean value
+, -	into “positive” and “negative” directions

CONTENTS

1. INTRODUCTION

1.1 Aim, research questions and scientific contribution of thesis

The aim of the work behind the thesis is to develop plate glass heat treatment machines. Then the primary question is *how glass temperature develops in the heat transfer process of the heat treatment machine*. The aim of the thesis is to give solving methods for the question.

The thesis is focused on a float glass tempering process in which glass is heated up to 600-650ºC, depending on the glass thickness, and then cooled with air jets. Tempering makes the glass tough and safe. A compherensive introduction to glass tempering is given by Chaps. 3-5. In a tempering furnace the glass is exposed to radiation emitted by radiant heaters, rollers and other surfaces inside the furnace. Also the glass is emitting radiation. Convection heat transfer between hot air and glass affects both surfaces. On the lower surface also contact heat transfer between glass and rollers takes place. The heat transfer problem is formulated in Chap. 7 where Eq. (7.1) is the general form of the one-dimensional heat transfer problem to be solved in the thesis.

Next three paragraps give the main research questions relating to each heat transfer phenomena above.

There is plenty of solution methods in the literature suitable for solving radition heat transfer in clear float glass, two of which are shortly introduced in Sec. 10.1. The methods are developed to take radiation heat transfer into account even in cases in which the glass temperature increases up to glass melting point. The methods are complicated and it is very difficult to adopt them as a part of the float glass heat treatment process modelling code in which the furnace temperature, for instance, is time-dependent. It is even more difficult to develop them as suitable for a coated float glass. Thus, the methods cannot be used now. The research questions are: *How thermal radiation behaves in clear and coated float glass? How to model the radiation heat transfer in clear and coated float glass in a tempering process? Could the treatment of radiation be simplified based on the fact that during tempering process glass temperature is always below 700ºC, for instance?*

As shown in the introduction of Chap. 12 many scientific papers have focused on heat transfer between an axisymmetric impinging air jet or an array of impinging air jets and a flat plate. Some researchers have even developed correlations on the basis of their experimental data with which the heat transfer coefficient can be solved. The following research question comes up: *Can literature correlations be used for solving the heat transfer coefficient between the jets and glass in a glass tempering process? In addition to answering to the research question, the aim of the thesis is to solve how a single jet develops and how different factors affects to the heat transfer it generates on a surface of a flat plate.*

In a tempering furnace glass moves on the top of rotating rollers made from fused silica. Heat conducts from the rollers to the glass via contact points between them. The subject is very unique in the literature. It is not even clear how important this heat transfer phenomena is in relation to thermal radiation and forced convection in a tempering furnace. The main problem is that contact heat transfer coefficient between glass and rollers is very difficult to solve. The research question is: *How to model the contact heat transfer between the glass and ceramic rollers in tempering furnace?*

In addition to tempering a glass heat-soak process is selected as a subject of the thesis. The aim of the heat-soak test is to break down tempered glasses which would probably get broken spontaneously afterwards. A heat-soak furnace is a huge circulating air oven in which glasses are heated up to 280-300°C. In a heat-soak process glasses are separated by narrow channels in which air flow creates forced convection. The heat transfer problem is introduced in Sec. 15.1 where Eqs. (15.1) and (15.2)

are the general forms of the heat transfer problems to be solved in the thesis. Different kinds of solution methods for a turbulent and laminar channel flow are available in the literature, four of which are cited in the introduction of Chap. 15. The methods are given in a very general form and they as such are not applicable to the heat soak process where for instance the air temperature at the channel inlet changes with time. The research questions are: *How to develop the existing solving methods for a turbulent and laminar channel flow and apply them to heat-soak process? How glass loading, air velocity and channel width affects to the heat transfer in a heat soak furnace?*

The heat transfer modelling methods presented in the thesis are also valid for other types of float glass heat treatment processes like annealing, bending and laminating.

The thesis is a selected collection from many years of work. A portion of the material has been published earlier in conference proceedings and another portion only in in-house reports. In addition to these the thesis contains a great deal of a new material.

The scientific contribution of this thesis is:

- Radiation heat transfer between clear glass and a blackbody: a new simplified method to model radiation heat transfer in a glass tempering process, for instance, is presented and the results are compared with the results of more sophisticated methods in the literature.
- Radiation heat transfer in low-emissivity coated glass: unique data of radiative properties of low-e coating is presented and the method above is developed also for low-e coated glass.
- Emissivity and emissive power of clear and low-e coated glass: new theoretical results solved with the method developed in the thesis are presented.
- Forced convection under an air jet or an array of jets: new experimentally solved heat transfer coefficients are presented and literature correlations are compared with them.
- Contact heat transfer between glass and a roller: the estimate for effective contact heat transfer coefficient of glass on top of ceramic rollers in tempering furnace is solved.
- Forced convection in a channel flow: the literature methods for solving forced convection in a turbulent and laminar channel flow are applied to practice, i.e., to tempered float glass heat-soak process, and theoretical results are compared with data from a real process.

In addition to topics relating to heat transfer, the thesis contains detailed information especially of glass tempering technology. The thesis introduces the glass heat treatment machinery for a technically orientated reader and gives new information also for a specialist in the industrial field.

1.2 Content of chapters

The material processed in glass heat treatment machines is clear or coated soda-lime float glass to be handled in Chap. 2. The basics of tempering and tempered glass are given in Chap. 3. The history of glass is discussed shortly in the previously mentioned chapters. Chap. 4 shortly describes the development of residual stresses in tempering. Chap. 5 contains detailed information of a common tempering line and defines the main differences between various types of tempering lines. The quality of tempered glass is also handled in this chapter as well as the problems in a thin glass tempering. Chap. 6 describes glass bending, laminating and autoclaving processes. Chap. 7 defines the heat transfer problems of float glass tempering, the solving of which the thesis is focused on. Chaps. 8-13 handle the solutions of the problems. Chap. 8 gives the basics of radiation heat transfer, and also the radiative heat flux to glass from a typical resistor used in heat treatment machine is dealt with. Chap. 9 describes how radiation behaves when it hits glass and it also presents extensively the radiative properties of soda-lime glass. The chapter also gives the basics of the Averaged Net Radiation method (ANR-method) developed in the thesis and Chap. 10 introduces the method in detail. The results of

the ANR-method are compared with the results of other methods. In Chap. 11 the radiative properties of low-emissivity coated glass are presented. It is shown that the modelling of radiation in a low-e coated glass is a much more complicated problem than in a clear glass. Chap. 12 handles an air jet from its development to the convection heat transfer it creates on a glass surface. The chapter continues with the research of the forced convection under an array of jets. The contact heat transfer between glass and rollers in tempering furnace is discussed in Chap. 13. Some results of the theoretical modelling relating to tempering process are presented in Chap. 14. Chap. 15 describes the heat-soak process, where hot air flow in channels between glasses transferring heat to glass. Both laminar and turbulent solutions for such a forced convection in a channel flow are presented. The solution method is applied to an actual heat soak furnace. The chapter contains measured data and results of theoretical modelling. Chap. 16 contains conclusions.

2. GLASS

Glass is a very useful material which refers to a hard, brittle and transparent solid used for windows, bottles, lenses, and so on. In the technical sense glass is an inorganic material which has been cooled to the solid state without crystallizing. [1]

The history of glass reaches far into the past. It includes many important details and milestones, from which some are listed below. [2][3][4][5][6][7]

- 3000 B.C. or earlier: Archaeological evidence suggests that the first true glass was made in the coast of northern Syria, Mesopotamia or Old Kingdom of Egypt. The earliest known glass objects in the mid third millennium BC were beads, perhaps initially created as accidental by-products of metal-working slag. Also a legend of Phoenician sailors who transported blocks of soda lives on. According to the legend they anchored on the coast, which is now Lebanon, and lit up a camp-fire to cook food. Then the soda-blocks supporting their pots mixed with the sand and turned into liquid and the surprised sailors witnessed the forming of glass.
- 300 B.C.: Glass compression moulding was invented in Alexandria, which was the centre of glass manufacturing during that time in Egypt. Melted glass was spilled into a bottom mould and a top mould was pressed on it to give a planned shape to glassware.
- First century B.C.: Glassblowing is a glass forming technique which was invented by the Phoenicians in approximately 50 B.C. somewhere along the Syro-Palestinian coast. A long thin metal pipe was dipped onto melted glass to grip a glass blob on its end, after which the blob was blown to a hollow glass article.
- 15th century Clear glass: Glass masters from Venice in Italy managed to choose such raw materials by adding manganese so that glass built up almost uncoloured and clear. The Venetian ability to produce this superior form of glass (Cristallo) resulted in a trade advantage over other glass manufacturing lands.
- 1675 Silica glass: Englishman George Ravenscroft produced crystal-clear glass by using flintstone as a raw material. At first, the glass was very brittle, but the trouble was avoided by adding lead oxide to the recipe. Ravenscroft was the first to produce clear lead crystal glassware on an industrial scale. Clear and heavy silica or lead glass is used as crown glass and in optics.
- 1884 Fireproof glass: The Jena glass factory in Germany started to manufacture glass which contained borosilicate. Friedrich Otto Schott was a German chemist, glass technologist and the inventor of borosilicate glass. Borosilicate glass is also called a fireproof glass, because due to its very low coefficient of thermal expansion high thermal shocks and temperature differences are allowed. As an example laboratory tests tubes and liquid crystal displays (LCD-screens) are often made of borosilicate glass.
- 1909 Safety glass: At the beginning of 20^{th} century the need for unsplitterable glass came to be used in cars. In 1909 the first successful patent for safety glass was taken out by the French artist and chemist Edouard Benedictus who used a piece of celluloid bond between two pieces of glass. After a strong hit the glass was broken but it did not split. At first laminated glass was used in gas masks during the First World War. The first car windshields with laminated safety glass were installed in 1924, which was a huge improvement to safety, because before that the injuries to drivers and passengers were mainly caused by sharp fragments of broken windshield. In 1936 the celluloid was replaced with polyvinyl butyral, which is used as a laminating film nowadays.

- 1918 Flat drawn sheet: The method to produce window glass in a continuous process was applied in the glass industry by the Belgian Emile Fourcault and American Irving Coldburn. In this method glass ribbon was drawn vertically from the tank as a flat sheet until it cooled sufficiently to allow the glass to be cut.
- 1953 Float glass: Between 1953 and 1957 Sir Alistair Pilkington and Kenneth Bickerstaff of the UK's Pilkington Brothers developed the method in which a layer of molten glass floats on a bath of molten tin. In the float method the smoothness of the molten tin is reproduced on the glass surface, which makes it optically superior. Thus, the reflection from float glass surface is mirror-like without any distortion. This is the standard method of producing flat glass today.

2.1 Soda-lime glass - Float line

There are a wide range of glasses, which all have different chemical compositions and physical properties. The formation, structure and properties of different glasses are widely dealt with in the literature [8].

Soda-lime glass accounts for 90 percent of all manufactured glass. Soda-lime glass is mainly used as windows in buildings and in the automotive industry. The most common soda-lime glass for windows is a mixture of silicon dioxide, i.e., quartz sand (weight percentage, 72%), sodium oxide (14%) and calcium oxide (9%) [7]. Other materials may be used as colorants, refining agents or to adjust the physical and chemical properties of the glass. Magnesium oxide (4%) is added to lower the melting point and aluminium oxide to improve durability. Colours in glass may be obtained by adding colouring ions that are homogeneously distributed and by preparation of dispersed particles as in photo-chromatic glasses [1]. Ordinary soda-lime glass appears colourless to the naked eye, when it is thin and green in thick sections. The green colour is due to iron oxide. When iron oxide impurity in raw materials is higher, the glass becomes greener, which reduces its light and solar transmission. Slightly green glass is commonly used in car windows. Low iron oxide impurity makes glass colourless. Low-iron glass is used as an example in solar power collectors, because its low light and short-infrared absorption yields to higher efficiency of the collector.

The float glass process starts by mixing the raw materials mentioned above. Usually, some crushed recovery glass is also added to the glass recipe. Mixed raw materials are fed into a furnace that is natural gas or fuel oil fired, and heated to approximately 1500°C. In a furnace the raw materials mix together and form a large pool of molten glass, the temperature of which is stabilised to 1200°C. The molten glass is fed through a delivery canal into a bath of molten tin which is about 4 m wide, 50 m long and 6 cm deep. The amount of glass allowed to pour into the molten tin is controlled by a refractory gate called a tweel. The tin bath is provided with a protective atmosphere consisting of a mixture of nitrogen and hydrogen to prevent oxidation of the tin. The glass ribbon flowing on the tin bath gets a perfectly smooth glossy surface on both sides, with an flat thickness of approximately 6 mm. Thinner glass is made by stretching the glass ribbon to achieve the proper thickness. Thicker glass is made by not allowing the glass pool to flatten to 6 mm. Machines called attenuators are used in the tin bath to control both the thickness and the width of the glass ribbon. When the glass flows along the tin bath, the temperature gradually decreases from 1100°C until the sheet can be lifted from the tin onto rollers at approximately 600°C. The total length of the float line shown in Figure 2.1 can even be 500 m. Typically a float line can be operated by about 10 persons in a shift. [7][9]

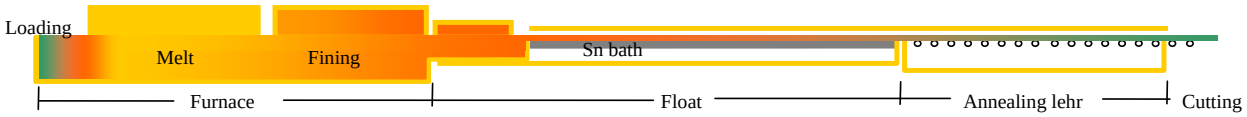

Figure 2.1. Schematic of float line.

When a continuous glass-strip has been formed at a high temperature, it must be cooled in such a way that it will be free of strains, which enables cutting without cracks. In glass annealing lehr the cooling speed during glass transition range (approximately 600-480°C) has to be slow, while residual stresses depend on the cooling speed, and at lower temperatures the release of permanent strains is not possible. A typical demand for the residual mid-plane tension in 4 mm annealed glass is about 1 MPa. Figure 2.2 shows examples of the annealing and cooling cycles, which are based on the method of Adams & Williamson as presented in [10]. The method gives a rather good estimate of real annealing cycles, but in actual practise the cooling curves are more like linear lines [11][12]. Thicker glass needs a longer annealing cycle, which in practice means a slower line speed. The production range of different float lines varies, but at least standard glass thicknesses between 0.5 and 25 mm are available in the glass markets today. The production capacity of the newish float line is typically between 500 and 1000 metric tons per day.

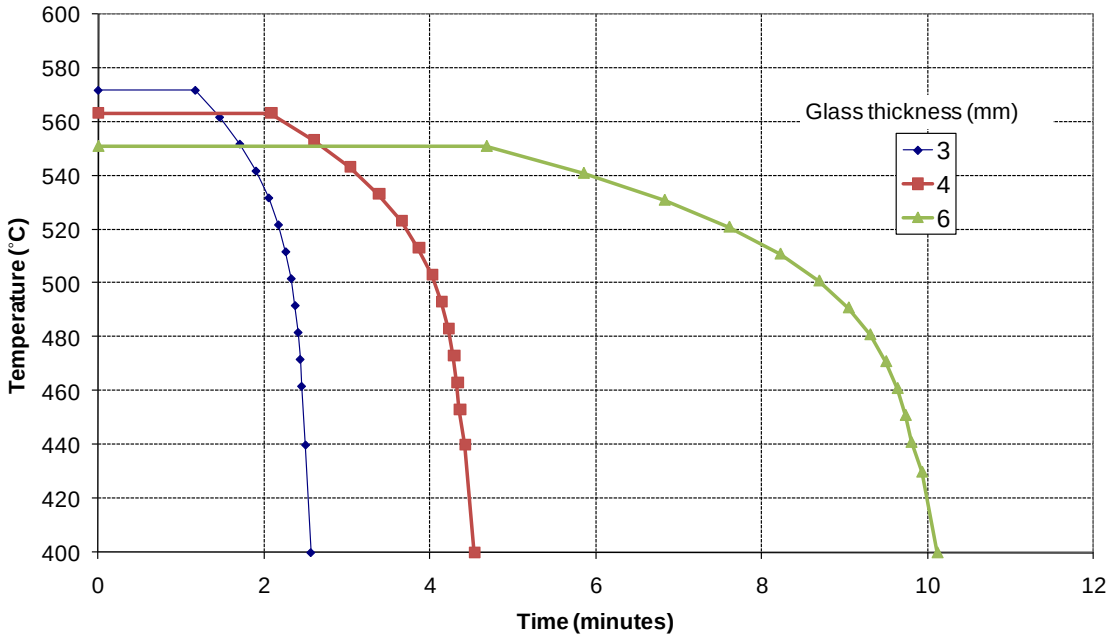

Figure 2.2. Annealing and cooling cycles of glass strip of various thicknesses according to the Adams & Williamson method.

After annealing, the glass-strip is cut into jumbo sheets, which have a common size of 3.21 m × 6 m. On-line quality control is of major importance in float glass manufacturing and as an example in some float lines an automatic quality control system marks defects like air bubbles with white paint. If the jumbo sheet coming out from the float line contains many marks, it is conveyed directly back to raw material storage. Accepted jumbo sheets are lifted directly off from the float line to glass racks or conveyed to a glass cutting line, where it is cut into smaller pieces. Marked glass pieces are rejected after cutting.

Jumbo or smaller sheets are delivered as raw material to float glass refining factories. Annealed glass sheets are cut to the right size and used in windows and in applications where strength and safety are not of major importance.

In 2009 about 380 float lines existed in the world, of which one half was located in China and 63 in Europe [7]. The world float glass market is still dominated by four companies: Asahi Glass, Nippon Sheet Glass (which includes Pilkington), Saint-Gobain, and Guardian Industries. Other companies like Pittsburgh Plate Glass, Fuyao Glass Industry, Sisecam, Central Glass, Euroglass, Visteon Corporation and Cardinal Glass Industries are clearly smaller manufacturers. Float glass production in Finland ended in July 2009, when the NSG/Pilkington float line located in Lahti was run down. The float line was small and old and it manufactured clear glass thicknesses from 1 mm to 6 mm. The market price of float glass depends on the global economic trend. As an example during the years 2007-2009 the price of clear float glass dropped from 450 to around 200 euros per metric ton in Europe.

During the float process some tin is absorbed into the glass, and with a proper ultraviolet light a sheen can be seen which differentiates the tin side from the non-tin side. A glass surface can be coated with a thin film to improve its properties in the final application. Coating can be made as an on-line process added to a float line or afterwards by conveying glass sheets through a coating line.

2.2 Coated glass

One of the first architectural coated glass products was introduced by Pittsburgh Plate Glass in the 1960s. This was known as light heat reflecting glass. Since then the development of coatings and coating methods has been intensive. Low-emissivity, i.e., low-e coating (1983) is one of the most notable inventions. One of the latest inventions is titanium-oxide based coating (2003), which gives self-cleaning properties for glass. Nowadays the development of the coatings on glass focuses particularly on solar energy applications.

Two common coating processes are chemical vapour deposition (CVD), and magnetron sputtered vacuum deposition. Chemical vapour deposition is an on-line coating method, in which the coating is applied to hot (about 600˚C) glass during float glass production. In the CVD-process, reactive precursors are vaporized into a carrier gas stream. The resulting vapour feed is directed to the glass surface where it reacts to form a coating. One of the most notable CVD-coatings is fluorine-doped tin oxide [13]. This is a low-emissivity coating, which is sold for instance under the brand name Pilkington K-Glass. CVD-coatings are also known as hard or pyrolytic coatings. Usually CVD-coatings are very resistant to rubbing, air and moisture. Most of the CVD-coatings are temperable.

In the magnetron sputtered vacuum deposition (MSVD) process material to be deposited, i.e., target material, and glass are in a vacuum vessel, where sputtering gas is ionized creating the plasma which is confined by magnets in front of the target material. Then, ions from the plasma are attracted to the target material by bombarding it and ejecting target material [14]. Next, sputtered target material atoms are attached as a thin film on the glass surface. MSVD is an off-line coating method, in which coating is applied to stock or cut sized glasses. Sputtered low-e coatings on the glass surface are multilayer coatings containing silver and metal oxides such as zinc oxide, tin oxide or titanium dioxide. In the low-e coatings shown in Figure 2.3 the functional layer is the silver layer, which reduces glass emissivity and similarly forms the glass surface almost as a radiant heat reflecting mirror. Usually, the innermost layer in the MSVD-coating is dielectric material layer, which reduces the reflectance of visible light from the metal layer. The total thickness of the sputtered coating is about 100 nm.

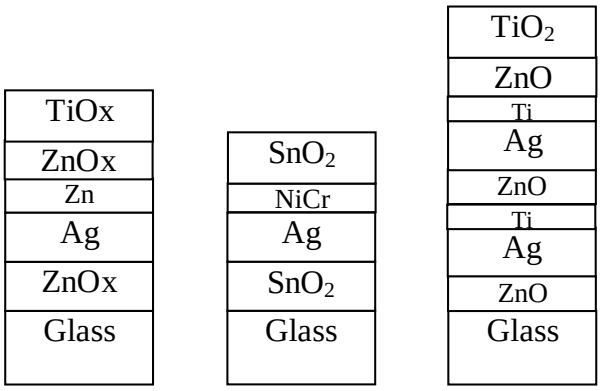

Figure 2.3. Compositions of some standard MSVD low-e coatings. [14]

MSVD-coating is often called soft-coating, because the coating is more susceptible to damage than CVD-coating, when exposed to air and moisture. Therefore, soft-coated glass is applied in insulated multiple-pane windows such that the coated side is in a gas-gap inside the window. In addition to that the coating should be removed from the sealant area near the edges of the IG-unit excluding some new coatings. Some of the MSVD coatings are temperable, and many high performance low-e coatings are among them. The energy saving performance of MSVD low-e coatings is better than that of CVD low-e coatings, and mainly due to that MSVD low-e coatings are much more common in windows nowadays.

Solar control and low-e coatings are two main applications of architectural glass coatings. The thermal performance is the key to using these products, either to solar control or insulation. These coatings are used to keep heat in or out from the room depending of the dominant climate, in which case heating or cooling costs decrease.

The primary purpose of a solar control coating is to reduce the heat gain by reducing the transmission of solar energy. A traditional solution to this problem has been to add such a material in a float glass recipe that absorbs solar energy. Sputtered solar control coatings are based on thin coatings of stainless steel and titanium nitride. These materials are very hard, durable and they absorb and re-radiate part of solar energy. Solar control coatings have typically from low to medium transmission in a visible spectral region and they have a higher reflectivity of solar infrared radiation than that of standard clear glass.

Low-e coatings are based on the lowering of a glass surface emissivity by adding a reflective layer to it. The low-e refers to a mid- and far infrared region above wavelength 5 μm of the spectrum, which is the region where surfaces near the room temperature radiate. The operating principle of a low-e coating is based on the behaviour of radiation on it. The sun emits light and short wavelength infrared radiation, which is mainly transmitted through the clear and low-e coated glass, while conventional low-e coating does not significantly change the glass surface reflectivity at these wavelengths. Instead, the glass itself emits thermal radiation at longer wavelengths, which is very effectively reduced by the low-e coating. Also, such a low-e coating is available, which effectively reduces the transmission of short wavelength infrared radiation. Thus, it keeps solar heat out of the building. The selectivity of the coating is defined as a ratio between visible light (wavelengths between 380↔780 nm) transmissivity and solar (780↔2500 nm) transmissivity.

Table 2.1 shows the main functions of different MSVD low-e coatings. The radiative properties of MSVD low-e coatings are dealt more closely in Chap. 11.

Table 2.1. Main functions of sputtered low emissivity coatings. [14]

Conventional low-e	High visible and solar transmission Low visible reflection High reflection of mid- and far infrared (room heat) Low absorption of energy Low emissivity
Solar control low-e	Reduced visible and solar transmission
Double silver-layer low-e	High visible with low solar transmission

Heat loss through a window (without frames) can be calculated by multiplying its heat-transmission value (U-value) with the temperature difference over the window. The major purpose of a low-e coating is to reduce the U-value. As shown in Table 2.2, in addition to the coating, U-value depends on the number of glasses in the window, the widths of the gas-gaps between glasses and the gas inside them. In practice, the U-value depends also on the wind speed (convection) outside.

In Table 2.2 the emissivity 0.837 is valid for clear glass, emissivity 0.16 is a typical value for CVD-coated low-e glass (for instance, Pilkington K-glass), and emissivity 0.04 is typical value for the MSVD low-e coating containing two silver layers. Conventional MSVD low-e coating contains one silver layer and has an emissivity of 0.08. Also, three silver layer containing MSVD coated glass is available.

Table 2.2. U-values as W/(m^2K) for insulating glass window. [16]

Glass number	Gas-gaps	Gas / Emissivity			Gas / Emissivity			Gas / Emissivity		
		Air	Air	Air	Argon	Argon	Argon	Krypton	Krypton	Krypton
layers	mm	0.04	0.16	0.837	0.04	0.16	0.837	0.04	0.16	0.837
2	9	1.9	2.2	3.0	1.6	1.8	2.8	1.1	1.5	2.6
2	12	1.6	1.9	2.8	1.3	1.6	2.7	1.1	1.4	2.5
2	15	1.4	1.7	2.7	1.1	1.5	2.6	1.1	1.4	2.5
2	18	1.4	1.7	2.7	1.2	1.5	2.6	1.1	1.5	2.6
3	9	1.2	1.3	2.0	0.9	1.1	1.9	0.6	0.8	1.7
3	12	0.9	1.1	1.9	0.7	0.9	1.7	0.5	0.7	1.6
3	15	0.8	1.0	1.8	0.6	0.8	1.7	0.5	0.8	1.6
3	18	0.7	0.9	1.7	0.6	0.8	1.6	0.5	0.8	1.6

Usually, low-e coating is only at one glass surface in a window. To keep solar heat out of the house in hot climates, low-e coating should be applied to the outside pane of the window (IG-unit). In Figure 2.4 low-e coating on the inside pane of a window reduces the infrared radiation from a warmer pane of glass to a cooler pane, thereby lowering the U-factor of the window, which cuts down the net heat loss from 108 to 70 W/m^2. Windows manufactured with low-e coatings typically cost from 10% to 15% more than regular windows, and they reduce energy loss through window by as much as 30% to 60%.

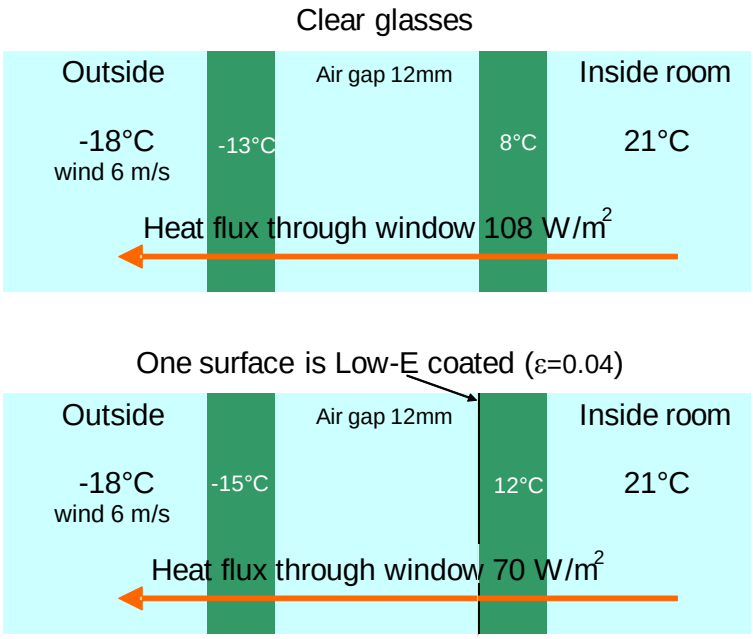

Figure 2.4. Performance of clear and low-e coated glass in a double glass window.

Other products that are commonly made with large coating units are mirrors of various kinds. A normal light and solar reflectivity of a clear glass surface is about 4%, which can be reduced with so-called anti-reflective coatings (SiO_2 and TiO_2 layers on glass surface). Anti-reflective coated glass is used for example in solar panels, monitors and picture frames. The glass used in photovoltaics solar panels is coated with electrically conductive transparent coating. In addition, there is a wide range of coatings used on the surface of glassware to improve the case-specific feature [15]. Anti-abrasion coatings are used in containers, defogging coatings in supermarket freezers and water repellent coatings in aircraft windows.

3. TEMPERED GLASS

The effects of "tempering" glass have been known for centuries. In the 1640s, Prince Rupert of Bavaria brought the discovery of what is known as "Prince Rupert's Drop" to the attention of the King. The drop is a teardrop shaped piece of glass which is produced by allowing a molten drop of glass to fall into a bucket of water, thereby rapidly cooling it. The heat treatment gives rise to unusual features, such as the ability to withstand a blow from a hammer on the bulbous end without breaking, but the whole drop will break explosively into fine-grained glass powder if the thin weak tail end is only slightly damaged. [17]

Early quotations dealing with the thermal strengthening of glass can be found at least from the New York Times - June 8th 1875, and from Chemical News - June 23rd 1876. These are short definitions of the process and improved glass properties, and the name of Alfred de la Bastie is mentioned in them. De la Bastie believed that the rapid quenching of glass hardened its surface in the same manner as that of quenched steel. Victor de Luynes (1828-1904) was a professor of chemistry in France, who around 1875 prepared several samples of tempered flat glass, which still exist at the CNAM-museum in Paris. The tempering was probably performed with oil. Luynes also designed testing methods for the strength of tempered glass plates, which are rather similar to methods used today. [7]

3.1 Basic idea of tempering and benefits of tempered glass

Float glass coming from the glass manufacturing factory is annealed. In an annealed glass the residual stresses are very low, which enables the cutting of the glass into smaller sheets. Glass tempering and heat strengthening are very similar processes in which the strength of float glass is improved with a heat treatment. In both processes the glasses are heated up to about 640°C and then cooled with air jets. Cooling creates a temporary thickness-wise temperature profile in glass, which creates residual stresses. The residual stress level depends on the cooling speed above 480°C, while at lower temperatures glass acts like an elastic plate. However, residual stresses level will still decrease if the cooling speed decreases totally at 480°C. In tempering the cooling speed of glass is much higher than in heat strengthening. Because of the lower cooling speed, heat strengthened glass is only about two times stronger than annealed glass, and it will fall apart in totally different fragments as tempered glass. A short review of how residual stresses are formed is given later on in Sec. 4.2. It should be noted that glass can be tempered because of the relatively sharp transition of its mechanical material properties in a temperature range between 480-600°C.

Figure 3.1 shows residual stress distribution inside a tempered glass plate. Compressive stress exists on the glass surfaces and tensile stress in the mid-layer. The surface compression is from 2 to 2.4-times higher than the mid-layer tension. According to [18] the the ration between surface compression and mid-layer tension can be clearly different if the cooling speed undergoes a step change during tempering. Typical surface compression in annealed glass is 2 MPa, in heat-strengthened glass 40-60 MPa, and in tempered glass 90-110 MPa. In a fire resistant tempered glass (FRG-glass) surface compression is about 160 MPa.

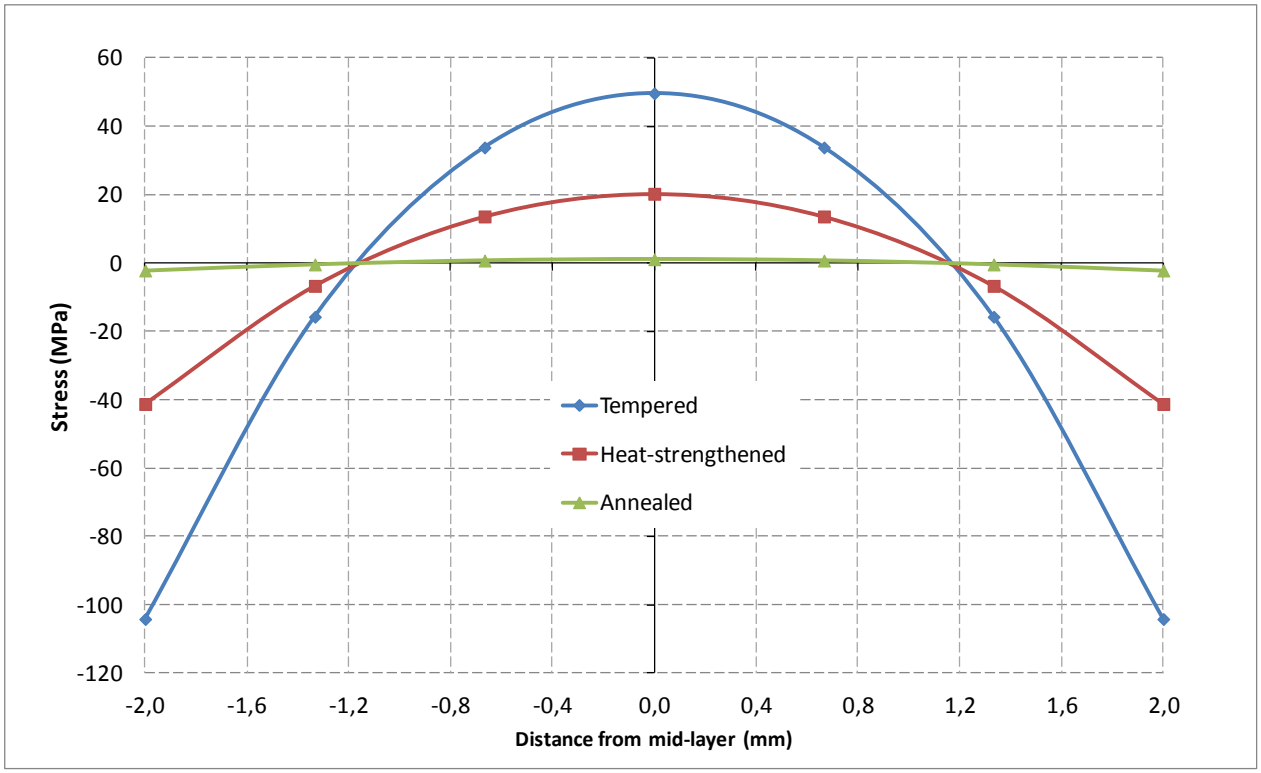

Figure 3.1. Typical thickness-wise stress profile inside annealed, heat strengthened and tempered glass.

In actual practise, what breaks a glass is tension stress at the glass surface. Annealed glass withstands about 30 MPa surface tension stress. In tempered glass high residual compression stress exists on glass surfaces. Strength depends directly on the surface compression level, while an external load must first overcome the surface compression before tension stress occurs at the surface. For this reason, tempered glass can endure many times more load than annealed glass. Tempered glass will sustain shock to the extent that it can be repeatedly struck by a hard object without breaking. It will also sustain a much higher thermal shock and sharper temperature gradients than ordinary annealed glass. Microfractures and scratches on glass surfaces have a significant effect on the strength of glass and they vary between glass plates. The strength of glass is a statistically predefined value. Standards define the testing methods for the strength of glass. As an example the Modulus of Rupture (MOR) strength of glass is determined by bending strength tests defined in standard ASTM C 158. The probability of breakage of annealed glass in 60 second load duration is 0.8% (typical design modulus of rupture), when the load is 19 MPa, and 50% (mean modulus of rupture), when the load is 41 MPa. Table 3.1 defines bending tensile strength and stress at breaking according to standard DIN EN 1288. The experimental relation between the strength of tempered glass and residual compression stress at glass surface is widely discussed in [19].

Table 3.1. Bending tensile strength and stress at breaking according to standard DIN EN 1288.

Stress at break due to impact	Annealed	Heat strengthened	Tempered
Characteristic tensile bending strength, static load (MPa)	45	70	120
Permissible bending stress with impact load (MPa)	80	120	170

The most popular device for glass surface stress measurement is the polarimeter called GASP, which is a registered trademark of Strainoptics Technologies Inc. Scattered light polariscope SCALP manufactured by GlasStress Ltd. is another device used for glass residual stress measurement. The accuracy of the measured surface stress depends on the device and its calibration. At best the accuracy is ± 3%.

Because of the internal stresses, tempered or heat strengthened glasses cannot be cut or drilled. Tempered glass plate will break instantly and totally into small fragments. These fragments are harmless differently as big sharp bits, which are formed when annealed or heat strengthened glass gets broken. This safe fragmentation, shattering, is the second main benefit of tempered glass. Thus, tempered glass is also called safety glass together with laminated glass. Laminated glass cannot fall apart into sharp fragments because of the tough film layer, which keeps fragments together. As described in Figure 3.2, cracks in heat-strengthened glass travel instantly to the glass edges, differently from annealed glass, where the propagation might even take years depending on external load. This difference in fracturing behaviour is due to different residual stress levels. The crack propagation and fracturing of tempered glass is widely discussed in [20]. The relation between particle count (see Table 3.3) and residual stress is studied in [21][22]. Surface compression needed for the same particle count decreases with glass increasing thickness. Also the shape of the thickness-wise stress profile in glass affects fragmentation. In [23] it was observed that the particle count is dramatically decreased if the depth of the compressive layer is less than approximately 20% of the glass thickness. The propagation speed of cracks in tempered glass is about 1466 m/s [24].

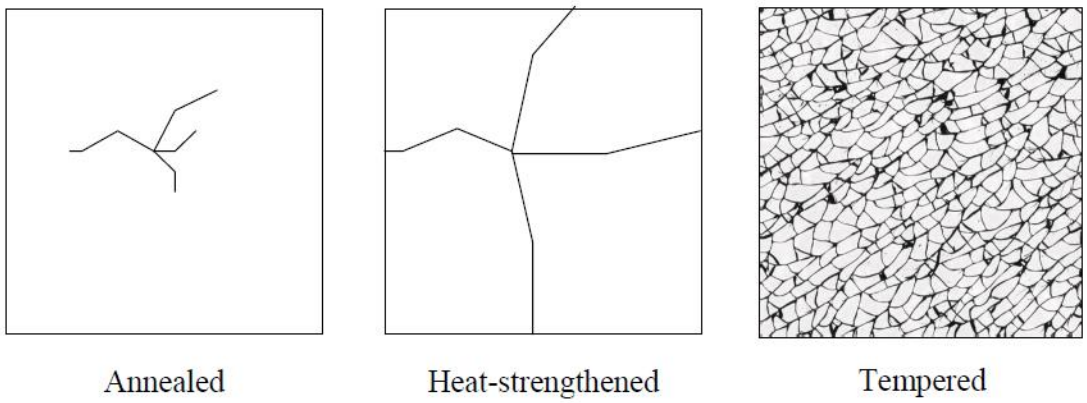

Figure 3.2. Fragmentation of annealed, heat strengthened and tempered glass.

Several standards have been developed for commercially used tempered glass, particularly for safety glazing in automobiles and buildings. Standards specify, for instance, tolerances, edgework, physical and mechanical characteristics, test methods, and fragmentation of tempered glass. Some important European standards are listed in Table 3.2. Tempered glass can be classified as safety glass if it fractures as standard EN 12150-1 defines. In tempered glass which has been fractured with a pointed steel tool the largest permitted length of the longest particle is 100 mm. In addition to that, the amount of particles in all 50 × 50 mm sized squares excluding border strip and the area near the impact point should be at least as high as Table 3.3 defines. In calculation of the fragment count each particle fully within the square is one, and each particle partially within the square is one half.

Different continents or countries have different standards. ANSI Z97.1 and JIS R 3206, for example, are the standards used for specifying tempered glass in the United States of America and in Japan. Glass should be broken with a certain pendulum according to the American (ANSI) standard, and the weight of the ten largest crack free particles should weigh no more than the equivalent weight of 10 square inches of the original specimen. Standard EN12600 specifies the European version of the pendulum test. The Japanese standard JIS R 3206 includes pendulum and ball drop tests. In practice,

the fulfilling of the EN-12150 standard demands higher residual stresses for tempered glass as the other standards above. Thus, it demands a stronger cooling rate in a chiller.

In general, the demands for automotive safety glass are clearly tighter than for architectural safety glass. In standard tests for automotive glass the breakage point is in the centre of glass, which gives clearly fewer fragments than breakage near the edges.

Table 3.2. Some important European standards.

EN 1863-1	Glass in buildings - Heat strengthened soda lime silicate glass - Part 1: Definition and description
EN 12150-1	Glass in buildings - Thermally toughened soda lime silicate safety glass - Part 1: Definition and description
EN 14179-1	Glass in buildings - Heat soaked thermally toughened soda lime silicate safety glass - Part 1: Definition and description
EN 1288 1-5	Glazing in buildings - Determination of the bending strength of glass
EN 12600	Glass in buildings - Pendulum test - Impact test method and classification for flat glass

Table 3.3. Minimum particle count values of fractured safety glass according to EN 12150-1.

Glass type	Nominal thickness in mm	Minimum particle count inside 50 × 50 mm area
Float and drawn sheet	3	15
Float and drawn sheet	4 to 12	40
Float and drawn sheet	15 to 19	30
Patterned	4 to 10	30

3.2 Range and use of tempered glass

Nowadays the range of different thicknesses to be tempered varies from a little below 3 mm to 19 mm. Also thinner tempered glasses down to 2.0 mm are coming onto the markets due to the newest inventions relating to tempering machines. The most common thicknesses of glasses to be tempered are 4 and 6 mm. Coating or paint on the glass surface is not an obstacle for tempering if it itself withstands high temperatures. The uncoated side is always placed in contact with rollers on the tempering line.

The glass size varies from small pieces to large sheets. The smallest temperable glass size is practically dependent of the roller pitch, which is typically 120 mm in a tempering line, where glass contact continuously with three rollers is a must. The largest temperable size is dependent on the furnace width and length. Today, the maximum furnace width is about 3.3 m. Thus, a jumbo sheet fits in the biggest furnaces.

Tempered glass is used in applications where safety and durability are important. Such applications are defined, for instance, in building regulations, which vary in different countries. Tempered glass is used in architectural windows, cars, facades, shower doors, solar panels, glass roofs, doors and rails, furniture, refrigerators racks and bus stop walls, to mention just a few. In many cases also laminated glass can be used instead of tempered glass.

3.3 Chemical strengthening

The chemical strengthening of glass is widely discussed in [20]. In chemical strengthening normal small ions are replaced with larger ions on glass surfaces. Due to ion exchange surfaces try to expand, which is not allowed by bulk glass and produces high compressive stress at the surfaces. In soda-lime silica glass the ion exchange of sodium ions (Na^+) in the glass surface with 30% larger potassium ions (K^+) has been found to give sufficient compressive stress at glass surfaces, but the time required to get a sufficiently thick (at least 0.1 mm) compression stress layer is relatively long. The strengthening is done by placing the glass in a hot bath of molten potassium nitrate.

Chemical strengthening has several advantages over thermal strengthening. Much thinner glass and unusual shapes can be strengthened. The strength of chemically strengthened glass can be even fivefold greater than in thermally strengthened glass. Chemical strengthening does not develop noteworthy tension stress to glass interior like thermal strengthening, and due to that it shatters into large sharp fragments like normal annealed glass. Thus, chemically strengthened glass cannot be used as a safety glass without lamination. Chemically strengthened glass is used, for instance, as windshields in high-speed trains and aircrafts, screens, laboratory pipettes, lenses and architectural panels.

4. STRESSES IN GLASS IN TEMPERING

4.1 Thermal stresses in elastic slab

Thermal stresses are a limiting factor in a tempering process because they can cause the bending of the glass during heating and can even break the glass.

At the beginning of the heating the glass interior is cooler than the surface layers. Because of temperature difference, the surfaces and the interior of the glass have a different rate of thermal expansion, but they must have the same length, which creates thermal stresses in the glass. In the centre the stress is tensile and in the surfaces compressive. The stress profile inside a free plate in which temperature field *T(x)* is one-dimensional is obtained as [25]

$$\sigma_{zz} = \sigma_{yy} = \frac{\alpha E}{1-\nu}\left(-T + \frac{1}{L}\int_0^L T dx + \frac{3x}{2(L/2)^3}\int_0^L T x dx \right) \tag{4.1}$$

where α is the coefficient of linear expansion, E is the modulus of elasticity and v is Poisson's ratio.

The glass interior stands much higher tension, than the surfaces, which are weakened by micro cracks. If the tensile stress in the centre is too high during heating, the glass will break into small crumbles almost like a tempered glass. These kinds of experiences have been obtained from actual tempering furnaces, when thick glasses are heated too rapidly. Even though, it is not known from where, at the edges or the interior the breaking has started, or if there have been problems in the glass quality.

The figure presented in [26] shows the temperature and stress distribution in the glass plate, which has been heated either with radiation or convection. In the modelling the convection heat transfer coefficient has been selected in such a way that the heating time is the same for both cases. In the glass which is heated with convection, the temperature differences and tensile stresses are larger than in the glass heated with radiation. Unlike convection, in which heat is totally transferred to glass via the surfaces, radiation is partly transferred directly to the glass interior, which evens the temperature profile.

The common problem caused by the thermal stresses is bending of the glass during heating or tempering cooling. The glass does not bend immediately when the thickness-wise temperature distribution is unsymmetrical, while gravity tends to keep the glass flat. However, in actual practise it is easy to create such an unsymmetrical heating recipe that glass bends. Transient bending during heating causes quality problems to be discussed in Sec. 5.6. A large square shaped glass is the most difficult one from the point of view of bending problems, which can be avoided by accurate furnace controlling actions. Some furnaces have better control possibilities than others.

4.2 Development of residual stresses in tempering

When the glass temperature is below about 480°C, its internal structure is very stiff. The coefficient of thermal expansion increases rapidly, and the elastic modulus decreases rapidly when the temperature rises from 480 to 600°C. At the same time the glass viscosity decreases, its structure became looser and internal stresses disappear, which is called glass relaxation.

In a tempering process the hot glass (over 600°C) is cooled with air jets. In that case the surface layers of the glass cool rapidly and become stiff. At the same time, the glass interior is still loose and contracts because of thermal contraction of the surface layers. When the interior still cools, it tends

to contract more, which is not possible because of the stiff surface layers. This creates a parabolic stress profile in the glass. There is a high compression stress in the surfaces and a high tension stress in the mid-plane. Due to the fact that residual stresses depend on the temperature difference between glass surfaces and mid-plane, a thin glass has to be cooled through the transition range much more rapidly than a thick glass. Cooling at the glass (whole thickness) temperatures below 480°C has not much effect on the tempering stresses. Thus, in practice tempering stresses in a thin glass are formed during the first few seconds of cooling.

Bartenev [27] introduced in 1949 the concept of instant freezing, which is the simplest method for calculating tempering stresses in glass. According to the assumption, the glass freezes instantly at an empirically determined temperature T_f, which is about 550°C for soda-lime glass. Above the freezing temperature the glass is characterized as a liquid with a zero viscosity. Thus, the glass above T_f offers no resistance to the distortion and is incapable of supporting any stress. Below T_f, the glass is treated as an elastic solid. A one-dimensional calculation method for tempering stresses using the instant freezing assumption is presented in [28]. The calculation method gives the basic understanding how stresses develop at glass temperatures above T_f and gives a rough estimate of the residual stress profile obtained in tempering. More sophisticated methods with practical results are presented in the literature [29][30][31][32]. The transient stresses during cooling at glass temperatures below T_f in a glass slab can be solved when the instant freezing method is coupled together with Eq. (4.1).

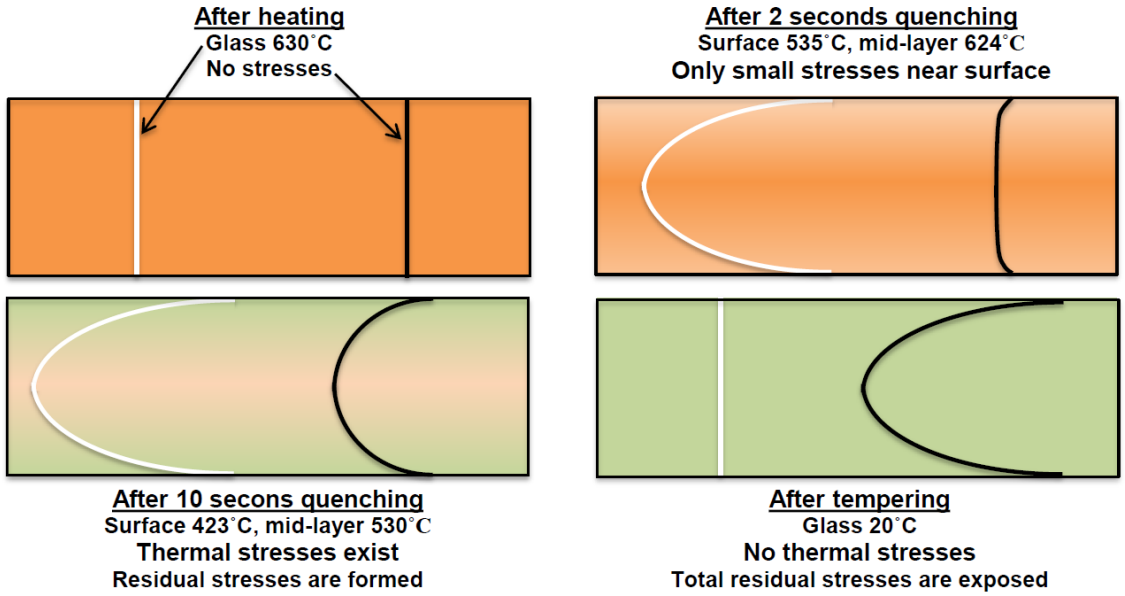

Figure 4.1 Transient thickness-wise temperature (left, white line) and stress (right, black line) distributions in 6 mm glass during tempering.

Figure 4.1 shows an example of the development of temperature and stress profile in a glass slab during tempering cooling. Just before cooling both temperature and stress profiles are straight lines. At the very first moments at the beginning of the cooling transient tension stress occurs on glass surface the level of which depends on the cooling rate, glass thickness and glass initial temperature [33]. It might even break the glass if the cooling speed is too fast or glass is too cold for tempering. After 2 seconds cooling the 6 mm glass in the Figure 4.1 is still at the transition temperature and the stresses are small. At temperatures just below the transition range the glass has still a full thickness-wise temperature distribution, which generates stress distribution to glass in the opposite direction to tempering. Thus, the total transient stress distribution has still quite a low-gradient, while stress distributions weaken each other. Finally, temperature distribution disappears and the full magnitude of residual stresses is exposed.

5. FLAT GLASS TEMPERING PROCESS

Plate glass tempering on a commercial basis was developed with the technical collaboration of the Saint Gobain Company. The first patent was granted to Boussois Plate Glass works in France in 1928. Marketed under the trade name Securit, tempered glass started to replace ordinary glass in the automotive field [34]. Nowadays, in addition to vehicles tempered glass is commonly used in buildings, furnishings, and many other products. Architectural tempered glass is mainly flat and tempered automotive glass is often curved.

There are a wide range of companies in the markets producing glass tempering machines. The Finnish company Glaston Finland Oy (former Tamglass Engineering Oy) has long been a dominating manufacturer of flat glass tempering machines in the Western World. At the moment its competitors are companies such as TCME (Taiwan), LandGlass Tech. Co. Ltd. (China) and Luoyang Northglass Tech. Co. Ltd (China), which is the biggest furnace deliverer in China. The situation is typical of global markets today; relatively new Chinese companies offer machines with lower investment costs, and more experienced companies respond with higher utility value. It is estimated that in 2007 the total number containing also the smallest new float glass tempering lines delivered in the world was about 700 and the total value of the market was about 300 million euros [109]. A typical delivery price in 2012 of western made average-sized flat glass tempering line was 0.6-1.2 million euros depending on the furnace model and accessories.

In this chapter a short overview is presented concerning different types of flat glass tempering lines in use in the market today. A typical tempering line is introduced in detail as are also the main quality defects of tempered glass. The pre-processing before tempering is treated very briefly, because all processes without heat treatment are outside the scope of the present thesis.

5.1 Pre-processing

The first process in a flatware glass factory is glass cutting, in which large jumbo sheets of float glass coming from a float factory are cut into the sizes defined in the orders. The second pre-processing step is edge removal and grinding. All these treatments are coupled together in a modern pre-processing line. The strength of glass is very dependent on the quality of these treatments. Holes can also be drilled into glass and glass can also be partially painted. Before further processing the glass has to be washed and dried. For example, fingerprints must be cleaned before heat treatment, which would make them more visible and permanent. Washing and drying are usually done with automatic cleaning machines.

5.2 Tempering furnaces

Tempering lines are either horizontal or vertical. In the past before a horizontal method was invented, glasses were tempered in a hanging position. A vertical furnace can still be useful if the glass is painted or coated on both sides or if the glass is not flat. In a horizontal furnace the glass moves on the top of rotating rollers made from fused silica.

The furnaces used today can be divided on the basis of the following factors:

- Movement of glass: continuous or oscillating
- Heating energy: electricity or gas

- Top resistors: open coil or enclosed coil (coil = resistor wire spooled around ceramic tube)
- Main heating principle: radiation or convection
- Convection system: circulating air or flow-through air convection
- Phasing: one chamber or two chambers

In continuous tempering glass plates move along the entire furnace length in a continuous flow. The furnace is rather long, at least 20 m, so that the glass has time to heat up properly. A process like this has proven to be best for long serial production runs. In the mid-70s a furnace was developed in which glass is moved back and forth until the heating time is past [35]. Such oscillating batch-type furnaces were quickly found to solve many problems for varying production and they became very popular among manufacturers. Tempering using a horizontal oscillation is the most common tempering method today.

Burning natural gas or heating with electrical resistors inside the furnace creates heat for the process. Electricity is the preferred choice and gas is used in less than 5% of furnaces. The main advantage of electricity are: it is easy to control, the temperature settings are very accurate, there is no exhaust gas discharge in the factory and investments required for electricity are very competitive.

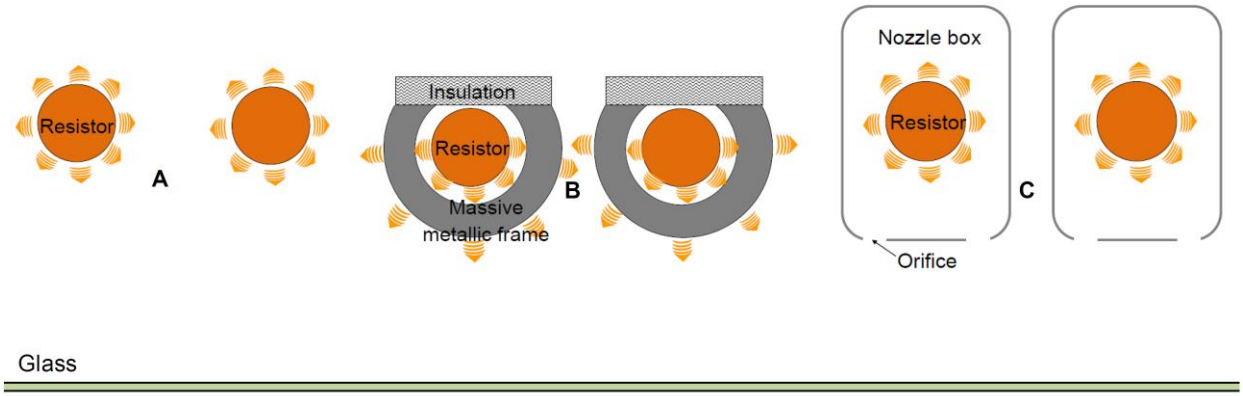

Figure 5.1. Different resistor assemblies used in tempering furnaces.

Top heating resistors inside the furnace are either open coils (see type A in Figure 5.1) or coils placed inside massive metallic casings (type B), which are able to store heat at the end of a heating cycle, when the electric power of resistors is higher than the power radiating to glass. Again at the beginning of heating the casings radiate stored energy to the glass. Thus, with the massive casings the electrical peak power of a furnace can be reduced. The electrical peak power of a tempering line is relatively high and it can be a problem in many places. High peak power leads also to additional costs due to high transformers and wiring sizes. Outdated control technology used relay switches to control the delivery of electric current to the resistors. The use of massive metallic casings decreased the amount of on/off -switching during a heating cycle, which gave more lifetime to the relays. Modern control technology uses semiconductor switches, the lifetime of which is independent on/off –switching. Open coil heaters (type A) with most recent control technology also enables balanced furnace operation and gives a much faster response to control actions than the resistors in massive metallic casings. Usually, bottom heating resistors are open coils covered with a thin metallic casing or a mesh, the function of which is just to protect the open coils against broken glass. Previously handled resistors radiate heat directly to the glass or rollers. They also transfer heat to air, but not very effectively. In circulating air convection systems open coil resistors are located in air channels (see Figure 5.2) or inside nozzle boxes (type C in Figure 5.1). Particularly, the resistors located in air channels first transfer heat mainly to air, and then heat is transferred from air to glass. With the

invention presented in [36] air velocity on the surface of the C-type resistor can be accelerated and shared evenly to whole length of the resistors. This intensifies and evens the heat transfer from air jets to glass and decreases resistor temperature, which gives more lifetime to it. In new furnaces in the market resistor types A and C are used. The manufacturing of furnaces equipped with type B resistors was common for a long time. Though this ended a few years ago such furnaces are still common in the world.

In the simplest tempering furnaces the heating of glass is based on thermal radiation exchange between resistors and glass, and in addition to radiation also natural convection and contact heat transfer from rollers to glass occurs. When low-e glasses appeared in the market at the end of the 80s, the use of forced convection in tempering furnaces became necessary. The low-e coated glass surface can reflect as much as 90% of the thermal radiation emitted by the furnace resistors. With forced convection the heating of the coated side of glass can be intensified to keep the glass flat in the furnace. Usually, the forced convection is arranged with air jets, which are focused to impinge on the glass surface. Nowadays, forced convection is used together with radiation to intensify heat transfer even for clear glass. In a radiation-convection furnace thermal radiation is clearly the main heat transfer phenomenon. In a typical radiation-convection furnace the convection is arranged by blowing compressed air coming from an air compressor outside the furnace toward the glass surface through holes in pipes. This kind of convection is flow-through air convection, because the same amount of air blown into a furnace is also blown out from the furnace.

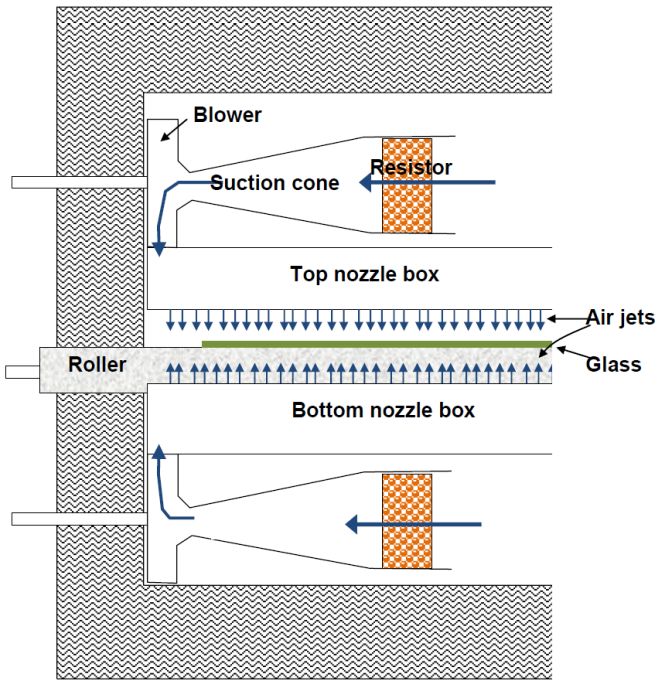

Figure 5.2. Basic principle of circulating air forced convection system.

In a high-convection furnace the idea is to heat glass as much as possible by hot air convection rather than by radiation. In a typical high convection furnace fans blow hot air through nozzles toward the glass surface and heat input is arranged with air heating resistors inserted in air channels as in Figure 5.2 or in nozzle-boxes. This kind of convection is called circulating air convection, while the same air flow is circulated in the furnace. The functioning of a circulating air convection furnace is dealt with in detail in [37]. Particularly when low-e coated glasses are heated, the convection heat transfer rate must be much higher on the top side than on the bottom side of glasses. Circulating air convection is typically stronger than flow-through air convection, but on the other hand a circulating air convection system clearly costs more than a flow-through air convection system. This fact has been

considered in so-called hybrid-convection furnaces, where circulating air convection occurs on the top surface of the glass and flow-through air convection occurs on the bottom [38]. Such a solution is quite optimal, because the bottom convection is a good tool to for keeping glasses flat during early stages of the heating, which often succeeds in quite low convection rate.

The concept in which a high-convection pre-heating furnace is added to a radiation-convection furnace has been in the market since 80s. At first glass is heated in a high-convection chamber up to 400-500°C, after which the glass is moved into a second chamber, where the rest of the heating is done. Such a two chamber furnace is dealt in [35]. Heat transfer in a high-convection pre-heating furnace is theoretically and experimentally presented in [39]. In a two chamber system the heat-shock exposed to glass at the beginning of heating can be reduced, which helps to keep glass flat at the early stage of heating. The production capacity of such a furnace is 1.5-1.7 times larger compared to that of a one chamber furnace. In some rare cases three furnaces are combined together and glass can be processed in a continuous or oscillating flow depending on the glass thickness.

5.3 Glass tempering cooling

Cooling in a tempering process is arranged by blowing cold air with a high velocity towards the hot glass surface. The air flow is arranged with fans blowing air via flow channels and nozzle boxes to nozzles. Then air discharges and forms air jets, which hit the glass surface. Residual stresses created in tempering are dependent on the temperature difference between the glass surfaces and mid-layer during cooling. It is more difficult to create sufficient temperature difference when the glass thickness decreases. Thus, the cooling power needed for tempering increases strongly with decreasing glass thickness. In Figure 5.3 the fan power needed to create air jets is shown as a function of a glass thickness. The curve in the figure is based on Eq. (12.19) and on the data from the real tempering process. The results are expressed for a glass square meter and it is assumed that the chiller area is full of glass. For instance, if glass thickness is halved from 8 mm to 4 mm, then P_{fan} becomes 42-times higher. Glass thicknesses above 12 mm can be tempered almost without forced convection. For a 3 mm glass the needed power is 130 kW/m^2. The fan power needed for thinner glass could be reduced clearly if the chiller could be designed only for them. In actual practice, for instance the diameter of the rollers in the chiller is determined by the maximum glass weight. A bigger roller diameter leads to weaker convection because it reduces the proportion of the nozzle area in a chiller.

Cooling sections in glass tempering can be divided into two groups;

- Oscillating chiller with or without compressed air boost system
- Pass-through chiller with oscillating or continuous after-cooling chiller

In traditional tempering after-cooling happens in the same chiller as tempering cooling, i.e. quenching. Glass moves back and forth from the beginning to the end of the chiller until it is cold enough to be conveyed on an unloading board. For glass thicknesses clearly below 4 mm an air compressor is needed in addition to fans to produce compressed air. Such a chiller is described in detail in Sec. 5.5.

In a pass-through chiller a thin glass up to 4 mm is tempered when it moves through a relatively short (about 2 m) tempering cooling, i.e., quenching section. The rest of the cooling happens in an after-cooling chiller, where the glass moves back and forth (not in a continuous tempering line) until it is cold enough. In a pass-through chiller a high cooling rate is arranged with two powerful fans, the blow of which is focused on a relatively small area. The maximum available overpressure in nozzle boxes is much higher than in a traditional chiller mentioned above. Thus, compressed air jets are not needed.

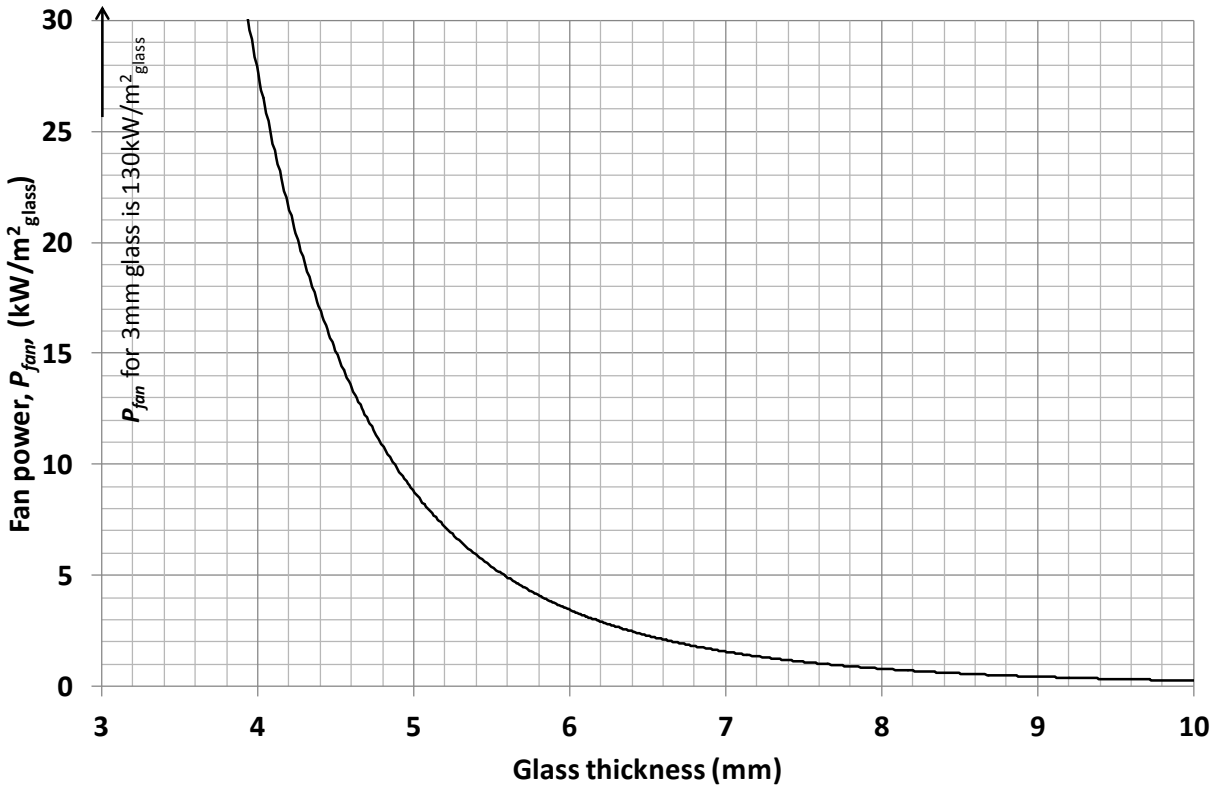

Figure 5.3. Fan power needed to create jets per glass square meter to fulfil the demands of EN-standard for tempered glass.

5.4 Problems in thin glass tempering

The major disadvantage of air jet tempering is the need for high electric power when thin glass is processed. The total input power of a chiller can be one megawatt. The energy consumption in a tempering cooling of 3 mm glass takes about 1.5 kWh per glass square meter depending on the chiller type, production capacity and loading degree. Thus, in the worst cases cooling takes clearly more energy than heating, which for 3 mm glass takes 1.4 kWh per glass square meter and losses depending on the furnace model.

The problem of thin glass thermal tempering has been realized already many decades ago. Many patent applications have been written during the last century which have attempted to arrange cooling with a water mist, water vapour, contact heat transfer, liquid nitrogen and carbon dioxide snow. Recent research [40] concerning the water mist tempering of glass indicates the potential for substantial energy savings. Contact heat transfer tempering is under new research also [41]. In both of the previous references small pieces of glass were tempered quite successfully, but the tempering was far from easy and unfailing, which is not promising for true-scale production of tempered glass. With air jets the breakage of glass during tempering is very rare as long as the glass is warm enough for tempering. However, in spite of a wide range of ideas, glass (thermal) tempering in today's world is arranged with air jets.

The minimum glass temperature needed to make tempering possible increases with decreasing glass thickness. The typical temperature just before cooling for 3 mm glass is about 650ºC. From the point of view of residual stresses and energy saving it would be advantageous to use higher temperature, while the cooling rate needed for tempering decreases up to a certain limit with increasing glass temperature. Unfortunately, glass stiffness decreases also with increasing temperature and then the

glass bends and creeps more during heating on the top of rollers in a tempering furnace, which leads to increasing roller waves and edge lifts (see Figure 5.16). Thus, in addition to cooling, the problem of thin glass tempering concerns heating also. The solution to the problem has been looked for from air float tempering, where glass floats supported by a thin pressurized air layer above a heating plane. The devices in [42] have a small drift angle so that the lower lateral edge of glass is in contact with a plurality of rotating driving discs. The air layer is generated by air flow through holes in the heating table below the glass. The glass will bubble up in the centre in the device, with air inlet holes only in its heating table. With air outlet holes in the heating table it is possible to create a more uniform support bed. The manufacturing of car side-glasses succeeds with the horizontal air flotation technology just described. In such an existing furnace the ceramic air flotation table slowly changes from a flat surface to the desired curvature of a car side-glass. The problem caused by non-uniform air support increases with decreasing glass stiffness. Thus, success is not sure if it is attempted to process clearly thinner, larger and hotter glass than car side-glass with horizontal air floating technology. The corners of such a glass can even creep through a thin (below 1 mm) air bed on contact with the heating plate below the glass. In the device in [43] the glass is in a vertical position between two vertical heating plates. Now, the jets discharging towards the glass from the holes in the heating plates keep the glass apart from the heating plates and the glass is supported only by driving discs from the glass bottom edge. It is apparent that such support will cause local bending near the bottom edge of thin hot glass.

On the other hand, the market for tempered glass thinner than 2.8 mm is still small or does not even exist. Even the standard defining the quality demands for such glass is missing. However, it is evident that the markets would grow rapidly if such a glass with acceptable quality and price were on sale. Increasingly thinner tempered glass would be advantageous, for instance in solar panels, because smaller glass thickness improves their efficiency. Such a glass could be used also in applications where lightness is advantageous.

The new tempering technology called GlastonAir^{TM} can temper 2.1 mm glass up to surface compression level 130 MPa without the roller wave distortion problems. It consists of a preheating furnace and final heating furnace. In the preheating furnace the glass is on rollers and in the final heating furnace it floats above an almost horizontal air flotation table. In the tempering chiller the glass moves on top of rotating rollers as in a traditional chiller. First GlastonAir^{TM} was sold to Tecnoglass S.A at the end of 2014 and it is planned to be in production at 2016 in Columbia.

5.5 Typical tempering line

Figure 5.4 shows a common batch-type tempering line, which consist of the following sections

- Loading table (a)
- Heating furnace (b)
- Cooling section (c)
- Unloading table (d)

In addition to the sections above also a fan room and electric cabinets are parts of the tempering line.

In the most common line the furnace length is about 6 m and the size of glass load can be 4.8 × 2.4 m. The lengths of the chiller, loading table and unloading table are about the same as the furnace length. Thus, the total length of a typical line is about 24 m. Heating is arranged with radiation and forced convection in the furnace in Figure 5.4. In addition, contact heat transfer occurs between glass and ceramic rollers. Figure 5.5 shows an inside-view of the furnace.

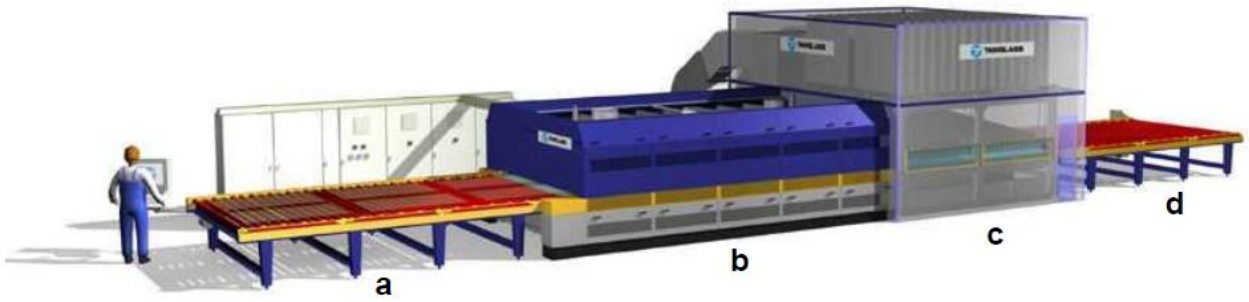

Figure 5.4. Tempering line. [109]

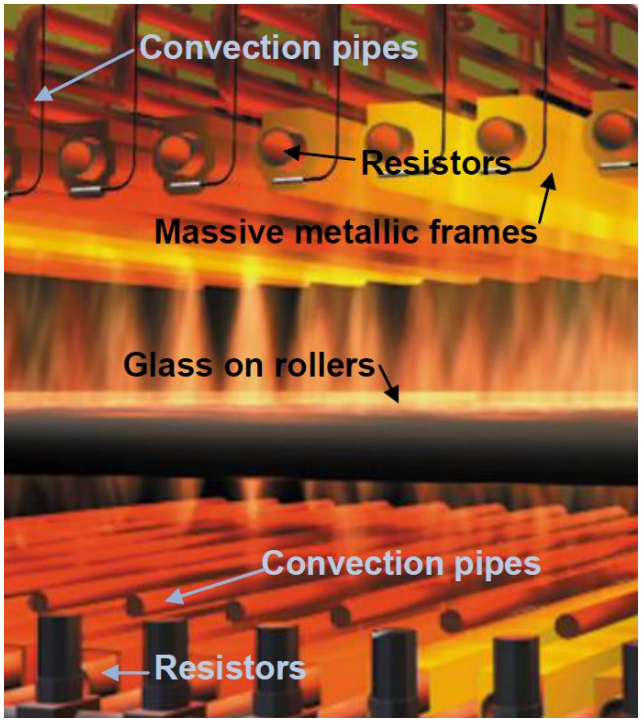

Figure 5.5. Inside view of tempering furnace. [109]

Usually the resistors are longitudinally orientated, which makes it possible to profile heat transfer in a lateral direction. In the furnace in Figure 5.5 the upper side electrical resistors are located inside massive metallic casings. The temperature of each casing is measured with thermocouples, which enables exact temperature control. A typical control temperature is 700°C. At the beginning of heating when a cold glass loading is conveyed into a furnace the radiation from the casings to glass is higher than the electrical power of the resistors. Correspondingly, during the end phase of heating the radiation to glass is smaller than the electrical power and then the massive metallic casings store energy. In practice, this means that the temperature of the casings decreases during the early phase of heating and increases back to the control value after that. In this way the electrical peak power is reduced. The function of the resistors described above during different heating cycles was studied in [39]. Bottom side heaters have thin steely covers over them to protect them against broken glass. On the bottom side of a furnace the ceramic rollers are able to store and transfer energy. The most common roller diameter is 95 mm. Glass and the roller have a contact line at the distance of the rollers, which is typically about 120 mm. Contact heat transfer from rollers to glass is a spontaneous phenomenon which cannot be controlled during heating. The direct radiation from the bottom resistors to the glass is relatively quite low due to the narrow gap between rollers. Thus, the main heat

transfer path to glass at the bottom side is that the bottom resistors radiate to the rollers and the rollers radiate to the glass.

The furnace in Figure 5.5 is equipped with longitudinally orientated top and bottom convection pipes. In Figure 5.6 cold air fed by an air compressor flows along a pipe into a furnace. Compressed air flows in a hot convection pipe into the furnace and heats up almost to furnace temperature before it flows into the first orifice. Air jets are formed when hot compressed air discharges from small diameter orifices in convection pipes into the furnace. At the same time an equivalent amount of hot air is blown out from the furnace via open shutters in a ceiling. Energy loss along with hot escaping air is the major weakness of this kind of convection system, when it is compared to the circulation air convection system. On the other hand, this is a very reliable way to create air jets, because there are no moving parts in a hot furnace. Forced convection heat transfer from air jets to glass is controlled with the pressure in the pipes. Convection is used to intensify the heating, and with convection it is quite easy to balance heat transfer on the top and bottom surfaces of the glass and avoid the bending of glass during heating. The bending of glass due to thermal stresses caused by unbalanced heat transfer is a problem particularly at the early stages of the heating cycle. Convection is effective at the early stages, when the temperature difference between air and glass is high. At the final stages of heating the air and glass temperatures are close to each other, which makes convection rather useless. For these reasons the pressure controlling convection changes during the heating cycle and at the final stages pressure is often switched off. Valves of the convection pipelines, which are located outside the area of glass loading, can be closed and convection heat transfer can be focused to the selected width of glass loading. Such a width-wise profiling of heating is a very useful control method, which enables better glass quality and energy savings [44]. All valves are closed at once when the furnace is empty. In some furnaces energy losses are reduced by using heat exchangers in which hot escaping air is used to preheat the cold incoming compressed air.

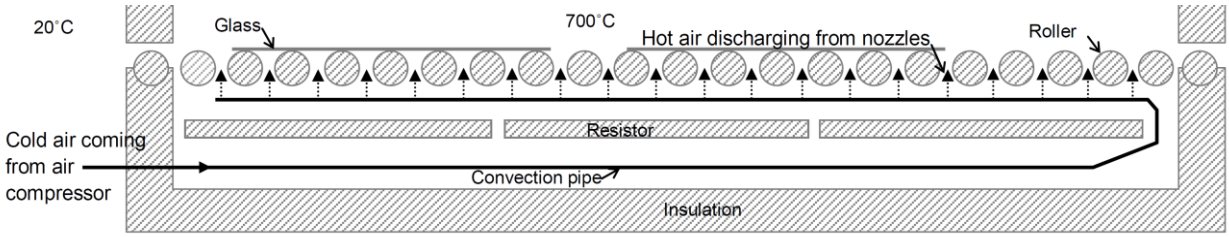

Figure 5.6. Schematic of bottom convection pipe in furnace viewed from side direction.

The control of glass heating is based on heating recipes which have been developed on the basis of practical and theoretical know-how. After heating, the glass temperature should be uniform and between 610 and 650°C depending on the glass thickness. The result of the heating is monitored. A thermal scanner measures the glass temperature when it moves from the furnace to a cooling section. Figure 5.7 is an example of the thermal image taken from the glass loading with six glasses. The uniformity of glass temperature is not acceptable in the figure due to too large temperature variation. Usually the thermal image is scanned from the glass upper surface. If the upper surface is low-e coated, the measured temperatures are unreliable, but the uniformity of glass temperature can be detected.

An operator controls the furnace using an operating panel. The operating panel shown in Figure 5.8 is used in the furnace model in the market nowadays. The operator selects heating and cooling recipes according to a new glass loading from the loading table. The most important factors to take into account in the recipe selection are the glass thickness and type (clear glass, low-e glass, other). Also the loading rate and glass size have an effect on the heating recipe. The most difficult glasses to be tempered are large square-shaped low-e coated glasses, because it is particularly difficult to keep

them flat during heating and cooling. After the main recipe is chosen, an operator makes changes if needed. The operator can change the control temperatures, convection pressure-time curves, heating time, and some other factors. If a new recipe is worth saving, then the operator saves it in to the recipe library. More details concerning the heating control system can be found in [45].

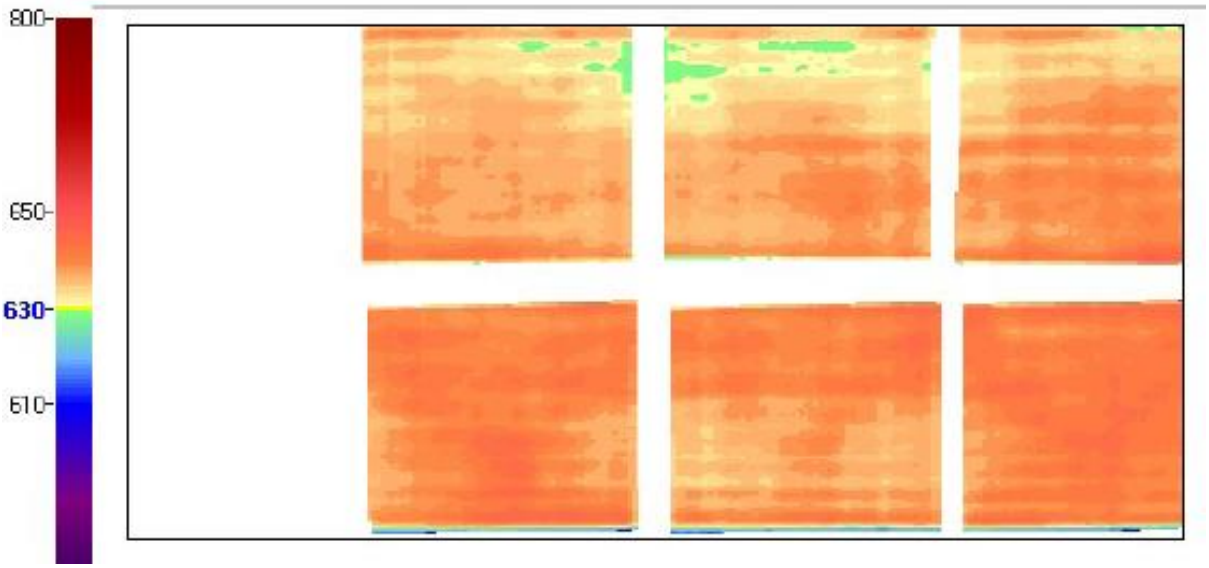

Figure 5.7. Thermal image of glass loading just after heating. [109]

Figure 5.8. Operating panel of modern tempering furnace. [109]

An advantage of longitudinal resistors is that heat transfer can be profiled with them according to the glass width. This means that the control temperatures of resistors next to each other can be different. For instance, if glass lateral edges tend to be heated more than other glass width, then the control temperature of the resistors just above and below the lateral edges could be decreased to prevent overheating.

Automation in process control is increasing, but automatic process control almost without an operator is still just a distant vision. An automatic process control includes a machine vision system which can identify the glass type, thickness and loading pattern on the basis of which a computer selects heating and cooling recipes automatically. Upcoming projects and years will show how comprehensive this kind of process control can be. One major problem is quality control, because the computer does not know if the glass is still unbroken, flat and optically good after tempering. A skilled operator can see from the thermal image or from the heated glass loading if the heating is well-timed and balanced and makes the necessary control actions. The thermal image can be delivered as numbers to the computer, but the data analysis behind correct control actions is very complicated.

The glass loading moves back and forth in the furnace described above, and when the heating time runs out the glass is conveyed into a cooling section.

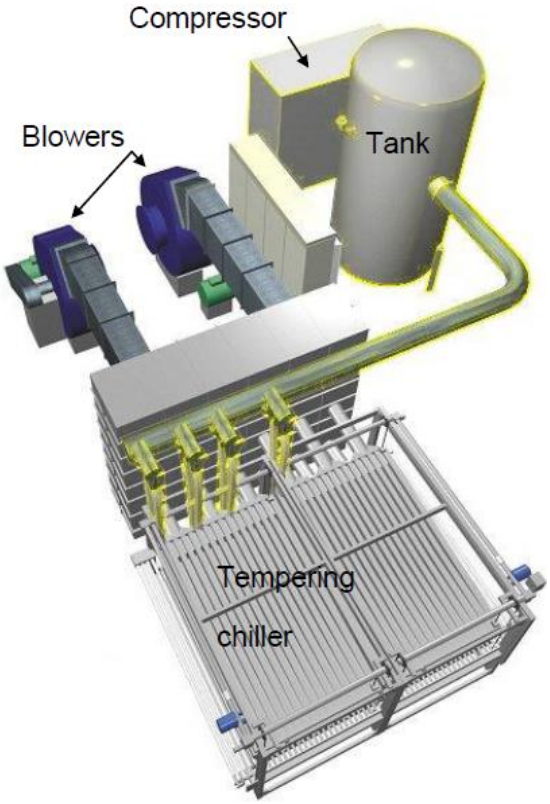

Figure 5.9. Cooling section in a tempering line. [109]

Figure 5.9 shows a schematic of the cooling section, where the glass is cooled with air jets. During cooling the glass moves back and forth over rollers, which are sparsely spooled with a cord made from an aramid fibre. The cooling section in Figure 5.9 consists of two fans, flow channels and a chiller with nozzle boxes. The fan impeller diameter is about 1.5 meters and the motor shift power is 300 kW. The cooling rate depends on the overpressure in a nozzle box, which is controlled by blocking the fan's air intake with a vane adjuster or by changing the rotating speed of the fan's impeller with a frequency converter. The rotation speed control enables significant energy savings when compared to the throttle control. Typically, the maximum overpressure which the fans can create in the nozzle boxes is about 7.5 kPa, which in the chiller in Figure 5.9 is a little more than is needed for tempering 4 mm glass. The tempering of thin glasses requires just a few seconds of powerful forced convection, after which the rest of cooling is handled by using much lower overpressure. In addition to the overpressure the cooling is also controlled by changing the vertical distance between nozzle box and glass. The minimum distance is about 15 mm, which is typically used for thin glasses.

In a boost tempering system compressed air is used in addition to the fans to intensify forced convection [46]. In that case an air compressor with a compressed air tank is a part of the cooling section, as in Figure 5.9. The main nozzles are rounded holes in nozzle boxes, and as seen in Figure 5.10, compressed air discharges from a small diameter nozzle via the main nozzle towards to the glass surface. A typical boost system enables the tempering of 3 mm glass.

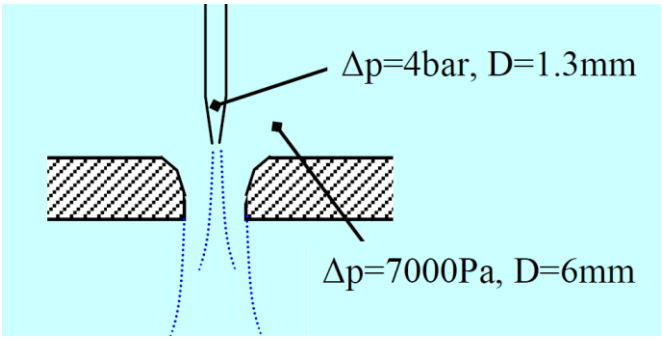

Figure 5.10. Structure of boost tempering nozzle.

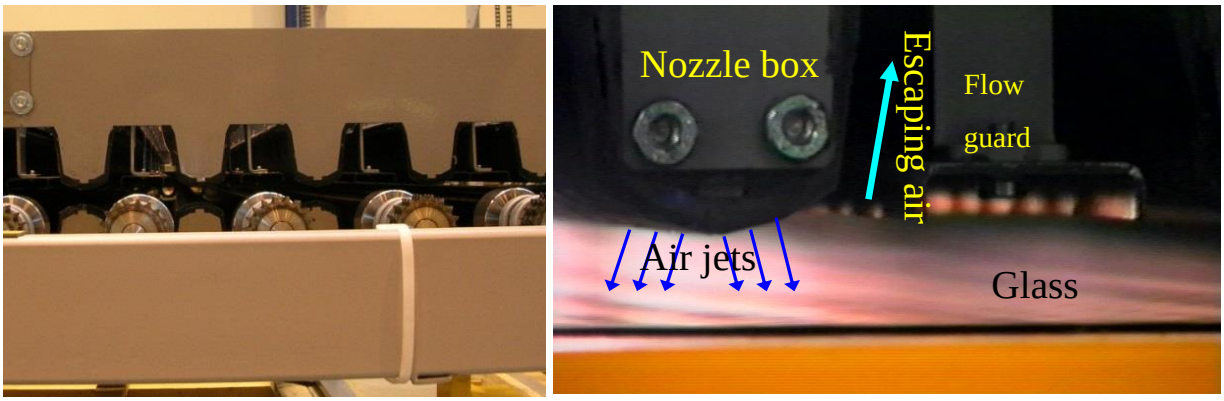

Figure 5.11. Nozzle boxes viewed from the side.

Escaping air is guided out from the cooling section via channels between nozzle boxes, which have flow guards between them (see Figure 5.11). The function of the flow guards is to block escaping air flow to the same extent as the rollers do on the glass bottom side. Without them the air static pressure below the glass would be higher than that above the glass and glass would be lifted off from the rollers. The whole cooling section is inside the hood, which blocks off uncomfortable outflows and noise from the factory hall. Sometimes glasses get broken in the chiller, because of too low tempering temperature or failure in the glass. For that reason it is important that glass crumbles have enough space to drop down, although it usually requires laying down bottom nozzle-boxes. When the glass is cooled enough for handling it is conveyed to an unloading table.

5.6 Quality of tempered glass

Annealed glass on the loading table of a tempering furnace is flat, smooth and its optical quality is excellent. It is impossible to maintain the same flatness and optics when glass is tempered, but still the quality of tempered glass can be very good. Most of the optical and mechanical defects in tempered glass are caused by improper heating. Quality defects caused by tempering are handled in [47][48]. Gravity tends to keep glass flat on the rollers, but in spite of that the glass can bend when it is conveyed into a tempering furnace. The bending is due to too unequal heating of the upper and lower surfaces. As an example, if heating of the glass top surface is less efficient than on the bottom surface, glass bends in convex shape in relation to the rollers. Bending focuses the total weight of the

glass on a small area, which causes white haze and local optical failures on the glass bottom surface as is seen in Figure 5.12.

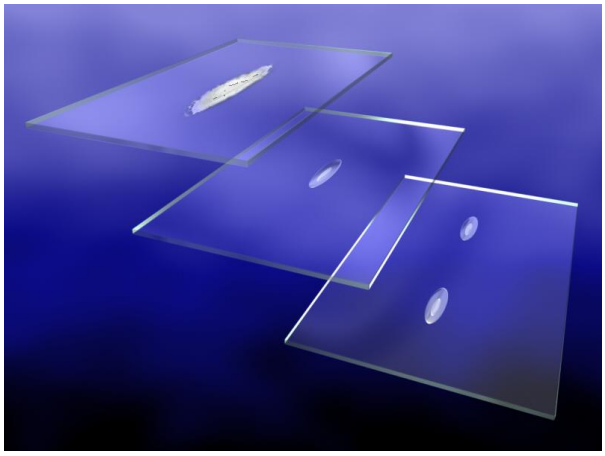

Figure 5.12. White haze and local optical failures on glass surface. [109]

If the tempering cooling is not balanced on both sides, it results in bended glass. The bending can be local or the whole glass might get a symmetrically bended shape as shown in Figure 5.13.

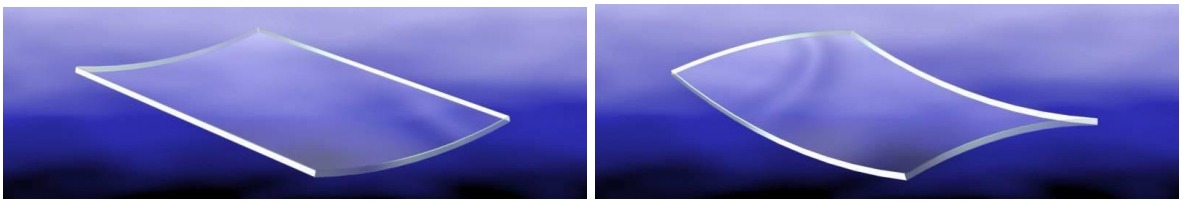

Figure 5.13. Convex and saddle-shaped tempered glass. [109]

Temperature differences in a glass area during cooling through the transition range between 600 to 480°C yield differences in residual stresses. The variation of stresses leads to variation of light refraction and polarization when it goes through glass. The phenomenon is known as mechanical birefringence or photo-elasticity [49]. Stress differences can be seen extremely well when polarised light coming through a glass is observed through a polarization filter. In Figure 5.14 lower stresses are located on the darker area. As shown in Figure 5.14, lower residual stresses lead to bigger crumbles, when tempered glass shatters. If the local crumble size is larger than the standard determines, glass cannot be used as a tempered safety glass. A common reason for the non-uniform stress distribution over the glass area is uneven heat transfer in a tempering furnace. The temperature of the glass in Figure 5.14 has been locally too cold for tempering, which can be seen as longitudinal stripes in the stress pattern (left) and biggers fragments in the broken glass (right).

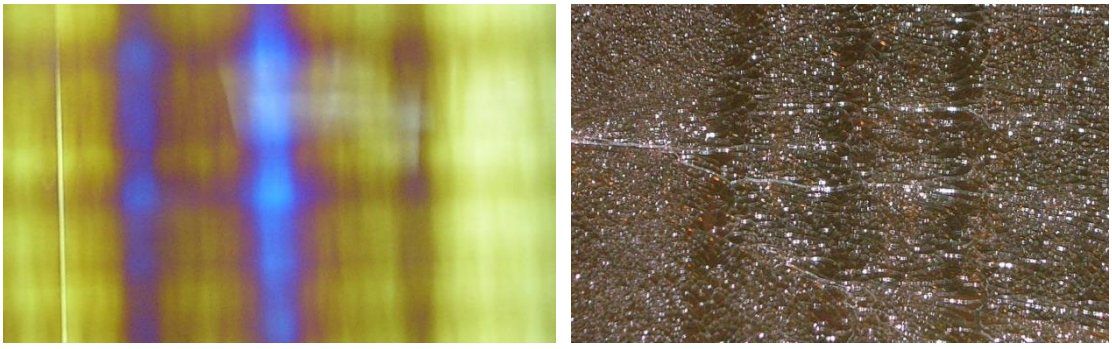

Figure 5.14. Same glass viewed through polarization filters (left) and after shattering (right).

The glass in Figure 5.14 is manufactured to show the effect of uneven heating in a tempering furnace. In actual practise stress differences in stress pattern are much smaller if the furnace and chiller are working correctly. Uniform stress distribution is especially important in glasses which are made to be placed in architecturally important buildings, because polarized light occurs also in normal daylight and the stress pattern may become visible at a certain angle of view. Nowadays, the market requests concerning the stress pattern (also called as anisotropy of glass) are rather common. The stress pattern should be smooth and not eye-catching, but a standard defining the acceptable level is still missing. This might be better in the near future, when a device for measuring stress pattern is under development [50].

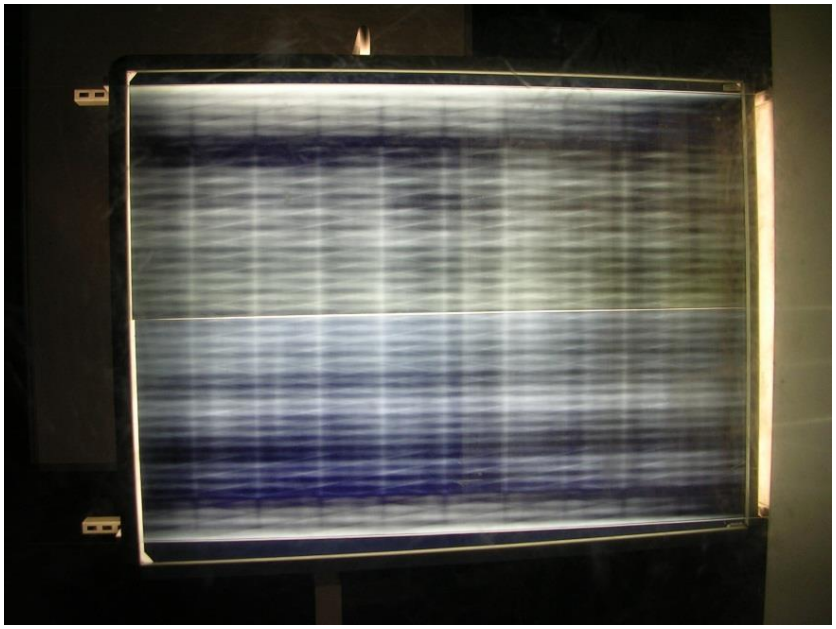

Figure 5.15. Typical stress pattern of flat tempered glass seen through polarized filters.

Figure 5.15 is a photo taken through a polarization filter from the tempered glass in the front of a polarized light panel. The stress pattern like in Figure 5.15 is typical of glass tempered in oscillating lines, while light vertical stripes are an indication of contacts with hot rollers at the turning point when the moving direction of the glass changes in a furnace. The stress pattern gets better if the turning point is altered during heating. Also, a vertically orientated diamond pattern can be seen in Figure 5.15. Such a pattern is formed due to contact between glass and rollers in the chiller because of the aramid fibre cord spooled and glued sparsely around the rollers.

The method used to examine the stress pattern of glass in Figure 5.15 detects even small stress differences, which can be found in all tempered glass pieces. The stress differences in glass in Figure 5.15 are so small that they can hardly be seen in natural light. The stress pattern produced by a tempering machine depends, for instance, on glass movements during the process, arrangement of resistors and air jets. The stress pattern is clear and visible if the glass does not move during quenching. For instance, from car rear-windows it is easy to observe the hitting locations of the air jets.

Particularly at temperatures above the transition range glass stiffness is relatively weak and it starts to creep, which creates quality problems like the roller waves and edge bending (also called edge lift and edge kink) shown in Figure 5.16. Both of these shape defects are dependent on factors like the width of the roller pitch, glass movements, heating time and glass type. They increase with glass temperature and with decreasing glass thickness [52]. Overheating is the most common “mistake” in glass tempering even if it secures glass staying unbroken and increases residual stresses. In practice, roller waves and edge lifts are much smaller than in Figure 5.16. However, in an overheated glass the

roller waves are very eye-catching as in the left glass in Figure 5.17, where also a clear frame effect typical of certain low-e coatings can be seen. The frame effect is formed when the side edges and ends of glass bend towards the coating side, i.e., the edges bend upwards [53].

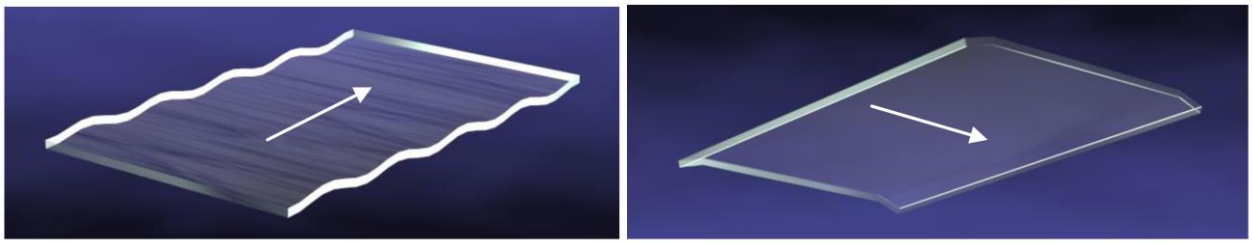

Figure 5.16. Roller waves and edge lifts (direction of glass movement is marked with arrow). [109]

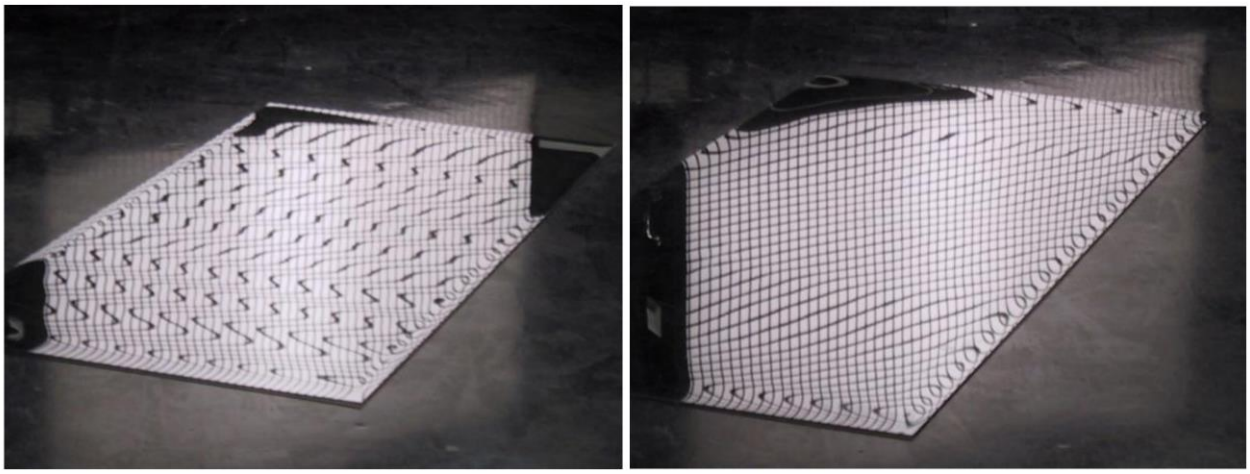

Figure 5.17. Roller waves in overheated (left) and quite sufficiently heated low-e glass (right).[109]

A common way to control the glass quality in a tempering process in addition to direct ocular control is to observe light coming from the light panel with a black net via reflection from tempered glass, as in Figure 5.18. The operator makes the necessary control actions if he observes problems in the straightness of the glass.

Figure 5.18. Illuminated grid board and reflection of it via properly tempered 3 mm glass. [109]

According to the European standard [54] the roller wave and edge lift should be measured by using a straight edge and feeler gauge. The length of the straight edge should be between 300 and 400 mm. In a roller wave measurement the straight edge is placed so that it bridges across adjacent peaks as in Figure 5.19. The gap between glass and straight edge is measured with a feeler gauge. The measurement is done at all waves over the glass surface and the roller wave distortion, *W*, is the maximum gap value measured. The edge lift measurement is a very similar procedure to the roller wave measurement above. In it the straight edge is placed as in Figure 5.19. Some more details considering both measurements are written in the standard. According to the standard the roller wave in uncoated horizontally toughened glass should be equal or smaller than 0.3 mm, and the equivalent limiting value for the coated glass is 0.5 mm. The maximum allowable value for the edge lift is 0.5 mm, when the glass thickness is 3 mm or the glass is coated. The equivalent limiting value for clear glass thicknesses between 4 and 5 mm is 0.4 mm. For glass thicknesses between 6 and 25 mm it is 0.3 mm. The standard [55] defines the test methods for roller wave in United States of America. The measuring procedure is rather similar to the European standard, but the results are presented as an optical distortions, $D = 4\pi^2 W/L^2$, where *W* is the roller wave distortion and *L is* the length of the roller wave. In general the optical distortion in flat glass is the optical power, $D = 1/F$, due to the local curvature in glass shape. Above *F* is the focal length. Usually *D* is expressed in millidiopters (mdpt) and $D < 200$ mdpt is the acceptable level for tempered glass.

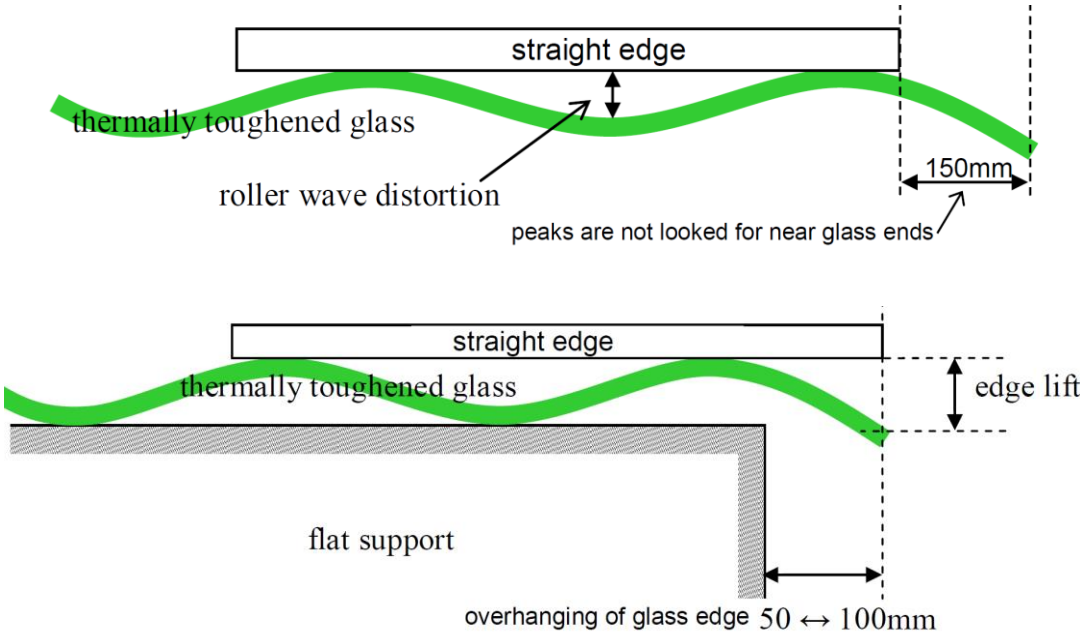

Figure 5.19. Roller wave distortion and edge lift measurement according to European standard. [54]

In addition to roller waves and edge lifts there is also a third kind of distortion in horizontally tempered flat glass. The total deflection of glass is rated with the value of an overall bow. According to [54] the overall bow in uncoated glass should be equal or smaller than 3.0 mm/m. The equivalent limiting value for coated glass is 4.0 mm/m. The glass must be in a vertical position when its straightness is rated. Bowed tempered glass can also be bi-stabile, which means that it has at least two alternate shapes. When bi-stabile glass is forced as straight, it suddenly and spontaneously bows as bow to opposite direction than at first. Such an effect is caused by the differences in residual stresses over the glass area.

An automatic glass shape measurement device uses laser beams and a machine vision system to define the glass shape. The device is located at the beginning of the unloading table. Thus, it measures a glass shape immediately after the tempering process. The directions of laser beams reflected from the glass surface are dependent on the local distortion in glass. The local variation between reflections of

the sequential laser beams can be accurately converted to local optical powers D_y of glass. Also the shape curve of glass such as in Figure 5.20 can be quite accurately solved from the raw data of such measurements. The data coming from an automatic glass shape measurement can be used for the glass quality control and even to the process control. For instance, the heating time for the next loading can be automatically decreased if a too large roller wave is measured. The straight edge defined in the standard above can be fitted to the measured shape curve with a computer code and in such a way simulate the standard measurements of roller wave distortion and edge lift. Then, it is important to be aware that the roller wave distortions and edge lifts measured are not generally acceptable standard values, because the measuring procedure is totally different to that mentioned in the standard. This is a little annoying, because the standard measurements are time-consuming and in practice the results depend substantially on the measurer. The measured edge lift depends on the glass shape under the whole length of the straight edge, and the shape is not always as ideal as in Figure 5.19. The straight edge can be in a skew angle (peaks under the straight edge have different highs) and it can even stand on a convex surface (only one peak under the straight edge). Thus, the measured result is not always the "true" edge lift. One particular problem concerning automatic on-line measurements is the support under the glass, which differs from the standard. A glass on a roller conveyor has a roller support at every roller spacing (about 100 mm). Thus, the measured glass shape is dependent on the locations of edge lifts, wave peaks and wave hollows in regard to rollers. American standard [56] defines the test method for measuring optical distortion in flat glass products using digital photography of grids. In it the grid image gets distorted when it is reflected from the glass to the screen. The distorted grid image is measured and converted to local optical powers D_y and D_z, where y is the direction of glass movement and z is the cross-wise direction. The local optical power is proportional to the local change in the grid spacing. The method analyses the slope of the glass distortion inside short bits over the whole glass length and width. Such an evaluation way of a glass distortion best fits on-line measurements, because inside a short bit the glass shape is very stable against the variation in the support of the glass.

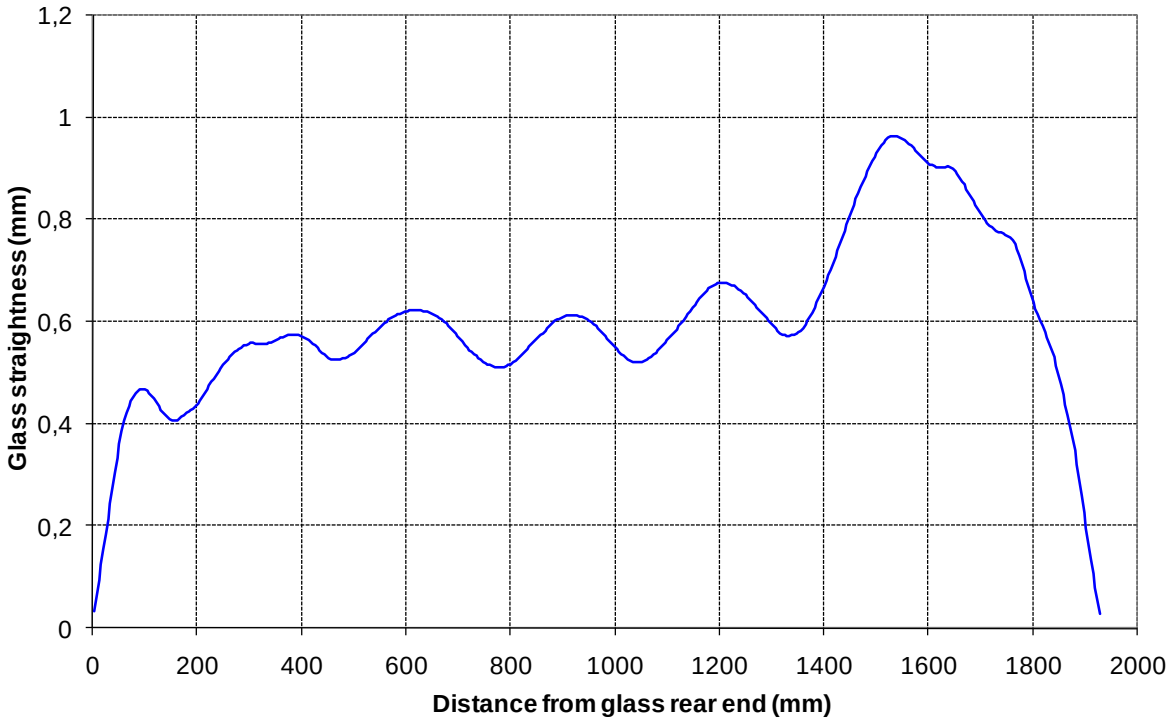

Figure 5.20. Measured shape curve of glass (length 1930 mm, thickness 3 mm) given by automatic measurement with laser beam instruments and machine vision.

An automatic measurement device enables fast and systematic quality control, which leads to substantially smaller quality costs of a glass tempering line.

In addition to the quality defects mentioned above, at least a coating burn or spots may appear on glass surface in a tempering process.

The circumstances in a furnace depend on the recent production history. For instance, after a break in production the temperatures of the surfaces in a furnace are higher than when production has been on. Such a variation of temperatures will cause variation of heat transfer and might even cause quality defects in the glass. Thus, good repeatability of a heating cycle is very important feature for the furnace in avoiding quality problems caused by over-, under- or unbalanced heating.

6. OTHER HEAT TREATMENT PROCESSES OF FLOAT GLASS

In addition to glass tempering there are some other float glass processes in which heat transfer know-how is of major importance. For instance, the windscreen production line in Figure 6.1 contains three different heat treatments. Next, the basics of bending, laminating and autoclaving processes are discussed.

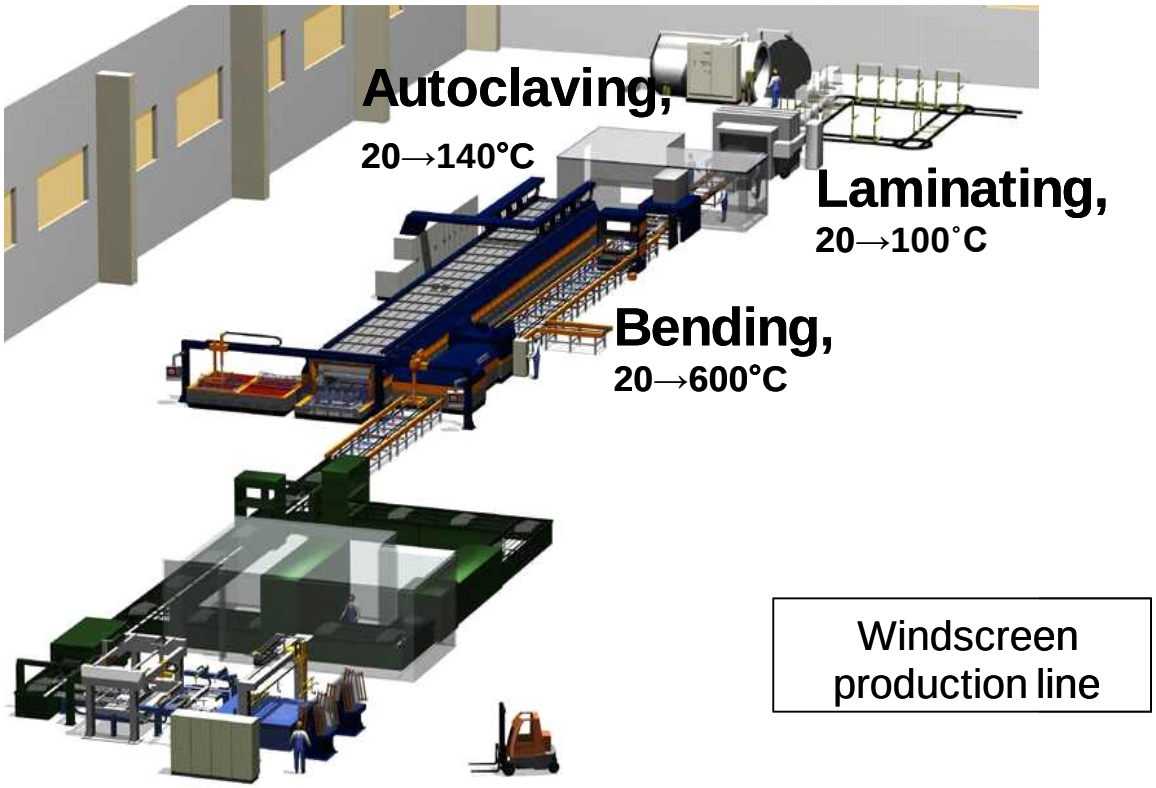

Figure 6.1. Windscreen production line. [109]

6.1 Bending

One of the basic float glass processes is glass bending. Curved glass is used in vehicles. Nowadays the use of curved windows in new buildings is also rather common and mirror coated curved glass is used in concentrating solar power collectors.

There are several types of bending furnaces in the market. In a windscreen bending process the glass pair (car windscreens consist of two glasses laminated together) is located on a ring mould, as shown in Figure 6.2, which supports the glass pair at the ends. Separation powder is dusted between glasses to enable easy loosening after bending. In a bending furnace uniform heating is important at the beginning. If the heating is too strong, then the contact between glasses is lost at the glass centre region, which might cause permanent shape differences between glasses. In the bending phase, due to gravity, hot glass creeps into contact with the ring mould at its edges. Some moulds are equipped with mechanisms containing interlinked counterweights causing bending forces on the glass to make the bending of sharp curves easier.

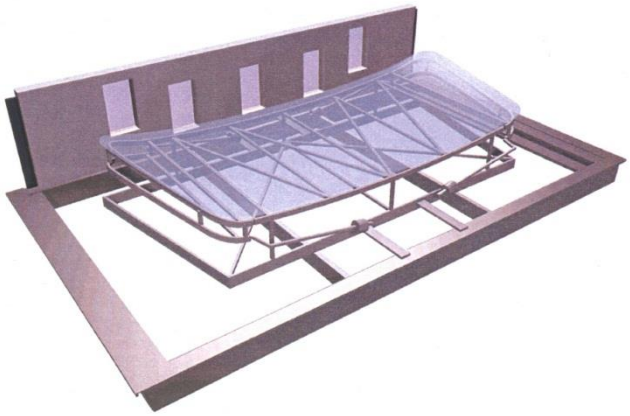

Figure 6.2. Glass on ring mould. [109]

A schematic of an energy efficient windscreen bending line particularly suitable for varying production (spare part windscreens), is shown in Figure 6.3. It consists of different chambers, which all have a wagon carrying glass on a mould within. After a cycle time all the wagons move ahead to the next chamber. Bended glass is lifted off from the mould and one new glass is placed on the empty mould.

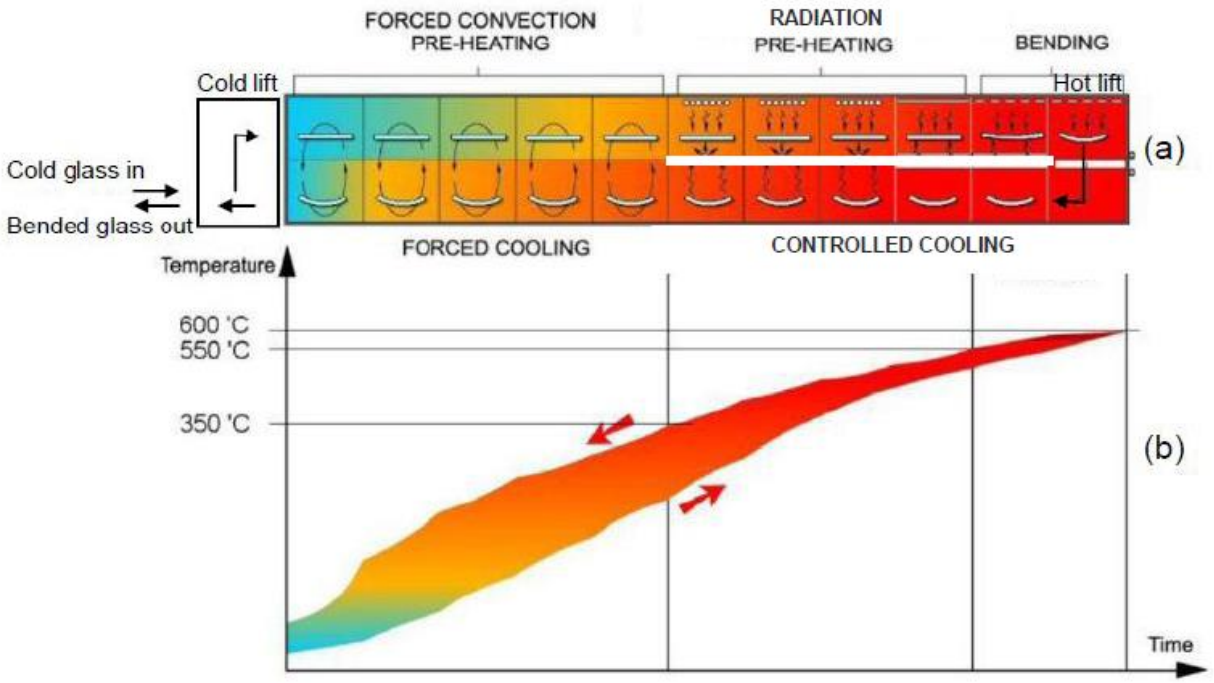

Figure 6.3. Schematic of modern windscreen bending line (a) and glass temperature during process (b). [109]

In the bending line in Figure 6.3 the energy saving is utilized in a special way. The fans circulate air between the upper (forced convection pre-heating) and lower (forced cooling) chambers with the result that heat is transferred from the warmer wagon, bending mould and glass to the ones in the colder chamber. After the last forced convection pre-heating chamber a glass moves in to a radiation chamber in which electrical resistors radiate heat to the glass. In the bending chamber focused radiation is used for glass heating in order to achieve the designed glass shape. More radiation is focused on the glass edges and particularly on the glass area at which the desired bending shape has

a tight curve. The maximum glass temperature in the bending process is about 600°C. After bending, cooling must be slow enough to avoid unwanted residual tension stresses in ready-made windscreens, but there should also be a sufficient compressive edge stress, which complicates the process. Residual stresses depend on the cooling speed at glass temperatures above 480°C. In controlled cooling chambers the cooling of glass can be intensified with air cooling pipes in which cold air flows through a hot chamber. The cooling power can be controlled by changing the rotation speed of the fan feeding air in to cooling pipes. In the last forced cooling chamber fans blow ambient air into the chamber to speed up cooling.

The bending method described above is called sag bending or gravity bending, because in it glass is allowed to sag under its own weight. The second basic windscreen bending process is press bending. The simplest form of press bending is die assist sag bending, in which a die is used to press the shape in selected areas during the final process steps of sag bending. Where there is a need for full control of the windshield shape, glasses are press bent between a full surface male die and a peripheral female die to give a precisely formed shape. With press bending technology more complex shapes can be bent than with sag bending. [57]

Bending and tempering can also be done in the same processing line, which is a typical process for car side and rear windows. Bended and laminated glass is also used for side windows in some luxury cars. In the process the tempering cooling starts immediately after bending.

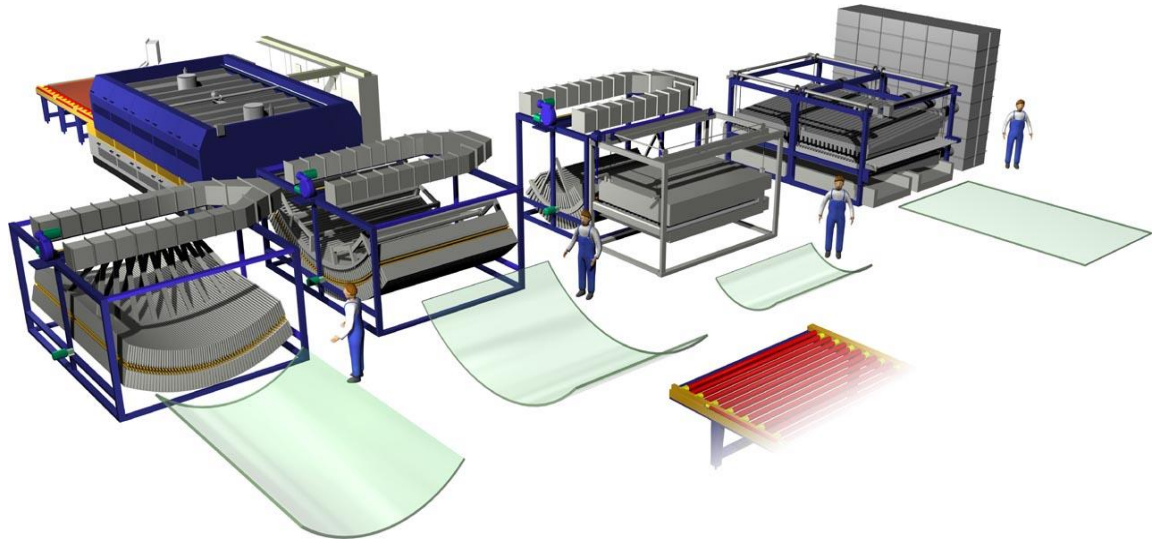

Figure 6.4. Bending and tempering line for architectural glass. [109]

In Figure 6.4 a glass bending and tempering line for big architectural glasses is shown. It is possible to equip the line with several tempering-bending units, and when the units are on rails, a unit can be switched relatively quickly to another unit.

6.2 Laminating and autoclaving

In a glass laminating process glasses are stuck together with a polyvinyl butyral (PVB) film between them. Typical PVB-film thickness is 0.76 mm. Adhesion to glass depends on hydrogen bonding bridges between the water compatible groups of the glass surface and those of PVB. At first, PVB is placed between glasses in a laminating room where air temperature should be between 18 and 20°C and the relative humidity between 25-30%. Then, the whole sandwich in Figure 6.5 containing glasses and films is heated up in a de-airing conveyor in which heating is arranged with thermal radiation and forced convection.

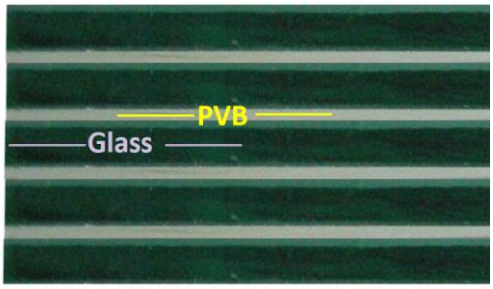

Figure 6.5. Glass-film sandwich before de-airing.

In a flat glass de-airing conveyor glass-film sandwiches are located on rotating rollers and conveyed through a heating chamber in a continuous flow. There is a roll nip before and after the furnace. Even lines without the first roll nip exist. The air from glass-film interfaces is pulled out when a sandwich goes through the nip. Air removal is important because air prevents adhesion. The major function of the de-airing conveyor in addition to sticking and air removal is edge sealing, which prevents air re-penetration into a sandwich. In a flat glass de-airing conveyor the sandwich is heated up to a surface temperature of approximately 60-70°C. Usually heating is arranged with conventional resistors located near the ceiling and roof in a heating chamber. Also hot air jets are used to activate the heating and in such a way increasing line speed. Clear and low-e coated glass-film sandwiches can be processed with a same speed, when hot air jets are used.

Both materials, i.e., glass and PVB have low thermal conductivity. So, it takes time to transfer heat in to the inner film in a multi-film layer laminate, when at the same time the overheating of the outer film must be avoided. That limits the heating speed of multi-film layer laminates. As to heat transfer, an interesting detail is that glass and PVB are semi-transparent for thermal radiation, and both materials have their own spectral absorption properties. In theory, the most efficient means for heating the multi-film layer sandwich is to use near- or mid-infrared radiation, which penetrates through glass but is absorbed into film. In practice, the matter is not as simple, as it is difficult to realize theoretically determined radiation conditions.

So-called quartz tube heaters, in which a very hot resistance wire is inside a quartz tube containing shielding gas, emit near- and mid-infrared radiation. Quartz tube heaters are used in some flat glass de-airing conveyors or before them for preheating the glass-PVB sandwiches to about 35°C, which is the optimum temperature for air removal [58].

The most common application of laminated glass is a car windscreen, where two thin and curved glasses are laminated together with PVB. In a windscreen de-airing conveyor shown in Figure 6.6 glass-film sandwiches are placed upright and hot air flows between them. Air removal from the sandwich is arranged by placing suction rings over the glass edges. In a windscreen de-airing conveyor glass is heated up to approximately 90°C.

In de-airing the transparency of glass-film sandwiches increases. Particularly windscreens are transparent after de-airing, because they are heated in a higher temperature. Next, the chemical bond between glass and film is stabilised in an autoclave, which is a hot pressure chamber. High pressure minimizes the size of the remaining air bubbles between layers and presses layers tightly together, which stimulates the bonding between layers. Autoclaving presses and breaks remaining air bubbles smaller and then dissolves them into the film. Autoclaving is a fairly time- and energy-consuming process. Therefore, some PVB-producers have tried to develop special films and some machine manufacturers or private inventors have tried to develop autoclave-free flat glass laminating processes [59]. Autoclave-free large scale laminating is still, and has already been for a long time, one of the biggest visions in the flat glass laminating industry.

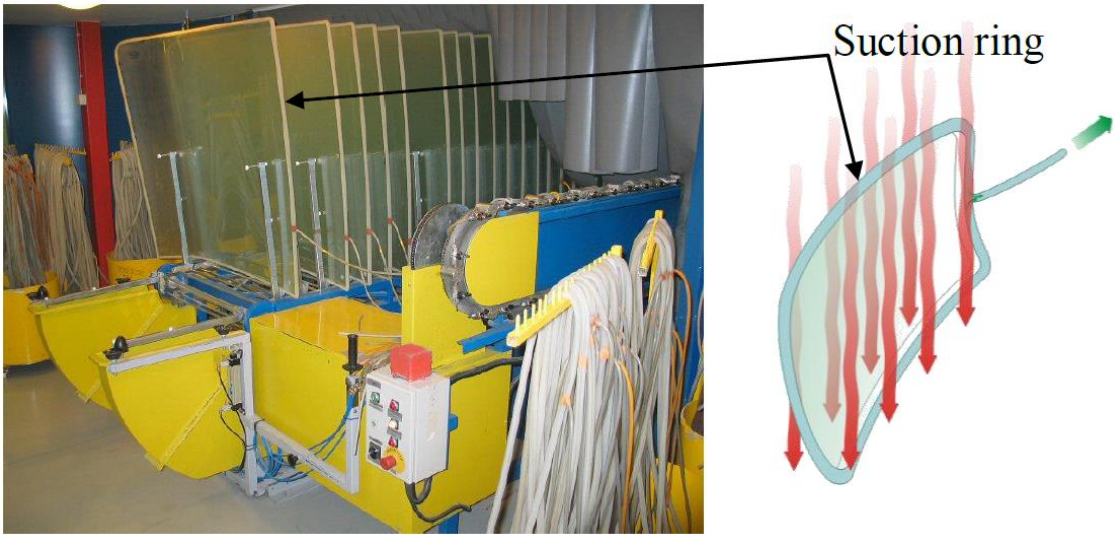

Figure 6.6. Windscreen de-airing conveyor. [109]

Figure 6.7. Glass loading in autoclave.

In the autoclave glasses are vertically located in a glass track as in Figure 6.7. Typically, the air gap between glasses where hot air flows is about 15 mm. Glasses are heated by circulating air through heating resistors and glass chamber. In the biggest autoclaves the total mass of one glass load can be even 20 000 kg. When considering the energy consumption, incomplete loadings as in Figure 6.7 should be avoided, because in addition to glass also the steel structures and air inside the autoclave must be heated. Also pressurization and cooling consume energy.

Figure 6.8 presents typical temperature and pressure curves as a function of time in an autoclaving process, when the total thickness of sandwiches is between 6 and 9 mm. The heat treatment process in Figure 6.8 requires 30 minutes holding time at a temperature of 140°C and overpressure of 12 bar. Thicker sandwiches need longer holding times. Glasses are cooled from 140°C to 40°C by circulating air through glass chamber and water cooled heat exchanger. Cooling water can be taken from the tap or there can be a closed water circuit with a refrigeration unit or/and cooling tower. In autoclaving the air density changes very substantially during the process, which has a significant effect on convection.

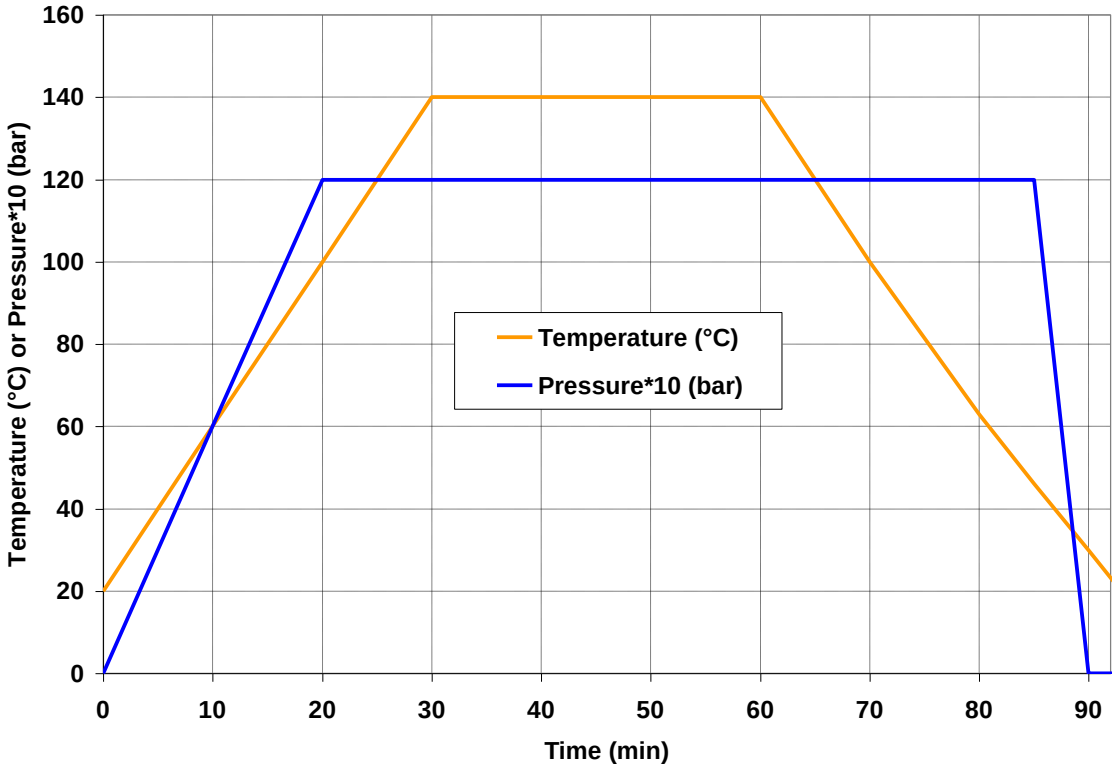

Figure 6.8. Typical autoclaving temperature and overpressure for two 3 mm or 4 mm glass and 0.76 mm PVB-film between them given by [58].

Autoclaving is not necessarily needed when special laminating films such as ethylene-vinyl acetate (EVA) and SentryGlas® are used. In that case the de-airing is done, for instance, in a huge circulation air oven similar to the heat soak oven discussed in Chap. 15, and removal of air from the glass-film sandwiches is arranged by inserting them in vacuum bags. Also PVB is used as a film in this kind of low scale production of laminated glass, but then some air bubbles might appear in laminate particularly when PVB pre-handling is not as it should be.

Laminating makes glasses tough, strong and secure, because it keeps sharp fragments together if the glass gets broken. In special applications such as a transparent floor and bullet-proof glass the laminated sandwich contains several glass- and film layers.

7. FORMULATION OF HEAT TRANSFER PROBLEM IN TEMPERING

Figure 7.1 shows the schematic of glass inside a tempering furnace. The glass is exposed to radiation emitted by radiant heaters, rollers and other surfaces inside the furnace. Also the glass is emitting radiation, and the emission increases when glass gets hotter. Convection heat transfer between hot air and glass affects both surfaces. On the lower surface also contact heat transfer between glass and rollers takes place. The velocity of glass is equal to rollers circumferential speed.

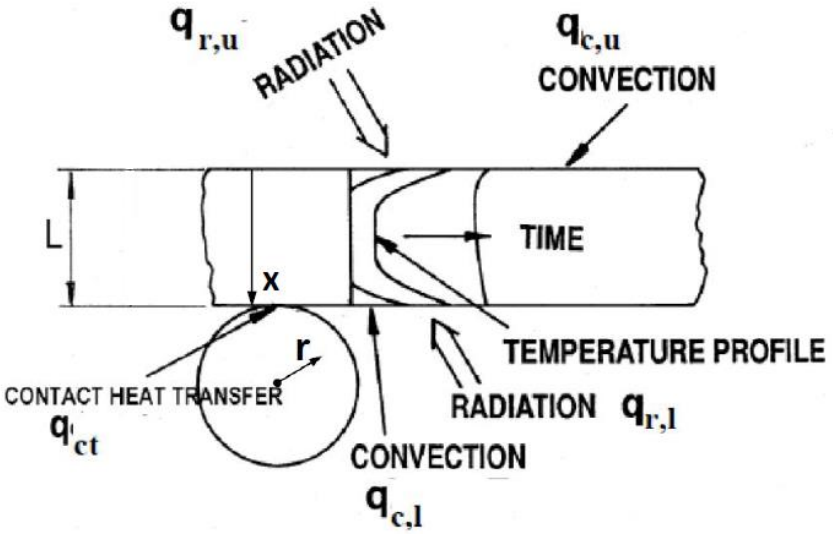

Figure 7.1. Heat transfer phenomena in tempering furnace.

The problem is to solve the development of glass thickness-wise temperature profile during heating in a tempering furnace. The problem is time-dependent, because glass temperature T increases with heating time. Also roller temperature T_r depends on time, when heat is transferred from rollers to glass. In practise, also the temperature of air and radiant surfaces inside a furnace decreases at the beginning of heating, when cold glass is conveyed in.

At first, let us consider internal heat transfer in glass. If the effect of edges is excluded and the velocity of glass is fast enough to make the length-wise conduction in glass insignificant, the energy equation of glass in Figure 7.1 is

$$\rho c_p \frac{\partial T}{\partial t} = \frac{\partial}{\partial x}\left(k \frac{\partial T}{\partial x} \right) + \frac{\partial q_r}{\partial x} \tag{7.1}$$

where the first term on the right side stands for conduction. In Eq. (7.1) ρ is density. Specific heat c_p and thermal conductivity k of glass depends on temperature, as shown in Appendix A. Coordinate x is the perpendicular distance from glass top surface and t is time. Term $\partial q_r/\partial x = S$ (S is the net radiation source term) takes into account net radiation heat transfer inside the glass, the modelling of which is considered later on.

The required equation for the roller is

$$\rho_r c_{pr} \frac{\partial T_r}{\partial t} = \frac{1}{r} \frac{\partial}{\partial r}\left(k_r \frac{\partial T_r}{\partial r} \right) \tag{7.2}$$

where r is the radius-orientated distance and subscript r refers to the roller.

For solving the equations above initial and boundary conditions are needed which couple temperatures together. The glass plate can experience different types of heat transfer depending on the type of furnace. Convection, either natural or forced, is always present and it is the same with radiation. Unlike radiation heat transfer, the convection and contact heat transfer occur only at the surfaces of the glass.

In the upper surface of glass, radiation and convection are taken into account as

$$k\frac{\partial T}{\partial x}(0,t) = q_{r,u} + q_{c,u} \tag{7.3}$$

In the lower surface heat transfer is composed of three components: radiation, convection, and contact heat transfer between glass and rollers. It can be expressed as

$$-k\frac{\partial T}{\partial x}(L,t) = q_{r,l} + q_{c,l} + q_{ct} \tag{7.4}$$

The initial condition is $T(x,0) = T_0$.

In order to solve Eq. (7.1), which is the general form of the heat transfer problem to be solved in the thesis, the equations for heat fluxes in Eqs. (7.3) and (7.4) are needed. Especially an equation for radiative heat flux q_r is difficult to formulate. Convective heat flux q_c can be easily specified using a convection heat transfer coefficient and temperature difference between air and glass surface $q_c = \bar{h}(T_a - T)$. The evaluating of the correct value of the convection heat transfer coefficient is often difficult. A similar type of difficulty also exists when the contact heat transfer coefficient is defined between glass and the roller. Heat flux with contact heat transfer q_{ct} is a product between contact heat transfer coefficient and temperature difference between roller surface and glass bottom surface $q_{ct} = \bar{h}_{ct}(T_r - T)$. The contact heat transfer between a roller and a point at glass bottom surface occurs only during the contact time $t_{ct} = l_{ct}/u$, which is a very short period of time. Next contact heat transfer pulse starts after time $(L_{rp} - l_{ct})/u$, when the point in glass bottom surface contacts the next roller. The contact heat transfer coefficient $\bar{h}_{ct}$ above is the average value over the time period L_{rp}/u, l_{ct} is the contact length, L_{rp} is the roller pitch and u is the glass velocity.

Chaps. 8-11 are relating to solution of the radiative heat flux q_r. Chap. 12 is relating to solution of the convective heat flux q_c and Chap. 13 to solution of the contact heat transfer heat flux q_{ct}.

8. BASIC CONCEPTS OF RADIATION HEAT TRANSFER

Only the basic concepts of radiation heat transfer to understand the importance of thermal radiation in a tempering furnace are dealt with below. Details can be found in the literature [60][61]. Thermal radiation in glass is dealt with later on in Chap. 9.

8.1 Thermal radiation

All objects emit radiation on the basis of their temperature, which is called thermal radiation. Thermal radiation is a part of electromagnetic radiation, which follows the laws for transverse waves oscillating perpendicular to the direction of travel. The speed of propagation for electromagnetic radiation in a vacuum is the same as that of light: $c_0 = 2.9979 \times 10^8$ m/s. In a participating medium the propagation speed is $c = c_0/n$, where n is the index of refraction.

The types of electromagnetic radiation can be classified according to the wavelength λ in vacuum (≈ air). Electromagnetic waves of different wavelengths carry different amounts of energy and their behaviour is often quite different. Depending on the behaviour of radiation it is classified into several types according to its wavelength. These types include radio waves, microwaves, infrared radiation, visible light, ultraviolet radiation, X-rays and gamma rays.

Thermal radiation is important for heat transfer considerations. The wavelength region of thermal radiation is 0.1 μm < λ < 100 μm. Thus, it consists of ultraviolet radiation (0.01 μm < λ < 0.4 μm), visible light (0.4 μm < λ < 0.7 μm) and infrared radiation (0.7 μm < λ < 1000 μm). The infrared radiation is divided into near-infrared (0.7 μm < λ < 2.5 μm), mid-infrared (2.5 μm < λ < 10 μm) and far-infrared (10 μm < λ < 1000 μm).

8.2 Radiation of surfaces

8.2.1 Emissive power of blackbody

In Figure 8.1 an elemental surface area dA_1 is surrounded by a hemisphere of radius R. The emitted spectral intensity is emitted heat flux per unit solid angle expressed in watts/(m^2-μm-steradian). The solid angle Ω is defined by differential element of area dA_s on the hemisphere

$$d\Omega = \frac{dA_s}{R^2} \tag{8.1}$$

In Figure 8.1 in spherical coordinates $dA_s = Rd\theta R\sin\theta d\varphi$. Thus, the solid angle is

$$d\Omega = \sin\theta d\theta d\varphi \tag{8.2}$$

where θ is the angle between a surface and its normal and φ is the circumferential angle.

The spectral intensity $i_b(\lambda,T)$ emitted by a blackbody refers to the radiation in a wavelength interval $d\lambda$. The total intensity

$$i_b(T) = \int_{\lambda=0}^{\infty} i_b(\lambda, T) d\lambda \tag{8.3}$$

contains all wavelengths.

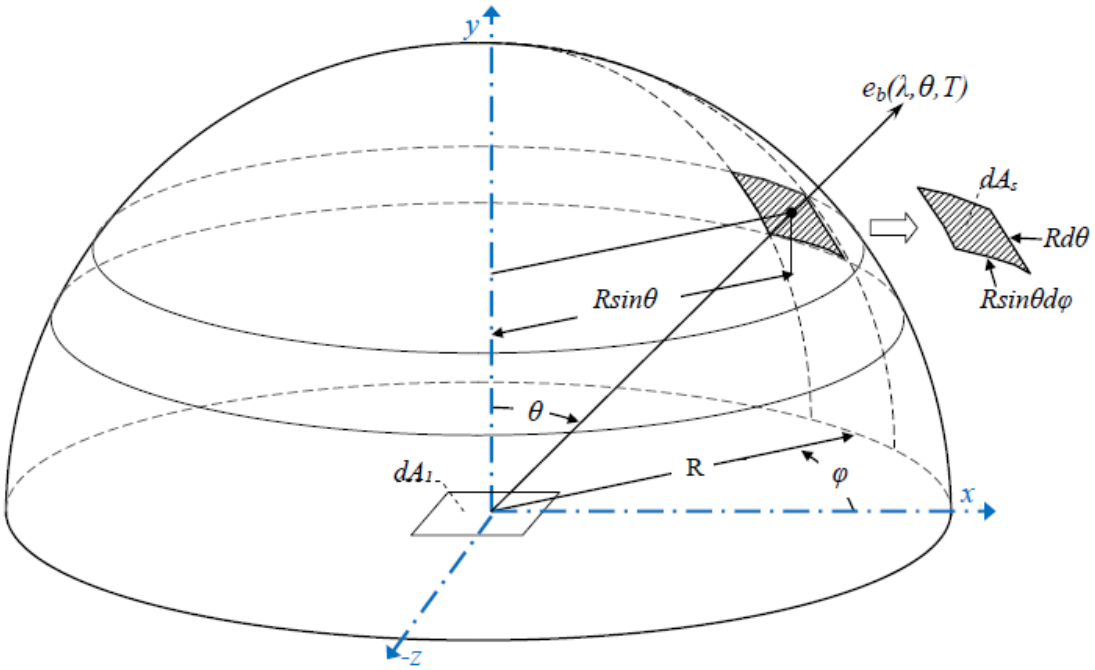

Figure 8.1. Emission from area dA_1 into hemisphere.

In Figure 8.1 the emissive power is the rate of radiative energy emission per differential element of area dA_1 from the surface. The directional spectral emissive power of a blackbody is defined as

$$e_b(\lambda, \theta, T) = i_b(\lambda, T) \cos\theta \tag{8.4}$$

The hemispherical spectral emissive power of a blackbody is

$$e_b(\lambda, T) = i_b(\lambda, T) \int_{\varphi=0}^{2\pi} \int_{\theta=0}^{\pi/2} \cos\theta \sin\theta d\theta d\varphi = \pi i_b(\lambda, T) \tag{8.5}$$

Note that in Eq. (8.5) the spectral intensity $i_b(\lambda,T)$ is taken out from the integrals, because blackbody intensity is independent of direction. The spectral distribution of the hemispherical emissive power of a blackbody is given as a function of a wavelength and absolute temperature (K = °C+273) by

$$e_b(\lambda, T) = \frac{C_1}{\lambda^5 \left(e^{C_2/\lambda T} - 1 \right)} \tag{8.6}$$

This is known as *Planck's* spectral distribution of blackbody emissive power. In Eq. (8.6) $C_1 = 2\pi hc_0^2 = 3.7419 \times 10^{-16}$ Wm^2 and $C_2 = hc_0/k = 14\,388$ μmK, where k is *Boltzmann's* constant and h is *Planck's* constant. Eq. (8.6) is solved for three surface temperatures in Figure 8.2.

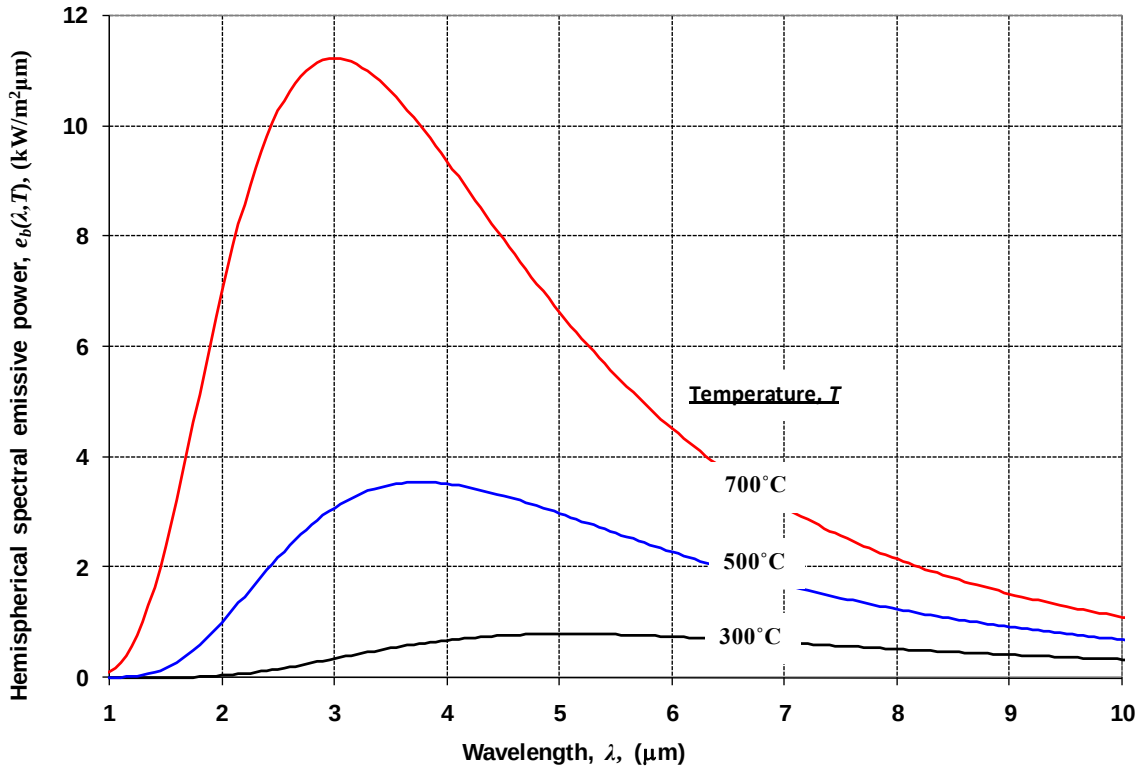

Figure 8.2. Hemispherical spectral emissive power of blackbody at various blackbody temperatures.

The spectral distribution of the emissive power shifts towards shorter wavelengths when the temperature of a blackbody increases. The wavelength λ_{peak} at the peak of the spectral distribution can be calculated from *Wien's* displacement law

$$\lambda_{peak} T = C_3 \tag{8.7}$$

where $C_3 = 2897.756$ μm. The effective surface temperature of the sun (5762K) gives λ_{peak} equal to 0.5 μm, which is in the middle of the wavelength band of visible light. At certain wavelength regions solar radiation attenuates significantly when it penetrates through the atmosphere due to absorption of carbon dioxide, water vapour, ozone and oxygen.

In Figure 8.2 the area between curves and the wavelength-axis is equivalent to the total emission of a blackbody and is obtained from the *Stefan-Boltzmann* equation

$$e_b(T) = \int_0^\infty e_b(\lambda, T) d\lambda = \sigma T^4 \tag{8.8}$$

in which $\sigma = 5.6703 \times 10^{-8}$ W/(m^{2}K^4).

8.2.2 Emissivity

An ideal black surface has complete emission and absorption of incident radiation at all wavelengths, and from all directions. The emissivity ε is the property of a body which describes its ability to emit radiation as compared with the emission of a blackbody at the same temperature. The emissivity of a surface is between zero and one.

Usually the emissivity of a real surface is independent of the circumferential angle, but it varies as a function of the surface temperature, the wavelength, and the direction of the emitted radiation. In spite of that surfaces are commonly approximated as grey and diffuse in radiation calculations. A grey surface has emissivity independent of wavelength, and a diffuse surface has emissivity independent of direction. The total emissive power for a grey diffuse surface is obtained from

$$e(T) = \varepsilon\sigma T^4 \tag{8.9}$$

where ε is the emissivity of a surface.

The spectral emission of glass is strongly wavelength-dependent. It will be shown later on in Sec.9.1 that the spectral emission of glass can be approximated using at least three wavelength bands inside which the absorption coefficient is set as a constant. The hemispherical total emissive power of a surface divided into three wavelength bands is

$$e(T) = \left[\varepsilon(0,\lambda_2,T)F_b(0,\lambda_2,T) + \varepsilon(\lambda_2,\lambda_3,T)F_b(\lambda_2,\lambda_3,T) + \varepsilon(\lambda_3,\infty,T)F_b(\lambda_3,\infty,T)\right]\sigma T^4 \tag{8.10}$$

where $\varepsilon(\lambda_2, \lambda_3, T)$ is the mean emissivity of a surface between cut-off wavelengths λ_2 and λ_3 at temperature T. In Eq. (8.10) $F_b(\lambda_2,\lambda_3,T)$ is the fraction of radiative energy of a blackbody between the wavelengths λ_2 and λ_3 at temperature T. It can be solved by using Eq. (8.6). The equations and tabulated values for $F_b(0,\lambda_i,T)$ can be found from the literature, from which $F_b(\lambda_i,\lambda_j,T) = F_b(0,\lambda_j,T) - F_b(0,\lambda_i,T)$ can be solved. The emissivity of a glass surface is independent of the circumferential angle, but it depends on the direction of the emitted radiation, which will be shown later on in Chap. 9.

8.2.3 Absorptivity, reflectivity and transmissivity

When thermal radiation hits an opaque surface, a portion of it is reflected and the rest is absorbed to a surface. If the surface material is semi-transparent or transparent for radiation, a portion of radiation goes through the surface. The reflectivity ρ, absorptivity α and transmissivity τ are connected by the equation

$$\rho + \alpha + \tau = 1 \tag{8.11}$$

Most of the real surfaces are totally opaque for thermal radiation, i.e., $\tau = 0$. Glass is opaque to certain wavelengths and semi-transparent or transparent to others.

Radiation may be altered because of diffraction, refraction or reflection when it meets small particles like dust or ice crystals in air, or air bubbles in a solid medium. A normal plate glass does not scatter.

8.2.4 Kirchhoff's law

Kirchoff's law shows the equality of the directional spectral emissivity and the directional spectral absorptivity of material,

$$\varepsilon(\lambda,\theta,\varphi,T)=\alpha(\lambda,\theta,\varphi,T) \tag{8.12}$$

This is the most general form of Kirchoff's law. Various averaged emissivities and absorptivities are also equal if certain restrictions are made (see [61] p.70). Then, ε = α.

8.3 Radiation exchange between surfaces

8.3.1 View factors

Radiation heat flux from one surface to another is often of interest when radiation heat transfer in a heat treatment machine is outlined. The heat flux depends on the shapes and sizes of surfaces and distances between them. In other words, it depends on how surfaces see each other. View factors are used to take this view into account. The view factor is the fraction of radiant energy leaving one surface that is incident upon another surface. Heat flux from a black surface 1 to a black surface 2 can be written as

$$Q_{1-2} = F_{1-2}\sigma T_1^4 A_1 \tag{8.13}$$

where F_{1-2} is the view factor from a surface 1 to a surface 2. Next, two basic rules are useful, when view factors between surfaces are solved

$$F_{i-j}A_i = F_{j-i}A_j \tag{8.14}$$

$$\sum_{j=1}^{n} F_{i-j} = 1 \tag{8.15}$$

Let us consider radiation heat transfer in a tempering furnace. In Figure 8.3 a glass is under heating resistors (see Figure 5.1 b) in a tempering furnace. If the length and width of the furnace and glass are large, then the effect of sides can be ignored.

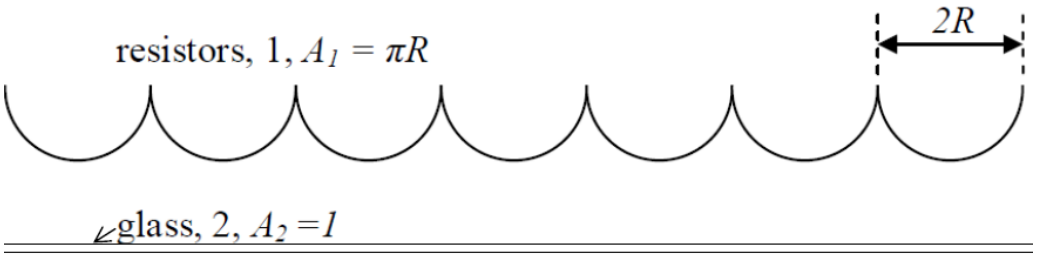

Figure 8.3. Schematic of glass under resistors in tempering furnace.

The view factor from glass to resistors F_{2-1} is 1, because the glass surface cannot see itself ($F_{2-2} = 0$). Accordingly, Eqs. (8.14) and (8.15) give $F_{1-2} = F_{2-1}(A_2/A_1)$ and $F_{1-1} = 1-F_{1-2}$.

Figure 8.4 shows a glass on rollers in a tempering furnace. The view factor F_{2-1} from rollers to glass is the difference between the view factor from the roller to an infinite glass plate and screening caused by other rollers. Screening is a half of the view from a roller to other rollers. Then, the view factor F_{2-1} is [39]

$$F_{2-1} = \frac{1}{2} - \frac{1}{\pi}\left[\left(X^2 - 1\right)^{0,5} + \sin^{-1}\left(\frac{1}{X}\right) - X\right] \tag{8.16}$$

In Eq. (8.16) $X = 1+B/(2R)$.

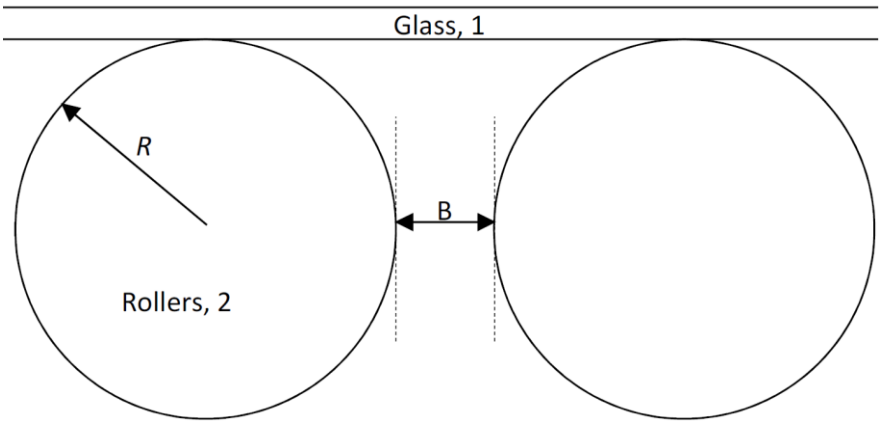

Figure 8.4. Glass on rollers in tempering furnace.

In the cases above the geometry was assumed to be infinite at least in one direction, which makes the solution of radiation heat transfer between surfaces easier. A lot of similar view factors can be written for the surfaces in a tempering furnace. These kinds of view factors are suitable only for solving the mean radiation between the bodies with uniform surface temperatures.

8.3.2 Radiation heat flux from tubular resistor to glass

A typical heating resistor consists of a resistance wire, which is spooled around a ceramic tube. Such a shape can be simplified as a long cylindrical tube shown in Figure 8.5.

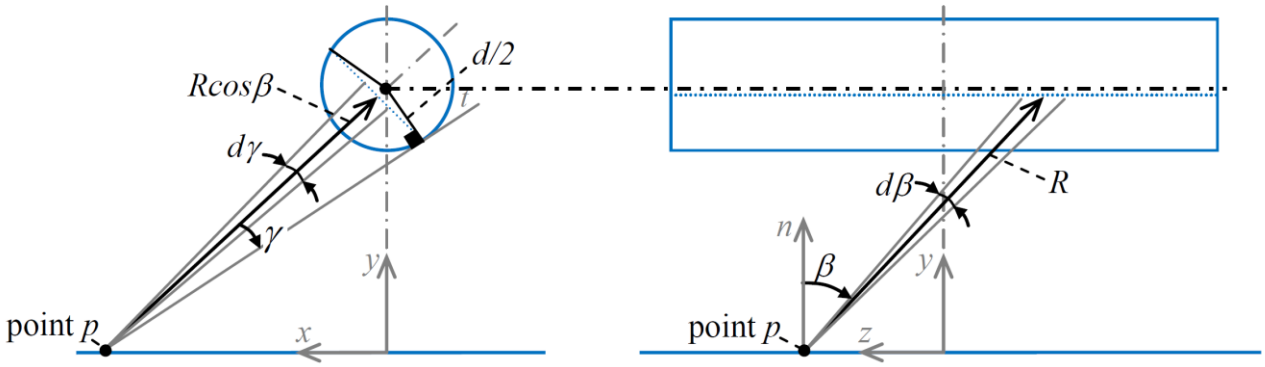

Figure 8.5. Angles γ and β between resistor and point p in plane.

By using the angles and coordinates defined in Figure 8.5 the projected area of a resistor viewed from point p can be written as

$$dA_s = Rd\beta R\cos\beta d\gamma \tag{8.17}$$

and then Eq. (8.1) gives solid angle

$$d\Omega = \cos\beta d\beta d\gamma \tag{8.18}$$

According to [62] the polar angle θ defined in Figure 8.1 can be written by means of angles β and γ as

$$\cos\theta = \cos\beta\cos\gamma \tag{8.19}$$

The radiation emitted by the resistor in Figure 8.5 to a point p on the plane surface can be solved by inserting Eqs. (8.18) and (8.19) in Eq. (8.5). Thus, the incoming radiative heat flux density in point p is

$$q_p^- = i_r^+ \cos\alpha \int_{\beta_2}^{\beta_1} \cos^2\beta d\beta \int_{-\gamma_1}^{\gamma_1} \cos\gamma d\gamma \tag{8.20}$$

In Eq. (8.20) i_r^+ is the emitted intensity of the resistor and α is the angle between normal of the plane and line S_1 in point p as shown in Figure 8.6. Line S_1 is the distance between resistor mid-point and point p viewed from z-direction. In Eq. (8.20) $cos\alpha$ takes into account that the projection of the elemental area dA_1 on plane surface toward the resistor is $cos\alpha$ -times smaller than the elemental area itself and thereby the incoming flux is equally smaller. The integration limits of angles γ and β are shown in Figure 8.7 and Figure 8.8. The vertical distance S_2 between midline of the resistor and its projection to point p is defined in Figure 8.8.

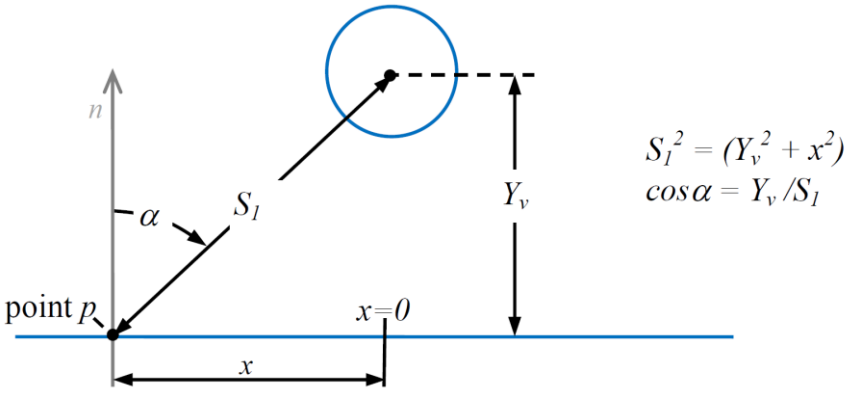

Figure 8.6. Angle α between normal of plane and line S_1 in point p.

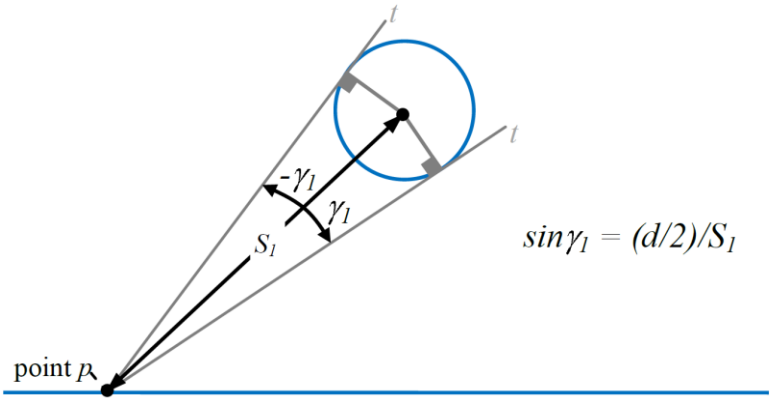

Figure 8.7. Integration limits of angle γ.

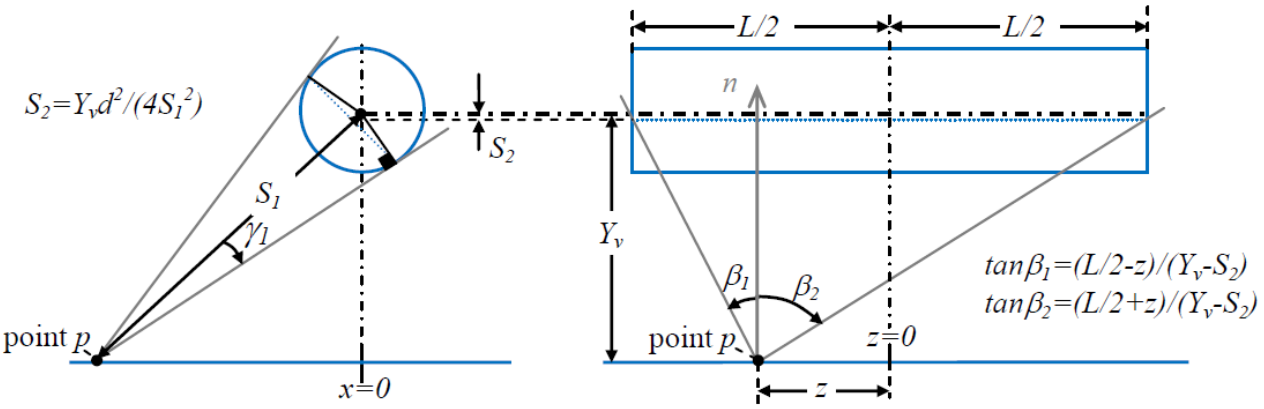

Figure 8.8. Integration limits of angle β.

The integration of Eq. (8.20) yields to

$$q_p^- = i_r^+ \frac{Y_v}{\sqrt{Y_v^{\,2} + x^2}} \left[(\beta_1 - \beta_2) + \frac{1}{2}(\sin 2\beta_1 - \sin 2\beta_2) \right] \sin \gamma_1 \tag{8.21}$$

where

$$\beta_1 = \tan^{-1}\left[\frac{(L/2 - z)}{(Y_v - S_2)}\right], \quad \beta_2 = -\tan^{-1}\left[\frac{(L/2 + z)}{(Y_v - S_2)}\right], \quad \gamma_1 = \sin^{-1}\left[\frac{d/2}{S_1}\right],$$

$$S_1 = \left(Y_v^2 + x^2\right) \quad \text{and} \quad S_2 = Y_v d^2/(4S_1^2)$$

Eq. (8.21) is ready to be used for practical problems because it includes three typical dimensions for a resistor above the plane geometry: resistor diameter d, resistor length L and vertical distance between the resistor and plane Y_v. Coordinates x and z define the point on the plane surface, where the radiative heat flux density is to be solved.

The intensity i_r^+ needed in Eq. (8.21) is

$$i_r^+ = \frac{q_r^+}{\pi} = \frac{Q_r}{\pi A_r} = \frac{Q_r}{\pi^2 dL} = \frac{\sigma T_r^4}{\pi} \tag{8.22}$$

when a resistor is approximated as a blackbody. In Eq. (8.22) q_r^+ is outgoing heat flux density from the resistor. Usually the temperature T_r of a resistor is not known, but the electric power $Q_{r,e}$ of a resistor is. In thermal balance the total outgoing heat flux Q_r from a resistor is the sum of the electric power of the resistor $Q_{r,e}$ and incoming heat flux to resistor from the surroundings.

$$Q_r = \sigma T_r^4 \pi dL = Q_{r,e} + \sigma T_\infty^4 \pi dL \tag{8.23}$$

In the case above only one half of the heating power of a resistor hits the plane (glass) under it, while another half is radiated in an opposite direction and hits a furnace ceiling. The ceiling is made from insulation material, which radiates incoming radiation back to a resistor and plane under it.

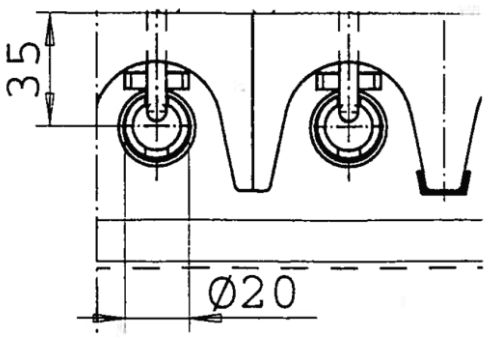

Figure 8.9. Cross section of resistors built in groove-shaped shade. [109]

Figure 8.9 shows a geometry in which resistors are located in groove-shaped shades. Such resistors are used when more focused radiation is needed, for instance in windscreen bending furnaces. The shade cuts the visibility from the plane to the resistor. The equations above are suitable for the case if the shading is considered in integration limits of angle γ. The emission upwards from the resistor hits the shade, which reflects and emits radiation back to the resistor and directly to the plane under it. Thus, similar equations as above for the resistor tube must be written for the shade also. Again, the temperatures of the surfaces are not known, and difficulties arise when they or outgoing heat fluxes from the resistor and shade are to be solved. The exact solution to such a multi-phased radiation heat transfer problem is complex. It can be solved by using the following assumptions and methods: the crosscut of the shade is semicircle-shaped, the surfaces are diffuse and grey, the temperatures of the resistor and shade are constant over the surface, and the radiative equilibrium temperatures for both surfaces are solved by using the net-radiation method presented in [61] page 391. Some results are shown later in Sec. 14.1.

Direct radiation heat flux from a tubular resistor to a plane underneath is a clear problem to be solved with self-written equations, but non-direct radiation via the ceiling or a groove-shaped shade is a much more complicated problem. A competent way to solve the problem above is to use commercial numerical modelling codes.

9. THERMAL RADIATION IN PLATE GLASS

The radiative properties of glass play an important role in glass industry, because the melting, heating and cooling of glass are partly determined by them. The thermal and light transmittance of a window glass and the efficiency of a solar energy collector depend on them, for instance.

The absorption, transmission and emission of an absorbing medium depend on the thickness of a material layer. A perfectly transparent medium does not take part in the radiation. How glass behaves depends on the wavelength of the radiation. Window glass can be opaque, semi-transparent and transparent.

The thermal radiation in a low-e coated glass is handled later on in Chap. 11.

9.1 Behaviour of incident radiation in glass

In Figure 9.1 the behaviour of incident radiation hitting a glass surface is shown schematically. A radiation beam hits the glass top surface from the direction θ, but in the glass the beam propagates in the direction θ'. The change of direction is due to refraction, which takes place at the interface between two materials with different refractive indices.

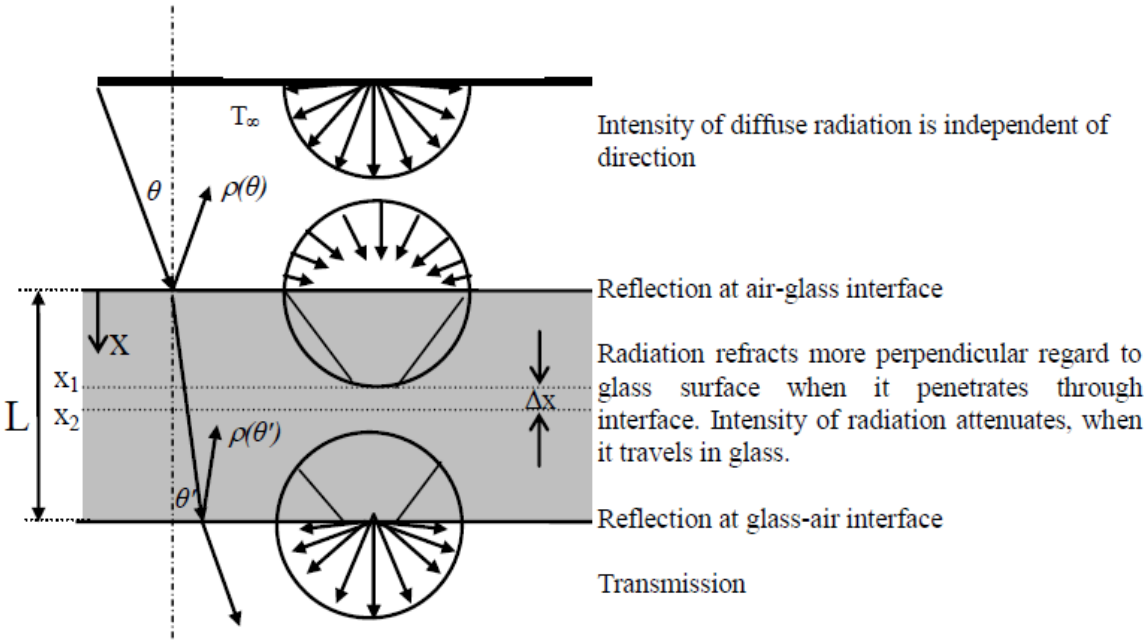

Figure 9.1. Behaviour of incident radiation in glass.

The refractive index of air n_1 = 1 (for example: exactly 1.000293, when λ = 589 nm, [49]). The refractive index of the glass n_2 depends on the wavelength of the radiation. The refraction obeys *Snell's* law

$$\frac{\sin\theta'}{\sin\theta} = \frac{n_1}{n_2} \tag{9.1}$$

At the air-glass interface a portion of the radiation is reflected. All surfaces are composed of molecules which have certain dimensions. According to the Rayleigh-criterion a surface is smooth

when $(k/\lambda)\cos(90°-\theta)\rightarrow 0$, where k is the surface roughness and λ is the wavelength of the incident radiation. In practice it is easy to observe that the reflection of visible light from the glass surface is specular (mirror-like). Thus, the glass surface is optically smooth for visible light, and due to the Rayleigh-criterion it is optically smooth also for infrared radiation.

Fresnel's equations describe the reflection characteristics of electromagnetic radiation at an optically smooth interface between media with differing refractive indices. Fresnel's equations lead to the following expressions for the reflectivity on the surface of non-metallic solid for the radiation polarized perpendicularly to the plane of incidence

$$\rho_{\perp} = \frac{\sin^2(\theta - \theta')}{\sin^2(\theta + \theta')} \tag{9.2}$$

and

$$\rho_{\Uparrow} = \frac{\tan^2(\theta - \theta')}{\tan^2(\theta + \theta')} \tag{9.3}$$

for the radiation parallel to the plane of incidence [64]. The effective directional reflectivity of glass-air interface $\rho(\theta)$ obeys *Fresnel's* equation

$$\rho(\theta) = \rho(\theta') = \frac{1}{2}\left[\rho_{\perp} + \rho_{\Uparrow}\right] \tag{9.4}$$

In a special case when the beam hits to the interface from the direction of surface normal ($\theta = 0$), the reflectivity is

$$\rho(\theta = 0°) = \rho_n = \left(\frac{n_2 - n_1}{n_2 + n_1}\right)^2 \tag{9.5}$$

The reflectivity at an optically smooth interface between air and glass depends only on the refractive index of glass, which varies as function of the wavelength. Figure 9.2 shows the directional reflectivity of a clear glass surface when the refractive index is 1.5. In Figure 9.2 the directional reflectivity of glass $\rho(\theta)$ is between 0.04 and 0.05 when θ is below 40°, but at bigger angles the reflectivity increases continually more sharply toward the total reflection. The angle of total reflection is the angle from the normal of the interface between two materials of different refractive index at which total reflection of the incident intensity occurs. The reflectivity from the glass-air interface $\rho(\theta')$ reaches total reflectivity when $\theta' = \theta'_c \approx 41.8°$ ($n = 1.5$). Due to the refraction, radiation hitting the top or bottom surface of a flat glass can propagate in glass only at angles $\theta' < \theta'_c$. Radiation hitting the edges of a flat glass can propagate in a glass at bigger θ' -angles and then it cannot exit from the glass through the glass top or bottom surfaces. Such radiation travels in the glass until it is totally attenuated due absorption or until it reaches the opposite edge. Optical fibres are based on this feature.

The reflectance of a glass consists of reflections from the air-glass interface and glass-air interface. The reflectance is about the sum of reflectivities $\rho(\theta)$ and $\rho(\theta')$ if absorption is minimal. Similarly, the absorptivity, transmissivity and emissivity are properties of the surface, but absorptance, transmittance and emittance consider the appropriate glass layer.

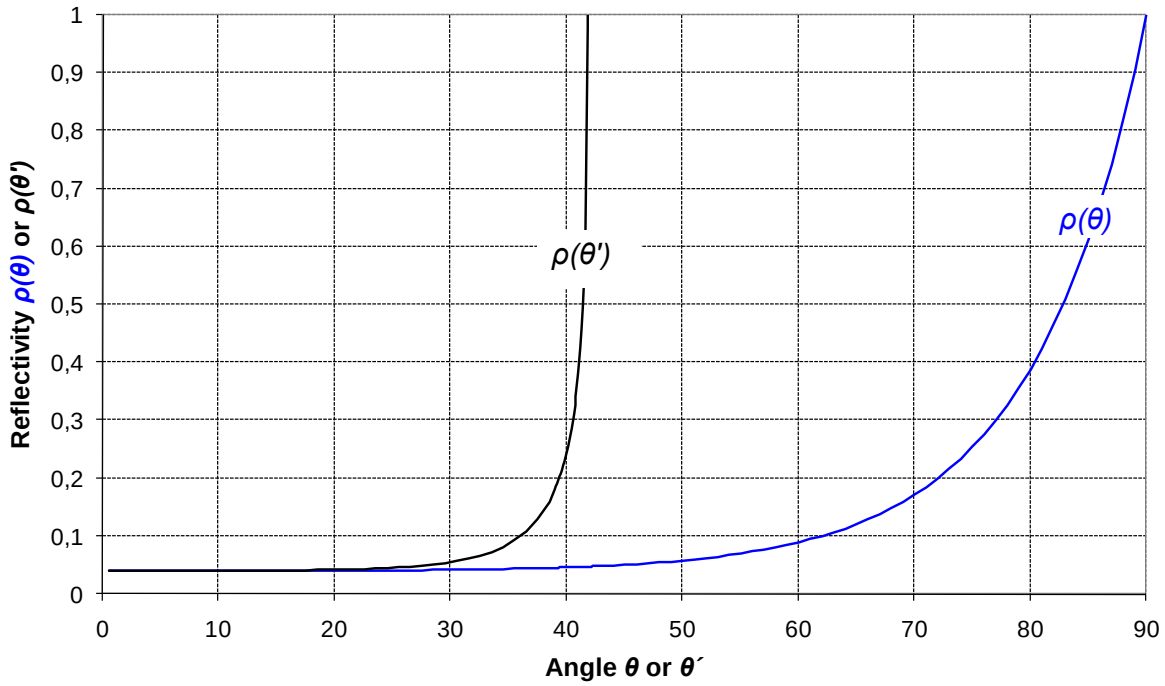

Figure 9.2. Directional reflectivity of clear glass surface, n = 1.5.

The refractive index of a clear glass and the reflectivity of the air-glass interface are only slightly dependent on the wavelength between 0.3 to 4.6 µm ($1.45 \leq n \leq 1.55$). As shown in Figure 9.3, at mid and far infrared radiation after dropping nearly to zero at 8 µm, the reflectivity shows two peaks centred around 9.5 and 21 µm attributable to Si-O stretching and bending influences by network modifiers. [63]

The directional spectral reflectivity $\rho(\lambda,\theta)$ of an opaque surface depends on both wavelength λ and the angle of incident θ measured from the surface normal. Averaging over the wavelengths gives the directional total emissivity

$$\varepsilon_o(\theta,T) = \frac{\pi}{\sigma T^4}\int_0^\infty [1-\rho(\lambda,\theta)]\, i(\lambda,T)\, d\lambda \tag{9.6}$$

where $i(\lambda,T)$ is the blackbody spectral intensity at the surface temperature T. Averaging over the hemisphere gives the hemispherical total emissivity

$$\varepsilon_o(T) = 2\int_0^{\pi/2} \varepsilon_0(\theta,T)\cos\theta\sin\theta d\theta \tag{9.7}$$

At room temperature (20°C) the wavelength λ_m of radiation is near the reflectivity peak at 9.5 µm, and 99.5 percent of the radiation is emitted at wavelengths which are opaque for glass. Thus, the total hemispherical emissivity for the window glass at room temperature solved from Eq. (9.7) is only ε = 0.837 [63]. When the glass temperature increases, the wavelength distribution moves ahead to shorter wavelengths and the glass cannot anymore be dealt with as opaque as in Eqs. (9.6) and (9.7).

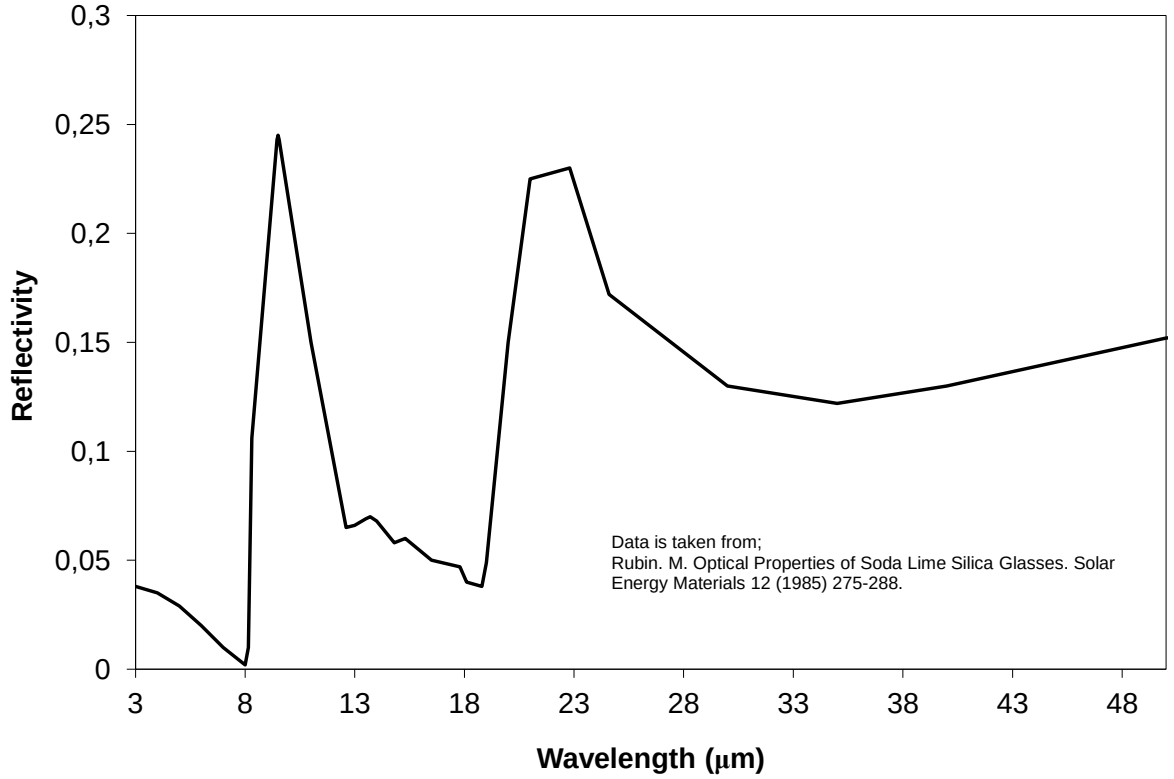

Figure 9.3. Normal *(θ=0°)* spectral reflectivity $\rho_n(\lambda)$ of clear glass surface according to [63].

Because of the low reflectivity of a clear glass surface, the main portion of radiation goes through the interface. The intensity of the radiation attenuates when it propagates in glass, because glass is an absorbing medium, which absorbs electromagnetic radiation and converts it into internal energy. Absorption into glass is strongly wavelength-dependent.

Bouguer's law is the mathematical relation describing the reduction in intensity of radiation as it travels along a path of a finite length within a medium. The intensity of radiation after a path distance x in a medium is

$$i_x = i_0 e^{-\kappa x} \tag{9.8}$$

where i_0 is the intensity at $x = 0$ and κ is the absorption coefficient.

The absorption coefficient κ is the property of a medium that describes the amount of absorption of thermal radiation per unit path length within the medium. Figure 9.4 shows the spectral absorption coefficient of clear soda-lime glass. Soda-lime glass has two cut-off wavelengths at which its absorption coefficient undergoes a large change. Practically, glass is opaque for thermal radiation when the wavelength is over 4.5 μm, whereas for wavelengths under 2.75 μm glass is transparent. At wavelengths between 2.75 and 4.5 μm glass has a relatively high absorption coefficient (semi-transparent band).

As can be seen in Figure 9.4, the variation of an absorption coefficient of glass between temperatures 200 and 600°C is quite small. According to the data presented in [60][64], the absorption coefficient at wavelengths between 1 and 2.75 μm is at its minimum at the temperature range of 800-1000°C.

The absorption coefficients at wavelengths below 4.5 μm are higher when the concentration of iron oxide in glass increases. Such a glass has a greener colour and its light transmission is also lower than it is for clear glass.

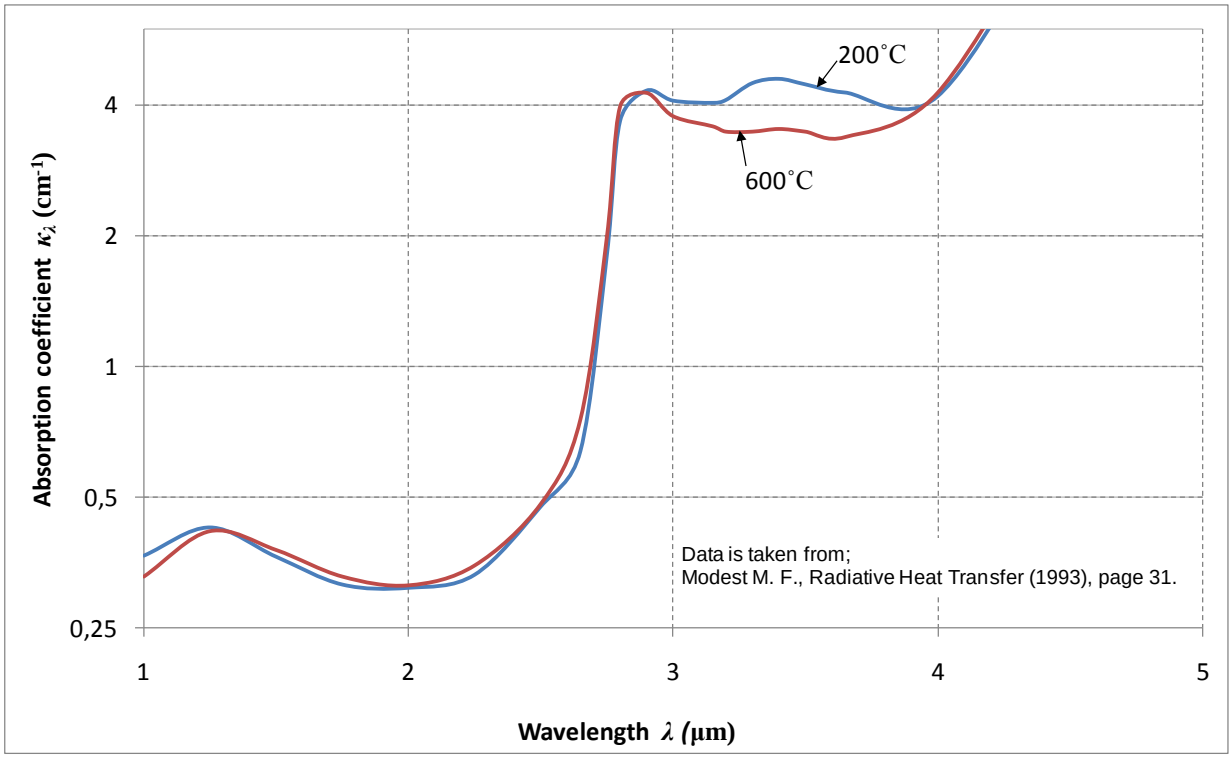

Figure 9.4. Spectral absorption coefficient of clear soda-lime glass according to [60].

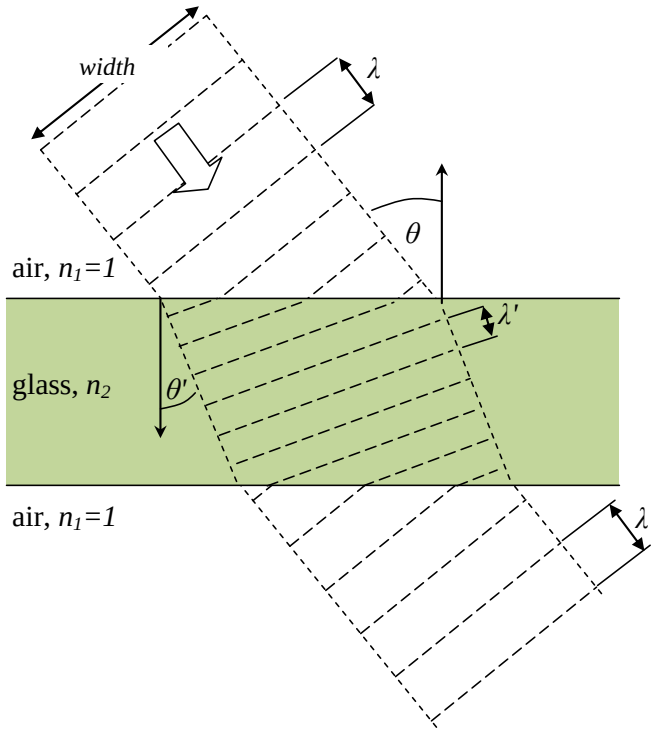

Figure 9.5. Refraction of radiation beam in air-glass and glass-air interface.

The travel of a radiation beam when traversing through glass is already shown in Figure 9.1. In addition to that, some other changes occur, which are described in Figure 9.5. The beam in the glass has a wider cross-section than the beam in the air. This means that the transmitted energy is spread

thinner in glass [49]. The frequency v is unchanged, but in glass the propagation speed of radiation decreases $\upsilon' = \upsilon/n_2$. Consequently, also wavelength $\lambda = \upsilon/v$ decreases to $\lambda' = \lambda/n_2$. The original direction, cross-section, speed and wavelength are recovered when radiation beam exits from the glass.

9.2 Emittance and emissive power of soda-lime glass

Glass spectral absorptance and emittance are connected together with *Kirchoff's* law Eq. (8.12). Thus, with the glass radiative properties data and equations presented previously, it is possible to calculate, for instance, the hemispherical spectral emissive power and hemispherical total emittance of glass. The next three figures are the results of such calculations.

The effect of glass thickness on the hemispherical spectral emissive power is shown in Figure 9.6 at a temperature of 600°C. Particularly, at wavelengths below 2.75 µm the emissive power of clear glass having a practical thickness is low as compared to that of a blackbody, but even a 1 mm glass is a good emitter at wavelengths above 4.5 µm.

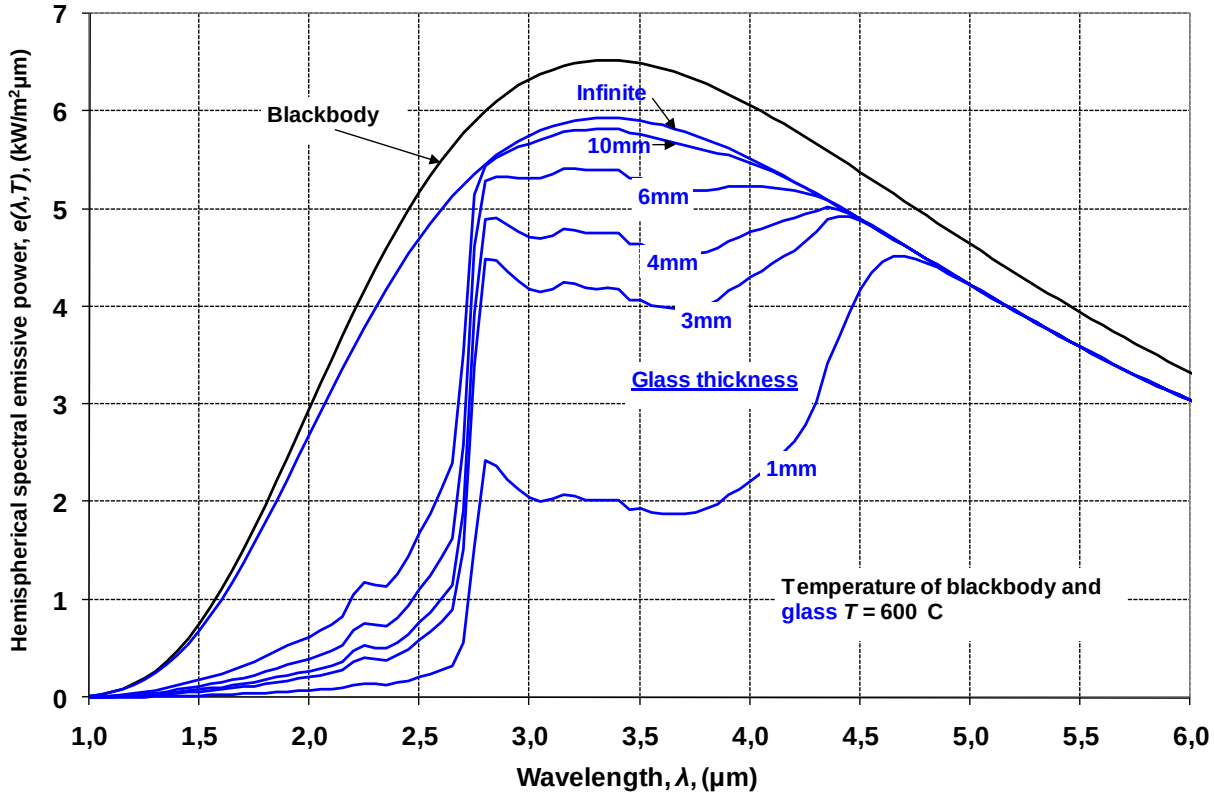

Figure 9.6. Hemispherical spectral emissive power of blackbody and that of various clear soda-lime glasses at temperature of 600°C.

The spectral distribution of the emissive power moves toward shorter wavelengths when the temperature of a blackbody increases. Thus, the higher portion of the emission occurs at wavelengths that are transparent for glass, which in Figure 9.7 yields to a smaller hemispherical total emittance of glass. At infinite thickness and initially also at the biggest thicknesses in Figure 9.7, the emittance increases with temperature. This is due to the increase of glass surface reflectivity at wavelengths above 8 µm, which was shown previously by Figure 9.3.

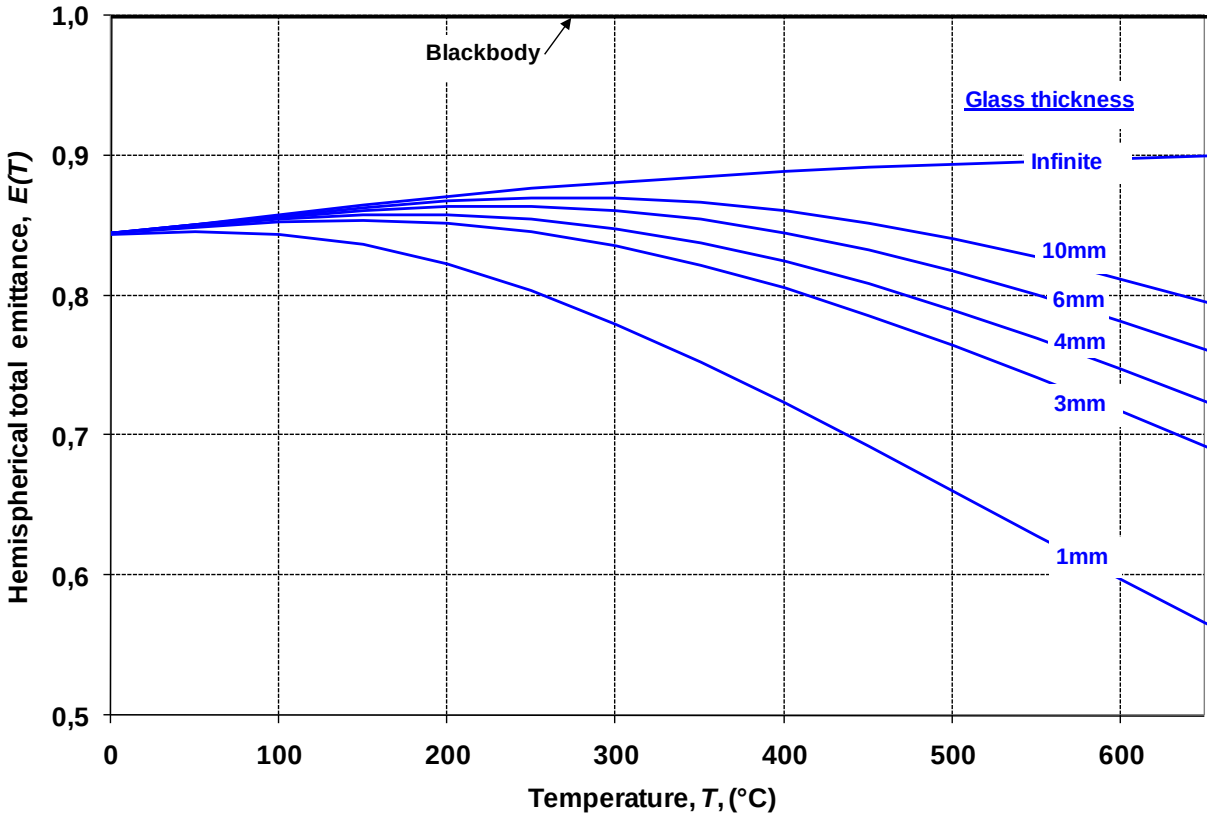

Figure 9.7. Hemispherical total emittance of various clear soda-lime glass thicknesses.

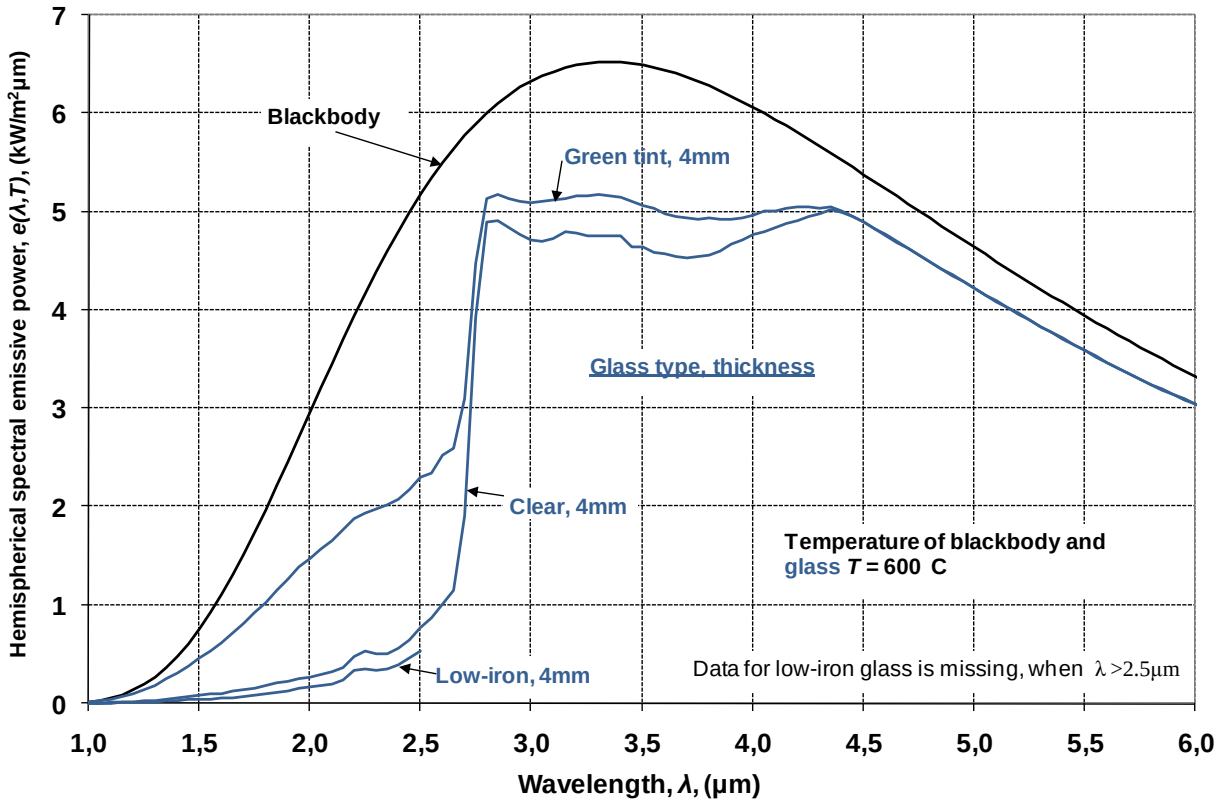

Figure 9.8. Effect of iron oxide concentration on hemispherical spectral emissive power of 4 mm glass.

In Figure 9.8 green tint glass has a higher emissive power than clear glass particularly at wavelengths between 1 and 2.75 μm, which is due to higher iron-oxide concentration. The low iron glass has lower iron-oxide concentration than clear glass, thus its emissive power is also lower at wavelengths between 1 and 4.5 μm. The calculation of the full curve for the low-iron glass in Figure 9.8 was not possible, because of the missing absorption coefficient data at wavelengths above 2.5 μm. The radiative properties of three different commercial glass compositions are compared with each other in [51]. The results show that clear glass has lower absorptance at wavelengths between 0.4 and 2.9 μm than glasses coloured grey or bronze, but at wavelengths between 2.9 and 3.9 μm it is the other way around.

9.3 Directional spectral absorption of glass

With the absorption coefficient and *Bouguer's* law Eq. (9.8) it is possible to formulate the directional spectral absorptance, emittance and transmittance of a glass layer. Figure 9.9 shows a schematic of the glass layer inside the glass, which is exposed to radiation from outside. Radiation coming from a blackbody hits a glass top surface with angle θ in which the intensity is $i_b(\lambda)$.

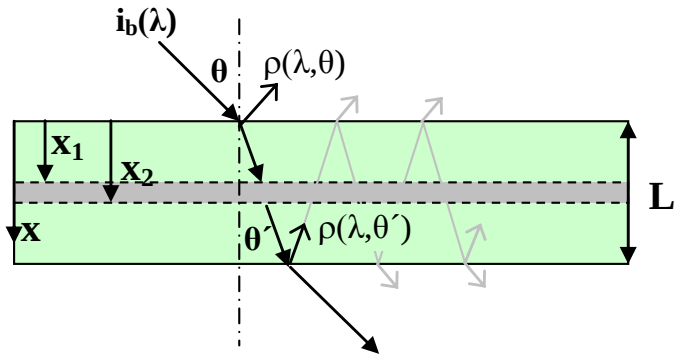

Figure 9.9. Schematic of incident radiation beam hitting glass.

Reflected intensity of the radiation from the top surface is $\rho(\lambda,\theta)i_b$, where $\rho(\lambda,\theta)$ is the reflectivity of a glass surface at the wavelength λ and at angle θ. The radiation intensity that crosses the surface is

$$i_0(\lambda)=\left[1-\rho(\lambda,\theta)\right]\ i_b(\lambda) \tag{9.9}$$

The propagation angle of radiation inside the glass is θ'. According to *Bouguer's* law, the intensity of radiation in depth x_1 is

$$i(\lambda,x_1)=i_0(\lambda)\ e^{-\kappa_\lambda x_1/\cos\theta'} \tag{9.10}$$

where κ_λ is the spectral absorption coefficient of glass. A portion of the radiation that penetrates the glass meets the glass-air interface, where the first reflection inside the glass takes place. The reflectivity of the glass-air interface obeys Eqs. (9.4) and (9.5). A portion of the reflected beam travels again through the glass and hits the glass upper surface, where second reflection takes place. In fact, an endless series of reflections occurs, which attenuates rapidly because of absorption to the glass and penetration out through the glass-air interfaces. The absorbed radiation from the direct radiation to the glass layer between depths x_1 and x_2 is proportional to $i_0\left(e^{-\kappa_\lambda x_1/\cos\theta'}-e^{-\kappa_\lambda x_2/\cos\theta'}\right)$. The absorbed radiation to glass from the direct radiation is proportional to $i_0(1-\tau)$, where $\tau=e^{-\kappa_\lambda L/\cos\theta'}$. The

transmitted radiation is proportional to $i_0\tau[1-\rho(\lambda,\theta')]$. For a clear glass the reflectivity on both sides is equal to $\rho(\lambda,\theta)=\rho(\lambda,\theta')=\rho$, where angles θ and θ' are connected with *Snell's* law. The reflected radiation from the glass-air interface is proportional to $(1-\rho)\tau\rho i_b$. The absorbed radiation to glass from the direct radiation and from the first and second reflections inside a glass is proportional to $(1-\rho)(1-\tau)i_b+(1-\rho)\tau\rho(1-\tau)i_b+(1-\rho)\tau^2\rho^2(1-\tau)i_b$. When all the multiple reflections inside a glass are considered, the directional spectral reflectance *R* absorptance *A* and transmittance *T* can be written as [60]

$$R(\lambda,\theta)=\rho\left[1+(1-\rho)^2\tau^2\left(1+\rho^2\tau^2+\rho^4\tau^4+...\right)\right]=\rho\left[1+\frac{(1-\rho)^2\tau^2}{1-\rho^2\tau^2}\right] \tag{9.11}$$

$$A(\lambda,\theta)=(1-\rho)(1-\tau)\left(1+\rho\tau+\rho^2\tau^2+\rho^3\tau^3+...\right)=\frac{(1-\rho)(1-\tau)}{1-\rho\tau} \tag{9.12}$$

$$T(\lambda,\theta)=\tau(1-\rho)^2\left(1+\rho^2\tau^2+\rho^4\tau^4+...\right)=\frac{\tau(1-\rho)^2}{1-\rho^2\tau^2} \tag{9.13}$$

9.4 Total absorption in glass from incident diffuse radiation

As shown above, the directional absorption of a glass layer is proportional to the difference between intensities before and after the layer. Combining that with Eq. (8.5) gives the hemispherical spectral absorption of glass as

$$a(\lambda)_{0-L}=i_b(\lambda)\int_{\varphi=0}^{2\pi}\int_{\theta'=0}^{\theta'_c}\left[1-e^{-\kappa_\lambda L/\cos\theta'}\right]\Psi'\cos\theta'\sin\theta'\,d\theta'\,d\varphi \tag{9.14}$$

The integration over wavelengths can be covered by using wavelength bands inside which the radiative properties are wavelength independent; then $i_b(\lambda) = F_b(\lambda_i,\lambda_j,T_\infty)\sigma T^4/\pi$. The insertion of that and $\int_0^{2\pi} d\varphi = 2\pi$ to Eq. (9.14) yields to the hemispherical band absorption of glass at wavelength band $\Delta\lambda$ between wavelengths λ_i and λ_j

$$a_{\Delta\lambda,0-L}=2F_b(\lambda_i,\lambda_j,T_\infty)\sigma T_\infty^4\int_0^{\theta'_c}\left[1-e^{-\kappa_\lambda L/\cos\theta'}\right]\Psi'\cos\theta'\sin\theta'\,d\theta' \tag{9.15}$$

where

$$\psi'=\frac{1}{2}\left[\frac{1-\rho_\perp}{1-\rho_\perp e^{-\kappa_\lambda L/\cos\theta'}}+\frac{1-\rho_\Uparrow}{1-\rho_\Uparrow e^{-\kappa_\lambda L/\cos\theta'}}\right] \tag{9.16}$$

is the effective directional transmittance [64].

Equations for the reflectivities $\rho_{\perp}$ and $\rho_{\Uparrow}$ are presented in Sec. 9.1. The integration in Eq. (9.15) is mathematically a complicated problem, which can be solved by converting the integral to a serial function.

$$a_{\Delta\lambda,0-L} = 2F_b\left(\lambda_i,\lambda_j,T_\infty\right)\sigma T_\infty^4 \sum_{\frac{\pi}{1800}(0.5,1.5,\ldots)}^{\theta'_c} \left[1-e^{-\kappa_\lambda L/\cos\theta'}\right]\Psi'\cos\theta'\sin\theta'\frac{\pi}{1800} \tag{9.17}$$

The accuracy of the conversion depends on the length of the angle-step used. In Eq. (9.17) the angle-step is π/1800, which ensures high accuracy.

Since the refractive index of soda-lime glass does not change significantly over the wavelength region of interest, it is reasonable to define certain mean values for glasses having a constant refractive index.

For an opaque wavelength region ($\lambda > 4.5$ μm) with a constant refractive index Eq. (9.17) gives

$$a_{o,0-L} = \alpha_{m,o}F_b\left(\lambda_i,\lambda_j,T_\infty\right)\sigma T_\infty^4 \tag{9.18}$$

where factor $\alpha_{m,o}$ is the mean hemispherical absorptivity of an opaque glass surface. An equivalent hemispherical emissivity is $\varepsilon_{m,o}$. Using n = 1.5 as a refractive index yields $\alpha_{m,o} = \varepsilon_{m,o} = 0.9082$. The value is valid (acceptable estimation) only at wavelengths below 6 μm, where $n \approx 1.5$.

Otherwise, like $\alpha_{m,o}$ and $\varepsilon_{m,o}$, the mean hemispherical reflectivity of a glass surface ρ_m is valid also for transparent and semi-transparent wavelengths regions requiring diffuse radiation. Using n = 1.5 as a refractive index gives $\rho_m = 1 - \alpha_{m,o} = 1 - 0.9082 = 0.0918$.

By using recent mean values for diffuse radiation, the hemispherical band absorption of glass is

$$a_{\Delta\lambda,0-L} = F_b\left(\lambda_i,\lambda_j,T_\infty\right)\sigma T_\infty^4 \left[1-e^{-\kappa_\lambda L/\cos\theta'_m}\right]\psi'_m \tag{9.19}$$

where

$$\psi'_m = \frac{\left(1-\rho_m\right)}{1-\rho_m e^{-\kappa_\lambda L/\cos\theta'_m}} \tag{9.20}$$

is the effective transmittance for diffuse radiation and θ'_m is the weighted mean propagation angle of diffuse radiation inside glass.

The propagation angles of external diffuse radiation in air and glass are given by Figure 9.10. The peak angle in incident radiation is 45°, which is also the weighted mean angle θ_m, while $\frac{q^-}{2} = I^- 2\pi\int_{\pi/4}^{\pi/2}\cos\theta\sin\theta d\theta = I^- 2\pi\int_0^{\pi/4}\cos\theta\sin\theta d\theta$. The weighted mean angle after reflection from the surface is a little smaller than 45º due to higher reflections at bigger angles. The weighted mean propagation angle θ'_m of external diffuse radiation in a glass slab fulfils the equation

$$\int_0^{\theta'_m}\rho(\theta')\cos\theta'\sin\theta' d\theta' = \int_{\theta'_m}^{\theta_c}\rho(\theta')\cos\theta'\sin\theta' d\theta' \tag{9.21}$$

Eq. (9.21) yields to θ'_m = 27.3°, when refractive index n = 1.5.

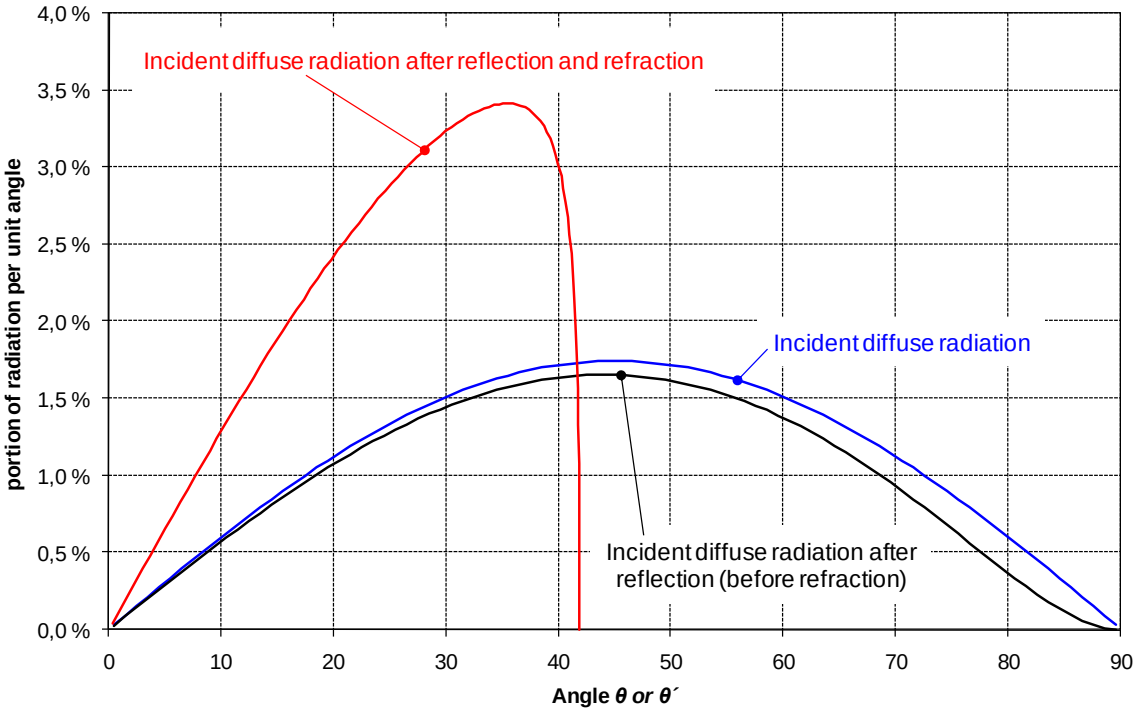

Figure 9.10. Directional distribution of external diffuse radiation in air and in glass (n = 1.5).

The accuracy of the averaged treatment Eq. (9.19) is clarified in Table 9.1 in which hemispherical band absorptances

$$A_{\Delta\lambda,0-L} = \frac{a_{\Delta\lambda,0-L}}{2F_b\left(\lambda_i,\lambda_j,T_\infty\right)\sigma T_\infty^4} \tag{9.22}$$

for a glass slab are plotted in relation to optical thickness. Glass with thickness of 3 mm has optical thickness of about 0.1 at wavelengths below 2.75 μm and 1 at wavelengths between 2.75 and 4.5 μm. In Table 9.1 the maximum difference between the exact solution and Eq. (9.19) is 1.7% when the weighted mean propagation angle of the diffuse radiation inside glass is taken into account. Considering the mean propagation angle in the averaged treatment is important because the maximum difference increases up to 12.5%, when $\theta'_m = 0$ is used.

Table 9.1. Hemispherical band absorptances of glass slab with different optical thicknesses and solution methods (n = 1.5).

κL	$A_{\Delta\lambda,0\text{-}L}$	$A_{\Delta\lambda,0\text{-}L}$	$A_{\Delta\lambda,0\text{-}L}$	$A_{\Delta\lambda,0\text{-}L}$
Solution method	Eq. (9.17) Exact solution	Eq.(9.19), $\theta'_m = 27.3°$	Eq.(9.19), $\theta'_m = 0$	Eq. (9.23), $\theta'_m = 27.3°$
0.01	0.0114	0.0112	0.0099	0.0111
0.1	0.1064	0.1053	0.0943	0.1046
0.5	0.4124	0.4124	0.3784	0.4113
1	0.6310	0.6323	0.5942	0.6317
5	0.9050	0.9052	0.9026	0.9052
10	0.9082	0.9082	0.9082	0.9082
100	0.9082	0.9082	0.9082	0.9082

Eq. (9.19) considers all the multiple reflections inside a glass. Figure 9.11 shows the first seven reflections of a radiation beam from glass-air interface.

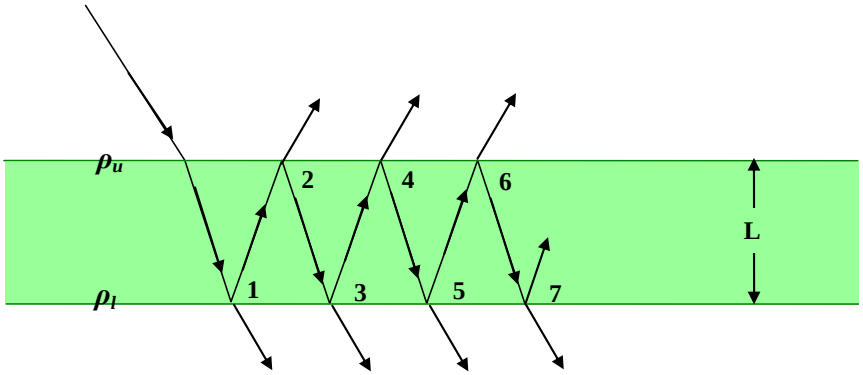

Figure 9.11. Series of reflections inside glass.

Table 9.2. Five first internal reflections given by Figure 9.11 for 3 mm glass. $\theta' = 27.3°$, $\rho_u = \rho_l = \rho = 0.0918$.

Reflection	Equation	κ=0.01 cm^{-1}	κ=0.1 cm^{-1}	κ=1 cm^{-1}	κ=5 cm^{-1}
1	$(1-\rho)\rho e^{-\kappa L/\cos\theta'}$	0.0915	0.0888	0.0655	0.0170
2	$(1-\rho)\rho^2 e^{-\kappa 2L/\cos\theta'}$	0.0084	0.0079	0.0043	0.0003
3	$(1-\rho)\rho^3 e^{-\kappa 3L/\cos\theta'}$	0.0008	0.0007	0.0003	5E-06
4	$(1-\rho)\rho^4 e^{-\kappa 4L/\cos\theta'}$	0.0001	0.0001	2E-05	8E-08
5	$(1-\rho)\rho^5 e^{-\kappa 5L/\cos\theta'}$	6E-06	6E-06	1E-06	1E-09

The order of magnitude of the first five reflections inside a clear glass with thickness of 3 mm is shown in Table 9.2, which is about the minimum thickness for a tempered glass nowadays. The effect of internal reflections decreases with increasing glass thickness due to higher absorption in a thicker glass layer.

The radiative power of internal reflections attenuates rapidly due to absorption and penetration through glass-air interfaces. The first internal reflection is at maximum about 9% of the incoming radiation in Table 9.2. In practice, only the first of the reflections inside the glass must be taken into account, because for instance the second internal reflection is below 1% of the incoming radiation.

By considering only the first internal reflection, the hemispherical band absorption of glass is

$$a_{\Delta\lambda,0-L} = F_b\left(\lambda_i,\lambda_j,T_\infty\right)\sigma T_\infty^4\left(1-\rho_m\right)\left\{\left[1-e^{-\kappa_\lambda L/\cos\theta'_m}\right]+\rho_m\left[e^{-\kappa_\lambda L/\cos\theta'_m}-e^{-\kappa_\lambda 2L/\cos\theta'_m}\right]\right\} \quad (9.23)$$

In Table 9.1 the maximum difference between the exact solution and Eq. (9.23) is 2.5%. Thus, Eq. (9.23) obtains almost the same accuracy as Eq. (9.19), which considers the whole series of internal reflections.

As Eq. (9.24) defines, the total hemispherical absorption of glass is the sum of all hemispherical band absorptions.

$$a_{0-L} = \sum a_{\Delta\lambda,0-L} \quad (9.24)$$

In Section 10.2 the method above for the solving of absorption from incident diffuse radiation into a glass slab is applied to a net radiation model.

10. NEW METHOD FOR MODELLING NET RADIATION IN PLATE GLASS

The simplest method to take radiation into account in the modelling of heat transfer is to assume glass as an opaque material and use a constant value of emissivity. This kind of simplification causes notable errors when the temperatures of glass and/or surroundings are high. The total emissivity of glass (emittance) is not a constant value, while it changes with glass temperature and thickness. As well as the opaque treatment ending up at an erroneous heating rate, it also over-predicts the temperature difference between a glass surface and mid-layer. This is due to the fact that besides the surfaces also the interior emits and absorbs radiation.

10.1 Methods in the literature

Field and Viskanta [66] have developed an analytical one-dimensional method for solving heat transfer in a plate glass. The physical model of a plane layer of glass exchanging energy with the surroundings by convection and radiation is shown in Figure 10.1. In the method the surrounding walls are black emitters.

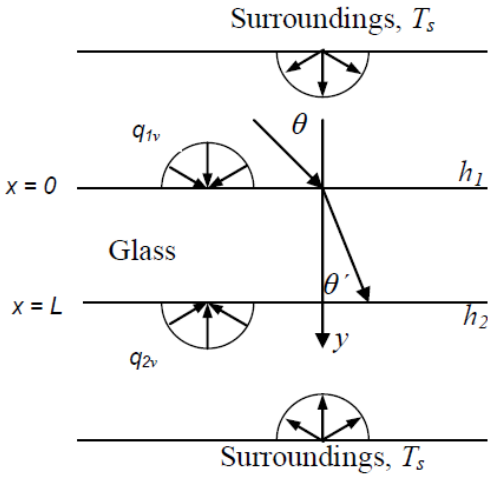

Figure 10.1. One-dimensional problem of Field and Viskanta.

The method is based on the following assumptions:

1. The glass is in local thermodynamic equilibrium; therefore, Planck's and Kirchhoff's laws are valid.
2. Heat transfer by conduction, convection, and radiation occurs only in the direction normal to the plate interfaces.
3. The glass is isotropic, homogenous, and able to absorb and emit but not scatter thermal radiation.
4. The thickness is much greater than the radiation wavelength, making coherence effects negligible.
5. The glass is semi-transparent to radiation for wavelengths $\lambda < \lambda_c$. and opaque for wavelengths $\lambda > \lambda_c$.
6. The variation of refractive index in the glass with temperature is negligible over the temperature range 20°C to 1000°C compared to variation with wavelength.
7. The variation of radiation and thermo-physical properties are known.

In the method *Bouguer's* law describes absorption in medium (glass). *Fresnel* equations and *Snell's* law describe the reflection and refraction at the glass-air interfaces.

Field and Viskanta express separate equations for the cold medium (capable of absorbing radiation only) and hot participating medium (capable on absorbing and emitting radiation). For the hot absorbing and emitting medium the angular integration must be carried out over the entire interval $0 \le \mu \le 1$ ($0 \le \theta' \le 90°$), where $\mu = cos\theta'$. Then the radiation heat flux is expressed as

$$q_r(\tau_v) = 2\pi \left\{ \int_0^{\tau_{Lv}} n_v^2 i_{bv}(\eta) \begin{bmatrix} R_{2,1}(\tau_v + \eta) + \\ R_{2,12}(2\tau_{Lv} + \tau_v - \eta) - \\ R_{2,2}(2\tau_{Lv} - \tau_v - \eta) - \\ R_{2,21}(2\tau_{Lv} - \tau_v + \eta) + \\ sign(\tau - \eta) E_2(\tau_v - \eta) \end{bmatrix} d\eta \right\} \tag{10.1}$$

Expressions for the reflection functions R and the exponential integral function E in Eq. (10.1) can be found from the reference. In Eq. (10.1) i_{bv} is the spectral intensity of blackbody radiation according to *Blanck's* law, τ_v is an optical depth and τ_{Lv} is an optical thickness. Symbol η is not defined in the reference, but it seems to be the variable considering at least the optical thickness coordinate.

Field and Viskanta used frequency v instead of wavelength, because it does not change as it traverses the interface between air and glass. Integrating Eq. (10.1) over the frequency range of the semi-transparent spectral region produces the total internal radiation flux at the optical depth. Computing the total radiation flux in the interior of the plate provides the definition of radiative source term $S = \partial q_r / \partial x$ required in the one-dimensional energy Eq. (7.1). The net radiation at opaque frequencies is considered in boundary conditions.

Gardon [67] has solved a very similar one-dimensional problem as Field and Viskanta above. Only one additional assumption is used. In Gardon's method it is assumed that the temperature distribution inside a glass is symmetrical, thus the glass is heated or cooled at equal rates on both sides. In the problem a plate of glass is exposed to radiation and convection from both sides. The heat balance equation for an elemental slice of glass with thickness Δx is

$$\frac{\partial T(x)}{\partial t} = \frac{1}{\rho c_p \Delta x} \left[q_C(x) + q_A(x) - q_E(x) + q_R(x) \right] \tag{10.2}$$

In the equation above:
q_C = rate of absorption of energy by the slice from the conductive flux of heat within a plate
q_A = rate of absorption by the slice of radiation from outside the plate
q_E = rate of emission of radiation by the slice itself
q_R = rate of re-absorption by the slice of radiation emitted in other slices of the plate

Equations for the heat fluxes above can be found from the reference. The one-dimensional method used by Gardon for solving the time-dependent thickness-wise temperature distributions in a glass plate is quite similar to the method in the next section, but the considering of radiation differs clearly.

Third reference of the methods given in the literature for solving one-dimensional radiation heat transfer in a plate glass is [68]. It gives main equations of the following three methods: the exact numerical solution, the Rosseland approximation and the method developed by Fraunhofer Institute of Mathematics.

10.2 Averaged method for net radiation between blackbody and plate glass

Both methods shortly described above for solving the radiation source term in Eq. (7.1) for a glass between black emitting walls are mathematically complicated. The methods are developed to take radiation heat transfer into account even in cases in which the glass temperature increases high above the glass softening point (≈725°C). Next, the treatment of radiation is simplified based on the assumption along which glass temperature is below 700°C as it is in glass tempering, bending and laminating processes.

The emission of glass volume element is a bulk, not a surface, phenomenon. The rate at which glass volume element inside glass emits radiation is proportional to $n^2\sigma T^4$. Volume emission within a glass is thus n^2 times that of a blackbody emission in air (vacuum), which leads to the fact that at least a portion n^2-1 of radiation is pure internal radiation inside a glass. The remaining part excluding the reflection from glass-air interface in the emission out of glass. The emission out of the glass is composed of the radiation that hits the glass-air interface at angles smaller than θ'_c, because at bigger angles all the radiation is reflected back.

The emission of a volume element inside a glass can be divided into two parts:

- Emission inside the glass to other volume elements
- Emission out of the glass

The glass volume-element emits radiation and absorbs radiation emitted by other volume-elements. Such an internal net radiation affects like thermal conductivity, which reduces internal temperature differences. The effect of internal net radiation increases greatly with glass temperature, due to higher intensities of the transparent and semi-transparent radiation. Internal net radiation is effective inside a molten glass, and it is emphasized by higher iron-oxide impurity, which magnifies the glass emissivity of non-opaque wavelengths below 4.5 μm. It is not overstating to write that the consideration of internal net radiation inside a molten glass is one of the most complicated problems in the field of radiation heat transfer. Fortunately, the effect of internal net radiation is not important inside a glass in a tempering process, where the glass temperature is always below 700°C.

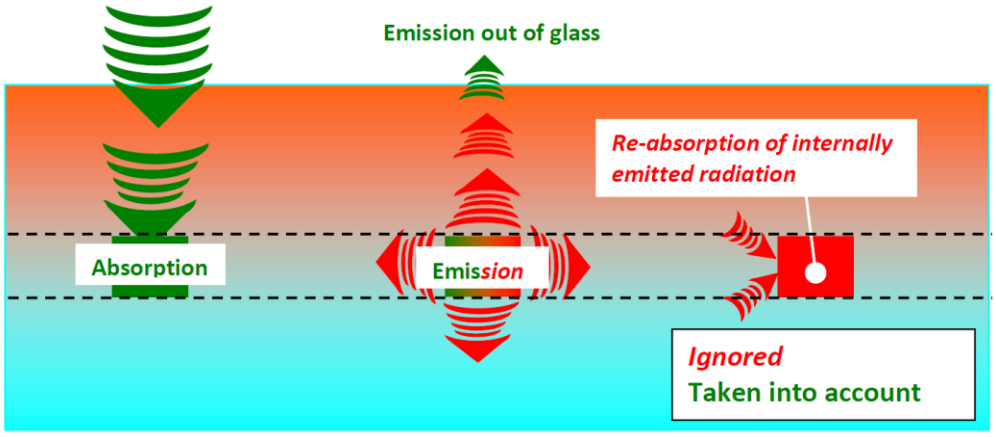

Figure 10.2. Schematic of glass internal radiation and simplified treatment of it.

The internal radiation in a plate glass is described by Figure 10.2. In the Averaged Net Radiation (ANR) method the radiation heat transfer between the glass volume elements and the surroundings is divided into two parts: absorption of external radiation coming from the surroundings and emission of the glass volume elements out of the glass. Net radiation between glass volume elements is ignored.

Based on the *Kirchhoff's* law, *Bouguer's* law and Eq. (9.12), the directional band emittance out of the glass by the glass layer between depths x_1 and x_2 from the surface in Figure 9.1 can be expressed as.

$$E(\theta')_{\Delta\lambda,x_1-x_2} = A(\theta')_{\Delta\lambda,x_1-x_2} = \frac{(1-\rho)}{1-\rho e^{-\kappa_\lambda L/\cos\theta'}}\left[\left(e^{-\kappa_\lambda x_1/\cos\theta'} - e^{-\kappa_\lambda x_2/\cos\theta'}\right)\right] \tag{10.3}$$

The directional band net radiative heat flux between surrounding and the glass layer is

$$q_r(\theta')_{\Delta\lambda,x_1-x_2} = \left[F_b(\lambda_i,\lambda_j,T_\infty)\sigma {T_\infty}^4 - F_b(\lambda_i,\lambda_j,T)\sigma T^4\right] E(\theta')_{\Delta\lambda,x_1-x_2} \tag{10.4}$$

Eq. (10.4) expresses the net heat flux between the glass layer and upper (x = 0) surrounding. For solving the total net radiation, considering both surroundings and integration over angles $0 \le \theta' \le \theta'_c$ and wavelengths is needed.

When the glass is heated symmetrically on both sides, the net radiation source term $\partial q_r/\partial x = S$ in energy Eq. (7.1) for the volume layer Δx in Figure 9.1 can be written as [65]

$$S_{x_1-x_2} = q_{r,x_1-x_2} = \sum_{i=1,\,j=2}^{i=k,\,j=k+1} \left\{ \begin{matrix} \left[F_b(\lambda_i,\lambda_j,T_\infty)\sigma {T_\infty}^4 - F_b(\lambda_i,\lambda_j,T)\sigma T^4\right]\psi'_m \\ \left[e^{-\kappa_\lambda x_1/\cos\theta'_m} - e^{-\kappa_\lambda x_2/\cos\theta'_m} + e^{-\kappa_\lambda (L-x_2)/\cos\theta'_m} - e^{-\kappa_\lambda (L-x_1)/\cos\theta'_m}\right] \end{matrix} \right\} \tag{10.5}$$

In Eq. (10.5) the integration over wavelengths has been considered so that spectral absorption has been approximated with k wavelength bands with mean absorption coefficients κ_λ, alike in the methods discussed in the last sections. In the method above the integration over the θ' is also eliminated by using mean values. Reflections at the surfaces of glass and the direction of propagation of radiation in a glass plate are taken into account by using previously solved mean values for diffuse radiation. As an example at wavelength bands in which refractive index n = 1.5, the mean reflectivity for diffuse radiation ρ_m = 0.0918 and the mean propagation angle of radiation inside glass θ'_m = 27.3°, as was proved previously in Sec. 9.4. These values represent well all transparent and semi-transparent wavelengths, while $n \approx 1.5$ at these wavelengths. At opaque wavelengths the mean propagation angle inside glass has no effect, because such radiation does not travel inside glass. Thus, only ρ_m is needed for opaque wavelengths. Eq. (10.5) is valid only when ambient temperatures are equal on glass both sides. If glass is heated non-symmetrically, then sides must be considered separately. Then the net radiation source term

$$S_{x_1-x_2} = \sum_{i=1,\,j=2}^{i=k,\,j=k+1} \psi'_m \left\{ \begin{matrix} \left[F_b(\lambda_i,\lambda_j,T_{\infty,u})\sigma {T_{\infty,u}}^4 - F_b(\lambda_i,\lambda_j,T)\sigma T^4\right]\left(e^{-\kappa_\lambda x_1/\cos\theta'_m} - e^{-\kappa_\lambda x_2/\cos\theta'_m}\right) + \\ \left[F_b(\lambda_i,\lambda_j,T_{\infty,l})\sigma {T_{\infty,l}}^4 - F_b(\lambda_i,\lambda_j,T)\sigma T^4\right]\left(e^{-\kappa_\lambda (L-x_2)/\cos\theta'_m} - e^{-\kappa_\lambda (L-x_1)/\cos\theta'_m}\right) \end{matrix} \right\} \tag{10.6}$$

Eq. (10.6) considers the series of multiple reflections inside a glass. If only the first reflection of incoming radiation inside glass is taken into account, then the net radiation source term

$$S_{x_1-x_2} = \sum_{i=1,j=2}^{i=2,j=k+1} \left\{ \begin{array}{l} \left[F_b\left(\lambda_i,\lambda_j,T_{\infty,u}\right)\sigma T_{\infty,u}^4 - F_b\left(\lambda_i,\lambda_j,T\right)\sigma T^4\right](1-\rho_u)\times \\ \left\{ \left[e^{-\kappa_\lambda x_1/\cos\theta'_m} - e^{-\kappa_\lambda x_2/\cos\theta'_m}\right] + \rho_l\left[e^{-\kappa_\lambda(2L-x_2)/\cos\theta'_m} - e^{-\kappa_\lambda(2L-x_1)/\cos\theta'_m}\right] \right\} + \\ \left[F_b\left(\lambda_i,\lambda_j,T_{\infty,l}\right)\sigma T_{\infty,l}^4 - F_b\left(\lambda_i,\lambda_j,T\right)\sigma T^4\right](1-\rho_l)\times \\ \left\{ \left[e^{-\kappa_\lambda(L-x_2)/\cos\theta'_m} - e^{-\kappa_\lambda(L-x_1)/\cos\theta'_m}\right] + \rho_u\left[e^{-\kappa_\lambda(L+x_1)/\cos\theta'_m} - e^{-\kappa_\lambda(L+x_2)/\cos\theta'_m}\right] \right\} \end{array} \right\} \tag{10.7}$$

In Eq. (10.7) it is possible to use different values for reflectivity on the upper and lower surfaces, which is needed as an example if another glass surface is coated. Thermal radiation in a coated glass is handled more in Sec. 11. For a clear glass surface $\rho_m = \rho_u = \rho_l$.

In addition to the assumptions of Field & Viskanta in Sec. 10.1, the averaged method described above is based on the following assumptions:

1. The net radiation between glass volume elements is insignificant (glass temperature is below 700°C).
2. The integration over the θ' can be eliminated by using mean values (reflectivity, propagation angle) for diffuse radiation.
3. In Eq. (10.7) only the first reflection of incoming radiation inside glass is taken into account.

10.3 Accuracy of Averaged Net Radiation method

In the explicit finite difference method the glass is divided into layers (volume elements), calculation proceeds by time-step Δt at once and the results after the last time-step are used as initial data for the next time-step. The limiting condition for the time-step is $Fo = k\Delta t/(\rho c_p \Delta x^2) < 0.5$, which yields to $\Delta t < 0.5\rho c_p \Delta x^2/k$. Also the condition $Fo(1+Bi) < 0.5$ written for surface layers, where $Bi = h\Delta x/k$ and heat transfer coefficient h covers all heat transfer phenomena, must be fulfilled. The method is very useful for solving many kinds of problems, and instead of time-steps also distance-steps can be used as an example if the air temperature or pressure development in the convection pipe presented in Figure 5.6 are to be solved. Sometimes an important initial value is not known, but a balance equation for it can be written. Then, the first initial value is just a good guess after which a better guess based on result and balance equation can be made. Finally, the result fulfils the balance equation and the problem is solved. The formulation and programming of such equations as a computation program is a relatively simple task, and as an example Microsoft Excel with its Visual Basic potential is a handy tool for the task.

As shown in Figure 10.3 glass thickness is divided into eleven layers, and the thickness of the surface layer is one half the thickness of the inner-layer, $\Delta x = L/10$.

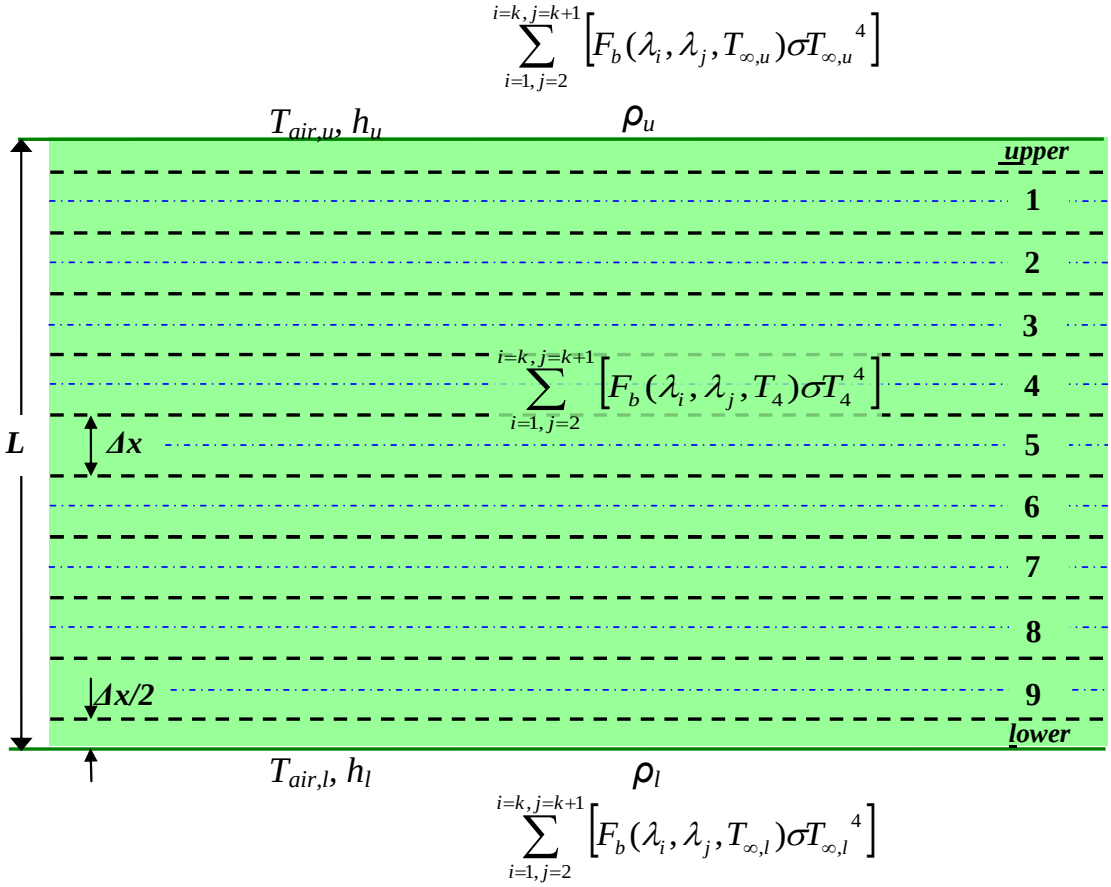

Figure 10.3. Computation model for heating and cooling of glass plate.

In glass inner layers heat transfer occurs by conduction between adjoining layers and net radiation between surroundings. For instance, the energy balance for the inner layer 4 in Figure 10.3 can be written as

$$\rho c_p \frac{T_4^{p+1} - T_4}{\Delta t}\Delta x = k\frac{T_5 - T_4}{\Delta x} + k\frac{T_3 - T_4}{\Delta x} + S_{4,u} + S_{4,l} \tag{10.8}$$

where superscript $p+1$ indicates the future after time-step Δt. In the energy balance the temperature T_4 covers the whole layer, but its accurate coordinate is in the middle of layer 4 at the thickness of $4\Delta x$ from the glass upper surface. Net radiation is taken into account with source terms S_4 written individually to opposite directions.

In addition to conduction and radiation, also convection occurs in glass surface layers. The energy balance for the upper surface layer in Figure 10.3 can be written as

$$\rho c_p \frac{T_u^{p+1} - T_u}{\Delta t}\frac{\Delta x}{2} = k\frac{T_1 - T_u}{\Delta x} + S_{u,u} + S_{u,l} + h_u\left(T_{air,u} - T_u\right) \tag{10.9}$$

Radiation source terms for the inner layer 4 are

$$S_{4,u} = \sigma \sum_{i=1,\,j=2}^{i=k,\,j=k+1} \left\{ \left[F_b(\lambda_i, \lambda_j, T_{\infty,u}) {T_{\infty,u}}^4 - F_b(\lambda_i, \lambda_j, T_4) {T_4}^4 \right] A_{4,u,i} \right\}$$
$$S_{4,l} = \sigma \sum_{i=1,\,j=2}^{i=k,\,j=k+1} \left\{ \left[F_b(\lambda_i, \lambda_j, T_{\infty,l}) {T_{\infty,l}}^4 - F_b(\lambda_i, \lambda_j, T_4) {T_4}^4 \right] A_{4,l,i} \right\} \quad (10.10)$$

where absorptances

$$A_{4,u,i} = (1-\rho_u)\left\{ \left[e^{-\kappa_\lambda 3.5\Delta x/\cos\theta'_m} - e^{-\kappa_\lambda 4.5\Delta x/\cos\theta'_m} \right] + \rho_l \left[e^{-\kappa_\lambda (L+5.5\Delta x)/\cos\theta'_m} - e^{-\kappa_\lambda (L+6.5\Delta x)/\cos\theta'_m} \right] \right\}$$
$$A_{4,l,i} = (1-\rho_l)\left\{ \left[e^{-\kappa_\lambda 5.5\Delta x/\cos\theta'_m} - e^{-\kappa_\lambda 6.5\Delta x/\cos\theta'_m} \right] + \rho_u \left[e^{-\kappa_\lambda (L+3.5\Delta x)/\cos\theta'_m} - e^{-\kappa_\lambda (L+4.5\Delta x)/\cos\theta'_m} \right] \right\} \quad (10.11)$$

The first term in Eq. (10.11) considers the primary net radiation, and the second considers the net radiation via reflection from the glass lower surface. The opaque radiation band is handled like any other wavelength band, while the use of very high value for the appropriate absorption coefficient produces the same results. Thus, the source terms for surface layers are like they are for inner layers. Only the multipliers of Δx, which consider the path lengths to surfaces, change. Factor $cos\theta'_m{}^{-1}$ in Eq. (10.11) takes the mean direction of diffuse radiation inside glass slab into account. As written in Sec. 9.4, θ'_m is equal to 27.3° (when n = 1.5), which yields $cos\theta'_m{}^{-1}$ = 1.125. In Eq. (10.11) only the absorption coefficient is subscripted as wavelength dependent. If required, then also both reflectivities and even θ'_m (unnecessary for soda-lime glass) can be treated as wavelength dependent by using the mean values for the each wavelength band.

Above the ANR-method above was coupled to explicit finite difference method. With such a combination method the development of glass thickness-wise temperature profile can be solved. Next, the method is used for solving heat transfer problems found from the literature in which a more sophisticated approach than the ANR-method is used to solve radiation heat transfer in glass. The aim is to study the accuracy of the ANR-method. In the cases studied the initial data used were set the same as in the literature examples. A comparison procedure was as follows: the results produced by the ANR-method were processed as an exactly analogous format with results in the literature, after which the result figures were placed alongside to be visually compared. Now only the results of the ANR-method are presented, and the analysis of the comparison is given in words. Only in the last case to be presented the results in the literature were in such a reading scale that it was possible to copy them exactly in the result figure.

Gardon solved theoretically the heating problem of glass in a radiation furnace [67]. The glass initial temperature was 27°C and it was placed in the ambient with black walls and at a temperature of 707°C. The glass thickness was 6 mm and convection was ignored. Thermal conductivity of glass was 0.8374 W/(mK) and specific heat times density was 2.512×10^6 J/(m^3°C), which gives specific heat of 993 J/(kgK) at density value of 2530 kg/m^3. The reflectivity of the glass surface was 0.09 at all wavelengths. The absorption coefficient was 0.5 cm^{-1} at wavelengths between 1 and 2.75 µm, and 5.0 cm^{-1} at wavelengths between 2.75 and 4 µm. The glass was opaque at wavelengths longer than 4 µm. Also the case in which glass was totally opaque was modelled. The results for the problem are given by Figure 10.4 and Figure 10.5. The ANR-method (coupled to explicit finite difference method) produced very closely the same results as those presented in [67].

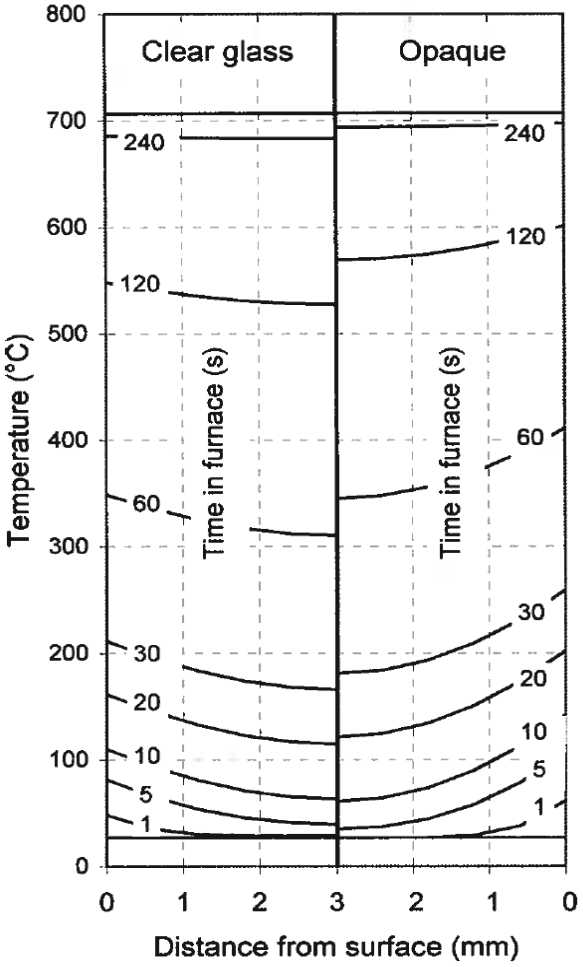

Figure 10.4. Calculated temperature profiles in glass plates heated in radiation furnace.

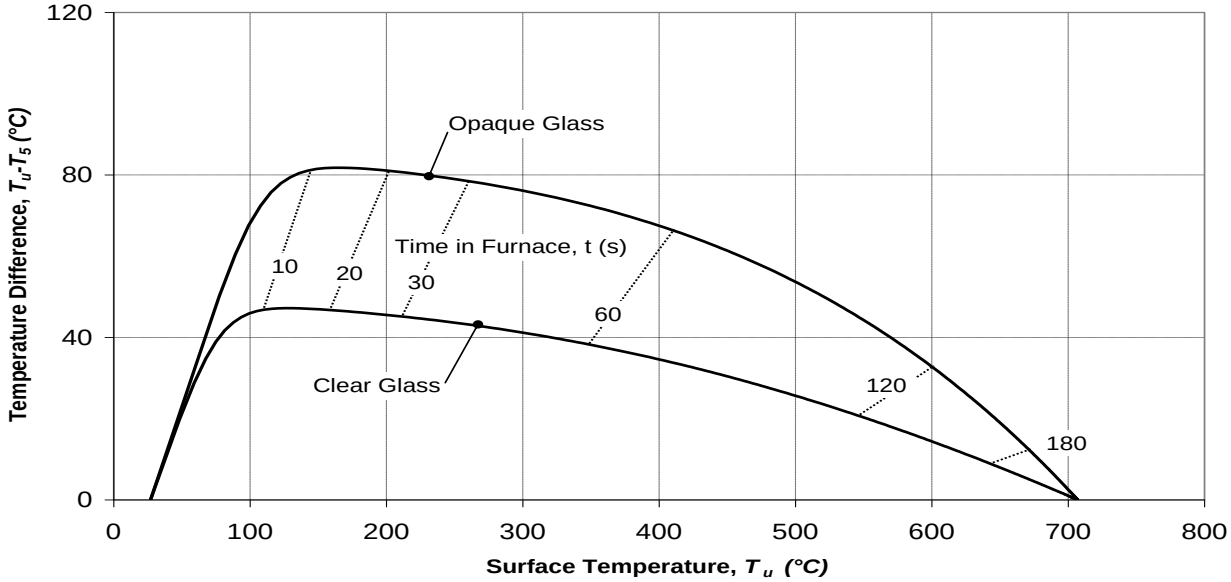

Figure 10.5. Calculated temperature difference between the surface and mid-plane for glass heated in radiation furnace.

Gardon also solved the tempering cooling and slow cooling problems, in which the initial temperature of the glass was 707°C and it was placed in the ambient [67]. During tempering the forced convection heat transfer coefficient was 209.35 W/(m^{2}K) and during slow cooling 12.56 W/(m^{2}K). Air and ambient temperature was 27°C and the rest of the initial data was as in the heating problem above. The new results for the problems are given below.

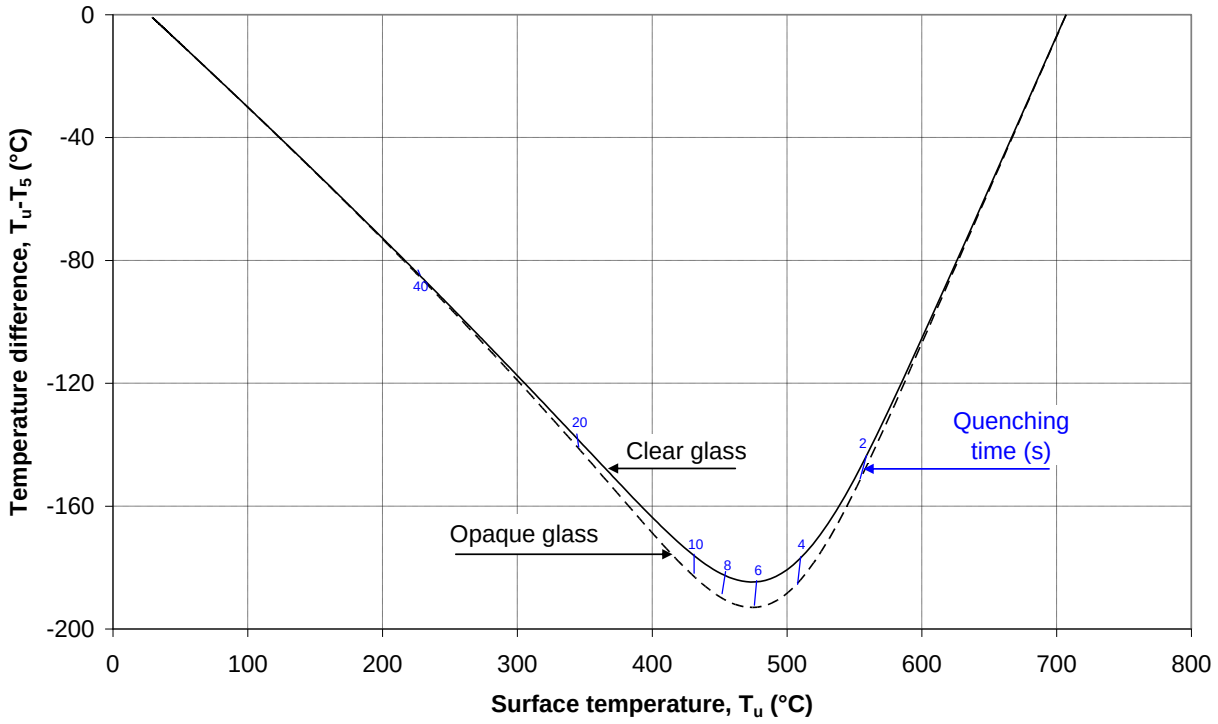

Figure 10.6. Calculated temperature difference between the surface and mid-plane for glass during tempering cooling.

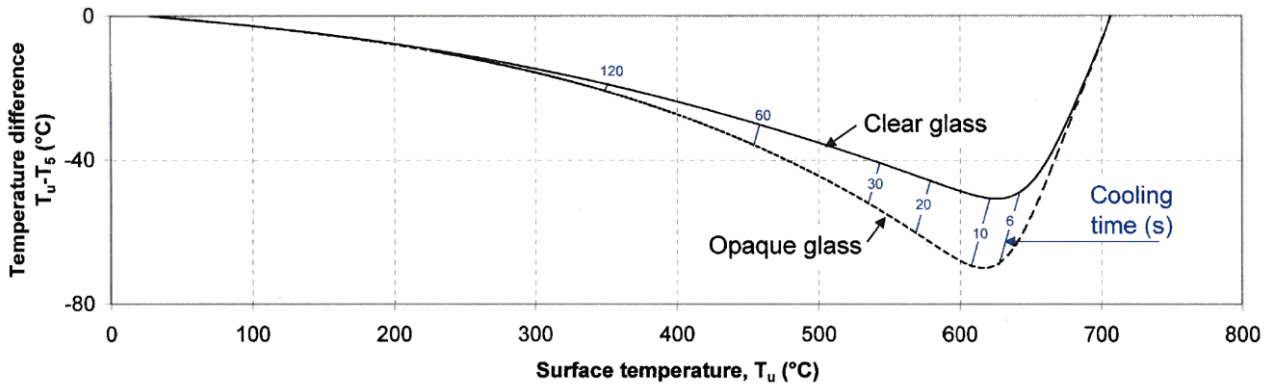

Figure 10.7. Calculated temperature difference between the surface and mid-plane for glass during slow cooling.

The results for the opaque glass plotted in Figure 10.6 and Figure 10.7 match perfectly the results presented in [67], but the results for clear glass differ slightly. Apparently, the difference is due to ignoring of the net radiation between glass volume elements, and due to that the ANR-method slightly over-predicts the temperature difference (max. error is 6%). In both problems the glass initial temperatures and particularly in tempering also the temperature differences in glass were high, thus the net radiation between glass volume elements had convenient conditions to even out the thickness-

wise temperature differences. It is evident that the error decreases when the initial temperature drops to 640°C, which is a typical initial temperature in glass tempering.

Field & Viskanta studied cooling of a glass in the laboratory ambient theoretically and experimentally [66]. The glass initial temperature was 550°C (in the results plotted in the reference the initial temperature seems to be 515-535°C depending on the glass thickness) and it was placed in the ambient with black walls and at temperature of 20°C. Glass thicknesses were 11.68, 6.76 and 3.71 mm. Natural convection was taken into account with heat transfer coefficient 4.25 W/(m^2K). The thermal conductivity of glass was considered with the equation shown in Appendix A. Specific heat was determined using the method of Sharp and Ginther [69] and the glass density was 2515 kg/m^3. Reflection obeyed *Fresnel's Equations* and the variation of refractive index in the glass with wavelength was considered. The absorption coefficient was 0.28 cm^{-1} at wavelengths between 0 and 1µm, 0.4 cm^{-1} at wavelengths between 1 and 1.8 µm, 0.28 cm^{-1} at wavelengths between 1.8 and 2.6 µm, and 3 cm^{-1} at wavelengths between 2.6 and 3.8 µm. the absorption coefficient was 60 cm^{-1} at wavelengths between 3.8-5 µm, which practically means that the glass was opaque, as it was at longer wavelengths than 5 µm.

Temperatures drop clearly more slowly in Figure 10.8 than in the corresponding results presented in [66]. As an example of the difference, the temperature of 300°C is reached at times 3.71 mm - 100 s, 6.76 mm - 180 s and 11.68 mm - 320 s according to theoretical results shown in the reference, but the equivalent times in Figure 10.8 are, 119, 208 and 375 s. The temperature differences shown in Figure 10.9 produced by the ANR-method are close to the measured values plotted in the reference. The theoretical results plotted in the reference predict clearly a higher temperature difference than the ANR-method, which is surprising, when ignoring the net radiation between glass volume elements should yield higher temperature profiles.

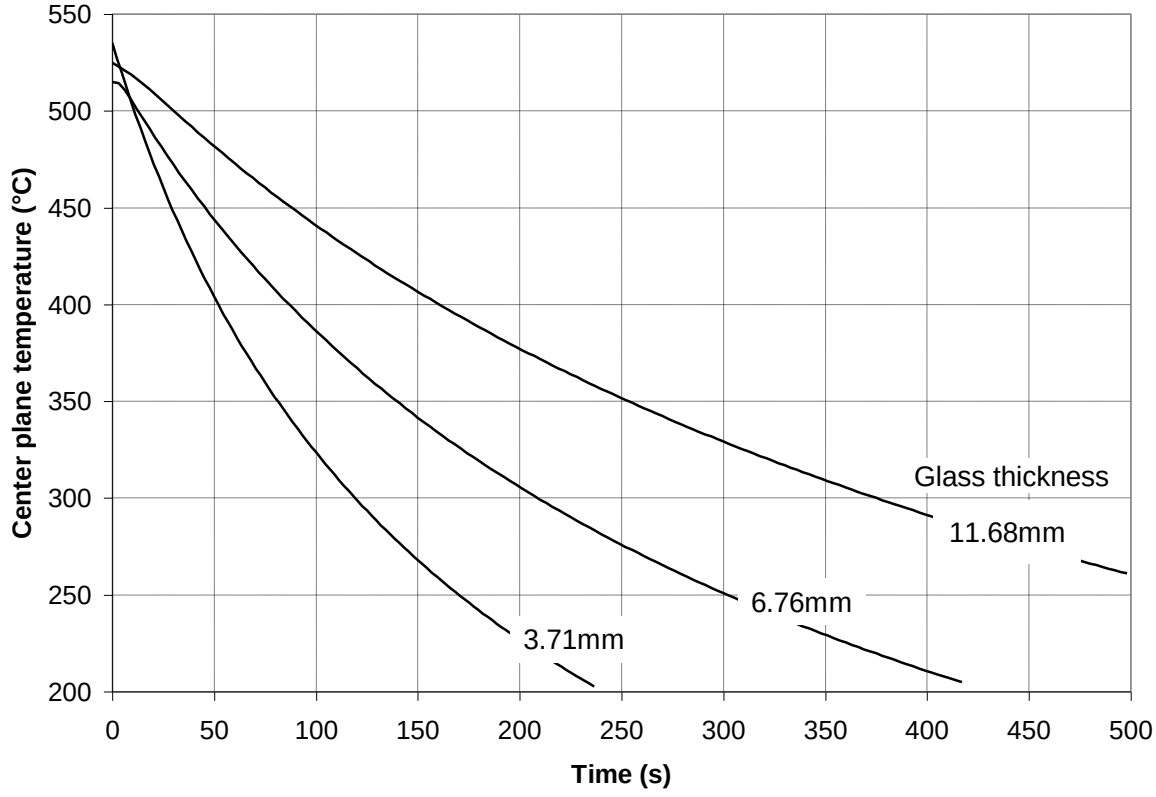

Figure 10.8. Calculated glass mid-plane temperatures during cooling.

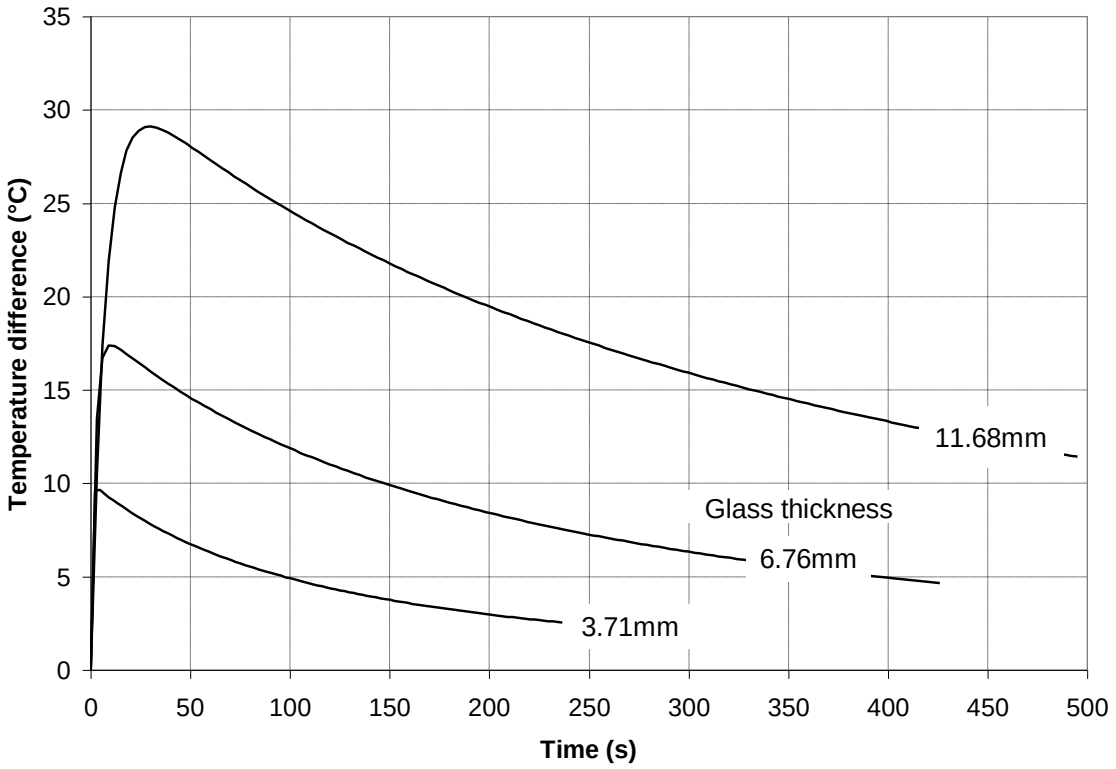

Figure 10.9. Temperature difference between glass front surface and mid-plane during cooling.

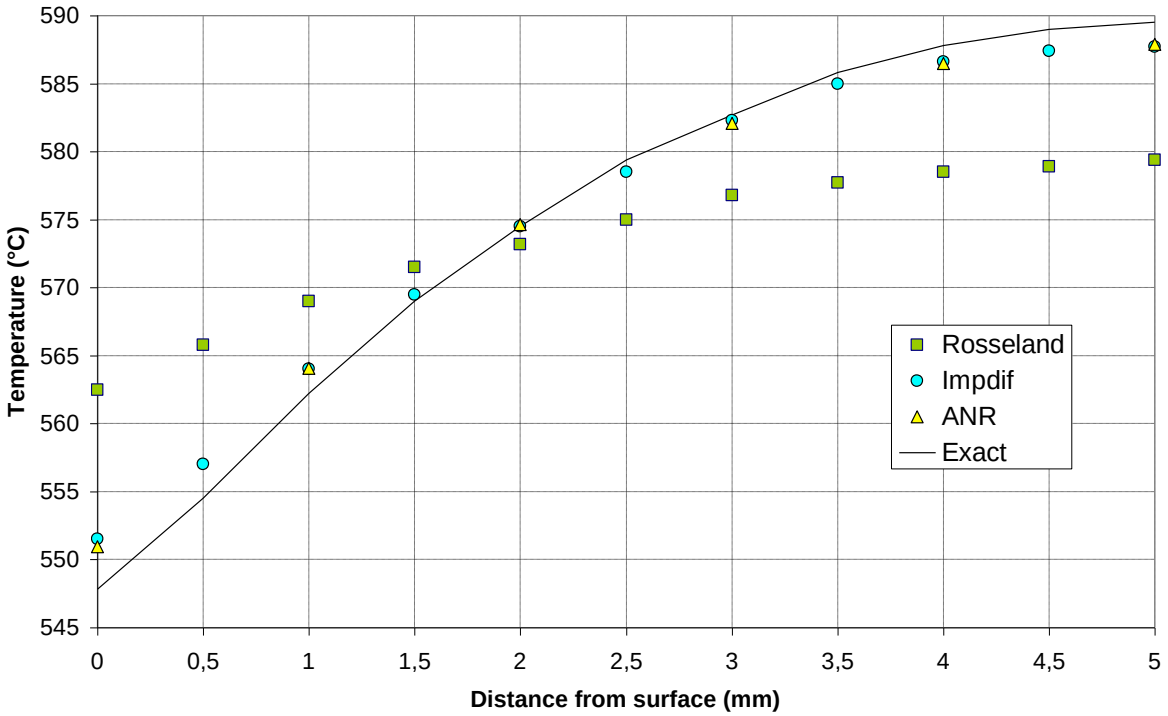

Figure 10.10. Comparison of the temperature profile in the middle of the glass calculated by different methods.

A cooling problem of glass slab in normal ambient conditions is theoretically solved in [70]. The glass initial temperature was 600°C and it was placed in the surroundings with black walls and at

temperature of 20°C. Convection was ignored. The thermal conductivity of the glass was 1 W/(mK) and specific heat times density was 1.988×10^6 J/(m^3°C). The refractive index of glass was 1.46, but other radiative properties were not specified in the reference. Therefore, the same absorption coefficients as were used previously in Gardon's case were also used in this case. The size of the glass plate was 100 × 100 × 10 mm. The thickness-wise temperature profile from the midpoint of plate after cooling time of 10 s was solved, thus practically the problem is one-dimensional, while it is evident that the edges do not have any effect on the result.

In the reference (values are copied to Figure 10.10) the Rosseland method predicts clearly smaller temperature gradient than the Impdif (improved diffusion) method, which ends near the exact solution. As seen from Figure 10.10 the ANR-method predicts very similar temperatures to the Impdif method.

10.4 Use of ANR-method in heat transfer modelling

The one-dimensional method in Sec. 10.3 in which the ANR-method takes radiation into account gives accurate results for heat transfer problems in which glass temperature is below 700°C. In the method the change of furnace temperatures and heat transfer coefficients in regard to time as well as the change of glass material properties in regard to temperature can quite easily be taken into account. The method can be applied to the case with diffuse grey or even wavelength dependent surroundings. The ANR-method has also been applied in a two-dimensional case in which the aim was to study overheating of the glass edges during heating in a tempering furnace.

The radiation heat transfer in glass bending and laminating processes is also modelled with the ANR-method. In a windscreen bending process two glasses are in contact with each other. Thus, the radiation heat transfer problem is more complex due to reflecting boundary (thin air gap due to separation powder) between glasses. In a flat glass laminating process radiation heat transfer occurs between a hot furnace and glass-film sandwich. Both glass and film (PVB) have spectrally varying radiative properties. The short wavelength infrared radiation emitted by an IR-heater penetrates through the glass and is partly absorbed by the film layer. In the cases mentioned above experimental data needed for verifying the radiation heat transfer model is still missing.

A coating on the glass surface makes the modelling of radiation heat transfer in glass much more complex. Nowadays, particularly low-e coatings are common among glasses to be tempered. In next section the ANR-method is adapted as applicable to a low-e coated glass.

11. THERMAL RADIATION IN LOW-E COATED PLATE GLASS

As shown before, the radiative properties of clear glass are well known and several methods for solving radiation heat transfer in clear glass are developed. In the case of low-emissivity coated glass only the data given by glass manufacturers is available. The standard structures of off-line low-e coatings were shown on page 8. There are many material layers on a coated surface, of which the silver layer is the one which changes the reflectivity. The reflectivities of clear and low-e coated (sputtered off-line coatings) glass surfaces are shown in Figure 11.1. Even one silver layer in a coating is enough to change the reflectivity of a glass surface totally, but reflectivity can still be reduced by adding more silver layers. Both coatings in Figure 11.1 have low visible light and high room wavelength reflectivity. Particularly the two silver layer coating has also high solar (wavelengths longer than the visible light emitted by the sun) reflectivity, a capacity which applies particularly to keeping heat out of the room in hot climatic conditions.

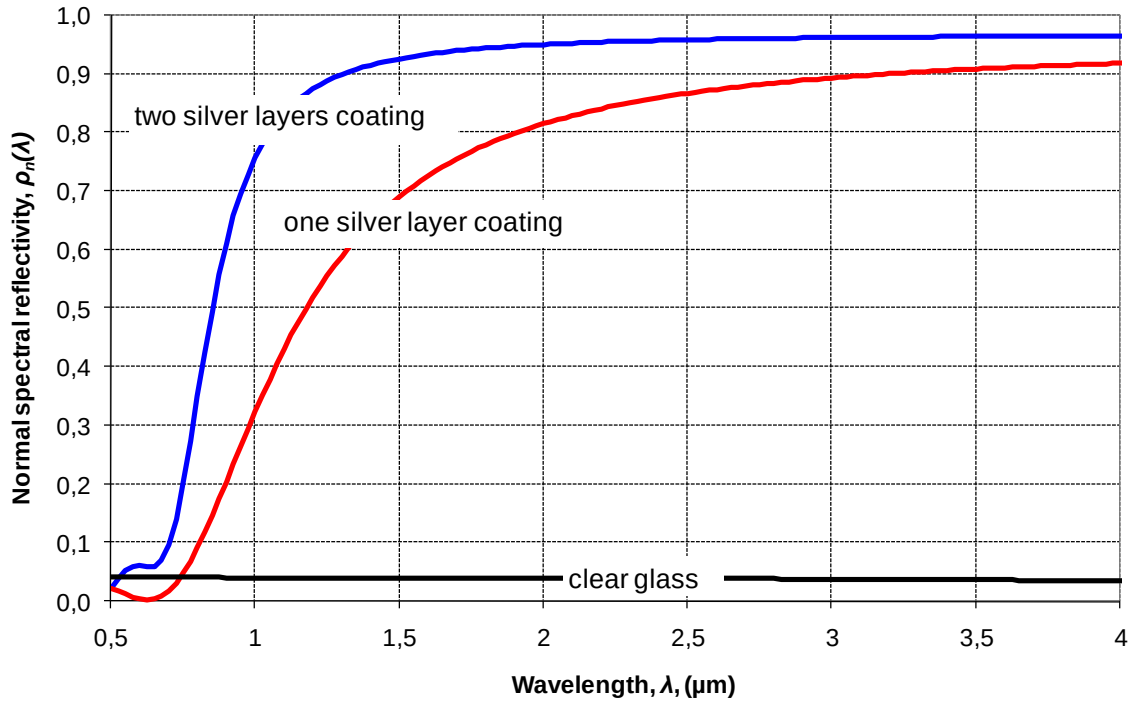

Figure 11.1. Normal spectral reflectivities of clear and two low-e coated glass surfaces. Low-e data is from [71].

Reflectivity, transmissivity and emissivity are connected with Eq. (8.11). So, as an example the reflectivity increase from 0.04 to 0.92 lowers the emissivity from 0.96 to 0.08 at wavelengths over 4.5 µm, in which case transmissivity $\tau = 0$.

Usually glass manufacturers publish one emissivity value of a low-e glass which is often between 0.02 and 0.2, depending on the coating. This value represents the total emissivity of a coated surface at room temperature, in which case the main proportion of radiation is between wavelengths 5 µm and 20 µm ($\tau = 0$). This emissivity value is not the correct value to be used in heat transfer calculations in a tempering process. The total emittance of glass depends on glass temperature and the spectral emittance of glass is equal to the spectral absorptance of glass. Thus, the total absorptance of glass in a tempering furnace depends on the temperature of the radiators. Eq. (10.7) for radiation source term already considers these details, but in the case of low-e coated glass, this is not enough. At first the

whole spectrum must be divided in such wavelength bands, with the help of which the spectral properties of both glass and coating can be comprehensively tabulated.

In Figure 11.2 the spectral reflectivity of low-e coated glass surface is presented at various temperatures. Temperature has a clear effect on the spectral radiative properties of low-e coating, which should be taken into account in detailed heat transfer calculations, for example when the development of glass temperature during tempering process is solved.

Wavelength band 4.8 to 5.3 µm is a common response range in pyrometers used to measure the temperature of the glass escaping from the tempering furnace. The selection of this response range is reasonable while emissivity is independent of glass thickness (glass is opaque for these wavelengths), clear glass emissivity is near its maximum and glass at temperature of 640°C emits a significant fraction at these wavelengths. In Figure 11.2 the reflectivity at the wavelength band is 0.94 at 27°C and 0.88 at 627°C. Equivalent values for emissivity are 0.06 and 0.12. Only the emissivity at room temperature is generally published by glass manufacturers. The use of small and wrong emissivity as a set value in a pyrometer leads to a totally invalid measuring result. Thus, it is especially important to consider the reflectivity change in set values for emissivity in pyrometers, although the radiative temperature measurement is often too inaccurate when surface emissivity is low. From the point of view of measuring accuracy the temperature of a coated glass should be measured from the uncoated bottom surface.

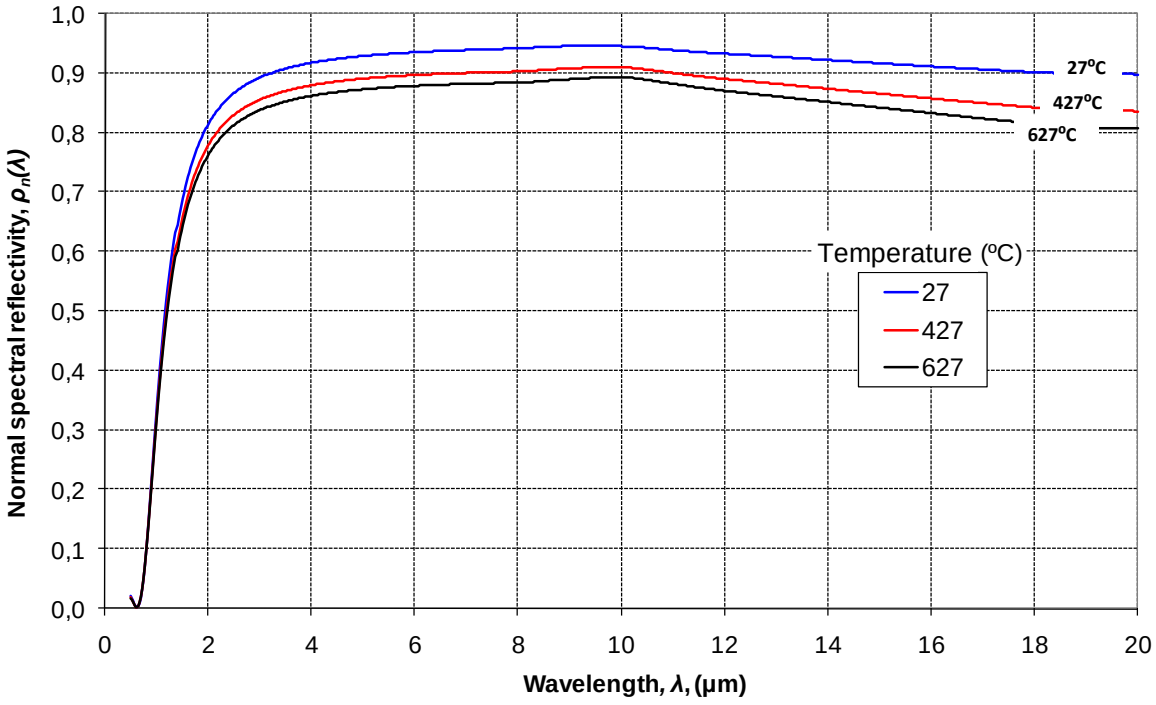

Figure 11.2. Normal spectral reflectivity of low-e coated (one silver layer) glass surface at various temperatures. Data is from [71].

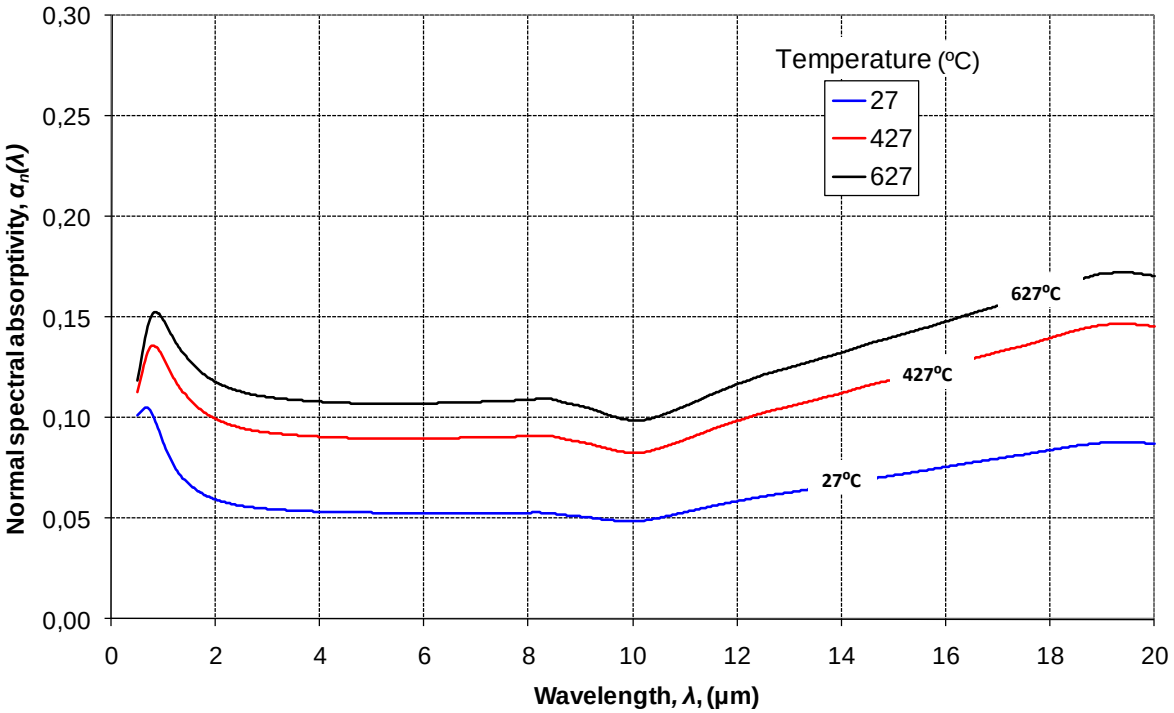

Figure 11.3. Normal spectral absorptivity of one silver layer containing low-e coating on glass surface at various temperatures. Data is from [71].

Spectral absorptivity of a low-e coating is given by Figure 11.3. Low-e coating has its own absorptivity, thus an extra part must be added on the radiation source term of a surface layer to take account the absorption into a coating. In addition to that, the absorption of the coating must be considered on the glass surface transmissivity when equations for source terms are formulated. If only the first reflection of incoming radiation inside the glass is taken into account, then the net radiation source term for a thickness layer x_1-x_2 in Figure 9.1 to a low-e coated glass (coating on upper surface) is

$$S_{x_1-x_2} = \sum_{i=1,j=2}^{i=2,j=k+1} \left\{ \begin{array}{l} \left[F_b(\lambda_i,\lambda_j,T_{\infty,u})\sigma T_{\infty,u}^4 - F_b(\lambda_i,\lambda_j,T)\sigma T^4\right](1-\rho_u-\alpha_u)\times \\ \left\{ \left[e^{-\kappa_\lambda x_1/\cos\theta'_m} - e^{-\kappa_\lambda x_2/\cos\theta'_m}\right] + \rho_l\left[e^{-\kappa_\lambda(2L-x_2)/\cos\theta'_m} - e^{-\kappa_\lambda(2L-x_1)/\cos\theta'_m}\right] \right\} + \\ \left[F_b(\lambda_i,\lambda_j,T_{\infty,l})\sigma T_{\infty,l}^4 - F_b(\lambda_i,\lambda_j,T)\sigma T^4\right](1-\rho_l)\times \\ \left\{ \left[e^{-\kappa_\lambda(L-x_2)/\cos\theta'_m} - e^{-\kappa_\lambda(L-x_1)/\cos\theta'_m}\right] + \rho_u(1-\alpha_u)^2\left[e^{-\kappa_\lambda(L+x_1)/\cos\theta'_m} - e^{-\kappa_\lambda(L+x_2)/\cos\theta'_m}\right] \right\} \end{array} \right\} \tag{11.1}$$

In Eq. (11.1) ρ_u is reflectivity and α_u is absorptivity of the coating. The equivalent equation for clear glass is Eq. (10.7). As presented above in Chap. 9, all radiation at wavelengths over 4.5 μm is reflected or absorbed on the glass surface. Thus, the absorptivity of a coating itself has an effect on glass radiation only at wavelengths below 4.5 μm. The radiation hitting the glass opposite surface (uncoated surface) and penetrating through the glass thickness is also partly absorbed by the coating. If only the first reflection of incoming radiation inside glass is taken into account, then the net radiation source term for a top surface layer between coordinates *0* - x_1 (coating is at x = 0) in a low-e coated glass is

$$S_{0-x_1} = \sum_{i=1,j=2}^{i=2,j=k+1} \left\{ \begin{array}{l} \left[F_b(\lambda_i,\lambda_j,T_{\infty,u})\sigma T_{\infty,u}^4 - F_b(\lambda_i,\lambda_j,T)\sigma T^4\right]\times \\ \left\{ \begin{array}{l} (1-\rho_u)\alpha_u + (1-\rho_u-\alpha_u)\left[1-e^{-\kappa_\lambda x_1/\cos\theta'_m}\right]+ \\ (1-\rho_u-\alpha_u)\rho_l\left[e^{-\kappa_\lambda(2L-x_1)/\cos\theta'_m} - e^{-\kappa_\lambda 2L/\cos\theta'_m}\right] + (1-\rho_u-\alpha_u)\rho_l e^{-\kappa_\lambda 2L/\cos\theta'_m}\alpha_u \end{array} \right\} + \\ \left[F_b(\lambda_i,\lambda_j,T_{\infty,l})\sigma T_{\infty,l}^4 - F_b(\lambda_i,\lambda_j,T)\sigma T^4\right]\times \\ \left\{ \begin{array}{l} (1-\rho_l)e^{-\kappa_\lambda L/\cos\theta'_m}\alpha_u\left[1+(1-\alpha_u)\rho_u\right] + (1-\rho_l)\left[e^{-\kappa_\lambda(L-x_1)/\cos\theta'_m} - e^{-\kappa_\lambda L/\cos\theta'_m}\right]+ \\ \rho_u(1-\alpha_u)^2\left[e^{-\kappa_\lambda L/\cos\theta'_m} - e^{-\kappa_\lambda(L+x_1)/\cos\theta'_m}\right] \end{array} \right\} \end{array} \right\} \quad (11.2)$$

In Figure 11.4 the reflectivity of a low-e coated glass surface is presented for opposite directions of incoming radiation. Low-e coating has still one special feature to be considered when radiation heat transfer on low-e coated glass is modelled exactly: the reflectivity and absorptivity of a coating is different for radiation coming from the air side than the glass side. This is not considered in the equations above to keep them shorter and more understandable.

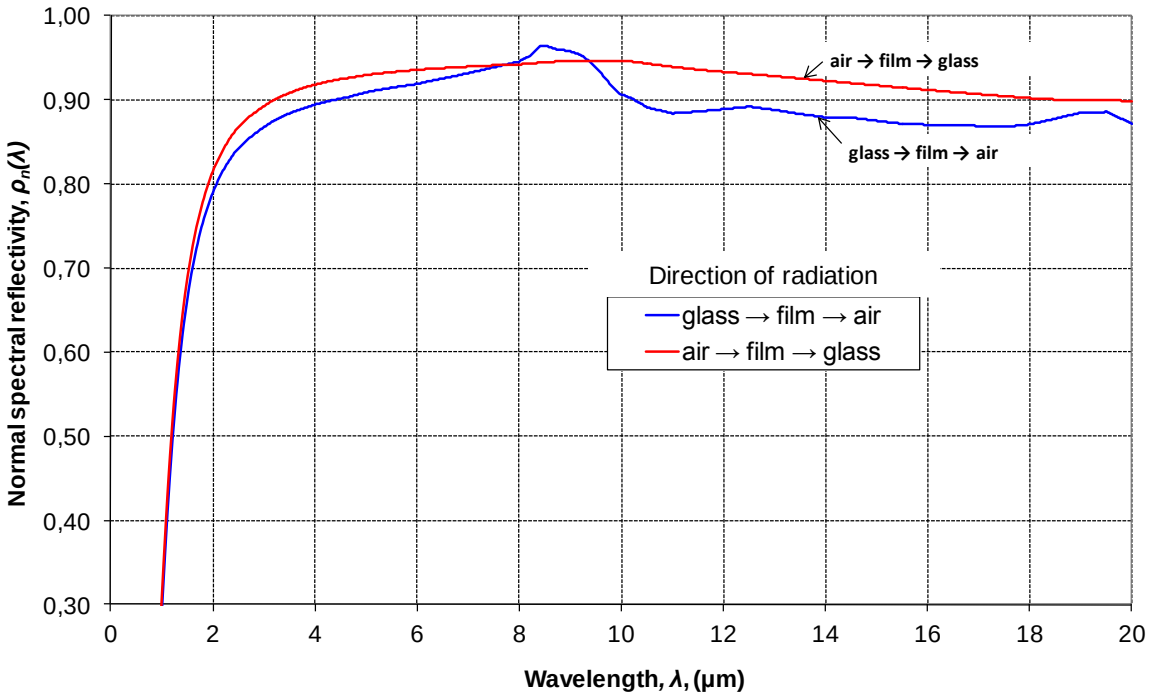

Figure 11.4 Normal spectral reflectivity of low-e coated (one silver layer) glass surface at opposite directions (T = 27ºC). Data is from [71].

The reflectivies and absorptivies in the figures above are valid for radiation hitting the interface from the direction of surface normal, $\theta = 0$. Directional dependence of the radiative properties of the coatings handled above is not known. The directional dependence of spectral reflectance R_λ of tin oxide coated glass (K-glass, see Sec. 2.2) is presented in [72]. When θ changes from 0 to 70˚, the spectral reflectance at wavelengths between 1 and 25 μm remains almost the same. The change of θ from 70 to 84˚ leads to the following changes: $R_{3\mu m}$ increases from 0.77 to 0.90 and $R_{10\mu m}$ decreases from 0.80 to 0.70.

Table 11.1. Order of magnitudes of internal reflections given by Figure 9.11, when glass thickness is 3 mm, $\theta' = 27.3°$, back side is low-e coated, $\rho_u = 0.09$, $\rho_l = 0.95$ and $\alpha_l = 0$.

Reflection	κ=0.01 cm^{-1}	κ=0.1 cm^{-1}	κ=1cm^{-1}	κ=5cm^{-1}
1	0.9468	0.9185	0.6778	0.1756
2	0.0866	0.0815	0.0444	0.0030
3	0.0820	0.0749	0.0301	0.0005
4	0.0075	0.0066	0.0020	9E-06
5	0.0071	0.0061	0.0013	2E-06

Table 11.1 details the orders of magnitudes of the first five reflections inside a low-e coated glass with thickness of 3 mm. On page 63 it was concluded that only the first of the internal reflections is significant when the glass is clear. For low-e coated glass equivalent accuracy demands the considering of the first three internal reflections.

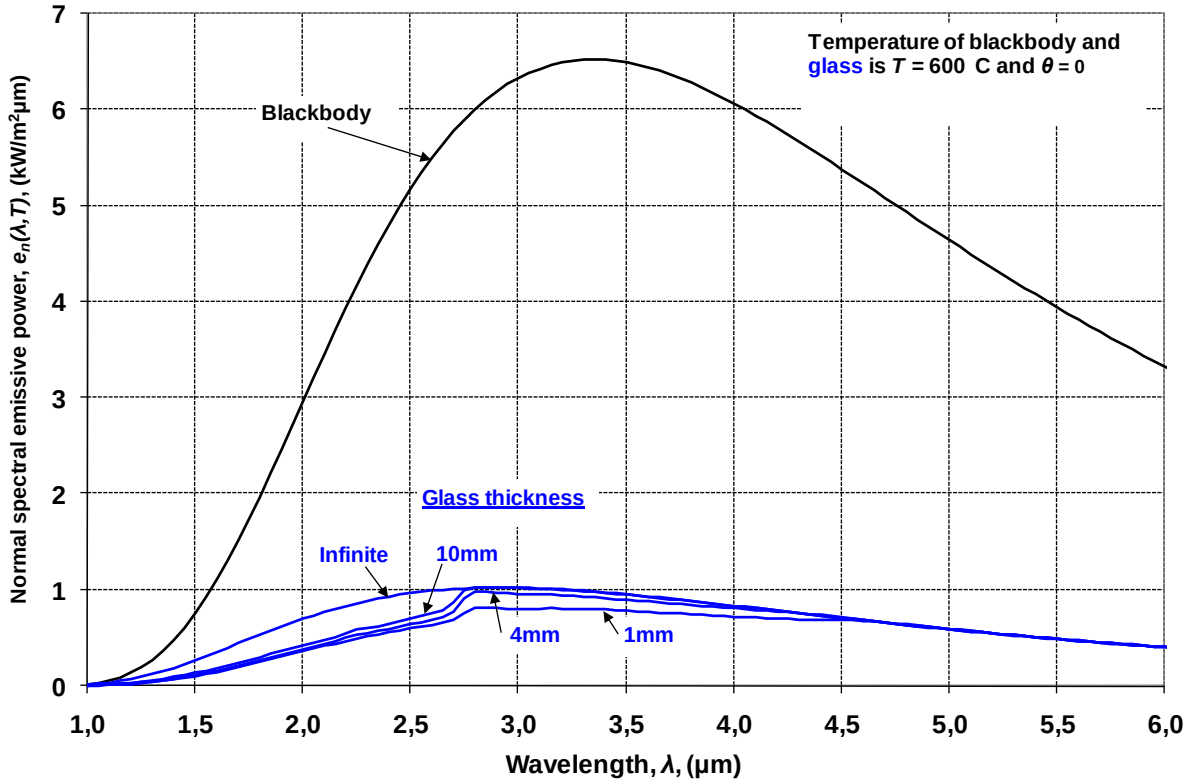

Figure 11.5. Normal spectral emissive power of blackbody and various low-e coated (one silver layer coating on front surface) soda-lime glass thicknesses at temperature of 600°C.

The normal spectral emissive powers of various low-e coated glass thicknesses are plotted in Figure 11.5 at temperature of 600°C. One silver layer coating is on the glass front surface and the back surface is clear. Figure 11.5 is similar to Figure 9.6, but now normal spectral emissive power is used instead of a hemispherical one, while only the radiative properties of the coating to the direction of its normal were available. Low-e coated glass is a poor emitter at all wavelengths and the changes in emissivity due to the cut-off wavelengths of glass are clearly flatter than for clear glass.

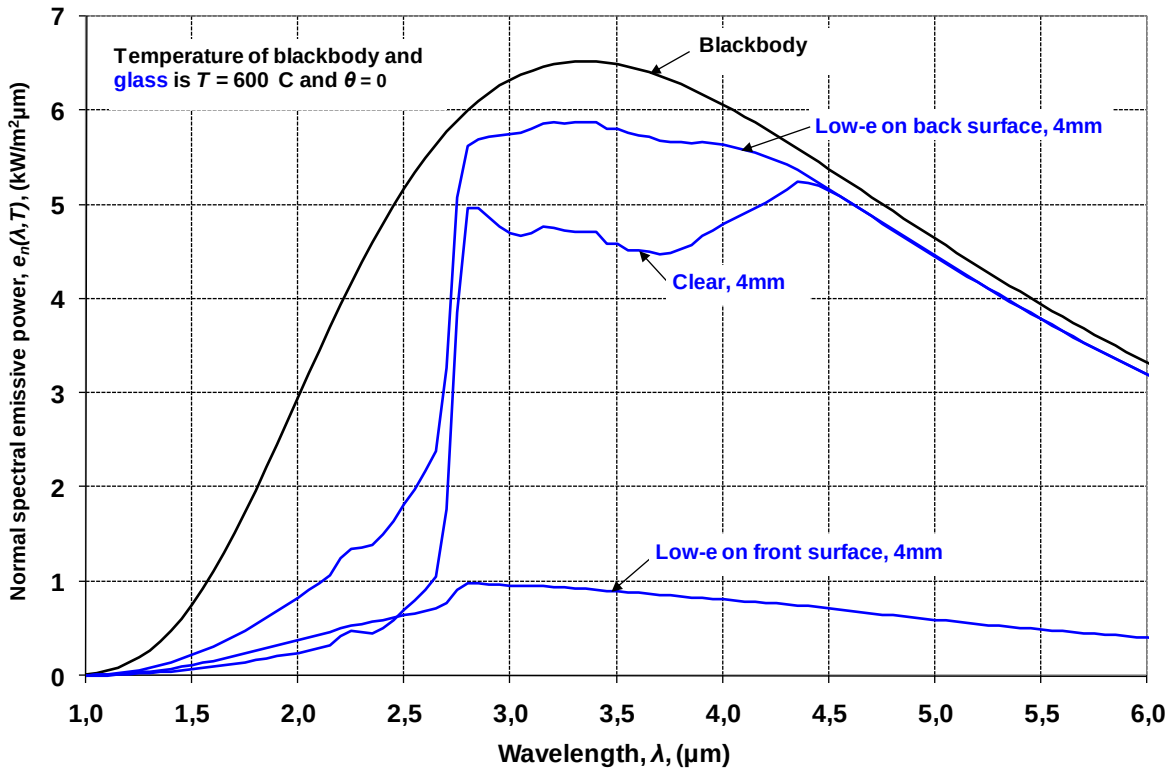

Figure 11.6. Normal spectral emissive power of blackbody, clear and low-e coated (one silver layer coating on front or back surface) of soda-lime glass. Glass thickness is 4 mm and temperature is 600°C.

The normal spectral emissive powers of clear and low-e coated 4 mm glass are shown in Figure 11.6 at temperature of 600°C. One silver layer coating is on the glass front or back surface. The normal spectral emittance of glass is the fraction between the emissive powers of glass and blackbody at the same wavelength, which both are given by Figure 11.6. The uncoated side of low-e coated glass has higher normal spectral emissive power and emittance than clear glass when the wavelength is below the opaque band. It is easiest to explain this by describing glass spectral absorption (according to *Kirchhoff's* law spectral emittance and absoptance are equal). The radiation which penetrates through glass thickness is mainly reflected back from the coating on the back surface and then partially absorbed to the glass, or directly absorbed to the coating. Due to that, glass spectral absorptance increases. In Figure 11.6 at wavelengths below 2.45 μm also the coated side of low-e glass has higher emittance than clear glass, which is caused by the emissivity of the coating itself. Clear glass emits only weakly such wavelengths.

Previous figures handled the spectral values of normal (directional, $\theta = 0$) emissive power. The normal total value is achieved when the whole spectrum is considered. Next, two figures show the total normal emittance of low-e coated and clear glass at various temperatures respectively to Figure 9.7 showing the total hemispherical emittance of clear glass. In Figure 11.7 the normal total emittance of low-e coated glass increases with increasing temperature, while also the emissivity of the coating increases. The thickness dependence of the emittance increases with temperature, but remains still relatively low at 600ºC. If the coating is at the back surface as in Figure 11.8, then the emittance acts with temperature like the emissivity of clear glass. The normal total emittance of glass, which has a low-e coated back surface, is higher than it is for clear glass. This emittance difference increases with temperature and decreasing thickness.

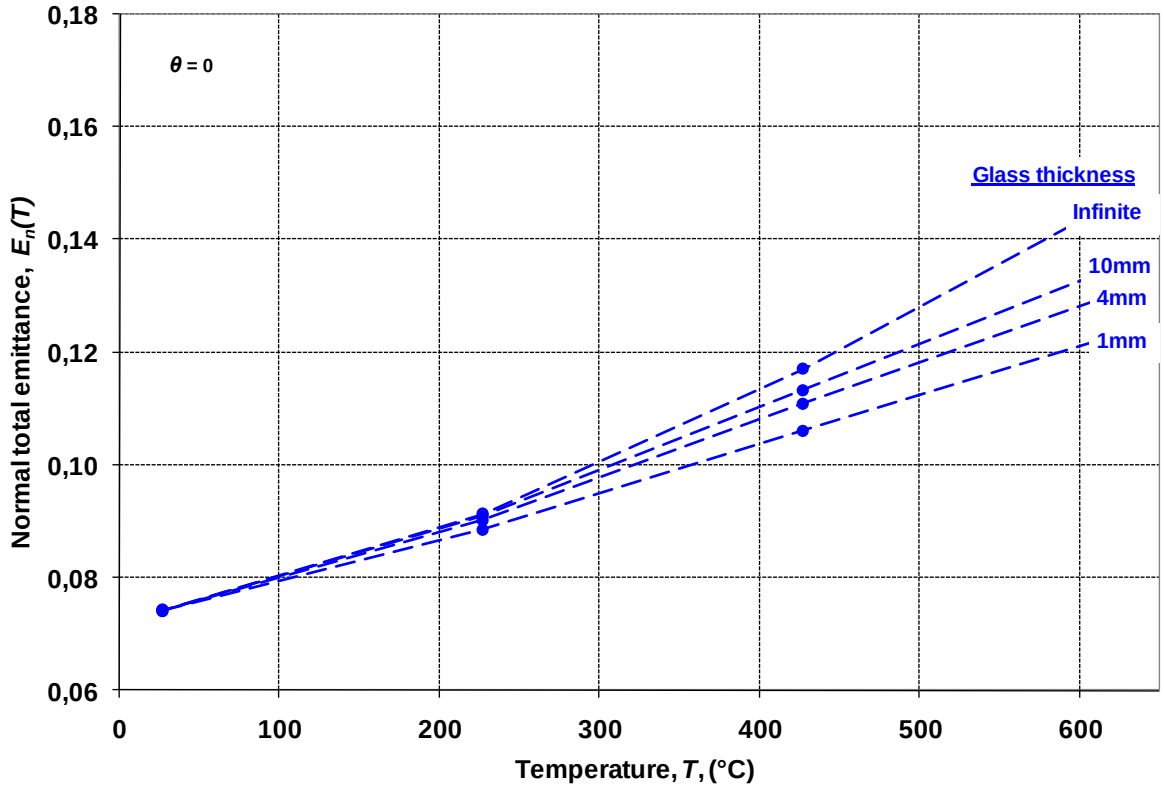

Figure 11.7. Normal total emittance of various thicknesses of low-e coated (one silver layer coating on front surface) soda-lime glass.

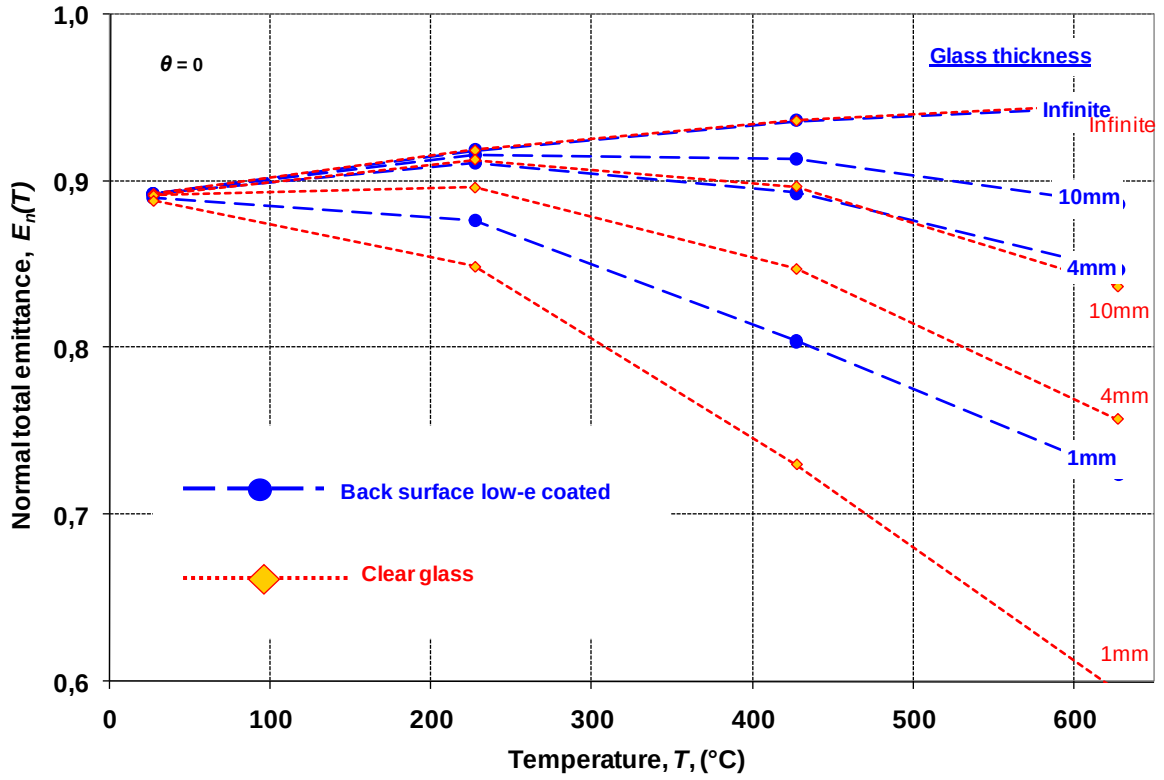

Figure 11.8. Normal total emittance of various thicknesses of low-e coated (one silver layer coating on back surface) and clear soda-lime glass.

Table 11.2 is an example of the input data defining the radiative properties of a low-e coated glass, when glass temperatures during heating were solved. In the case the top surface of a glass was coated and temperature dependence of the radiative properties of the low-e coating was taken into account by using average values on a temperature range from 20 to 600°C. For the coatings in question the effect of direction, from the glass side or the air side, of incoming radiation to reflectivity and absorptivity of the coating was rather low. Thus, it would have been totally acceptable to use only one value per wavelength band for them as in previous equations.

Table 11.2. Tabulated radiative properties of low-e coated glass in heat transfer modelling program.

GLASS RADIATIVE PROPERTIES		*air-glass surface reflectivity*		*glass-air surface reflectivity*		*film absorptivity air-glass*		*film absorptivity glass-air*	
wavelength band	*absorption coefficient*	*top*	*bottom*	*top*	*bottom*	*top*	*bottom*	*top*	*bottom*
µm	*1/cm*	*%*	*%*	*%*	*%*	*%*	*%*	*%*	*%*
0	**0,29**	**9**	**9**	**9**	**9**	**8**	**0**	**4**	**0**
0,9	**0,29**	**50**	**9**	**50**	**9**	**8**	**0**	**12**	**0**
1,7	**0,29**	**87**	**9**	**84**	**9**	**8**	**0**	**12**	**0**
2,7	**4,5**	**87**	**9**	**84**	**9**	**8**	**0**	**12**	**0**
4,5	**100**	**92**	**6**	**91**	**6**	**8**	**0**	**9**	**0**
8,7	**100**	**92**	**24**	**91**	**24**	**8**	**0**	**9**	**0**
10,4	**100**	**88**	**16**	**83**	**16**	**11**	**0**	**9**	**0**
12,4	**100**	**88**	**12**	**83**	**12**	**11**	**0**	**15**	**0**
19,4	**100**	**88**	**20**	**83**	**20**	**11**	**0**	**15**	**0**

On the basis of the facts presented in this chapter it can be concluded that the exact modelling of radiation heat transfer into a low-e coated glass during the tempering process is a very challenging task. Particularly, it must be noticed that the data presented above is unique and in practise it is very difficult to obtain similar data for different coatings in the market.

12. HEAT TRANSFER OF IMPINGING JETS

Many scientific papers have focused on heat transfer between an axisymmetric impinging jet or an array of impinging jets and a flat plate. Researchers have developed heat transfer correlations on the basis of their experimental data. Experiments have been performed using uniform heat flux or a uniform surface temperature arrangement, and the results have usually been given non-dimensionally in the form of *Nu, Re*, ratio *H/D*, ratio *r/D*, and *Pr*. Sparrow et al. [73] found the maximum heat transfer rate when a nozzle to surface distance - diameter ratio *H/D* was 6. Martin [74] wrote a comprehensive paper on heat transfer under a single impinging jet and an array of impinging jets. Goldstein and Behbahani [75] reported experimental results on heat transfer under an impinging circular air jet with and without cross flow. Hrycak [76] found that average heat transfer between an impinging jet and a flat plate was depending on the 0.7 power of *Re*. Lee and Lee [77] investigated the effect of shape of the nozzle orifice on jet heat transfer. Though all the orifices were at least quite sharp-edged with the same diameter and diameter-length ratio, heat transfer was noteworthily different. Hofmann et al. [78] found that the effect of nozzle-to-plate distance to convection near the stagnation point was negligible at small *H/D* values. Zuckerman and Lior [79] studied the physics of jet impingement heat transfer and collected available empirical correlations valid for single jets and jet arrays. Florschuetz et al. [80] studied heat transfer under an array of jets discharging from small diameter orifices with high velocity and after impingement air was constrained to flow in single direction along the channel formed by the jet orifice plate and the heat transfer surface. Such an outlet flow condition generated surface orientated cross-flow, which weakened heat transfer in a cross-flow direction.

It has long been a challenge to predict accurately heat transfer under an axial-symmetric unconfined impinging jet by numerical methods. Despite extensive exploration, a fully reliable way has not yet been found. At best the results of computational fluid dynamic (CFD) simulations fit sufficiently with experimental results. [81][82][83][84]

Both air compressors and fans are used to create an air discharge through rounded nozzles, which create axial-symmetric impinging jets used to heat and cool glass. High overpressures, small nozzle diameters, long nozzle-to-surface distances and long nozzle-to-nozzle distances are typical, especially in such tempering furnaces where radiation is clearly the main heat transfer phenomenon. Such a jet arrangement has been dealt with very seldom in the literature of heat transfer. The dimensions and overpressures in a typical glass tempering chiller jet arrangement fit fairly well with those in the literature reports.

Part of the material below dealing with single jets is published in [85].

12.1 Jet characteristics

12.1.1 Air discharge through nozzle

A jet is a stream of air blown out from a nozzle in Figure 12.1. The behaviour of the discharging air flow depends on the shape of the nozzle. In a well-rounded orifice, the flow area is the same as the minimum cross area of the orifice, whereas in a sharply edged orifice the flow contracts. The velocity of air in the vena contracta for choked flow when $p_1/p_\infty > 1.9$ is the sonic velocity

$$u_{vc} = C_v \sqrt{\frac{2\gamma R_u T_1}{M(\gamma+1)}} \tag{12.1}$$

The velocity in the vena contracta for incompressible flow is

$$u_{vc} = C_v \sqrt{\frac{2(p_1 - p_\infty)}{\rho_\infty}} \tag{12.2}$$

The air flow can be assumed to be incompressible at least when $p_1/p_\infty < 1.2$, which is usually true when fans are used. The corresponding equation for mass flow through the nozzle is

$$\dot{m}_{vc} = \rho_{vc} u_{vc} A_{vc} = \rho_1 \left(\frac{2}{\gamma + 1} \right)^{\frac{1}{\gamma - 1}} u_{vc} C_a \frac{\pi D^2}{4} \tag{12.3}$$

for a choked flow and

$$\dot{m}_{vc} = \rho_\infty u_{vc} C_a \frac{\pi D^2}{4} \tag{12.4}$$

for a low velocity flow. In the equations above C_a is the coefficient considering the contraction of a jet at vena contracta. Coefficient C_v considers the difference between true and theoretical velocity at vena contracta. Both coefficients are always below 1. Values for the coefficients depend on the shape of the nozzle. Some values are shown in Figure 12.2, and more can be found from the literature [86][87]. According to [88] the velocity coefficient C_v of sharp-edged orifice is even higher than 0.98.

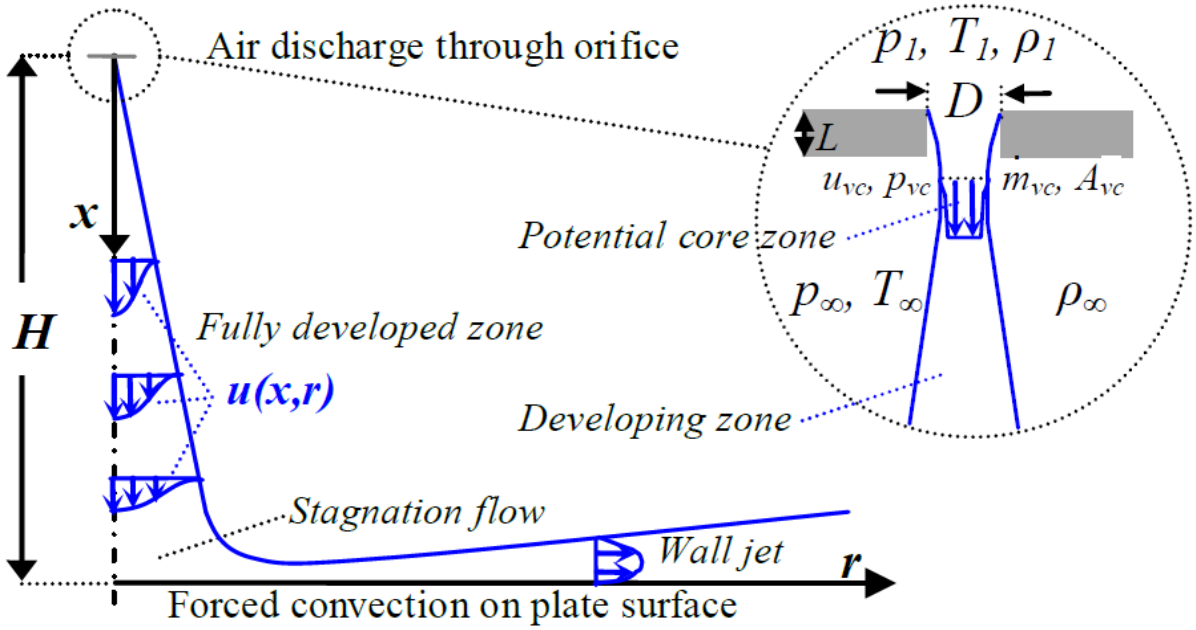

Figure 12.1. Details of jet flow.

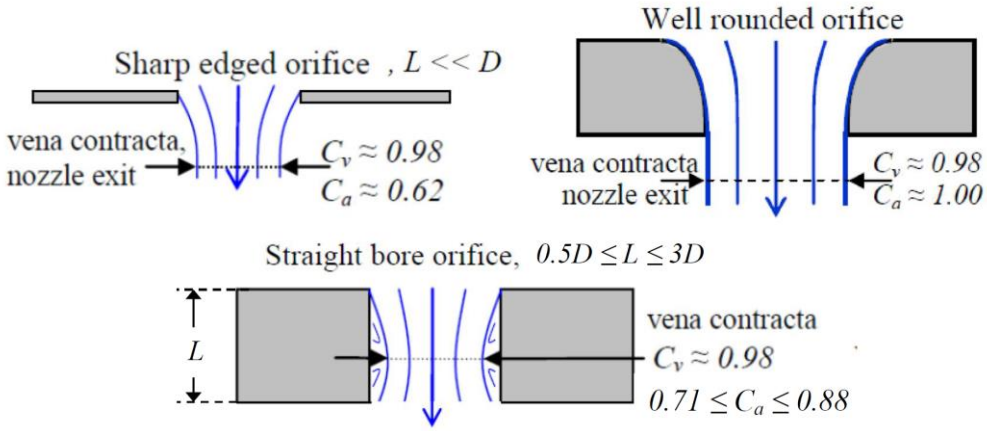

Figure 12.2. Types and coefficients of velocity and contraction for different orifices.

12.1.2 Single impinging jet

Air discharging from a circular nozzle forms an axisymmetric jet. Figure 12.1 shows the time-averaged details of a developing turbulent jet. After some nozzle diameters from the nozzle exit, the jet starts driving the surrounding air with it and spreading, with decreasing velocity and increasing mass flow. The momentum remains the same. The velocity profile of a fully developed (x/D >10) axisymmetric jet is according to White [89] as follows:

$$u(x,r) = \left[1 + \frac{3.31}{8}\left(\frac{r}{\delta}\right)^2\right]^{-2} u(x,0) \tag{12.5}$$

in which $\delta = 0.0848x$ is radius of jet at distance x from the nozzle exit and

$$u(x,0) = 7.41\frac{\sqrt{J/\rho_\infty}}{x} \tag{12.6}$$

The momentum J of a free jet in Eq. (12.6) is obtained as

$$J = \dot{m}_{vc} u_{eff} = \dot{m}_{vc} u_{vc} + (p_{vc} - p_\infty) A_{vc} \tag{12.7}$$

In Eq. (12.7) u_{eff} is the effective jet velocity, which governs the development of the jet. For pressure ratios $p_1/p_\infty < 1.9$ expansion is completed at the vena contracta, and $p_{vc} = p_\infty$. For overcritical pressures $p_1/p_\infty > 1.9$ the remaining overpressure in the vena contracta $p_{vc} = 0.528p_1$ creates a series of expansion waves, which affect the jet's momentum and behaviour. For incompressible jets

$$J = 2(p_1 - p_\infty) C_v^2 A_{vc} = 2(p_1 - p_\infty) C_D C_v \frac{\pi D^2}{4} \tag{12.8}$$

The mass flow of a jet after distance x from the orifice is

$$\dot{m}(x) = 2\pi \int_0^\infty \rho u(x,r) r\,dr = 0.404 x \rho(x) \sqrt{\frac{J}{\rho_\infty}} \approx 0.404 x \sqrt{J \rho_\infty} \tag{12.9}$$

In Eq. (12.9) it is assumed that the density of a jet is the same as in the surrounding air. This is true when the temperature of discharging and surrounding air are the same. In other cases the density assumption is more valid when *x/D* increases.

12.1.3 Measurement of jet momentum

Figure 12.3 is a schematic view of an air jet blowing against the surface of a weighing disk, which gives the weight *m* on the screen of the weighing machine. The jet causes the force $F_2 = mg$ to the disk. The momentum equation of the impinging jet in Figure 12.3 is:

$$p_{vc} A_{vc} + \dot{m}_{vc} u_{vc} = p_\infty A_{vc} + F_2 \tag{12.10}$$

Combining that with Eq. (12.7) gives $J = F_2 = mg$. Thus, an electric weighing machine can be used to measure the jet momentum.

During the measurements it was discovered that the distance affected the force so that it dropped clearly at a distance of less than 20 mm, because the surface-orientated air velocity (wall jet in Figure 12.1) lowered the static pressure on the surface of the weighing disk and produced a lifting force. Due to that the surface of the weighing disk surface was equipped with flow blocks to prevent the development of wall jet.

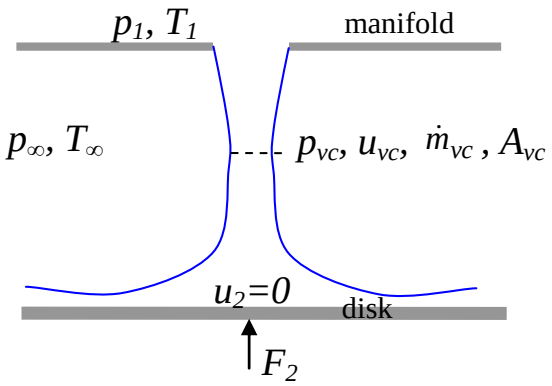

Figure 12.3. Schematic view of jet hitting the surface.

Table 12.1 shows some examples of measured and calculated momentums. The main inaccuracy in measured momentums arises from inaccurate measuring technique. The main inaccuracy in calculated momentums arises from the inaccuracy of nozzle diameters (± 0.05 mm) and discharge coefficient. The type names for orifices and values of discharge coefficients C_D at the vena contracta for calculations were taken from [87] and it was assumed that $C_v = 0.98$ at the vena contracta in all cases.

Table 12.1. Examples of measured and calculated momentums.

Nozzle diameter D (mm)	Nozzle length L (mm)	Orifice type	Discharge coefficient $C_D=C_aC_v$	Pressure difference p_1-p_∞ (10^3Pa)	Measured momentum J (10^{-3}N)	Calculated momentum J (10^{-3}N)	Ratio Mea. / Cal. momentum
4.9	1.5	Straight bore	0.65	3.23	70	77	0.91
4.9	1.5	Straight bore	0.65	0.57	12	13.5	0.89
7.7		Well rounded	0.98	1.34	129	120	1.08
7.7	16	Straight bore	0.86	1.33	91	105	0.87
1.5	2.3	Straight bore	0.80	100	226	213	1.06
2.0	2.3	Straight bore	0.79	300	1177	1001	1.18
1.0	1.0	Straight bore	0.80	140	132	126	1.05
1.0	1.0	Straight bore	0.80	230	234	198	1.18
1.0	1.0	Straight bore	0.79	330	334	274	1.22
1.0	1.0	Straight bore	0.78	425	432	344	1.26

With incompressible jets the typical difference between measured and calculated momentums was less than 10%, whereas with choked compressible air jets with a sonic velocity in the vena contracta, the measured momentums were from 4 to 35 % higher than the calculated ones. The difference tended to increase with pressure difference, which indicates that the term $(p_{vc}-p_\infty)A_{vc}$ in Eq. (12.7) does not fully account for the effect of the remaining overpressure at the vena contracta on the momentum. In addition to the unknown effect of expansion waves, the difference between measured and calculated momentums may be caused by the temperature drop due to substantial pressure decrease in discharging air, which was not taken into account. In any case, the remaining overpressure in the vena contracta clearly affected the results. Thus, the sonic velocity condition which defines the maximum discharging velocity of a choked jet does not restrict the increasing of the jet momentum due to increasing overpressure. What happens to the jet after the vena contracta because of the remaining overpressure is beyond the scope of this thesis and is not easy to solve. For instance, Chapman and Walker [90] bypass this detail by saying that "adjustment of the flow to be imposed must take place externally by multidimensional means." Oosthuizen and Carscallen [91] include some figures showing multidimensional expansion after the jet exit.

12.2 Heat transfer coefficients for single jets

12.2.1 Measured local heat transfer coefficients

In the local heat transfer coefficient measurements direct electric current (DC) was fed through a steel plate of thickness equal to 0.5 mm. Figure 12.4 shows the cross-section of the test apparatus. The plate was 400 × 324 mm, the smaller value indicating the length between the copper conductors. The back of the plate was insulated and thin thermocouples were mounted on it with which the local plate temperatures T_w were measured. The measurement points, located in line from the stagnation point, were 20 ± 1 mm apart. The ambient air temperature T_a, the voltage between plate edges U, and the electric current I through the plate were measured to determine the heat flux. The temperature distribution of the steel plate was also measured by using an infrared camera. The plate surface was painted with highly emissive paint to make the measurement more accurate. Figure 12.5 is taken with

such a method from the plate. The nozzle from which the jet discharged was a drilled hole in a steel pipe with wall thickness of 2.3 mm and inner diameter of 12.5 mm. The air temperature inside the pipe was almost the same as the ambient temperature T_∞ = 25°C.

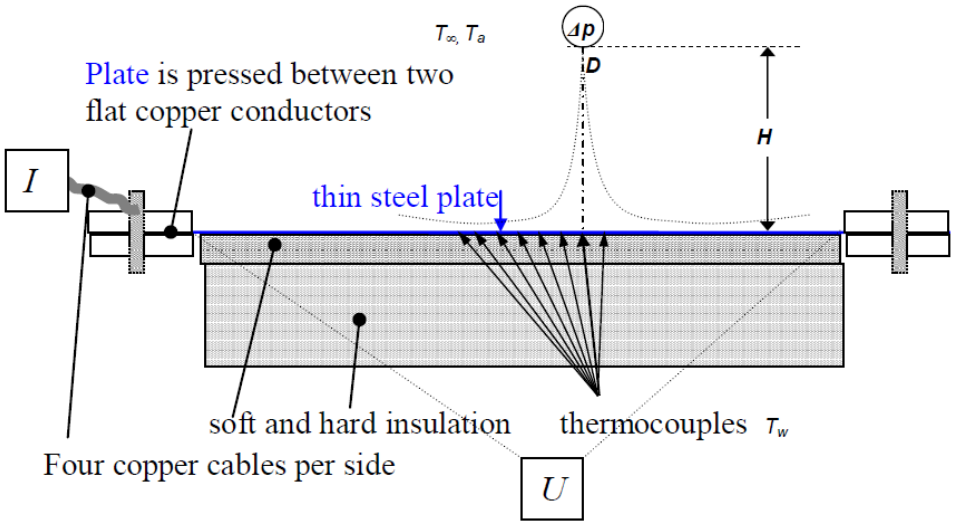

Figure 12.4. Schematic view of test apparatus.

Finally, the local heat transfer coefficient *h(r)* was solved from equation

$$h(r) = \frac{UI}{A_p\left[T_w(r) - T_a\right]} - \frac{\varepsilon\sigma\left[T_w(r)^4 - T_\infty^4\right]}{T_w(r) - T_a} \tag{12.11}$$

The last part of Eq. (12.11) takes radiation into account. The emissivity ε of the plate was determined by changing emissivity in the infrared camera until it gave the same temperature as the thermocouples.

Figure 12.5. Temperature field under air jet in laboratory measurement.

The accuracy of the measurement depended mainly on the uniformity of electric power in the plate and on the temperature difference between the measuring points and ambient air. Obviously, the most inaccurate measurement point was near the stagnation point, which was the coldest area in the plate.

Conduction inside a plate in a radial direction and conduction through insulation are low compared to the convective heat flux, which meant that a constant heat flux boundary condition could be used.

When using smoke and threads to indicate air currents, it was observed that the boundary layer was turbulent. Hence, the measured heat transfer coefficients are also valid for a constant temperature boundary condition, because with turbulent boundary layers, the effect of varying temperature distribution on the heat transfer coefficient is very small.

In the measurements the plate of a constant heat flux was cooled with different air jets. The measured heat transfer coefficients are shown in figures below.

In Figure 12.6 the relation between absolute pressures and the local heat transfer coefficients is $h(r) \propto (p_1/p_\infty)^{0.52}$. Heat transfer coefficient decreases as a function of radial distance in the same relationship in all absolute pressures.

In Figure 12.7 the local heat transfer coefficient near the stagnation point increases strongly when the distance from nozzle to surface decreases. When the radial distance from the stagnation point increases, the effect H on local heat transfer disappears.

In Figure 12.8 the local heat transfer coefficient increases strongly with the nozzle diameter, because when the nozzle diameter is doubled, both the mass flow through the nozzle and the momentum of the discharging jet become four times larger. In Figure 12.6 the measured relation between the nozzle diameter and the local heat transfer coefficient is $h(r) \propto D^b$, where b = 0.75…0.85. In another case, when the nozzle-to-plate distance was 150 mm, b = 1…1.5. Above, b increases with the decreasing distance from stagnation point.

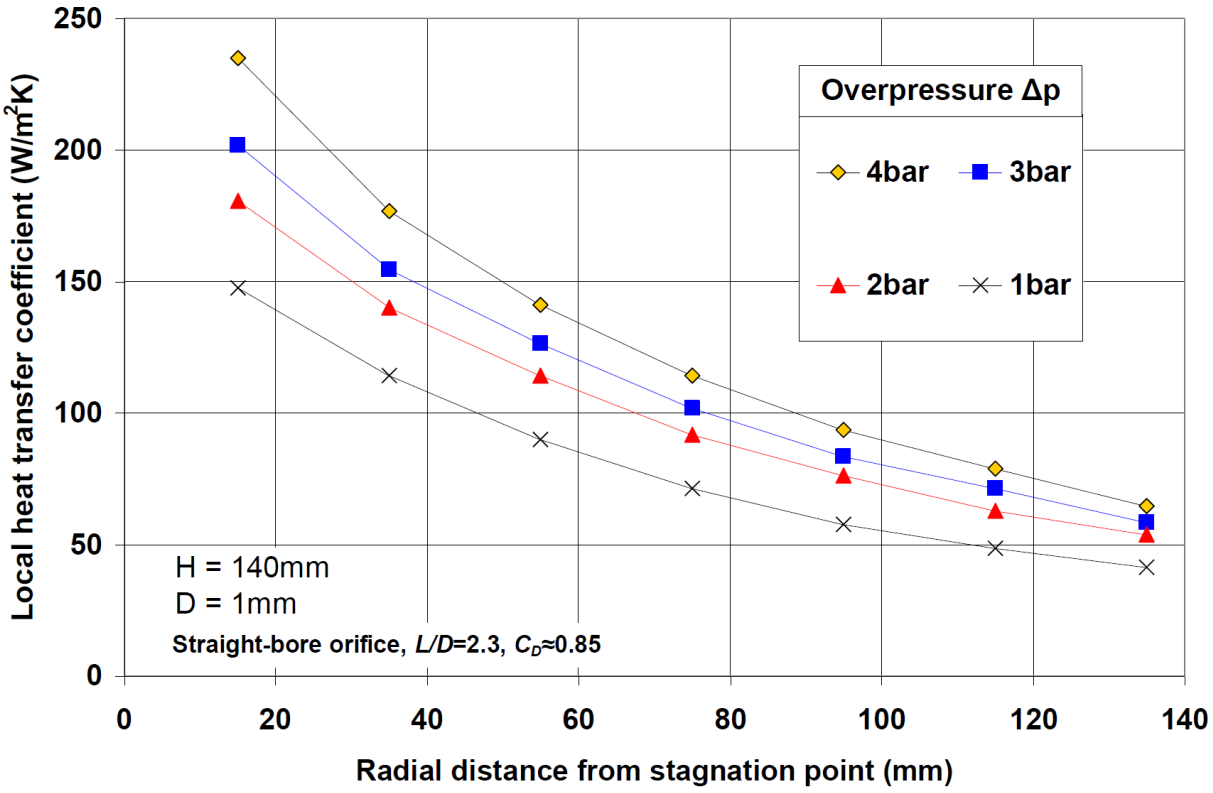

Figure 12.6. Experimental local heat transfer coefficients for various overpressures.

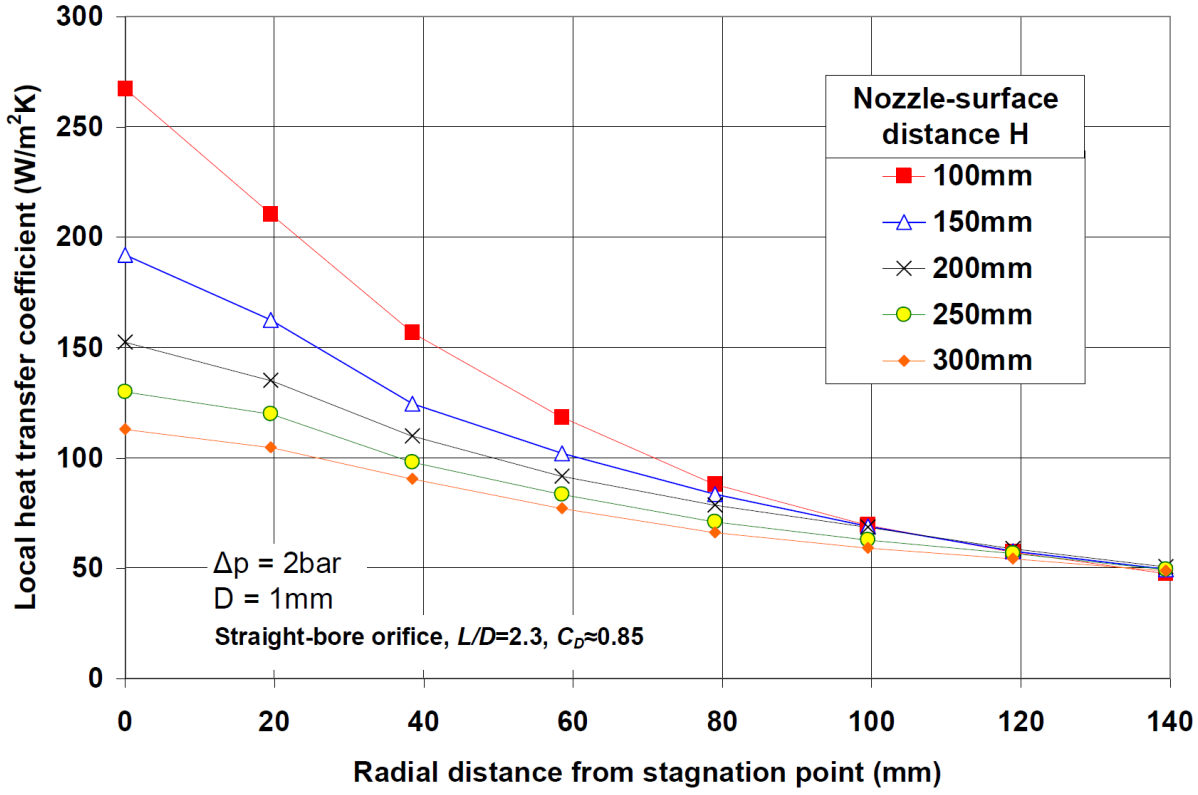

Figure 12.7. Experimental local heat transfer coefficients for various nozzle-to-surface distances.

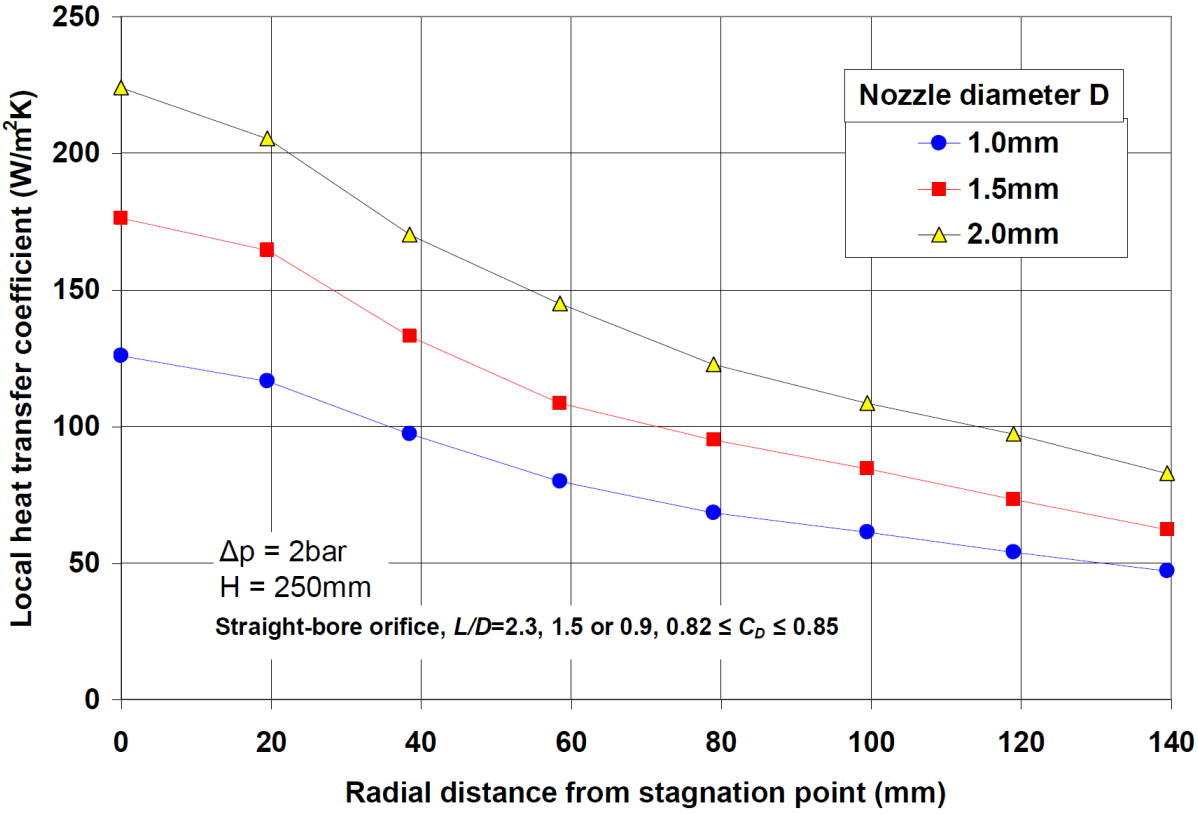

Figure 12.8. Experimental local heat transfer coefficients for various nozzle diameters.

12.2.2 Comparison of correlations and measurements

In Section 12.1 it was shown that the velocity profile of a developing jet depends on the momentum of discharging flow. Figure 12.9 shows the results of an experiment, in which the plate of a constant heat flux was cooled with different impinging jets with the same momentum. A constant momentum of jets with different diameters was obtained by changing the pressure in the manifold accordingly to Eq. (12.8). Later on, when discharge coefficients C_D where checked, it turned out that the calculated momentums were: 89×10^{-3} N for D = 2 mm case, 83×10^{-3} N for D = 3 mm and 80×10^{-3} N for D = 4 mm case. During the measurements the distance between the nozzle exit and the plate and the air temperature remained the same. In Figure 12.9 the results of orifice diameters 3 and 4 mm are almost the same, and also the results of 2 mm diameter are close to them. Thus, both momentums and heat transfer coefficients are almost the same.

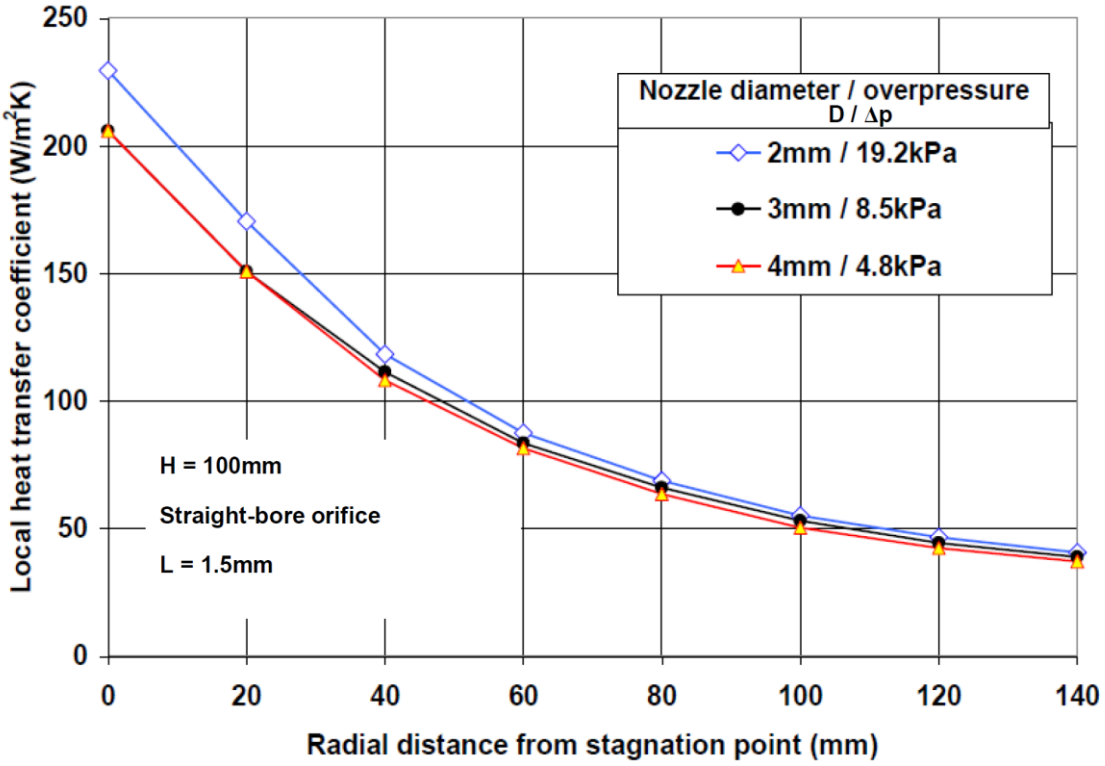

Figure 12.9. Experimental local heat transfer coefficients of three cases with constant momentum and nozzle-to-surface distance.

In the correlations given in the literature, Reynolds number $Re = u\rho D/\mu$ is used to define the discharging flow ($Re \propto J^{1/2}$). Surface averaged heat transfer under an impinging jet can be calculated from the correlation given by Martin [74].

$$\frac{\overline{Nu}}{\mathrm{Pr}^{0.42}} = \frac{2D}{r}\frac{1-1.1D/r}{1+0.1(H/D-6)D/r}\left[\mathrm{Re}\left(1+\frac{\mathrm{Re}^{0.55}}{200}\right)\right]^{1/2} \qquad (12.12)$$

The validation ranges of Eq. (12.12) are $2000 \le Re \le 400\,000$, $2.5 \le r/D \le 7.5$ and $2 \le H/D \le 12$. In Eq. (12.12) $\overline{Nu} = \bar{h}D/k$ is surface averaged Nusselt number and $\mathrm{Pr} = c_p\mu/k$ is Prandl number. Above $\bar{h}$ is surface averaged or mean heat transfer coefficient.

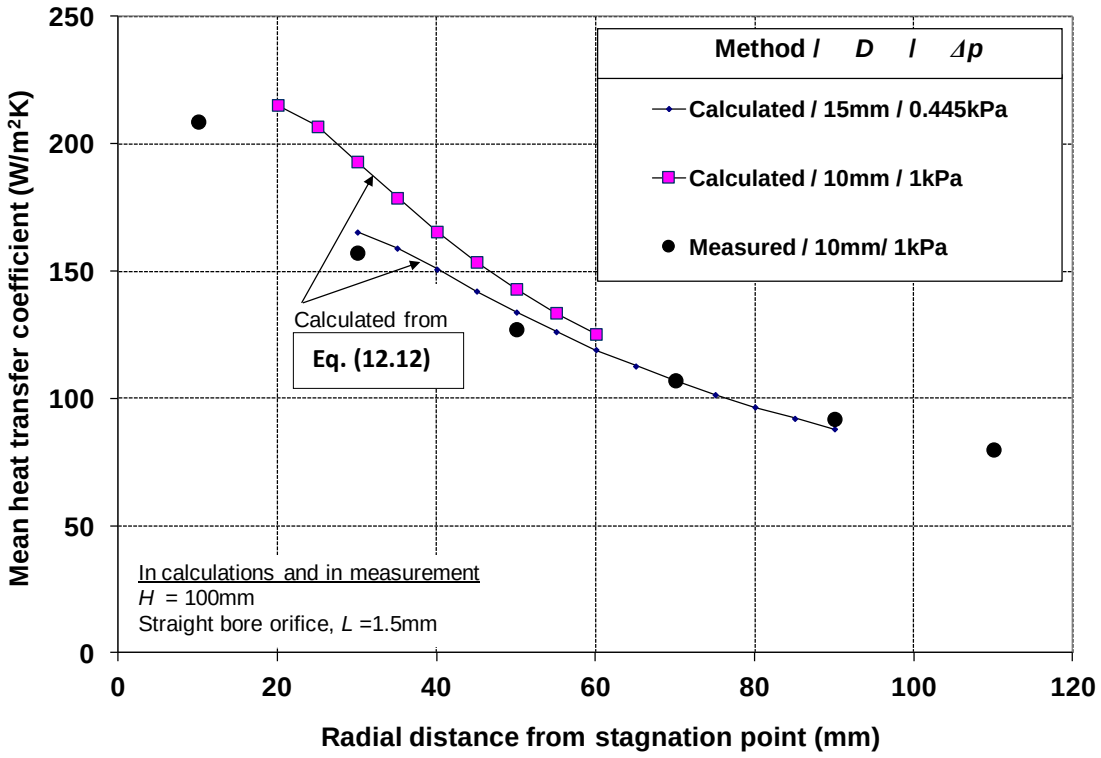

Figure 12.10. Calculated mean heat transfer coefficients for two single jets with same momentum and comparison with new measured data.

Figure 12.10 shows the results of Eq. (12.12) for two different jets, which have the same momentum. The dots in Figure 12.10 are new measured results with a constant heat flux method. For instance, when r = 40 mm Eq. (12.12) predicts an 8% stronger convection for the jet with D = 10 mm, and the result is 10% higher than the experimental result. Farther in the wall jet region the measured data agree even better with the results of the correlation. Eq. (12.12) seems to be valid much farther from the stagnation point than the validation range defines.

Eq. (12.12) and all the equations below are valid for nozzles in which C_D = 1. The contraction can be taken into account by using $D_{eff} = C_D^{0.5} D$ as a diameter D in Eq. (12.12) and also in the equations of Nu and Re. Diameter D_{eff} is the effective diameter of the orifice with the smallest diameter D and discharge coefficient C_D.

Hofmann et al. [78] published new correlations for local and surface averaged convection under an axisymmetric jet

$$\frac{Nu}{\mathrm{Pr}^{0.42}} = 0.055\left[\mathrm{Re}^3 + 10\,\mathrm{Re}^2\right]^{0.25} e^{-0.025(r/D)^2} \tag{12.13}$$

$$\frac{\overline{Nu}}{\mathrm{Pr}^{0.42}} = 0.055\left[\mathrm{Re}^3 + 10\,\mathrm{Re}^2\right]^{0.25} \frac{1 - e^{-0.025(r/D)^2}}{0.025(r/D)^2} \tag{12.14}$$

The validation ranges of Eqs. (12.13) and (12.14) are $0 \le r/D \le 10$, $0.5 \le H/D \le 10$ and $14\,000 \le Re \le 230\,000$. An interesting detail of these correlations is that the nozzle-to-plate distance H is missing.

Figure 12.11 is a similar type of comparison as Figure 12.10, but now the comparison is made with the correlation of Hofmann Eq. (12.14). Correlation (12.14) predicts a 25% stronger convection for

the jet with smaller D, when r = 40 mm. The result is 35% higher than the equivalent experimental result. At longer distances from the stagnation point the measured data agree better with the results of the correlation.

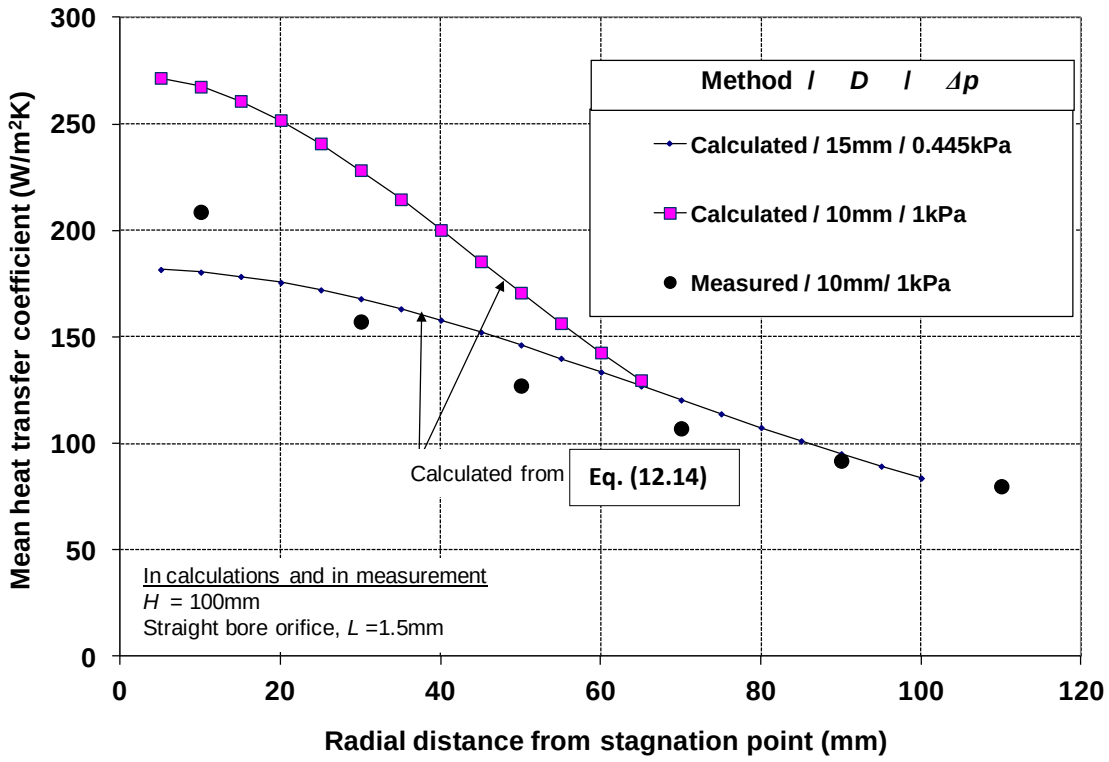

Figure 12.11. Calculated mean heat transfer coefficients of two single jets with same momentum and comparison with new measured data.

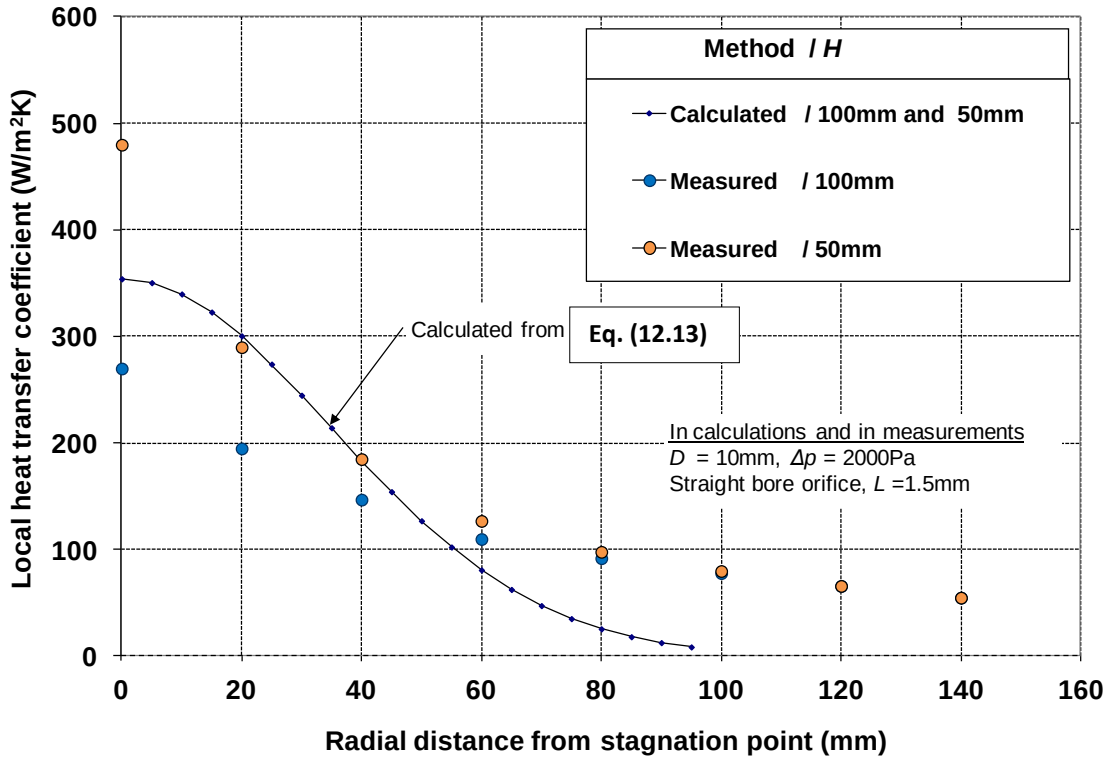

Figure 12.12. Measured and calculated local heat transfer coefficients.

Figure 12.12 shows the local heat transfer coefficient with two nozzle-to-plate distances. Eq. (12.13) gives the same heat transfer in both distances, which does not agree with the measured data presented. A clear effect of nozzle-to-plate distances $100 \leq H/D \leq 300$ on local heat transfer near the stagnation point was also observed in Figure 12.7. However, likely the effect of the nozzle-to-plate distance to heat transfer is very small at potential core zone, i.e., at $H/D < 3$ before jet starts spreading.

The measured case in Figure 12.12 was also modelled numerically. This was done by experts in two engineering offices using Fluent or Ansys-CFX, which are the names of commercial CFD codes. As shown in Figure 12.13, their results are rather near to the measured data.

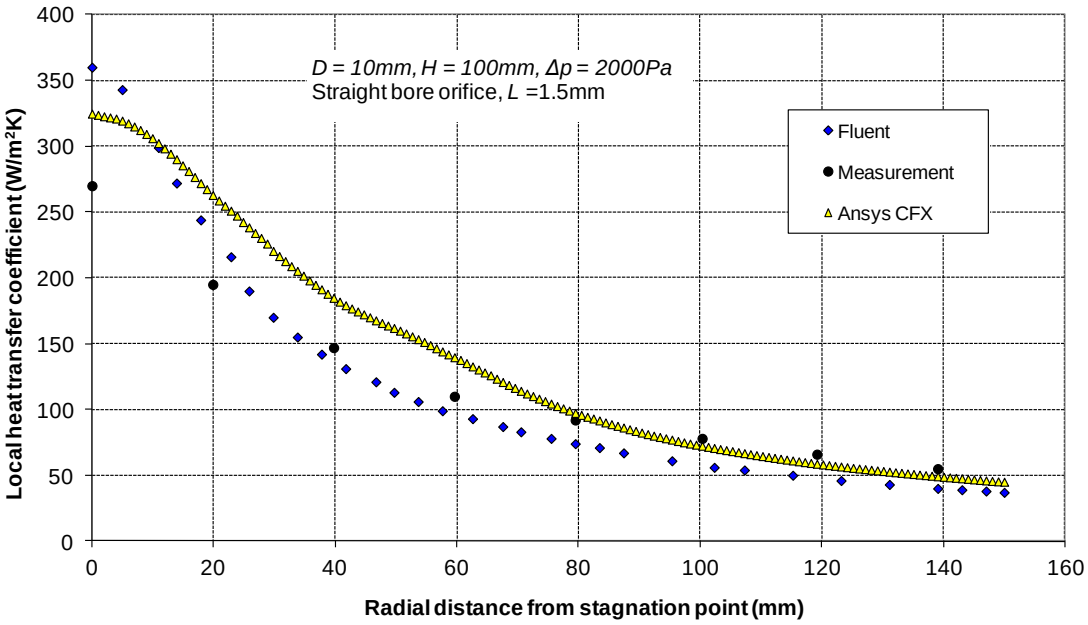

Figure 12.13. Local heat transfer coefficients for same jet along with different solution methods.

Table 12.2 shows a detailed example in which two diameters and overpressures are used to create a constant momentum air jet. Mean heat transfer inside a circle of radius r under the jet is calculated using previous correlations. The correlation of Goldstein [75]

$$\frac{\overline{Nu}}{\mathrm{Re}^{0.6}} = \frac{1}{A + B(r/D)^n} \tag{12.15}$$

is also included. In Eq. (12.15) $A = 3.329$, $B = 0.273$, and $n = 1.3$ when $H/D = 6$ and where $A = 4.577$, $B = 0.4357$, and $n = 1.14$ when $H/D = 12$. Eq. (12.15) is valid for r/D up to 40 and Re up to 120 000.

The results of different correlations are shown in Table 12.2. Eq. (12.12) predicts 8% higher, Eq. (12.14) 2% smaller, and Eq. (12.15) 4% higher heat transfer coefficient for a 5 mm diameter nozzle than for a 10 mm diameter nozzle when $r = 50$ mm. Corresponding values are 3% and -2% when $r = 100$ mm. Thus, all correlations support well the observation in Figure 12.9 that equal momentums lead to similar convection when the distance H between nozzle exit and surface is constant.

In Table 12.2 the difference in heat transfer coefficients between the correlations (12.12) and (12.15) varies from 18 to 34%, and in all four cases the correlation (12.15) predicts higher convection than correlation (12.12). Predictions for the correlations of Martin (12.12) and Hofmann (12.14) match greatly when $r = 50$ mm and $D = 5$ mm, or $r = 100$ mm and $D = 10$ mm. The case $r = 100$ mm and D

= 5 mm is clearly out of the *r/D* -range of correlations (12.12) and (12.14). Unlike the correlation of Martin, the correlation of Hofmann is very sensitive to exceeding *r/D* -range and due to that the results for the case with *r/D* = 20 are not plotted in Table 12.2.

Table 12.2. Mean heat transfer coefficients of jets with same momentum according to different correlations ($C_D = 1$).

D	mm	10			5		
$p_1 - p_\infty$	Pa	1000			4000		
H	mm	60			60		
J	N	0.16			0.16		
Re		26370			26370		
Correlation		Martin Eq. (12.12)	Hofmann Eq. (12.14)	Goldstein Eq. (12.15)	Martin Eq. (12.12)	Hofmann Eq. (12.14)	Goldstein Eq. (12.15)
$\bar{h}$ (r=50mm)	W/ (m^2K)	175	191	213	189	188	222
$\bar{h}$ (r=100mm)	W/ (m^2K)	100	94	134	103	-	132

It is well known that the experimental correlations of different authors do not agree satisfactorily in the stagnation zone, partly because of different turbulence levels at the nozzle exit. The turbulence in a discharging jet depends on practical factors such as the nozzle geometry and overpressure inside the nozzle box, which makes a perfect match between different experiments almost impossible. It can be concluded from the heat transfer coefficients presented above that also the agreement in the wall jet region is often only quite acceptable. The discrepancies between experimental correlations are probably partly caused by the different nozzle diameters and nozzle-to-surface distances used in experiments, though dimensionless ratios *H/D* and *r/D* have remained the same.

12.3 Heat transfer coefficients of jet array

When the heat transfer process in a glass tempering furnace or in a tempering chiller is under design, the aim is to find out the correct dimensions for a jet array and fans. In that case, it is important that surface averaged convection fulfils the planned heating or cooling rate of glass.

There are many research papers dealing with the heat transfer of an array of jets, where identical orifices are placed side by side. Figure 12.14 shows two commonly used ways to place orifices symmetrically at equal distances from each other.

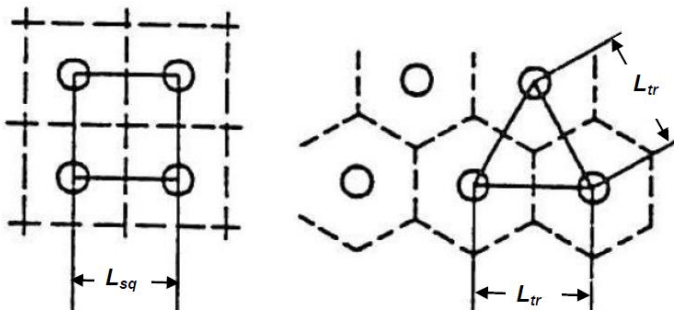

Figure 12.14. Orifices in square and triangular arrangement.

As presented above, heat transfer from a single jet to glass depends on the discharging velocity of an air jet, orifice diameter, nozzle type, distance between the orifice and glass, the angle of incidence of a jet to heat transfer surface, and the thermal properties of air. In addition, the heat transfer of jet arrays depends on the number of nozzle orifices in a given area, the distances between orifices, and of the free space through which air can escape from the heat transfer area after jet impingement.

Martin [74] has developed the following equation for surface averaged heat transfer under an array of round jets in square or triangular arrangement.

$$\frac{\overline{Nu}}{\mathrm{Pr}^{0.42}} = \left[1+\left(\frac{H/D}{0.6/\sqrt{A_f}}\right)^6\right]^{-0.05} \sqrt{A_f}\,\frac{1-2.2\sqrt{A_f}}{1+0.2(H/D-6)\sqrt{A_f}}\,\mathrm{Re}^{2/3} \tag{12.16}$$

$$2000 \le \mathrm{Re} \le 100000$$

$$0.004 \le A_f \le 0.04$$

$$2 \le H/D \le 12$$

In Eq. (12.16) the free area A_f is defined as a ratio of orifice area to surface area. The free area is for a square arrangement

$$A_f = \frac{\pi}{4}\left(\frac{D}{L_{sq}}\right)^2 \tag{12.17}$$

and for a triangular arrangement

$$A_f = \frac{\pi}{2\sqrt{3}}\left(\frac{D}{L_{tr}}\right)^2 \tag{12.18}$$

Eq. (12.16) is valid with a uniform surface temperature condition and for good outlet flow conditions. It does not contain a variable taking outlet flow conditions into account. The back pressure of a jet increases with narrower outlets of escaping air, which decreases the pressure difference with which the jet discharges from the nozzle. In this way the velocity and mass flow of the discharging jet decreases. Also the average temperature difference between a jet and heat transfer surface decreases due to bad air removal. According to [74] it is important to remove the exhaust on the shortest possible path to provide better uniformity and higher heat transfer coefficients. A clear free removal path between the nozzles is the most favourable.

The heat transfer coefficients for different jet arrays can be solved with numerical modelling or experimentally. Commercial CFD-codes are useful for heat transfer designers and a professionally skilled designer can achieve good results for many practical problems. Figure 12.15 shows an example of heat transfer coefficients on the glass surface between rollers in a tempering furnace. CFD-calculations are adapted to forced convection in glass tempering as an example in [92].

Experimental work is usually very important when heat transfer problems are solved. Experiments give an important contact with reality for a heat transfer process designer. Sometimes it is difficult to trust the results of theories or CFD-calculations without experimental data. Local heat transfer coefficients can be measured with the test apparatus described previously on page 89. Figure 12.16 shows an example of the temperature distribution of a constant heat flux plate. In the figures above the stagnation points of the jets are in the middle points of the circle-shaped patterns. Convection is weakest at the midway between stagnation points, where wall jets hit each other. In Figure 12.16 the

hottest point is where convection is weakest, which is in the white area inside the red circle. The measurement of the surface averaged heat transfer coefficient is described in the next section.

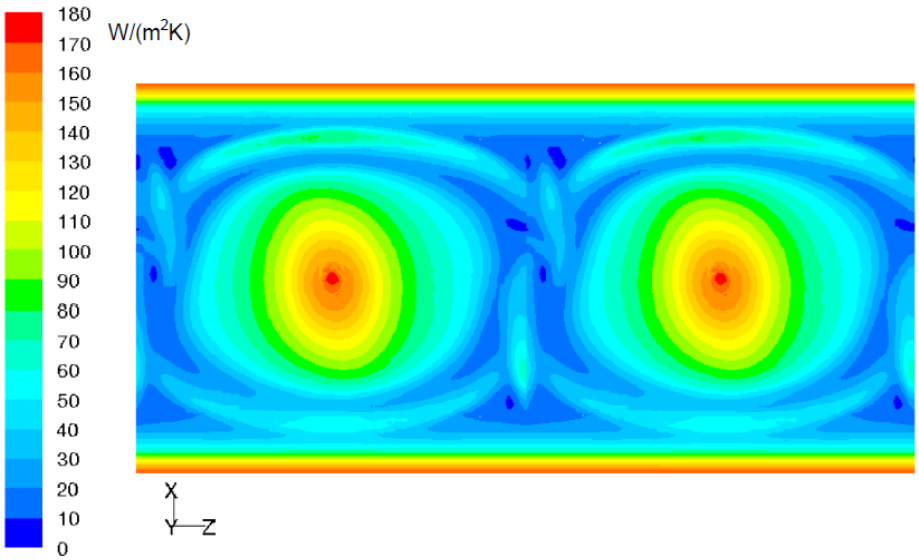

Figure 12.15. Local convection heat transfer coefficients on glass surface given by CFD. [108]

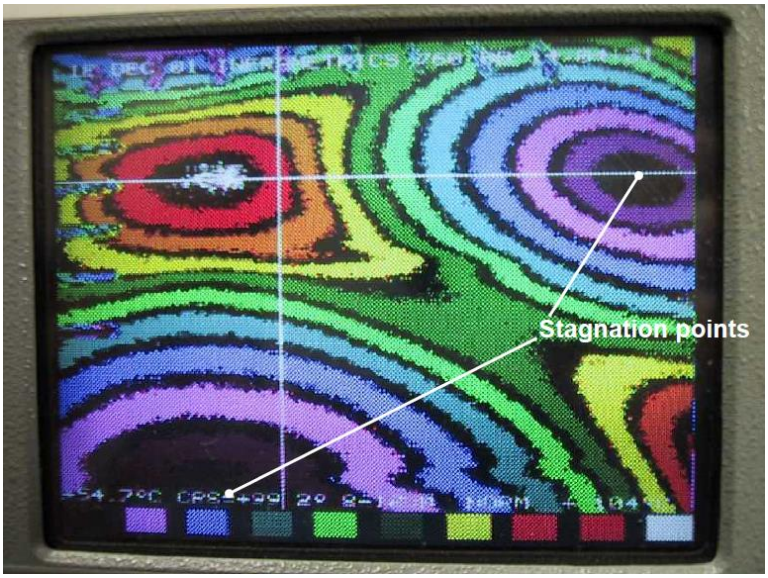

Figure 12.16. Thermal image of constant heat flux plate under array of impinging jets in laboratory measurement.

12.3.1 Measured mean heat transfer coefficients under jet array

Above in Sec. 12.2.1 forced convection on the plate surface under an air jet was handled. It was noticed that air jets with the same momentums and nozzle-to-plate distances produced rather equivalent local heat transfer coefficients. Next, a similar study is done for jet arrays.

In the experiment a hot thick copper plate was cooled under a jet array, which had a similar structure to the jet array in a real tempering chiller. The dimensions of the copper plate were 130 mm × 135 mm with a thickness of 46 mm. Only the upper surface was cooled with air jets, while other surfaces were insulated. As is seen in Figure 12.17, the jet array consisted of three nozzle boxes and the

distance between the midlines of the nozzle boxes was 120 mm. The vertical nozzle-to-plate distance H was 28 mm and the angle θ between the nozzle exit and surface normal was 25º. As is seen in Figure 12.18, there were two rows of nozzles in the nozzle boxes and the distance between nozzles in a row was 40 mm. Three different arrays were studied, but in all cases the nozzle-to-plate distance as well as the location of nozzles was the same. The only difference between the jet arrays was the different nozzle diameter, which was 5, 7.5 or 10 mm. The nozzles were like well rounded orifices as in Figure 12.2. During the measurements the copper plate was moved back and forth under the jet array and its temperature was measured by three thermocouples mounted in it.

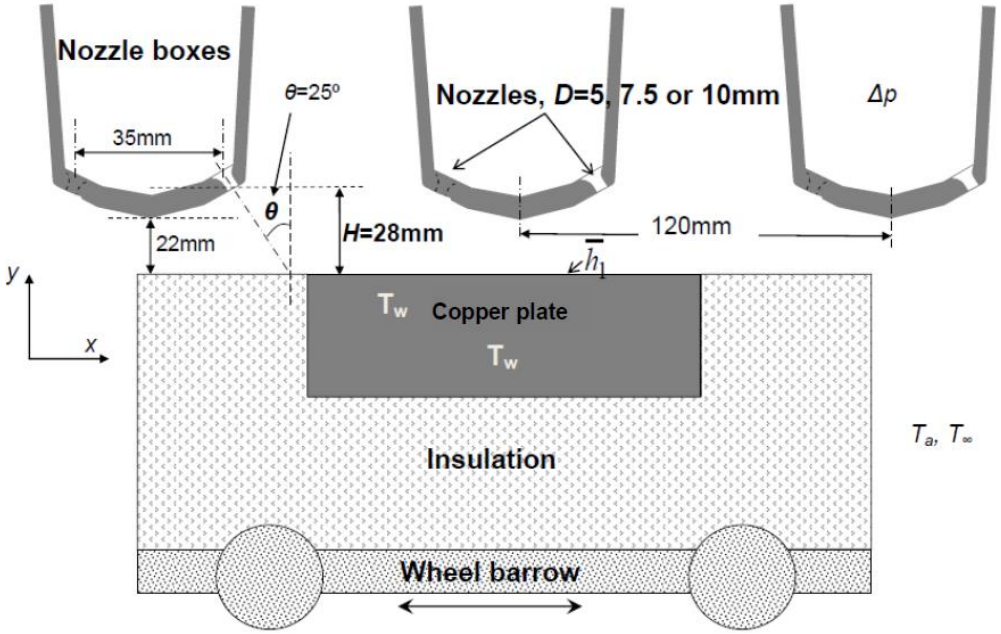

Figure 12.17 Experimental set up.

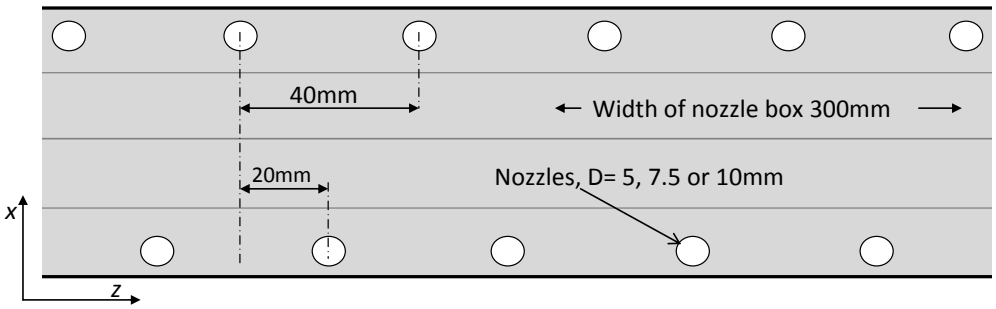

Figure 12.18 Location of nozzles in nozzle box used in measurement.

In measurement the overpressure Δp inside the nozzle box was adjusted to achieve the same momentum or energy consumption with each nozzle array. Overpressure was solved on the basis of Eq. (12.8) to even out the momentums, and on the basis of

$$P_{fan} = \frac{\Delta p \dot{V}}{\eta} \tag{12.19}$$

to even out the energy consumption. Eq. (12.19) defines the fan power P_{fan} needed to create jets without pressure losses in the air channels. In Eq. (12.19) $\dot{V}$ is the total discharging volume flow from nozzles and η is the efficiency of a fan. The typical efficiency of a centrifugal fan is 80%. Eq. (12.19) is valid for incompressible flow. Thus, its accuracy decreases with increasing overpressure. It gives 2% too high fan power at Δp = 6.7 kPa, which was the maximum overpressure in the measurement.

Different nozzle diameter – overpressure combinations used in the measurements are shown in the tables below. The convection heat transfer coefficient was solved from the measured cooling rate of the copper plate by changing the heat transfer coefficient in the calculations until the calculated cooling curve fitted the measured one. The heat transfer coefficient was also calculated using the correlation of Martin (12.16). Then the effect of nozzle angle was considered by using $H\cos\theta$ = 31 mm as a nozzle-to-plate distance. The results are shown in Table 12.3 and Table 12.4.

Table 12.3. Results for constant momentum and nozzle-to-plate distance

		Box 1	Box 2	Box 3	
Nozzle diameter	D	**5**	**7.5**	**10**	mm
Vertical nozzle to plate distance	H	28	28	28	mm
Nozzle angle	θ	25	25	25	º
Overpressure	Δp	**6.7**	**2.98**	**1.68**	10^3Pa
Jet momentum	J	253	253	253	10^{-3}N
Volume flow per nozzle (ρ=1.2kg/m^3)	$\dot{V}$	2.04	3.07	4.09	l/s
Fan power per nozzle (η =80%)	P_{fan}	17.1	11.4	8.6	W
Ambient temperature	T_a, T_∞	24	22	22	ºC
Cooling time from 200 to 100ºC		340	364	418	s
Measured heat transfer coefficient	$\bar{h}_{mea}$	386	354	309	W/(m^{2}K)
Calculated from Eq. (12.16)	$\bar{h}_{cal}$	326	302	275	W/(m^{2}K)
Ratio	$\bar{h}_{mea}$ / $\bar{h}_{cal}$	1.18	1.17	1.12	

According to the results in Table 12.3, the heat transfer coefficient of a jet array increases when the same momentum is created by using higher overpressure and smaller nozzle diameter. In the measured data the effect of the D-Δp combination to heat transfer coefficient is a little higher than Eq. (12.16) predicts. In Sec. 12.2.2 the heat transfer coefficient produced by a single jet was almost the same as long as the momentum of a jet was constant, which clearly differs from the results in Table 12.3. In the jet array a jet is not able to get ambient air with it during spreading as easily as a single free jet gets, because other jets, nozzle boxes and exhaust air flow prevents ambient air flow into a jet.

According to Table 12.4, the heat transfer coefficient of a jet array is almost the same when the same amount of energy is consumed to create air jets. The combination in which the nozzle diameter is largest is the most inefficient. This combination has also the highest volume flow. The escaping path of air after impingement becomes relatively narrower for increasing volume flow, which reduces convection. On the other hand smaller volume flow leads to higher temperature of wall jet and

escaping air. Thus, it is evident that convection starts to decrease when volume flow decreases enough even if the fan power per jet remains constant.

Table 12.4. Results for constant energy consumption and nozzle-to-plate distance

		Box 1	Box 2	Box 3	
Nozzle diameter	D	**5**	**7.5**	**10**	mm
Vertical nozzle to plate distance	H	28	28	28	mm
Nozzle angle	θ	25	25	25	º
Overpressure	Δp	**5.12**	**2.98**	**2.03**	10^3Pa
Jet momentum	J	193	253	306	10^{-3}N
Volume flow per nozzle (ρ=1.2kg/m^3)	$\dot{V}$	1.79	3.07	4.50	l/s
Fan power per jet (η =80%)	P_{fan}	11.4	11.4	11.4	W
Ambient temperature	T_a, T_∞	23	22	20	ºC
Cooling time from 200 to 100ºC		364	364	382	s
Measured heat transfer coefficient	$\bar{h}_{mea}$	357	354	333	W/(m^{2}K)
Calculated from Eq. (12.16)	$\bar{h}_{cal}$	298	302	293	W/(m^{2}K)
Ratio	$\bar{h}_{mea} / \bar{h}_{cal}$	1.20	1.17	1.14	

In the tables above the measured heat transfer coefficients are 12 to 20% higher than Eq. (12.16) predicts. Eq. (12.16) is valid for a good outlet flow condition where free upward is between the nozzles. In the experiments above the air outlet flow condition was even better, because in addition to the free upward between the nozzles, air could flow out from the heat transfer area via borders of the jet arrangement. A better outlet flow condition yields a higher heat transfer coefficient, but it hardly explains all of the difference between the measured data and correlation. However, the discrepancies between measurements and/or different correlations have also been observed by others with jet arrays. The comparison of different correlations shows a clear difference between the achieved non-dimensional heat transfer rates in [74] and [79]. Deventer et al. [81] compared their experimental results to the results of Eq. (12.16) and found even a 40% difference in Nusselt numbers. In addition to differences in the nozzle types and arrangements used in the experiments, the differences in outlet flow conditions explain partly the differences between different correlations. On the other hand, it would be much more reliable to compare heat transfer coefficients than the Nusselt numbers. The Nusselt numbers can vary clearly even if the heat transfer coefficients are the same if the nozzle diameter is not constant. The comparison should be made by using exactly the same initial values in all correlations. For instance, if some other correlation predicts 30% higher heat transfer coefficient as Eq. (12.16) with the same initial values, then Eq. (12.16) needs over 2-times higher overpressure for the same heat transfer coefficient. Over 2-times higher overpressure leads to over 3-times bigger fan power. Thus, in practice 30% difference between correlations can only be explained by a mistake or the validity to totally different jet arrays.

The accuracy demand for a correlation to be used in the design of a jet array is high. For instance, a 10% lack between the realized and designed heat transfer coefficient means that 30% more overpressure is needed to achieve the designed convection rate, which usually exceeds the fan capacity. In practice, there are many restrictions which must be considered in the design. Rollers

under glass cause the major restriction for nozzle placement in glass tempering furnaces and in chillers, where nozzles are placed in nozzle boxes between rollers. Such a placement differs from the arrangement from which the literature correlations are created. Thus, experiments are needed to clarify the applicability of the correlations to these kinds of practical nozzle arrangements. Generally, it can be said that there is no correlation in the literature which would give accurate values for a heat transfer designer. Despite the inaccuracy in absolute heat transfer coefficients, the literature correlations are still very useful as long as they reliably predict the effect of variables like overpressure, nozzle diameter and nozzle-to-plate distance on relative heat transfer coefficients. Below, Eq. (12.16) is exposed under such a test.

Table 12.5. Effect of overpressure on heat transfer coefficient.

		Box 3	Box 3	Box 3	Box 3	
Nozzle diameter	D	10	10	10	10	mm
Vertical nozzle to plate distance	H	28	28	28	28	mm
Nozzle angle	θ	25	25	25	25	º
Overpressure	Δp	**1.68**	**2.03**	**2.79**	**3.38**	kPa
Jet momentum	J	253	306	421	510	mN
Fan power (η =80%)	P_{fan}	8.6	11.4	18.4	24.5	W
Ambient temperature	T_a, T_∞	22	20	22	22	ºC
Cooling time from 200 to 100ºC		418	382	356	332	s
Measured heat transfer coefficient	$\bar{h}_{mea}$	309	333	362	389	W/(m^{2}K)
Calculated from Eq. (12.16)	$\bar{h}_{cal}$	275	293	326	348	W/(m^{2}K)
Ratio	$\bar{h}_{mea} / \bar{h}_{cal}$	1.12	1.14	1.11	1.12	

In Table 12.5 the measured heat transfer coefficients are 11 to 14 % higher than the predicted ones. The ratio $\bar{h}_{mea} / \bar{h}_{cal}$ is almost constant. Thus, the change in the overpressure changes the measured heat transfer coefficients in a same relation as it changes the measured ones. On the basis of the results above, Eq. (12.16) is useful for solving the mean heat transfer coefficients of a jet array in the glass tempering process. It does not give an absolutely correct heat transfer coefficient, but it predicts very accurately how the heat transfer coefficient changes relatively as a function of nozzle diameter and overpressure in a nozzle box. Eq. (12.16) can even be used a little outside of its validity range. It has also a weakness because it clearly over-predicts the effect of decreasing *H/D* –value, when *H/D* is below its validity range.

12.4 Natural Convection

Heat transfer causes temperature differences in air, which has a temperature-dependent density. Because of buoyant force, the density differences get air in movement. Such natural air movement at the surfaces generates convection heat transfer between the surface and air, which is called natural convection.

Glass moves slowly during heating in the tempering process. Thus, glass moves relatively to air. In that case convection is not natural. However, if the forced air movement is slow, the effect of natural

convection becomes significant and the heat transfer rate may be increased or decreased by natural convection. Such convection is called mixed convection. Because of the high demands of production capacity, natural or mixed convection is not an important issue in modern tempering furnaces, which are equipped at least with a top convection system. Natural or mixed convection exists in furnaces without a bottom convection system and also in other furnaces when forced air blow is turned off. Natural convection is more effective in the neighbourhood of the edges of horizontal plate, which is proved to be one reason for the overheating of glass edges in older furnaces [93]. The theory of natural convection on vertical and horizontal surfaces is widely presented in the literature. As an example, one literature equation gives $\overline{h}$ = 3 W/(m^{2}K) for upper surface and $\overline{h}$ = 13 W/(m^{2}K) for lower surface, when glass (1 × 1 m) at 20˚C is horizontally in a 700˚C furnace. Equivalent values are $\overline{h}$ = 2 W/(m^{2}K) and $\overline{h}$ = 7 W/(m^{2}K), when the glass temperature is 600˚C. Thus, natural convection is more effective on the bottom surface, where also contact heat transfer from rollers to glass occurs. The first air jet systems were installed in tempering furnaces to blow air onto the top surface of the glass just to help to balance the difference between upper and lower surfaces in heat transfer rates.

13. CONTACT HEAT TRANSFER BETWEEN GLASS AND ROLLERS

Heat transfer between contacting solid surfaces depends on the contact pressure, mechanical properties and surface topography of solids. As shown in Figure 13.1, contact heat transfer between surfaces can be divided into three parts: gas-gap conductance, solid spot conductance and radiation. Thus, the mean contact heat transfer coefficient is

$$\bar{h}_{ct} = \bar{h}_{gg} + \bar{h}_{sp} + \bar{h}_r \tag{13.1}$$

In Eq. (13.1) $\bar{h}_{gg}$ is mean heat transfer coefficient over gas-gaps, $\bar{h}_{sp}$ is mean heat transfer coefficient over contact points and $\bar{h}_r$ is mean radiative heat transfer coefficient. A rough estimation of a steady-state gas-gap conductance is obtained when the thermal conductivity of gas is divided by the average thickness of gas-gap δ, which is often very difficult to define. The conductance over solid spots is also very difficult to determine. There are different types of solutions in the literature [94] which are useful only for contacts between good conductors like metals. In a glass tempering furnace the contact is between hard ceramic materials with poor thermal conductivities, and the effect of contact resistance on heat transfer rate over a contact face is much more insignificant than for metals.

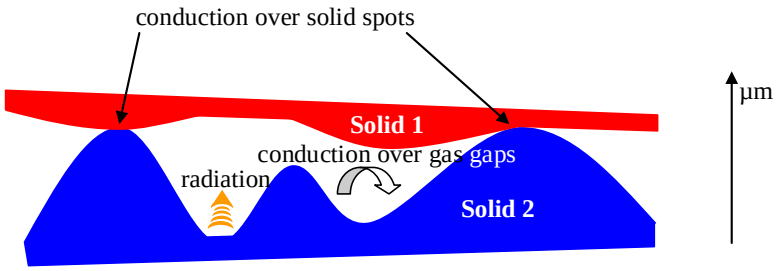

Figure 13.1. Schematic of contact heat transfer between two solids.

In a windscreen bending furnace two glasses are placed one on the top of another. If the contact between glasses is complete, then the interface does not resist heat transfer. In order to avoid adhesion between glasses silicon dioxide dust is powdered between them. Heat transfer over the interface is radically reduced if the contact is lost due to bending caused by thermal stresses or dust lump. The heat flux trough a thin air gap between flat surfaces can be obtained as

$$q \approx \frac{k}{\delta}\left(T_{s1} - T_{s2}\right) + \frac{\sigma\left(T_{s1}^4 - T_{s2}^4\right)}{1/\varepsilon_{s1} + 1/\varepsilon_{s2} - 1} \tag{13.2}$$

In Eq. (13.2) the first term stands for conduction through the air-gap and the second term stands for radiation heat transfer between the surfaces.

In a glass tempering furnace the contact is between the glass and the ceramic rollers. The glass surface is very smooth as well as the roller surface should be, which leads to the perfect contact spot assumption. In other words, heat transfer on the contact area is pure solid spot conduction between the roller and glass. Outside of the contact area the gas gap conductance affects. Figure 13.2 shows the values of k/δ near the contact area of the roller and glass. For instance, at horizontal distance of x = 1.66 mm from the contact line δ = 0.029 mm and k/δ = 2068 W/m^2°C. When the distance from the contact line increases, conduction over the gas gap decreases rapidly.

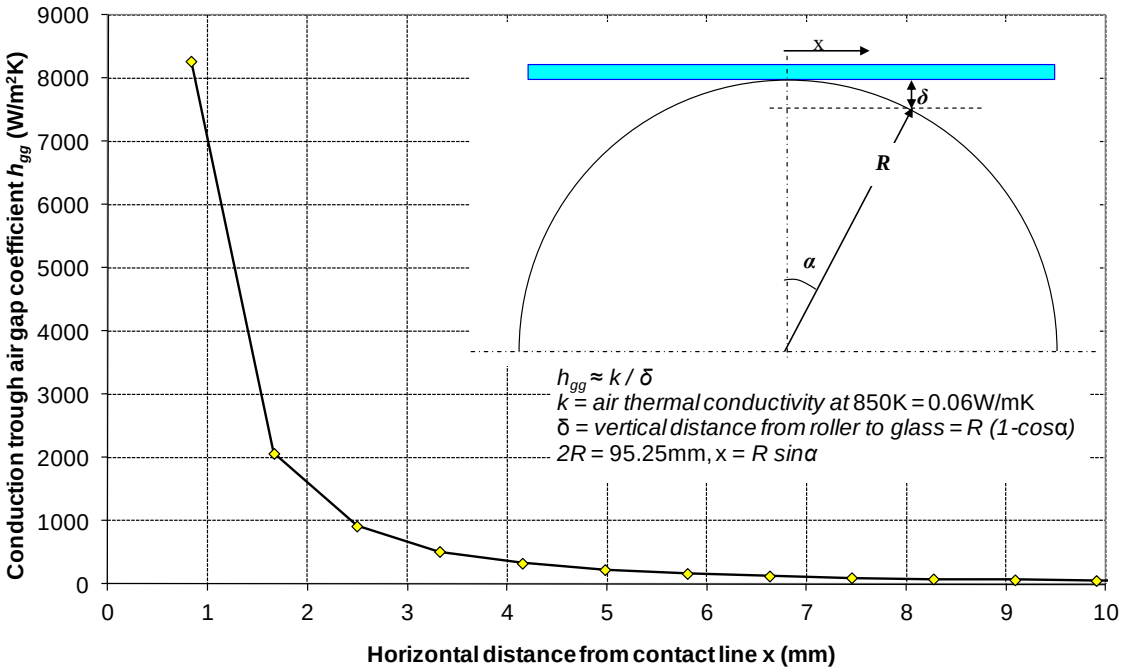

Figure 13.2. Conductive heat transfer coefficient between surfaces separated by gas gap.

Figure 13.3 is taken from the research report in which the aim was to solve convection heat transfer coefficient from air jets to the glass bottom surface (see also Figure 12.15). In the element grid used in the CFD modelling the minimum thickness of the air gap between glass and roller was 0.375 mm due to technical reasons (convergence problems) in the modelling. Figure 13.3 shows the convection heat transfer coefficient as a function of position in the cross direction (x) of rollers. In the x-direction the pitch between rollers was 0.12 m, as well as the distance between air jets in the lengthwise direction (z) of rollers. Heat transfer curves are in the same line at x values between $50 \leq x \leq 60$ mm, which indicates that wall jets are not able to penetrate as deeply into the gap between glass and the roller. In spite of that the convection heat transfer coefficient starts to increase and runs into a maximum value of 165 W/m^2°C. At this point δ = 0.375 mm and $k/\delta \approx$ 165 W/m^2°C, which leads to the conclusion that the increase of the convection heat transfer coefficient in Figure 13.3 is due to the gas-gap conductance.

When the local gas-gap conductance values from x = 1 to 10 mm presented in Figure 13.2 are converted to a surface averaged value over the roller pitch with the assumption k/δ = 0, when $1 > x >$ 10 mm, then the results is $\bar{h}_{gg} \approx$ 100 W/m^2°C, which is a clearly too big a value. This indicates that in a tempering furnace the situation in a gas gap is different to the results above. For instance, the results in Figure 13.3 are valid for a stationary condition in which the glass temperature (100°C), roller temperature (680°C) and incoming air (680°C) temperature are constants. This has not much effect on the convection heat transfer coefficients between an air jet and glass, but it has a major increasing effect on gas-gap conductance.

As seen in Figure 13.4, in the case of stationary condition the air temperature in an air gap decreases linearly from 680°C at the roller surface to 100°C at the glass surface. In a tempering furnace the typical circumferential speed of the rollers is 100 mm/s. In the case of actual transient condition in which glass is moving on top of rotating rollers, the air temperature gradient is much lower and more irregular than in the stationary case. In any case, the gas-gap conductance must have some effect in the regions where conduction parameter k/δ is much bigger than the convection heat transfer coefficient, but its effect on total heat transfer in a tempering furnace is small.

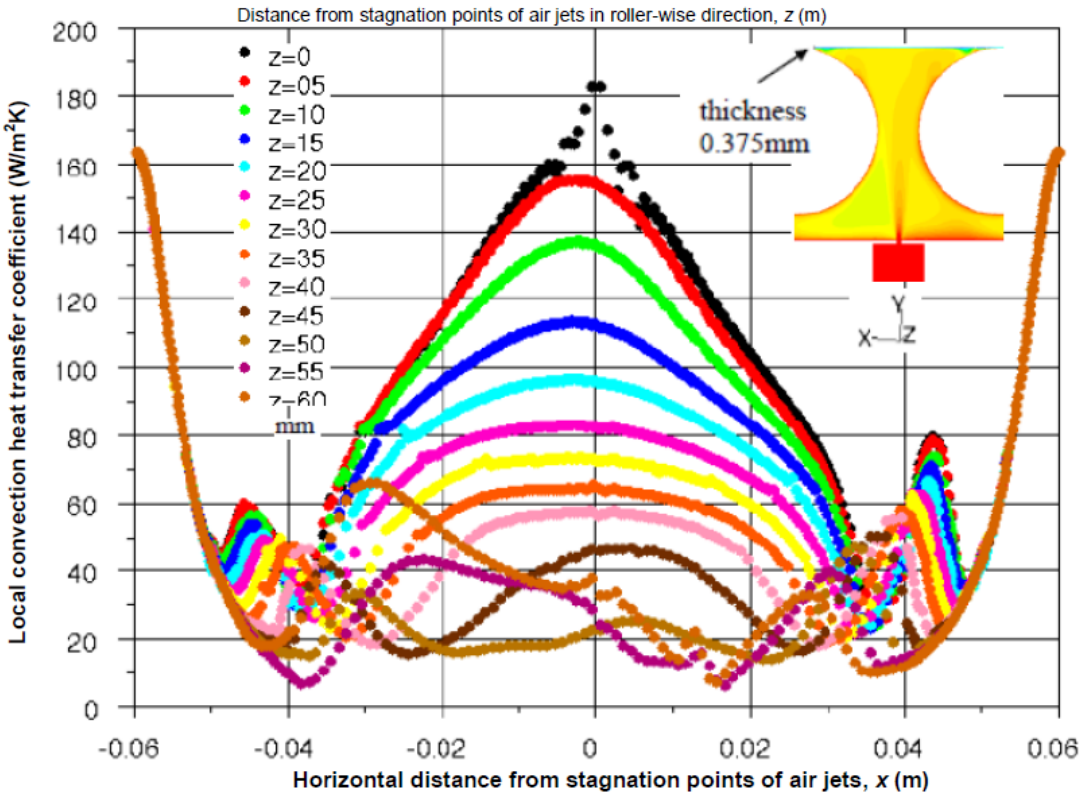

Figure 13.3. Convection heat transfer coefficient on glass bottom surface between rollers. [108]

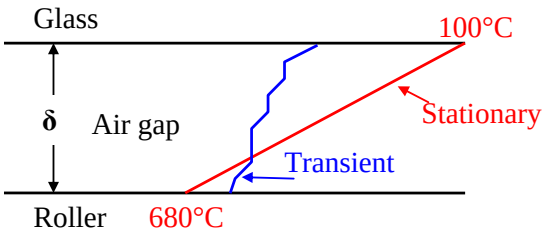

Figure 13.4. Schematic of air temperatures in stationary and transient (actual) conditions.

Radiation heat transfer between the glass and roller at and near the contact area is not an important factor in contact heat transfer, because it has no extra effect on the radiation heat transfer in a tempering furnace. Thus, in a tempering furnace between glass and roller $\overline{h}_r = 0$ in Eq. (13.1).

Solid spot conductance between glass and rotating steely rollers (in a float line) is theoretically studied in [95]. When the glass is assumed to be an elastic plate the contact force per unit width between glass and rollers is

$$F = \rho_g g S L_{rp} \tag{13.3}$$

and the contact length is

$$l_{ct} = 2\sqrt{\frac{4RF}{\pi}\left(\frac{1-\nu_g^2}{E_g}+\frac{1-\nu_r^2}{E_r}\right)} \tag{13.4}$$

In Eqs. (13.3) and (13.4) g is the gravity, L_{rp} the roller pitch, S the glass thickness, ρ the density, v the Poisson's ratio and E is the elastic modulus. Subscript g stands for the glass and r for the roller. When the thermal conductivity of the roller is much higher than that of glass, and assuming a high interface heat transfer coefficient, the heat transfer coefficient over the contact time $t_{ct} = l_{ct}/u$ may be approximated as [95]

$$h_{sp} = \sqrt{\frac{k_g \rho_g c_{pg} u}{\pi l_{ct}}} \tag{13.5}$$

where u is the glass velocity.

Finally, the effective solid spot conduction heat transfer coefficient on the glass surface is

$$\bar{h}_{sp} = \frac{h_{sp} l_{ct}}{L_{rp}} \tag{13.6}$$

Equivalent heat transfer coefficient on the roller surface is obtained when L_{rp} in Eq. (13.6) is replaced with $2\pi R$.

In the experiment in [96] aluminium plate was heated on top of the rotating rollers in a small-sized laboratory furnace. In the first measurement the contact between the plate and rollers was normal, but in the second measurement the contact was eliminated with thin frame placed between the plate and rollers. These experiments led to the result that the effective contact heat transfer coefficient $\bar{h}_{ct} L_{rp}$ was about 0.5 W/(mK). Although, the reanylysation of the measured temperature data presented in the reference yielded to higher values between 1.0 and 1.5 W/(mK). The values above include both, gas-gap conductance and solid spot conductance. Next, the equivalent solid spot heat transfer coefficient is calculated by using the theory presented above. In the experiment conductivities were the other way around as the theory expects, because aluminium plate had high thermal conductivity compared to ceramic rollers.

The following dimensions and speed were used in the experiment presented in [96]:

- Roller diameter D = 55 mm, $R = D/2$
- Roller pitch, L_{rp} = 100 mm
- Thickness of aluminium plate, S = 10 mm
- Rotating speed, ω = 0.208 r/s
- Plate velocity, $u = \omega\pi D$ = 0.036 m/s

The mechanical material properties of soda-lime glass are used for a ceramic roller:

- Poisson ratios, v_{al} = 0.33 and $v_{ce} \approx v_{glass}$ = 0.23
- Elastic modules, $E_{al} = 6.9\times10^{10}$ Pa and $E_{ce} \approx E_{glass} = 7.2\times10^{10}$ Pa

The thermal material properties of roller are used in Eq. (13.6), because now its thermal conductivity is low. The thermal material properties of soda-lime glass are used for a ceramic roller, thus:

- Thermal conductivity, k_g = 1 W/(mK)
- Specific heat, c_{pg} = 896 J/(kgK)
- Density, ρ_g = 2540 kg/m^3

Contact force is

F= 2707 kg/m^3 × 0.010 m × 9.81 m/s^2 x 0.1 m = 26.6 N/m

Contact length is

$l_{ct} = 2\,[(4RF / \pi) \times [(1 - \nu_{al}{}^2) / E_{al} + (1 - \nu_{ce}{}^2) / E_{ce}]]^{0.5}$ = 9.86×10^{-6} m

Solid spot conduction heat transfer coefficient is

h_{sp} = (1 W/mK × 2540 kg/m^3 × 896 J/kgK × 0.036 m/s / π / 9.86×10^{-6} m)$^{0.5}$= 51 443 W/(m^{2}K)

Solid spot heat transfer coefficient multiplied with contact length is

$h_{sp}\, l_{ct}$ = 0.5 W/(mK)

Effective solid spot conduction heat transfer coefficient on glass surface is

$\bar{h}_{sp} = h_{sp}\, l_{ct} / L_{rp}$ = 0.5 W/mK / 0.1 m = 5 W/(m^{2}K)

In a simple measurement a glass strip with width of 10 mm and thickness of 2.1 mm, the top side of which was insulated, was placed on a hot ceramic roller with diameter of 95 mm. Similar measurements were made with and without (1 mm gap) direct contact between the glass strip and roller, and in all cases temperatures from the glass and roller were recorded with thermocouples. After that the effective contact heat transfer coefficient was solved from the measured data by using theoretical modelling. This rough measurement indicated that the order of magnitude of the effective contact heat transfer coefficient from the stationary ceramic roller to glass is between 1.0/L_{rp} and 2.0/L_{rp} W/(m^{2}K) . It was also concluded that $\bar{h}_{ct}$ between the stationary ceramic roller and glass is rather near to that between the stationary ceramic roller and aluminium plate.

Some thermal and mechanical properties of glass change clearly with glass temperature. According to the theory above the effect of the temperature increase from 200°C to 600°C on the local solid spot heat transfer coefficient due to changes in the glass specific heat and thermal conductivity is +40%, and due to changes in ν and E the contact length increases by 40%. These changes cause the effective solid spot conduction heat transfer coefficient to increase by 66%. The theory presented above also indicates that the effective solid spot conduction heat transfer coefficient on the glass surface increases by 41% when the glass thickness is doubled. In the simple measurement described above also the effect of contact force was studied, which gives the result that the contact force has a minimal effect on contact heat transfer between the stationary ceramic roller and glass. Lastly, it is worthwhile to recall the definition of the theory above, which conditioned the metallic roller. The material combination of glass – fused silica differs from that condition, because both materials are very hard and thermal conductivities are low. It is not reliable to apply the theory to the situation where the glass is on ceramic rollers.

In practice full scale experiments are the only realiable method for solving the sum of the gas-gap and solid spot conductances, i.e., effective contact heat transfer coefficient between glass and ceramic rollers in a tempering furnace. In the experiments two glasses should be heated side by side in a tempering furnace, the second glass being lifted about 1 mm off from rollers by thin cords, for instance, on its bottom, and the temperatures of the glasses after heating should be measured with the thermal scanner of the tempering line. Then, the temperature difference between the glasses would be dependent only from the effective contact heat transfer coefficient. Now, only the following rough estimate for the effective contact heat transfer coefficient of glass on the top of ceramic rollers in a tempering furnace can be given: $1 \le \bar{h}_{ct} L_{rp} \le 3$ W/(mK), where $\bar{h}_{ct} = \bar{h}_{gg} + \bar{h}_{sp}$. The estimate is based on the results above and the calculations shown in Sec. 14.6.

14. NEW RESULTS OF THEORETICAL MODELLING

14.1 Radiation heat flux from tubular resistor to glass

In Sec. 8.3.2 the radiation heat flux from a tubular resistor to a plate under it was discussed. The figures below are from the research dealing with the development of the windscreen bending line in Figure 6.3. The roof of the bending chamber is equipped with 200 resistors, which can be independently controlled to focus the radiation on a selected area of the glass to be bent. The theory has also been applied in the research of a glass tempering furnace equipped with length-wise open coil heaters, which enables the profiling of radiation heat transfer in the width-wise direction of a glass loading.

Figure 14.1 shows the heat flux from one resistor defined in the figure to the plate underneath, with different resistor-to-plate distances and as a function of coordinate *x*. Figure 14.2 shows the same heat flux as a function of coordinates *x* and *z* at plate surface. The distribution of radiative heat flux and how the resistor-to-plate distance affects can be seen.

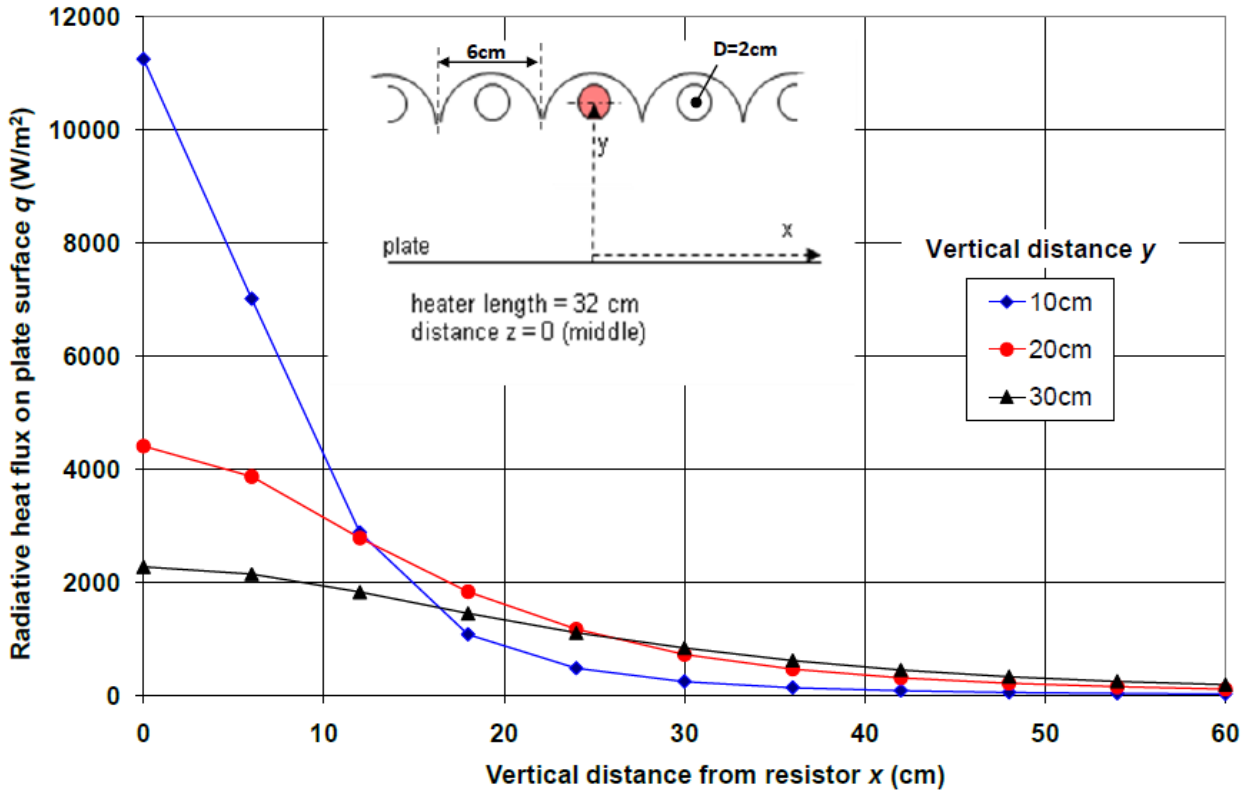

Figure 14.1 Heat flux from resistor to plate under it as function of distances x and y.

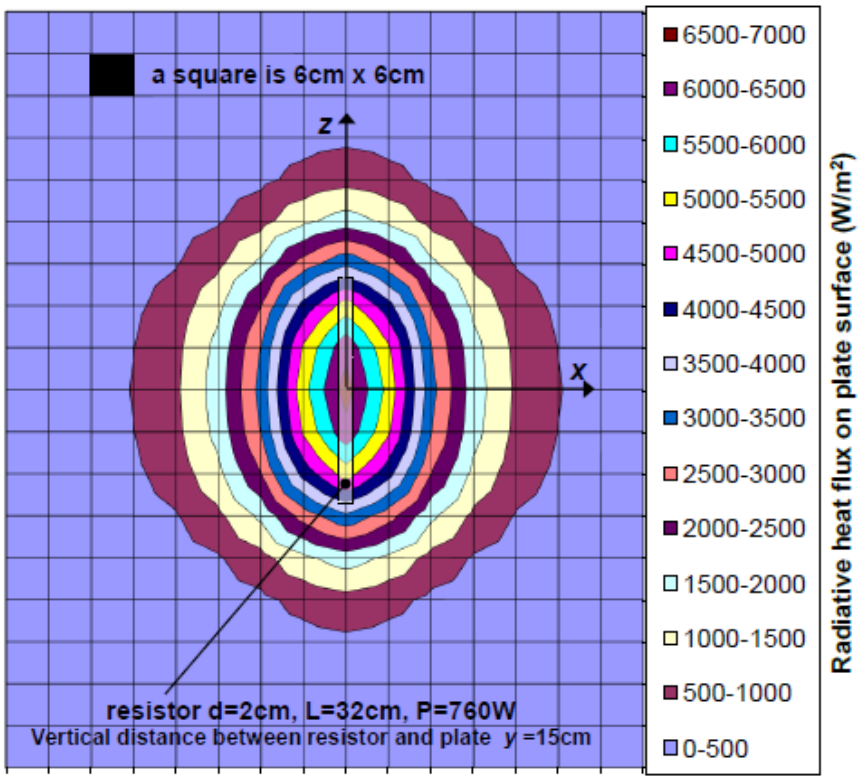

Figure 14.2 Heat flux density distribution from resistor to plate.

14.2 Behaviour of incident radiation in glass plate

The behaviour of incident radiation hitting the glass surface was discussed in Chaps. 9 and 11, in which many new results of theoretical modelling were already shown. In the next figures the glass thickness is divided into layers and the absorption of the layers is given.

Figure 14.3 shows the absorptance of glass layers as a function of wavelength band from the emission of a black radiator at 700˚C, which is a typical temperature of a tempering furnace. Glass is clear soda lime silica glass and its thickness is 4 mm. In the modelling the absorption coefficient of 100 cm^{-1} was used for the wavelength band over 4.5 μm, which still gives a little absorptance to the layer just under the surface layer. In practice, glass can be treated as opaque for thermal radiation when the wavelength is over 4.5 μm. At wavelengths between 2.75 and 4.5 μm significant absorption occurs everywhere. At wavelengths below 2.75 μm absorption is weak.

Figure 14.4 compares the absorption of various glasses with the same thickness in the tempering furnace. In the figure absorbed heat flux in separate glass thickness layers is shown in a clear glass, green tint glass and low-e coated (single silver in Chap. 11) clear glass. The green tint glass has higher absorption than a clear glass in all layers, and a low-e coating on the face surface of glass cuts absorption to glass effectively. In low-e coated glass the layers below the face surface layer have such small absorption that it hardly can be seen in the figure. The portion of radiation which is not reflected from low-e coating is mainly absorbed into it. If low-e coating is on the back surface and radiation hits the face surface, the absorption is higher in all layers than it is for a clear glass. It is even higher than for a green tint glass in a back surface layer, which is primarily due to absorption of the coating itself and secondarily to reflection backwards onto the glass from the coated surface.

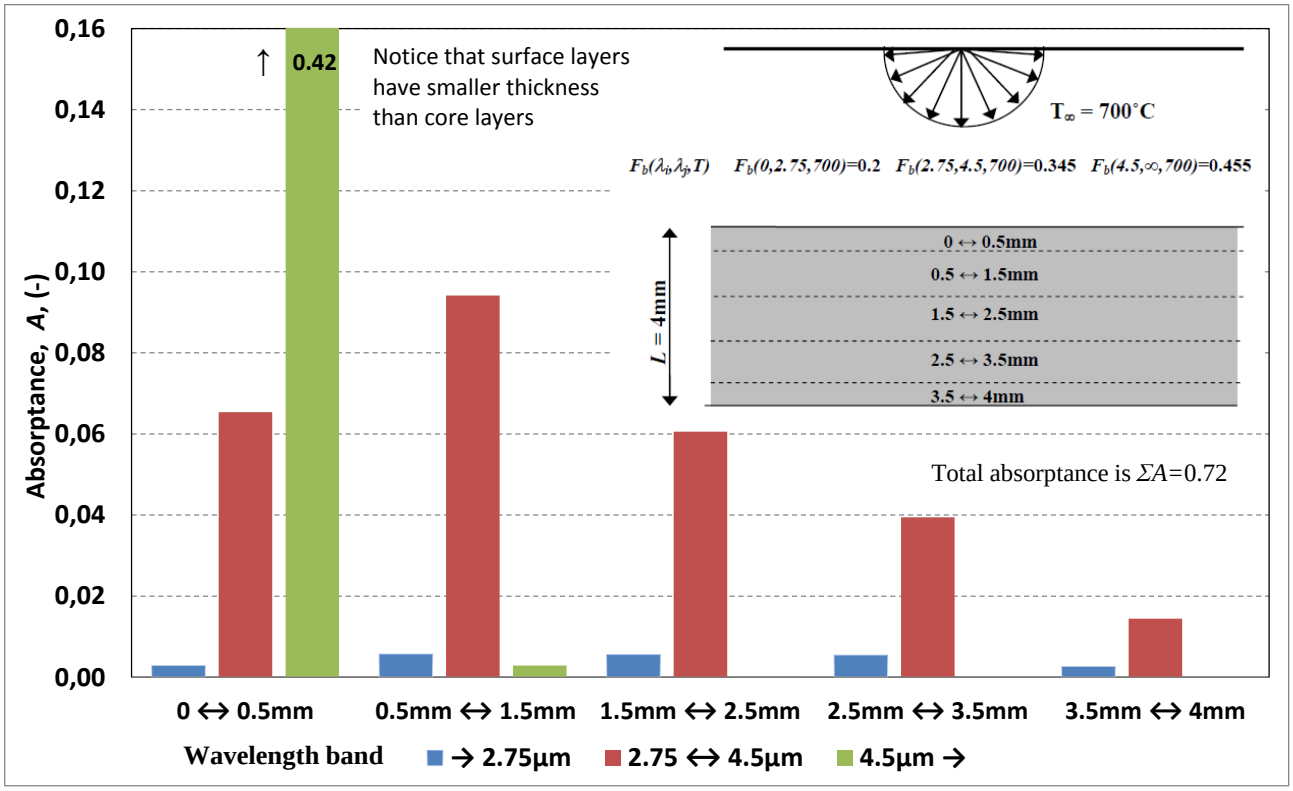

Figure 14.3 Fractions of absorbed incident radiation in clear glass layers as function of wavelength. Temperature of black radiator is 700˚C and glass thickness 4 mm.

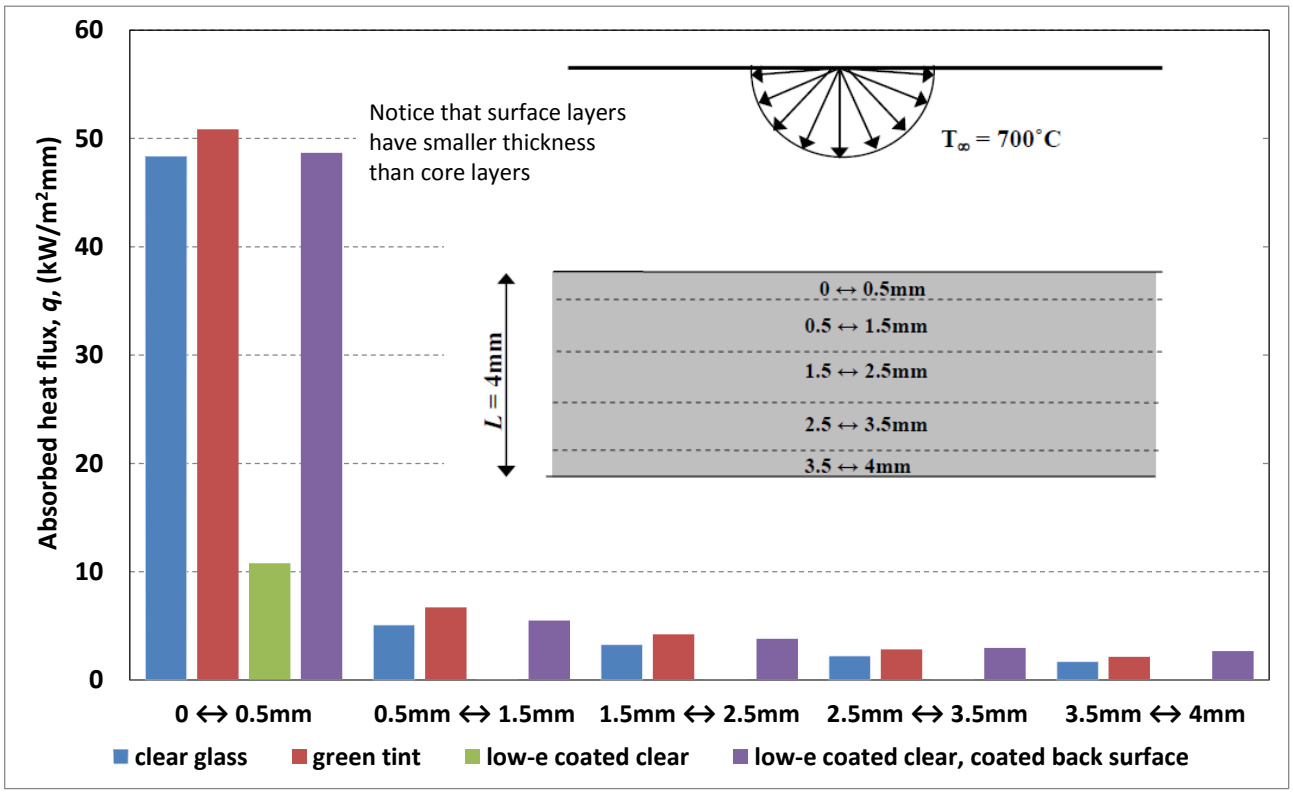

Figure 14.4 Absorbed heat flux in glass layers of different glass types. Temperature of black radiator is 700˚C and glass thickness 4 mm.

14.3 Heat transfer in tempering furnace

Next, the aim is to model glass temperature, heat fluxes and thermal stresses in the tempering furnace introduced in Sec. 5.5. The furnace initial temperature is set as 700ºC and its change during heating is taken into account based on the experimental data presented in [39]. The roller temperature needed in the modelling of contact heat transfer is considered with the furnace temperature also. In the modelling the emissivity of hot surfaces of the furnace is set as 0.85. The air temperature is 650ºC, which is just an estimate of the time-averaged temperature. Surface temperature, and particularly air temperature drops temporarily when full cold glass loading gets into the furnace. The rate of forced convection varies greatly depending on furnace types and models. In some flow-through air convection furnaces the mean forced convective heat transfer coefficient is only about 20 W/(m^{2}K) and in some circulating air convection furnaces it can even be 150 W/(m^{2}K). Now, the initial value of 40 W/(m^{2}K) is used for mean forced convective heat transfer coefficient on the glass top surface. Typically, the control parameter is set so that the overpressure inside the convection pipes decreases during heating. This is taken into account in the modelling and after 90 seconds forced convection ends. Natural convection on the bottom surface of the glass occurs during the whole cycle. The contact heat transfer coefficient is set as 15 W/(m^{2}K) as estimated in Chap. 13 for the roller pitch of 120mm.

In Figure 14.5 the glass temperature rises from 20 to 640˚C in 160 seconds. Such a heating speed (40 seconds per one thickness mm) is a typical value for tempering furnaces in the market. In the figure the heating is a little stronger via the top side than bottom side of the glass, which causes asymmetrical temperature distribution. Gravity tends to keep the glass flat, and the asymmetry in the figure is still so weak that thermal stresses cannot bend the glass. The temperature difference between the glass top surface and mid-plane has the maximum value of 42˚C when the heating time is 5 seconds, which generates transient 10 MPa tensile stress at the glass mid-plane.

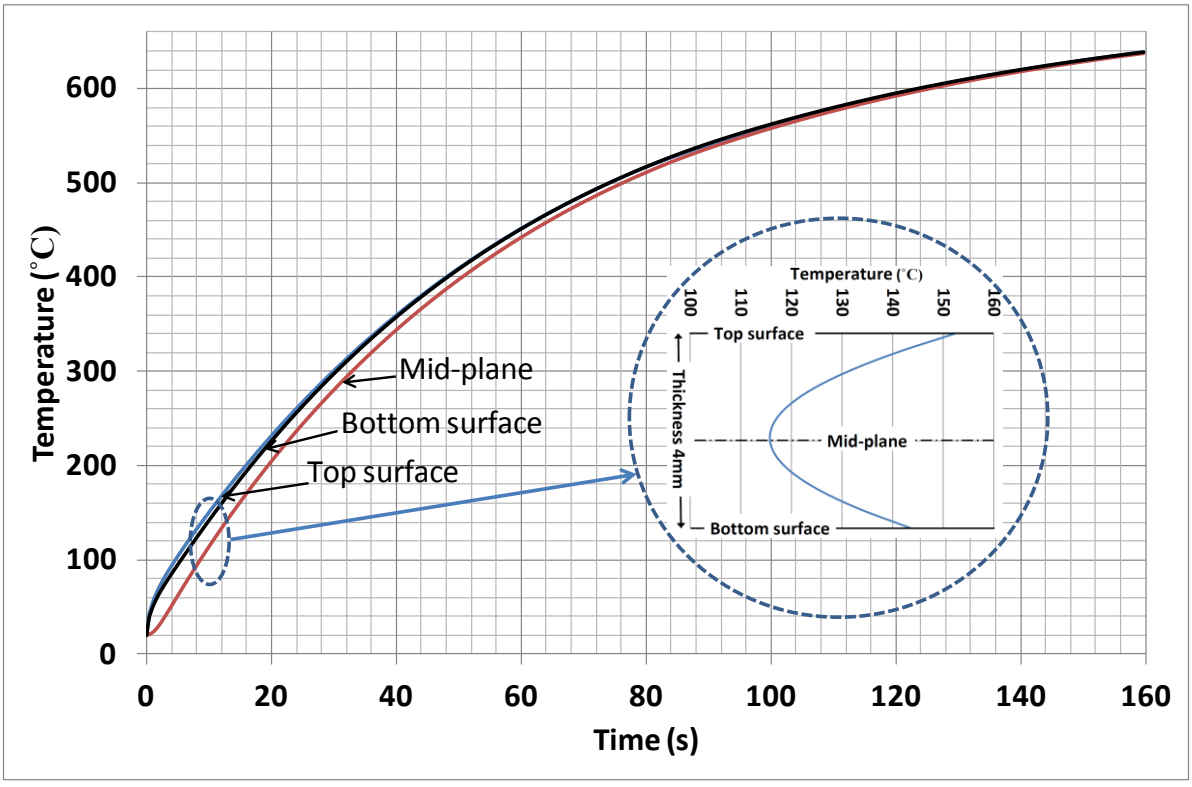

Figure 14.5 Development of glass temperatures in tempering furnace. Clear glass thickness is 4 mm.

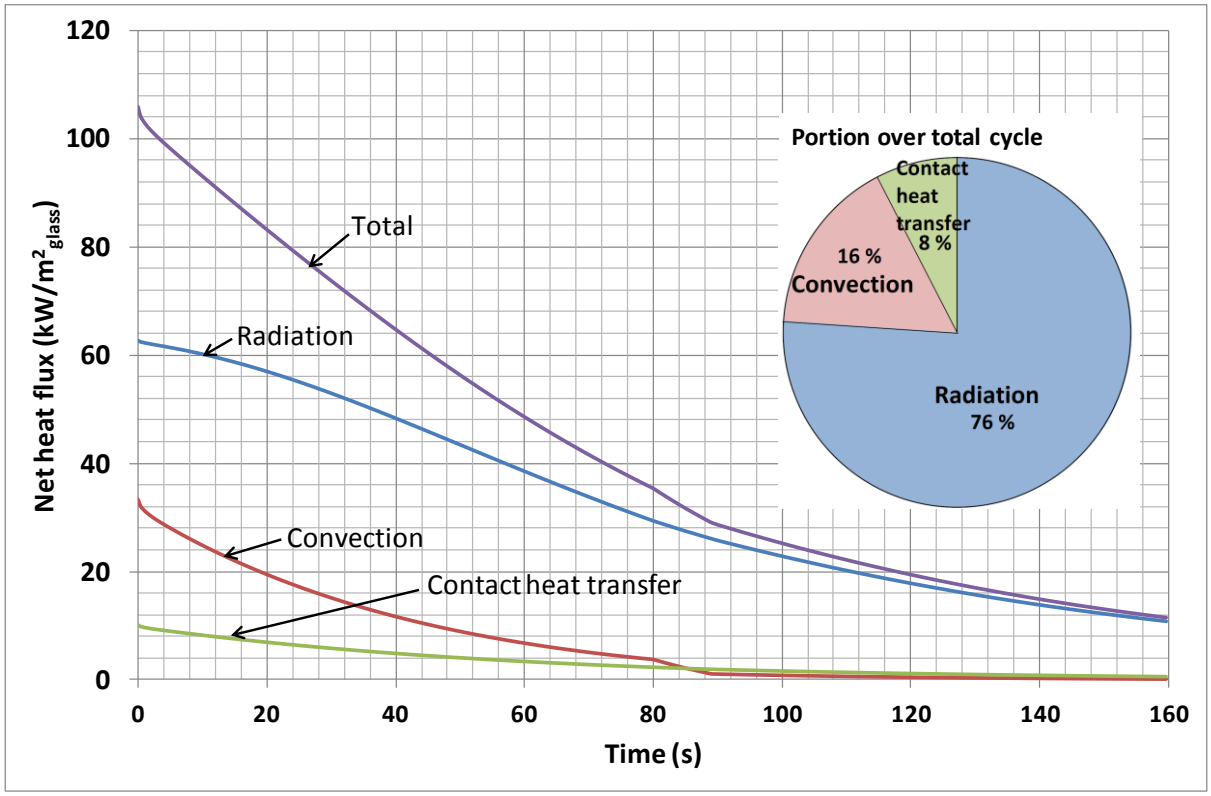

Figure 14.6 Heat fluxes by different modes to glass during heating in tempering furnace. Clear glass thickness is 4 mm.

Radiation is clearly the main heat transfer mode in the furnace modelled. At the beginning of heating its portion is 59% and at the end it increases above 90% in Figure 14.6. Radiation is dependent on the difference between fourth powers of furnace and glass temperatures, but convection and contact heat transfer are dependent directly on the temperature difference between the furnace air and glass. Because of that radiation attenuates less than convection when glass temperature increases. The decrease of convection heat transfer coefficient due to the overpressure adjustment partly explains the time-wise decrease of the portion of convection in the case modelled. The portions of transferred heat over the total cycle are radiation 76%, convection 16% and contact heat transfer 8%.

14.4 Heat transfer in tempering cooling

Next, the glass heated up to 640˚C in Sec. 14.3 is cooled in the tempering chiller shown in Figure 5.9. In the modelling the temperature of air and surrounding surfaces is set as 20ºC and the emissivity of the surrounding is set as 1. The mean forced convective heat transfer coefficients used are solved by inserting real dimensions and overpressures in Eq. (12.16). During the first 6 seconds the convection heat transfer coefficient is 434 W/(m^{2}K) and after that it changes in a few seconds to 300 W/(m^{2}K). Such a change is made because it reduces the energy consumption of the fans during cooling. Contact heat transfer between glass and rollers is ignored, because its effect in thin glass tempering is very small.

As seen in Figure 14.7 the temperature of the glass surface drops much more sharply than the temperature of the glass mid-plane. The maximum temperature difference between surface and mid-plane is 128˚C. After 6 seconds also the mid-plane temperature drops below 480˚C and the cooling rate can be reduced. In an oscillating glass tempering chiller the tail edge of the glass loading defines when tempering cooling can be stopped, while the leading edge is anyway a longer time in tempering cooling.

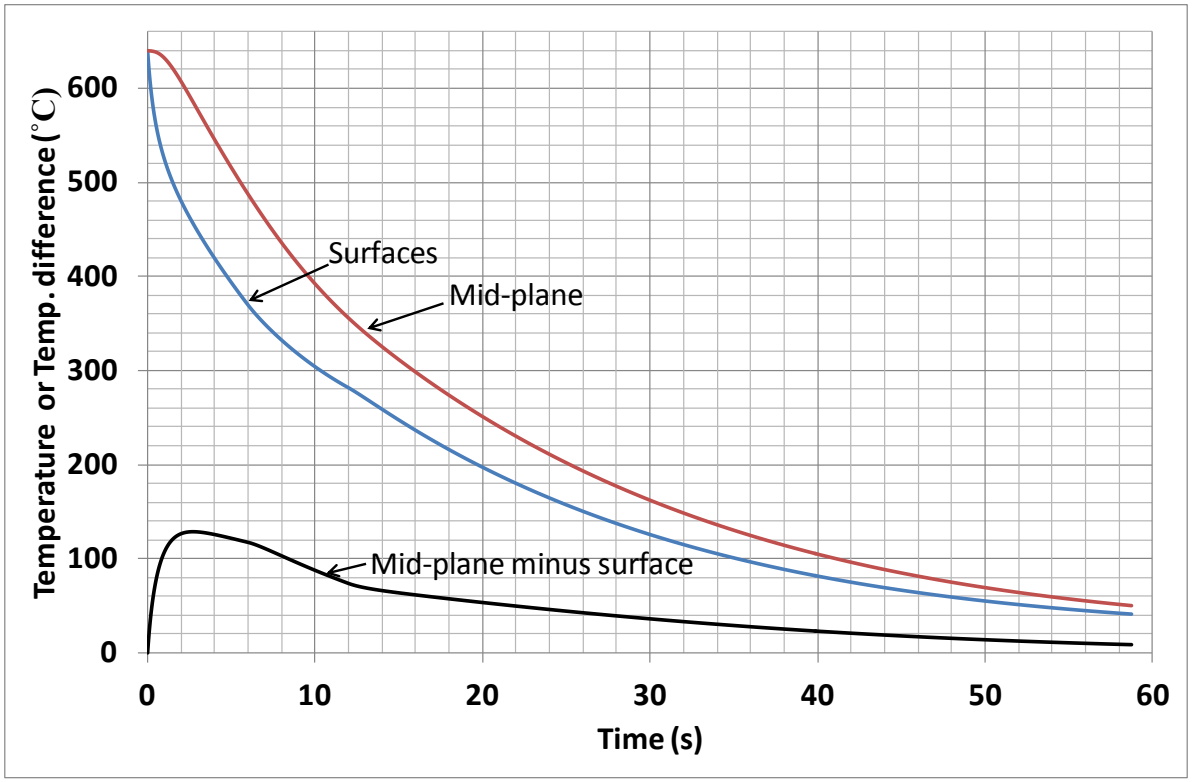

Figure 14.7 Development of glass temperature in tempering cooling. Clear glass thickness is 4 mm.

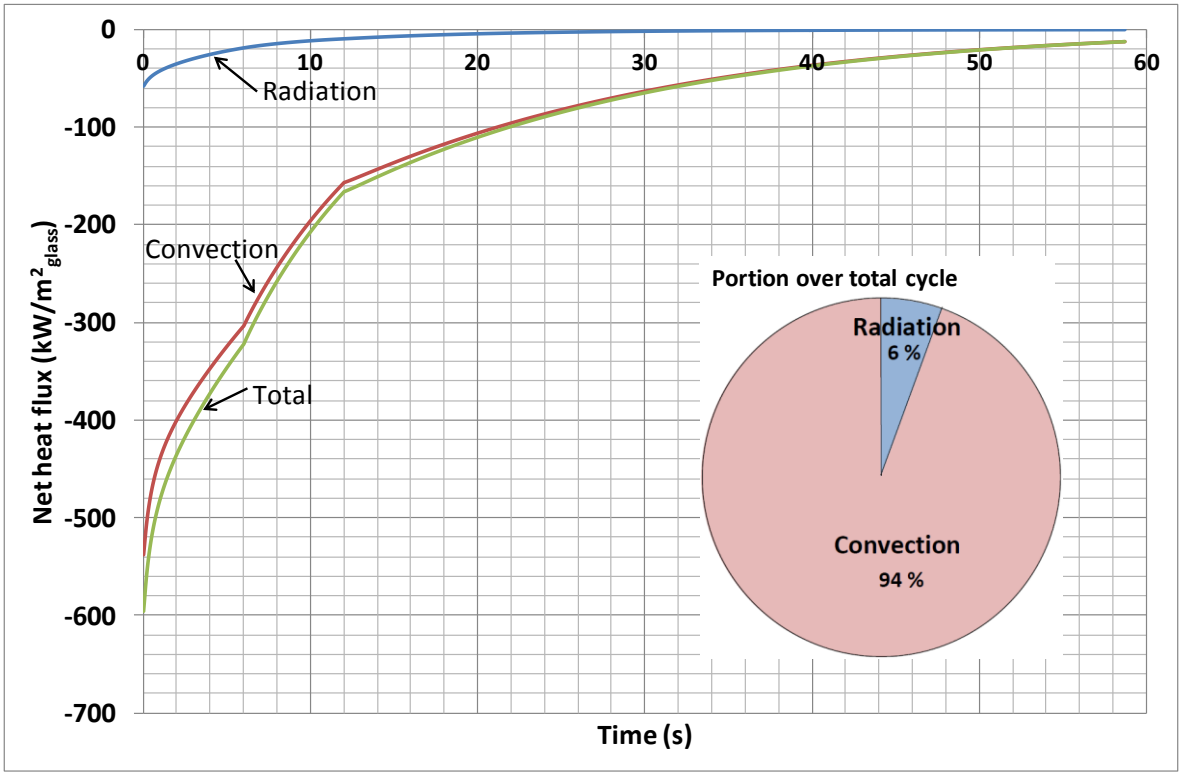

Figure 14.8 Heat fluxes by different modes away from glass during tempering cooling. Clear glass thickness is 4 mm.

In tempering cooling of 4 mm glass forced convection is strong and radiation stays small. At the beginning of tempering cooling in Figure 14.8 the portion of convection is 90 %. The portions of different heat transfer modes over total cycle are radiation 6% and convection 94%.

As a result of the process above glass surface gets about 110 MPa residual surface compressive stress and the mid-plane 50 MPa residual tensile stress.

14.5 Low-emissivity glass in tempering furnace

Figure 14.9 shows the development of clear and low-e coated glass temperature profiles in a radiation furnace without forced convection. Furnace temperature is 700°C and the incident radiation to glass surface is the same on both sides. Even then the temperature profile of clear glass is asymmetrical, because contact heat transfer occurs on the bottom surface and natural convection is stronger on the bottom surface than the top surface.

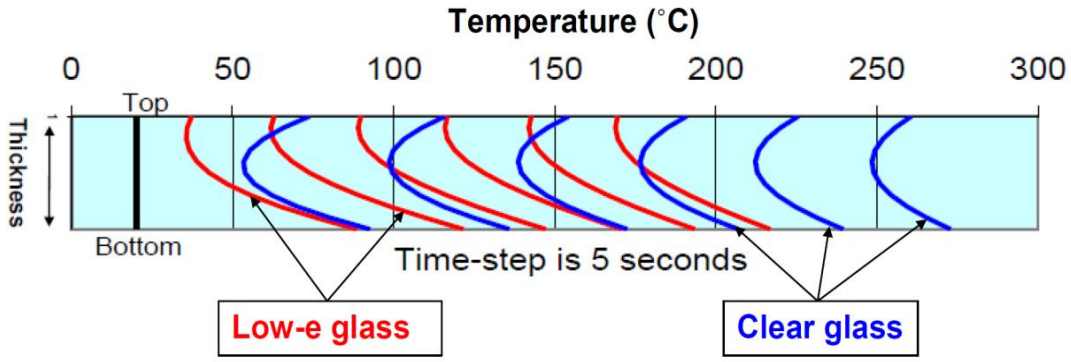

Figure 14.9 Development of thickness-wise temperature profiles in clear and low-e coated glass in radiation furnace without forced convection. Glass thickness is 4 mm.

In Figure 14.9 at least the temperature profile of low-e glass is so asymmetric that glass would bend clearly as convex in relation to rollers during heating. Low-emissivity coated glass reflects radiation strongly with its top surface in tempering furnace. Thus, it needs a different heating recipe to clear glass; forced convection on the glass top surface must be intensified.

14.6 Effect of contact heat transfer to glass temperature in tempering furnace

Figure 14.10 shows the effect of effective contact heat transfer coefficient defined in Chap. 13 on the temperature difference between glass bottom and top surface in a tempering furnace. In the furnace only radiation and natural convection occurs in addition to contact heat transfer. Most probably the actual value for the effective contact heat transfer coefficient of glass on the top of ceramic rollers is below 3.0 W/(mK), because at higher values the temperature difference at the early stages of heating is unbelievable high. In calculations glass also heats up to the tempering temperature clearly faster as in practice if the effective contact heat transfer coefficient is higher than the value above. In Figure 14.10 the temperature difference occurs even without contact heat transfer, because natural convection is stronger on the bottom surface than the top surface.

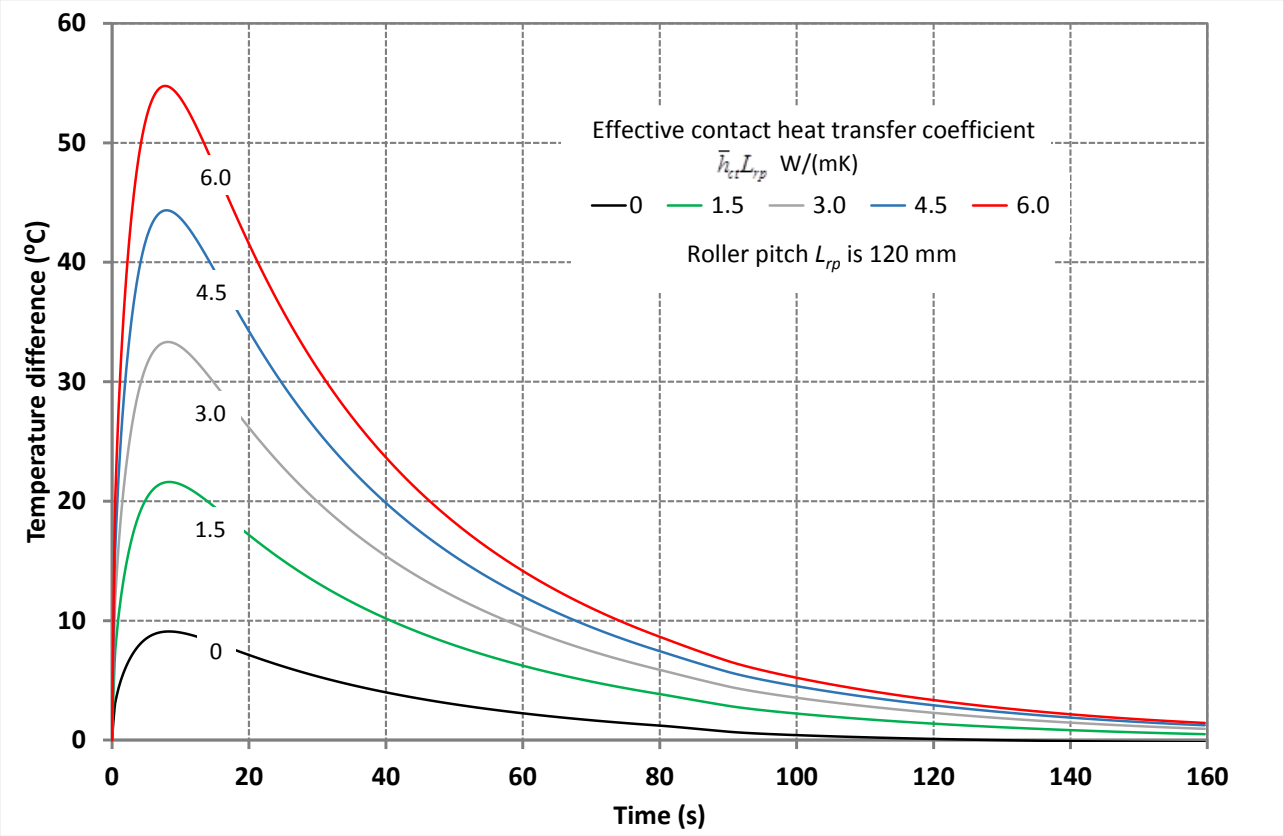

Figure 14.10 Temperature difference between glass bottom and top surface in tempering furnace as a function of effective contact heat transfer coefficient between glass and rollers.

15. HEAT TRANSFER IN HEAT SOAK FURNACE

Nickel sulfide (NiS), the origin of which is from the float glass manufacturing process, causes spontaneous breaking of tempered glass plates [97]. A heat soak test is developed to prevent the problem. The goal of the process is to break tempered glasses which contain NiS-stone before they are installed in buildings. In line with the European standard EN 14179-1 [98], a sufficient heat soak test is carried out when glasses are kept two hours at 280 to 300°C.

A typical heat-soak furnace is a huge circulation air oven, where tempered glasses are placed vertically on a glass rack in such a way that they are separated from each other. The free space *2H*, i.e., the width of the channel between glasses, is about 20 mm.

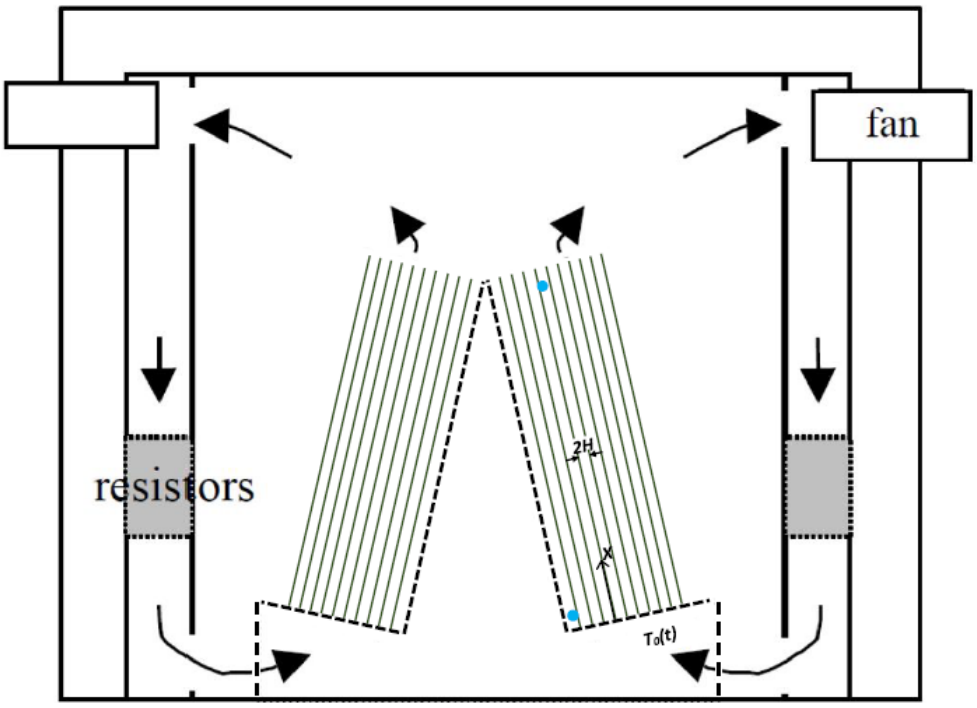

Figure 15.1. Cross-section of heat soak furnace.

The schematic of the heat soak furnace is shown in Figure 15.1. In the heat-soak furnace above, the air intakes of the fans are near the roof and delivery outlets near the floor. Air heating resistors are located in a flow channel between them.

During heating hot air flows in channels between glass plates and transfers heat to glass. The flow may be laminar or turbulent. The theory of steady-state forced convection is extensively presented in [99]. Also exact analytical solutions for a turbulent tube flow are available in the literature for time-dendent cases [100][101]. In the case of a laminar flow, different types of solutions are also presented in the literature [102]. Next, the methods for solving time-dependent heat transfer problems in a turbulent or laminar channel flow are presented and applied to a heat soak furnace.

15.1 Description of heat transfer problem

Figure 15.2 shows the schematic of the heat transfer situation in a channel between glass plates. Hot air flows into a channel and creates convection. Heat is transferred from the air to the surface of the glass, from which heat conducts deeper into the glass. The situation in the channels is symmetrical when glasses next to each other are similar. Thus, there is no heat transfer through the glass mid-plane and only a half thickness of glass and channel are needed in the analysis. Thermal radiation can be ignored because the net radiation between glasses is zero. When the heating speed of glass is slow, as in a typical heat soak process, the temperature of the glass in the thickness direction is almost uniform. Also, the conduction in axial direction is insignificant.

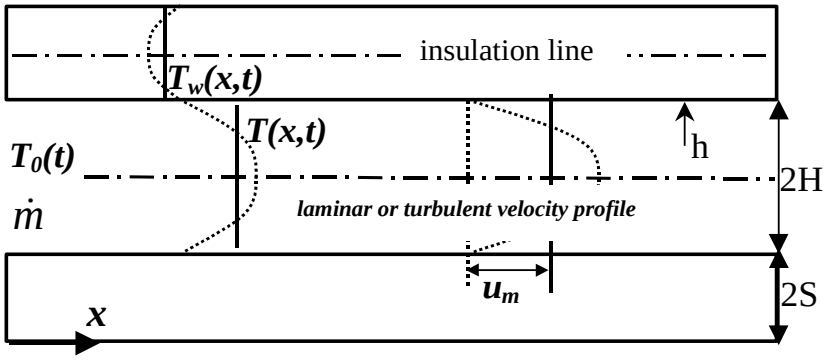

Figure 15.2. Time-dependent heat transfer in channel between glasses.

Initially air and glass are at room temperature T_∞. When the heating starts, the air temperature undergoes a step change to a new value T_0. The problem is to find glass and air temperatures, which depend on the stream-wise coordinate x and time t. Energy equations of air and glass are written as

$$\frac{\partial T}{\partial t} = -u_m \frac{\partial T}{\partial x} - \frac{u_m}{\dot{m} c_p} h\left(T - T_w\right) \tag{15.1}$$

$$\frac{\partial T_w}{\partial t} = \frac{h\left(T - T_w\right)}{\rho_w c_{pw} S} \tag{15.2}$$

where T and T_w are the mean temperatures of air and glass.

In Eq. (15.1) $\dot{m} = u_{m0}\rho_0 H$ is the mass flow of air in half-width H of the channel and u_{m0} is the mean air velocity at the channel inlet. The air density ρ_0 at the inlet depends on the air temperature $T_0(t)$ according to the ideal gas equation.

The convection heat transfer coefficient h is defined between the local wall temperature T_w and the local mean temperature of air T. The heat transfer coefficient depends primarily on the flow, which can be turbulent or laminar. There is no exact point where the flow changes from laminar to turbulent. For Reynolds numbers, $Re = u_m \rho d_h / \mu$, below 2000, the flow can usually be assumed to be laminar. In the previous sentence d_h is the hydraulic diameter and μ is the dynamic viscosity.

15.1.1 Turbulent flow in channels

For a fully developed turbulent flow, keeping h as a constant, Eqs. (15.1) and (15.2) can be solved analytically for the step change of air temperature. The solutions of them with boundary and initial conditions $T(0, t) = T_0$, $T(x,0) = T_w(x,0) = T_\infty$ are [100][101]

$$\vartheta = \frac{T - T_\infty}{T_0 - T_\infty} = e^{-\xi}\left[e^{-\eta} I_0\left(2\sqrt{\xi\eta}\right) + \int_0^\eta e^{-x} I_0\left(2\sqrt{\xi x}\right) dx \right] \tag{15.3}$$

$$\theta = \frac{T_w - T_\infty}{T_0 - T_\infty} = e^{-\xi}\left[e^{-\eta} \sqrt{\eta/\xi} I_1\left(2\sqrt{\xi\eta}\right) + 1/\sqrt{\xi} \int_0^\eta e^{-x} \sqrt{x} I_1\left(2\sqrt{\xi x}\right) dx \right] \tag{15.4}$$

In the equations above, I_0 and I_1 are modified Bessel functions. Variables $\eta = ht/(\rho c_p S)$ and $\xi = hx/(\dot{m} c_p)$ are non-dimensional time and distance, respectively. The solution above is valid with the following simplifying assumptions: wall temperature is uniform in the thickness direction and there is no conduction in the flow direction. On the basis of analytical solutions it has been observed that the time derivate of air temperature in Eq. (15.1) can be ignored when we are dealing with a heat soak furnace. In that case the equations can be solved quite easily also numerically using a finite difference method. In the method, the geometry is divided into control volumes Δx and computing proceeds with time intervals Δt. The computing proceeds as follows: At first, when T and T_w are known, at instant t a new temperature of air is obtained from

$$T(x,t) = T_0(t) - \int_0^x \frac{h\left[T(x,t) - T_w(x,t)\right]}{\dot{m} c_p} dx \tag{15.5}$$

After that a new glass temperature at instant $t+\Delta t$ is calculated from

$$T_w(x, t+\Delta t) = T_w(x,t) + \frac{h\left[T(x,t) - T_w(x,t)\right]}{\rho_w c_{pw} S} \Delta t \tag{15.6}$$

The results of the numerical solutions above were compared with the results of analytical solutions Eqs. (15.3) and (15.4) presented in [101], and they agreed. In Figure 15.3 and Figure 15.4, non-dimensional air and glass temperatures are shown for the step change of air temperature.

There are many heat transfer correlations in the literature for a fully developed pipe flow. The equation of Gnielinski

$$Nu = \frac{hd}{k} = \frac{\left(\mathrm{Re} - 1000\right)\mathrm{Pr}\, c_f/2}{1 + 12.7\sqrt{c_f/2}\left(\mathrm{Pr}^{2/3} - 1\right)} \tag{15.7}$$

in which c_f is a friction factor, correlates with the available data quite well over the range of Prandtl numbers from 0.5 to 2000 and Reynolds numbers from 2300 to 5×10^6 in a tube [99][103]. There are also many correlations for the friction factor c_f. For example, $c_f/2 = 0.039 Re^{-0.25}$ is valid for small Reynolds numbers. When a fully developed turbulent flow in other channel shape is is consired, the pipe diameter d is replaced by a hydraulic diameter $d_h = 4A_c/P$. In a heat soak furnace where the flow is between parallel plates $d_h = 4H$ and $Re = 4\dot{m}/\mu$.

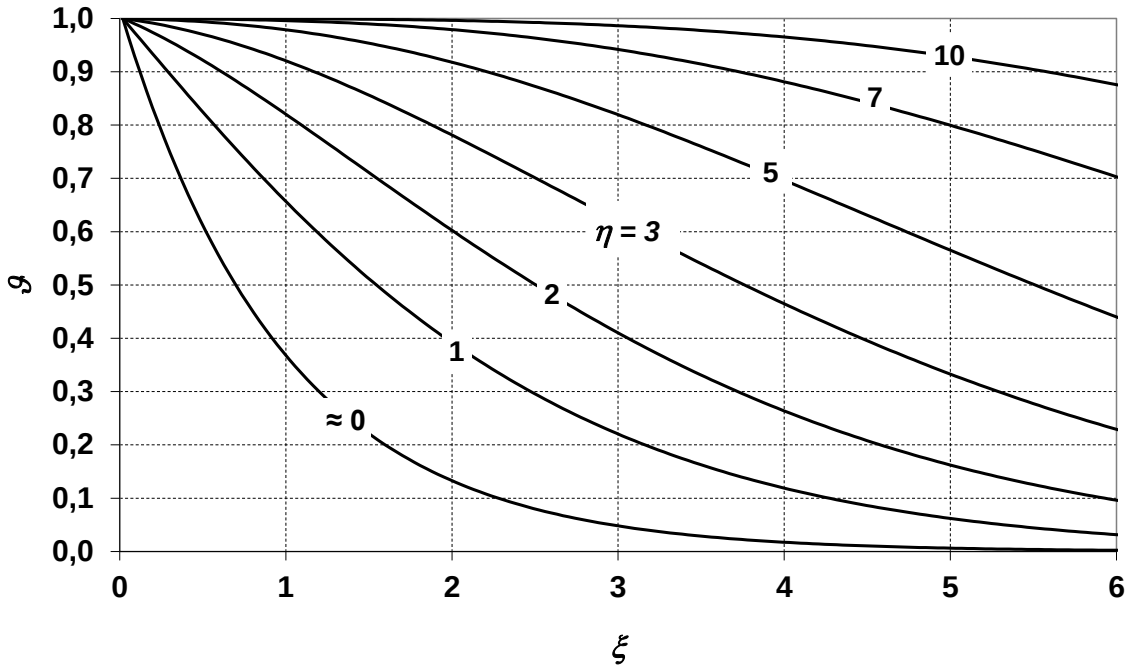

Figure 15.3. Non-dimensional air temperature ϑ in turbulent channel flow.

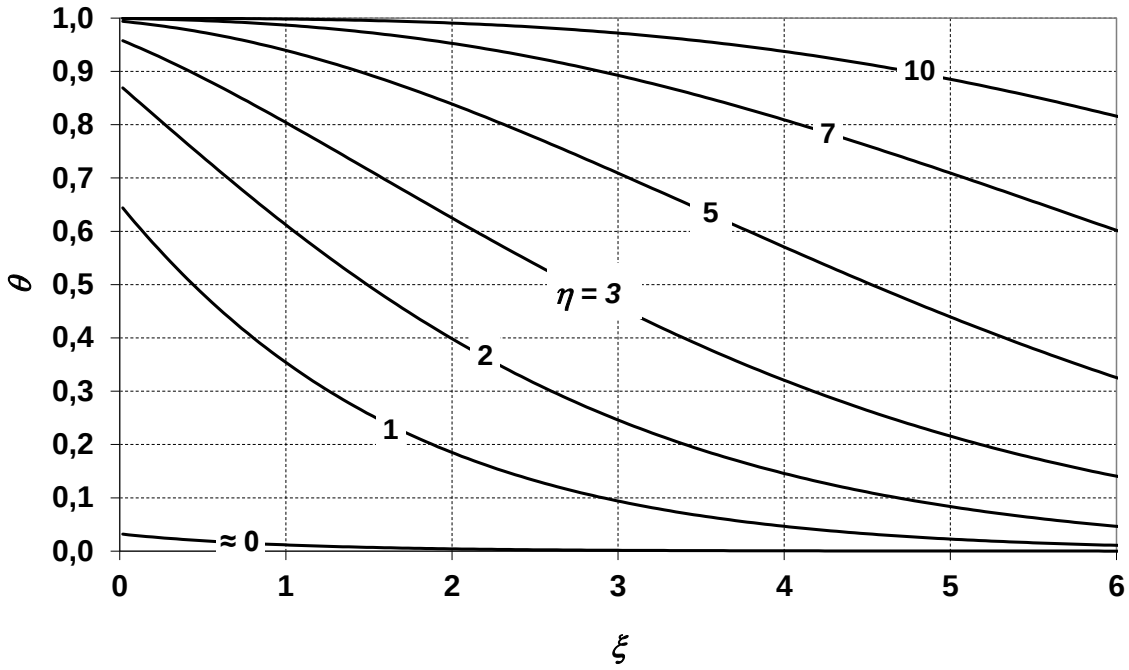

Figure 15.4. Non-dimensional glass temperature θ in turbulent channel flow.

In a heat soak furnace, velocity and temperature profiles start to develop simultaneously from the channel inlet, and when $x < 10d_h$, the heat transfer coefficient is greater than in a fully developed case. However, its effect on the overall heat transfer is small [104].

The advantage of the finite difference method described above is that the change of air and glass properties with temperature can easily be taken into account. New material properties are computed from the polynomial fit functions as a function of temperature after each time-step. Also, the variation in the heat transfer coefficient h in the entrance region is easy to consider. However, the most valuable

advantage is that the variation of the inlet gas temperature T_0 during heating can be taken into account. Also, heat conduction in a glass can be quite easily included to the modelling.

15.1.2 Laminar flow in channels

Turbulent flows can often be solved by neglecting the coupling of fluid and wall temperatures, because the effect of stream-wise temperature variation on the heat transfer coefficient is very small. In the case of a laminar flow, the thermal history effect on h is significant. This means that similar analytical solutions to Eqs. (15.3) and (15.4) for a turbulent flow cannot be found. Transient wall and fluid temperatures in a laminar channel flow can be solved with the so-called quasi-static method. Using this method, the equations for glass and air temperature for a fully developed laminar velocity profile are [105]

$$\rho_w c_{pw} S \frac{\partial T_w}{\partial t} = -\frac{k}{H} \int_0^{x^*} \sum_{n=0}^{\infty} G_n e^{-\lambda_n^2 \left(x^* - \xi\right)} dT_w(\xi) \tag{15.8}$$

$$T\left(x^*, t\right) = T_0 + \frac{1}{\rho c_p u_m H} \int_0^{x^*} q(\xi, t) d\xi \tag{15.9}$$

for which the eigenfunctions G_n and eigenvalues λ_n can be found in the literature [99][102] and are given in Table 15.1. Note that dummy non-dimensional distance ξ in Eqs. (15.8) and (15.9) is different to that in Eqs. (15.3) and (15.4). Above non-dimensional distance of channel $x^* = kx/(\rho c_p H^2 u_m)$.

Table 15.1. Eigenfunctions G_n and eigenvalues λ_n for parallel plates according to [99].

n	λ_n^2	G_n
0	15.09	1.717
1	171.3	1.139
2	498	0.952
n	$\lambda_n=(16n+20/3)\times(1/3)^{0.5}$	$G_n=2.68\lambda_n^{-1/3}$

The right-hand side of Eq. (15.8) presents convective heat transfer for a fully developed temperature and velocity profile. In the entrance region heat transfer is more effective if velocity and temperature profiles develop simultaneously, as in a heat soak furnace. However, the effect of simultaneously developing profiles is still quite small for air when the very first decimeters from channel inlet are ignored [106].

When the wall temperature is approximated by a series of constant temperature steps, the integral of Eq. (15.8) to the point $x^* = j\Delta x^*$ can be written as

$$\int_0^{x^*} \sum_{n=0}^{\infty} G_n e^{-\lambda_n^2 \left(x^* - \xi\right)} dT_w(\xi) = \Delta T_0 \sum_{n=0}^{\infty} G_n e^{-j\Delta x^* \lambda_n^2} + \sum_{i=2}^{j} \left[T_w\left(i\Delta x^*\right) - T_w\left((i-1)\Delta x^*\right)\right] \sum_{n=0}^{\infty} G_n e^{-(j-i+1)\Delta x^* \lambda_n^2} \tag{15.10}$$

where Δx^* is the length of each step. In the solving procedure it is assumed that wall temperature is constant during a small time-step Δt. After that a new glass temperature at the instant $t+\Delta t$ is calculated from

$$T_w\left(x^*, t+\Delta t\right) = T_w\left(x^*, t\right) + \frac{q\left(x^*, t\right)}{\rho_w c_{pw} S}\Delta t \tag{15.11}$$

where $q(x^*,t)$ is the right hand side of Eq. (15.8). For a laminar flow there is no universally applicable way to introduce results for a step change in air temperature non-dimensionally. It is worth mentioning that the non-dimensional way used in [105] for water flow is not applicable for air flow, when the heat capacity of the air flow is much smaller than the heat capacity of the wall.

15.2 Measured data

In the European standard the detailed calibration criteria for the heat soak test furnace are presented. Glasses should be heated up to 280 - 300°C and kept at least 2 hours at that temperature. The holding time starts when every measuring point in the glass has reached the temperature of 280°C. Temperatures should be measured from the inner, middle, and outer glasses and on both sides of a double-sided rack when the furnace operation is tested. Measuring points are in the corners of the outer glasses, in the centre, near side, top and bottom edges of the middle glasses, and near the top and bottom edges of the inner glasses. The detailed locations of thermocouples are defined in the standard. Figure 15.5 shows the measured data of the calibration test described above.

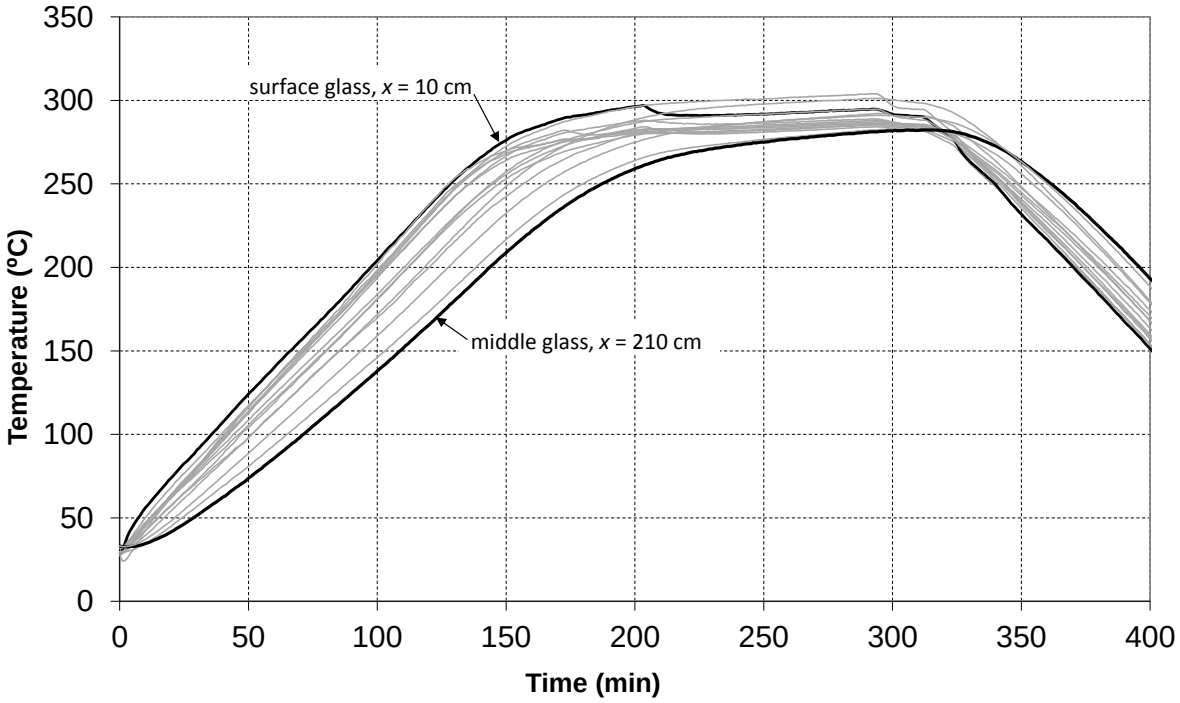

Figure 15.5. Measured glass temperatures in heat soak furnace.

In the measurements, ten glasses were located on both sides of the rack in Figure 15.1. The glass thickness was 6 mm and the length was 2.2 m in a direction of the flow (x). The loading was almost full in the length-wise direction of the furnace. In the measured data the slowest measuring point reaches 280°C 127 minutes later than the fastest measuring point, and the holding time of the slowest measuring point is only 46 minutes. The slowest, i.e., the lowest line in heating phase in Figure 15.5 is measured from the tail (top) edge of the middle glass at x = 210 cm (upper dot in Figure 15.1). In the next sections this point is taken into closer examination. The fastest measuring point was on the outer surface of the inner surface glass at x = 10 cm (lower dot in Figure 15.1). The air temperature

at the middle channel inlet during the heating phase of a full loading was also measured with the result $T_0 = [40+1.7t]$°C ($T_0 \leq 290$°C and t in minutes).

15.3 Comparison between measurements and calculations

The mean velocity of air at the channel inlet is an important factor when the heat transfer in a heat soak furnace is modelled. Measurements with a vane anemometer at room temperature showed a velocity 1.37 m/s. This means that the flow was most likely turbulent, because $Re \approx 4000$. The decrease in air density with rising temperature changes the operating point of fans. Velocity remains approximately constant, which means that the mass flow and Re decrease. The flow can change from turbulent to laminar at some point during the heating. Unfortunately, it is not possible to find out the flow model inside a hot furnace. This leads to an extra problem, when glass temperatures in the heat soak furnace are solved theoretically.

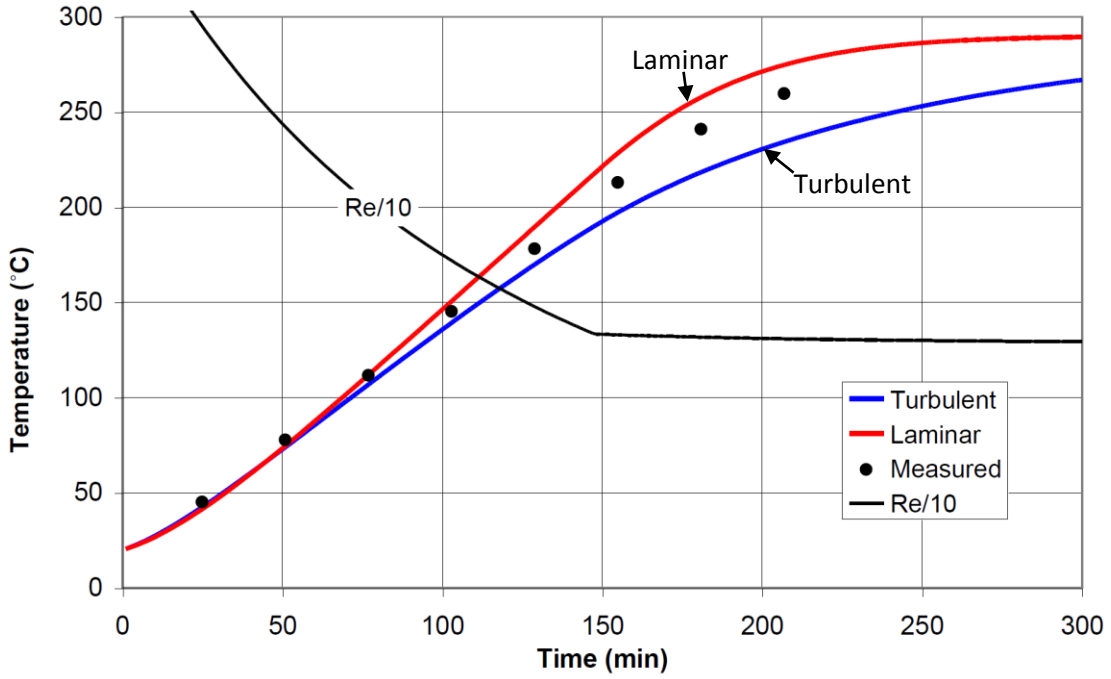

Figure 15.6. Reynolds number, measured and calculated temperatures of the tail edge (x = 210 cm) of the middle glass.

The lines in Figure 15.6 show calculated temperatures from the tail edge of the middle glass. The dots are the measured results. The lower line in Figure 15.6 is theoretically predicted for a turbulent flow using the finite difference method and the upper line is theoretically predicted for a laminar flow using the quasi-static method. In both methods the change in material properties with temperature was taken into account and the measured air temperature given in Sec.15.2 at channel inlet was used.

From the beginning to 75 minutes and at Reynolds numbers from 4000 to 2000 both methods produce almost the same results, which are in good agreement with the measured data. The laminar method is in better agreement with the measured values when $Re < 2000$. The turbulent method under-predicts glass temperature, which is expected because of the form and coverage area of Eq. (15.7)

The same heating situation was also modelled numerically, when heat conduction in glass in the length and thickness direction was included. The effect of length-wise conduction was practically negligible even in the entrance region, where the length-wise temperature gradients in glass are strongest. The conduction in the thickness direction of the glass can also be ignored.

15.4 Extended method for furnace designer

Despite the extensive work done here so far, it is still not much help for a furnace designer or operator. For that reason an extended solution method for heat transfer in a heat soak furnace is needed. In actual practice, the variation in T_0 depends on the heating power and the mass of glass in the furnace. As a matter of fact, a glass pile is like a plate heat exchanger, which cools down the air. Similarly, heating resistors heat up the air. Also the heat capacity of a glass rack and the furnace walls must be considered when the problem is solved.

The energy equation of air at a channel inlet is

$$m_i c_{pi} \frac{dT_0}{dt} = Q_r - \frac{dE_{tot}}{dt} - Q_L(t) \tag{15.12}$$

which yields to air temperature at a channel inlet at instant $t+\Delta t$

$$T_0(t+\Delta t) = T_0(t) + \frac{\left[Q_r \Delta t - E_{tot}(t) - Q_L(t)\Delta t\right]}{m_i c_{pi}} \tag{15.13}$$

where m_i is the total mass of the air inside the furnace and Q_r is the heating power of resistors. Heat losses through furnace can be approximated as $Q_L(t) = U_{fw}[T_0(t)-T_\infty]A_{fw}$, where U_{fw} is the heat transmission value trough the furnace walls, A_{fw} is the area of furnace walls, and T_∞ is the ambient temperature. Term $E_{tot}(t)$ is the total sum of the change in energy contents of all glasses, furnace walls and glass racks during the last time step. This leads to the problem that also the mean temperature of furnace inside walls and structures T_w must be solved.

The energy equation of furnace inside walls and glass racks is

$$m_w c_{pw} \frac{dT_w}{dt} = h_w\left[T_0(t) - T_w(t)\right]A_w - Q_L(t) \tag{15.14}$$

from which the mean temperature of furnace walls and glass racks at instant $t+\Delta t$

$$T_w(t+\Delta t) = T_w(t) + \frac{\Delta t}{m_w c_{pw}}\left\{h_w\left[T_0(t) - T_w(t)\right]A_w - Q_L(t)\right\} \tag{15.15}$$

In Eq. (15.15) m_w is the total mass and A_w is the total area of steel inside (walls, glass racks) a furnace. It is important to keep in mind that the furnace is treated as infinite in a length-wise direction. Thus, the values for masses, areas, mass flow, heating power and energy content are defined per unit of length of the furnace. The mean heat transfer coefficient h_w for the furnace walls in Eq. (15.15) is very difficult to define exactly, but sufficient estimates for it can rather easily be found. In the estimation method used the walls were divided into two groups, and then heat transfer coefficients (h_{w1}, h_{w2}) were solved for both of them. The correlation in Figure 15.7 written for the turbulent flow and free boundary layer at plate surface is rather suitable for the case. Now the furnace height was used as a dimension (x) in the correlation and velocities needed in Re_x were solved from the total volume flow and furnaces dimensions. Finally, h_w was solved as Figure 15.7 describes.

When the results of the extended method which main features are given above were compared with measured air and glass temperatures, a good correspondence was found.

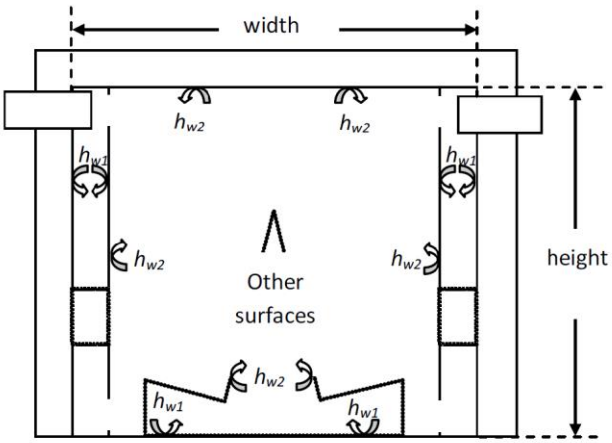

Turbulent flow at plate surface,
average *Nu* between 0 and x.

$$\overline{Nu}_x = \frac{hx}{k} = 0.036\,\mathrm{Pr}^{1/3}\left(\mathrm{Re}_x^{4/5} - 18700\right)$$

$$h_w = \frac{h_{w1}(4height + width) + h_{w2}(2height + width + othersur.)}{6height + 2width + othersur.}$$

Figure 15.7. Estimation method for mean heat transfer coefficient h_w.

15.4.1 Effect of different factors on heating speed

In this section the effect of different factors to heat transfer in a heat soak furnace is discussed. The basic situation is the same as in the measurements in Figure 15.5 and only one factor is changed at a time. The initial temperature is 20°C and the heating time ends when the glass temperature at x = 210 cm reaches the temperature of 280°C. The solution method changes from turbulent to laminar automatically, when *Re* is smaller than 3000.

When the operation of a heat soak furnace is optimized, the most interesting detail is the width of the channel between the glass plates. As seen in Figure 15.8, when the channel width is doubled from 22 to 44 mm, the heating speed remains almost the same, but when the channel width is decreased from 22 to 5.5 mm, the heating speed drops dramatically. This effect is based on the small heat capacity of air in a channel. In other words, the air temperature at the end of a narrow channel is almost as cold as the glass, which leads to weak heat transfer. In actual practice, the effect of the decreasing channel width on the glass temperature is even higher as in the results above, because the bypass flow via free space outside of the glass loading increases when the channel is narrow. Due to the increasing bypass flow, the velocity in channels between glasses decreases with the channel width, which leads to weaker heat transfer, as shown in Figure 15.10.

The effect of glass thickness on the heating speed is shown in Figure 15.9. The total mass of the glass inside the furnace is the same in all cases, i.e., 20 sheets of 6 mm glass, 10 sheets of 12 mm glass, and so on. The heating time increases clearly, when the glass is thicker. This effect is partly based on the small heat capacity of air flow in a channel. The heat transfer area of the glass pile decreases also when the glass thickness increases. This reduces heat transfer from air to glass load. It also reduces the heat transfer from resistors to air, because the air temperature reaches the set temperature sooner and due to that resistors are turned first time off sooner.

The effect of air velocity in a channel on heating speed is shown in Figure 15.10. At the velocity of 5.47 m/s the flow is totally turbulent and at the velocity of 0.68 m/s laminar. The heating time decreases with increasing velocity. The flow velocity in a channel can be boosted for example by selecting bigger fans when the furnace is designed. In Figure 15.10 the time saving due to the velocity increase is limited, because of the constant power of air heating resistors. The heating time can also be reduced by using more powerful air heating resistors or by raising the set value of air temperature.

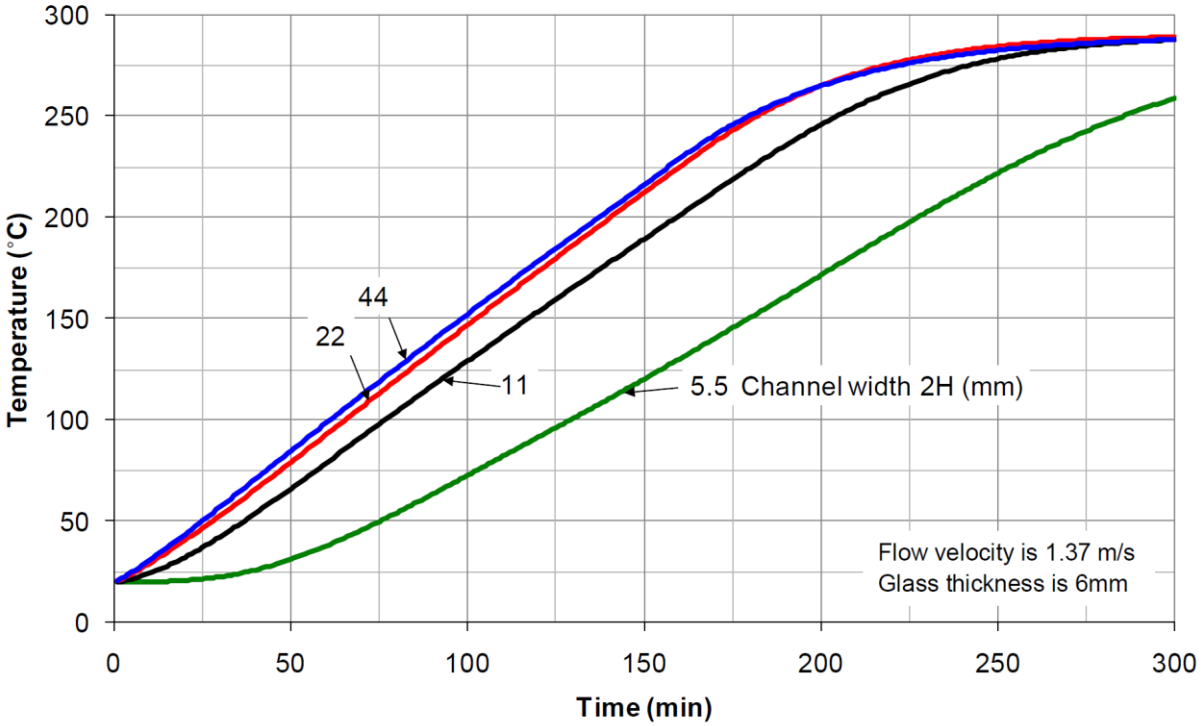

Figure 15.8. Effect of channel width on glass temperature at x = 210 cm.

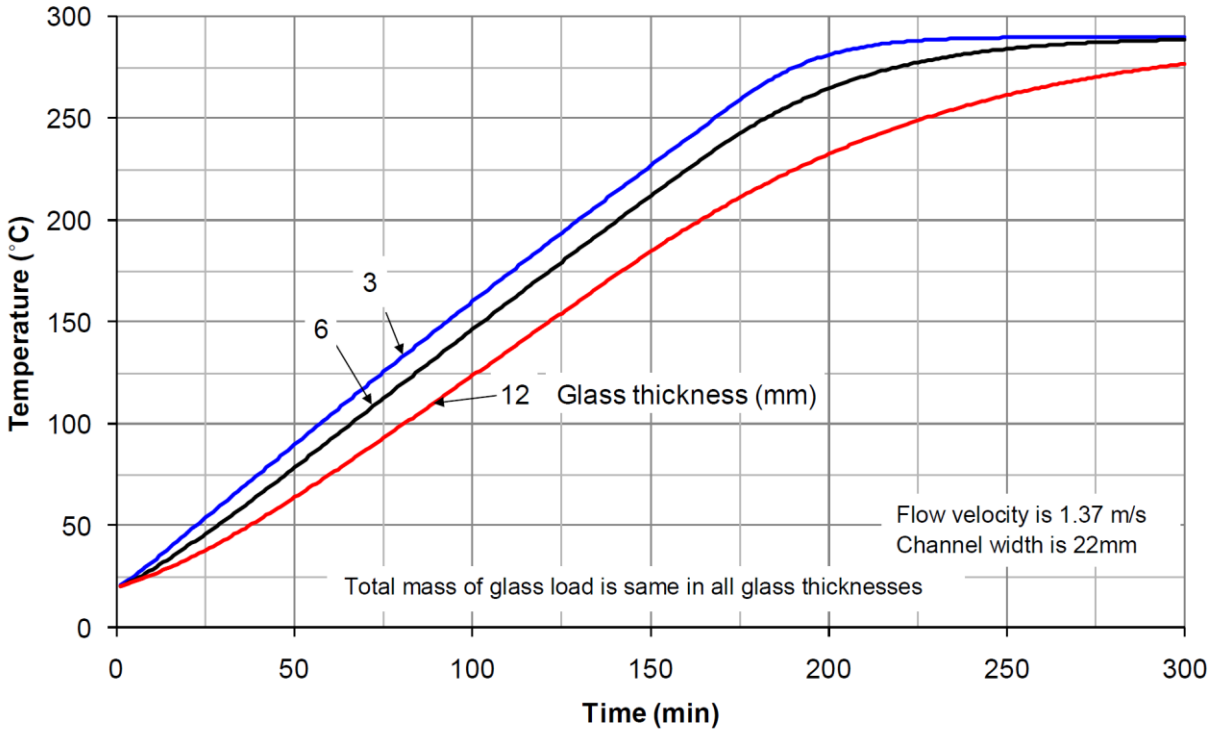

Figure 15.9. Effect of glass thickness on glass temperature at x = 210 cm.

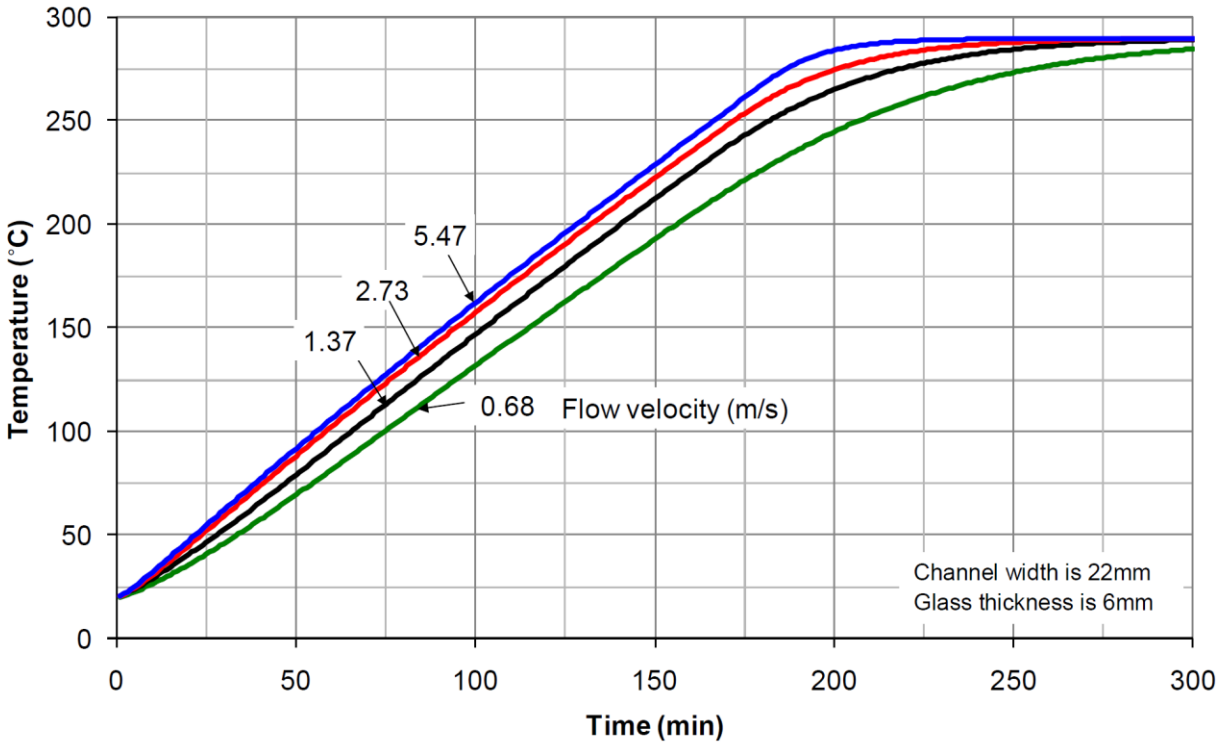

Figure 15.10. Effect of flow velocity on glass temperature at x = 210 cm.

16. CONCLUSIONS

16.1 Radiation heat transfer in glass

The radiative properties needed to solve radiation heat transfer in glass are absorption coefficient and glass surface reflectivity, which both depend on the wavelength of incident radiation. Reflectivity is also dependent on the angle of incidence of radiation. Soda-lime glass is opaque for thermal radiation when the wavelength is over 4.5 μm, whereas for wavelengths below 2.75 μm glass is transparent. At wavelengths between 2.75 to 4.5 μm glass has a relatively high absorption coefficient and the band can be called semi-transparent. Thus, in the simplest method only three different absorption coefficients are needed. The reflectivity of clear glass surface can be assumed as wavelength independent at wavelengths of 0.3 to 6 μm. Reflectivities and absorption coefficients can be assumed to be independent of temperature at the temperature range from 20 to 700ºC, which makes the hemispherical total absorptance of glass also independent of temperature. Hemispherical total emittance of glass decreases or increases with increasing temperature depending on glass temperature and thickness. Thin and thick glasses have the same hemispherical total emittance at room temperature, but at higher temperatures emittance increases with the glass thickness.

Low-e coating changes glass surface reflectivity selectively. For visible light, reflectivity remains almost constant, but at slightly longer wavelengths reflectivity sharply increases to 0.8 - 0.97 depending on the coating. The reflectivity of a low-e coating is dependent on temperature, and reflectivity is also a little different for radiation hitting the coating from the air side rather than the glass side. The coating itself also absorbs radiation and its absorptivity is dependent on temperature. Normal total emittance of low-e coated glass increases with increasing temperature, because the emissivity of the coating increases. The thickness dependence of the emittance of a low-e coated glass increases with temperature, but remains still relatively low at 600ºC. Glass with a low-e coated back surface has a higher normal total emittance than clear glass and the emittance difference increases with temperature and decreasing glass thickness.

With the Averaged Net Radiation (ANR) method developed in the thesis the radiation heat transfer between glass and diffuse surroundings can be solved in glass tempering, bending and laminating processes, where the glass temperature is below 700°C. In the method the net radiation between glass volume elements is ignored and the integration over the polar angle is eliminated by using the mean reflectivity of glass surface and the mean propagation angle at which diffuse radiation travels in glass, which differs from the methods presented in the literature. The ANR-method gives the same results as other methods with more sophisticated models. In the simplest version of ANR-method only the first internal reflection from glass-air interface is considered. Even then the accuracy of the method remains at a high level. For a low-e coated glass equivalent accuracy demands the considering of the first three internal reflections.

A coating on the glass surface changes the modelling of radiation heat transfer in a glass much more complex. In the thesis the ANR-method is adapted also as applicable to coated glass. This is done by dividing the spectrum into such wavelength bands with the help of which the spectral properties of both glass and coating can be taken into account. In addition to that, an extra part is added to the radiation source term of a glass surface layer to take absorption into a coating into account. The absorption of the coating is considered also on the glass surface transmissivity. For instance, the following simplifications can be considered when radiation heat transfer in coated glass plate is solved: the temperature dependence of the radiative properties of the coating is ignored or considered by using mean values over the temperature increase in question, only the first one of the internal reflections is taken into account, the reflectivity and absorptivity of the radiation coming from the air and glass side are assumed to be the same.

16.2 Heat transfer of impinging jet and jet array

High overpressure (1 to 6 bar), small nozzle diameter (1 to 2 mm), long nozzle-to-surface distance (100 to 300 mm) and sparse nozzle-to-nozzle division are typical for jet arrays in tempering furnaces where radiation is clearly the main form of heat transfer. The correlations reported in the literature for impinging jet heat transfer are not valid for such a case. In the thesis the heat transfer of various air jets with a constant heat flux boundary condition was experimentally solved. With long nozzle-to-surface distances and overcritical pressures, the relation between absolute pressure and local heat transfer coefficient was $h(r) \propto (p_1/p_\infty)^{0.52}$. The effect of nozzle to plate distance on local heat transfer was high near the stagnation point, but it ended when the radial distance from the stagnation point was over 100 mm. The measured relation between the nozzle diameter and local heat transfer coefficient was $h(r) \propto D^b$, where $b = 0.75 \ldots 0.85$ at $H = 250$ mm, $1 \ldots 1.5$ at $H = 150$ mm and b increases with the decreasing distance from stagnation point.

The momentum of a discharging jet is much more illustrative than the Reynolds number which is commonly used in literature correlations. According to the experiments in the thesis the momentum of a jet can quite accurately be defined by the force that the jet causes to the disc of a weighing machine.

In the experiments in the thesis the nozzle diameter and the overpressure were changed, but the momentum was kept constant. It was observed that equal momentums produced equal convection when nozzle-to-plate distance was constant. The correlations found from the literature for the convection under an impinging jet yielded the same conclusion.

The experimental correlations presented in the literature for a single impinging jet do not agree with each other satisfactorily in the stagnation zone, but the agreement in the wall jet region is quite satisfactory. The discrepancies between experimental correlations are partly caused by different nozzle diameters D and nozzle-to-surface distances H used in experiments, though the ratio of H/D has remained the same. It is much more reliable and practical to compare the heat transfer coefficients than the Nusselt numbers, because Nu depends on the nozzle diameter. Thus, even if the heat transfer coefficients are the same Nu is different, if the nozzle diameter is not constant.

In the experiments in which nozzle-to-plate distance was constant and nozzle diameter - overpressure combination changed, the mean heat transfer coefficient of a jet array was almost the same, when the same fan power was used to create air jets. In the measurements the effect of the combination on heat transfer coefficient was a little higher than Martin's correlation predicts. Measured heat transfer coefficients were from 11 to 20% higher than those obtained from the Martin's correlation and the changing of the overpressure changed the measured heat transfer coefficients in the same relation as it changed the predicted ones.

On the basis of thesis Martin's correlation, i.e., Eq (12.16), inside its validity ranges is useful for solving the mean heat transfer coefficients of a jet array in the glass tempering process. It does not give an absolutely correct heat transfer coefficient, but it predicts very accurately how the heat transfer coefficient relatively changes as a function of nozzle diameter and overpressure in the nozzle box.

16.3 Contact heat transfer between glass and rollers

Contact heat transfer between surfaces can be divided in three parts: gas-gap conductance, solid spot conductance and radiation. In a glass tempering furnace the contact is between glass and ceramic rollers. The heat transfer on the contact area is solid spot conduction between the roller and glass. Outside of the contact area the gas gap conductance has an effect. Radiation heat transfer between the glass and roller at and near the contact area is not an important factor in contact heat transfer, because it has no extra effect on the radiation heat transfer in a tempering furnace. In practice full

scale experiments with a tempering furnace are the only realiable method for solving the sum of gas-gap and solid spot conductances, i.e., the contact heat transfer conductance between glass and ceramic rollers in a tempering furnace. Without such measurements the thesis reached the rough conclusion that the effective contact heat transfer coefficient $\bar{h}_{ct}$ between glass and rollers in a tempering furnace is $1 \leq \bar{h}_{ct} L_{rp} \leq 3$ W/(mK), where L_{rp} is the distance between rollers. In the result example in the thesis the portion of contact heat transfer was 8% of the overall heat transfer during the heating cycle, when $\bar{h}_{ct} L_{rp}$ was 1.8 W/(mK).

16.4 Convection in heat soak furnace

In a heat soak furnace glasses are heated by internal forced convection. The problem is to find glass and air temperatures which depend on both the stream-wise coordinate and time. Heat conduction in the axial and the thickness direction is insignificant. In the case of a turbulent channel flow, the problem can be solved using the finite difference method presented in the thesis. Also analytical solutions, which can be used to validate the numerical modelling, are available for constant thermal properties and for the step change in air temperature. In a laminar channel flow, the thermal history effect on the heat transfer coefficient is significant, which makes the problem more complex. In the laminar case the glass and air temperatures can be solved using the quasi-static method presented in the thesis.

In the heat soak furnace researched in the thesis the channel flow can be laminar or turbulent. At the beginning of the heating flow is most likely turbulent, because *Re* is 4000. Due to increasing air temperature the *Re* decreases during heating and due to that also laminar flow can occur during the later stages of the heating when *Re* < 2000. Theoretically predicted and measured temperatures were in reasonable agreement particularly at the early stages of heating. At the later stages of heating the laminar flow assumption was in better agreement with measured values.

During the heating period heat is transferred from air to glass. The air temperature in a channel between glasses decreases in the flow direction. At the entrance region, glass is heated more quickly than deeper in a channel. The coolest point is located at the trailing edge of the glass. In the calibration criteria defined in the standard EN 14179-1 the total mass of glass loading and glass size are just defined with the words “full loading” or “10% loading”. In actual practice, these are dependent on glass size, thickness, and oven capacity. In order to produce well heat-soaked glass after a successful calibration test, the operator has to consider the following details in a heating recipe. The time of a heating phase should be raised when glass flow-wise length increases. The heating time also increases with the glass thickness, even if the mass of a loading remains the same.

Air temperature at the channel inlet is time-dependent. Three main factors that affect the inflowing air temperature are the glass load, the power of air-heating resistors, and the heat capacity of furnace walls and glass rack.

In a wider channel, heat transfer is improved and the length-wise temperature differences in glass are reduced. On the other hand, the glass load can be heavier when the channel is narrow. The minimum distance of 20 mm recommended in the standard seems suitable also from the point of view of heat transfer to ensure the balanced heat treatment of the whole loading. In a very narrow channel the heating time increases dramatically because the air temperature at the end of such a channel is almost as low that of glass, which leads to weak heat transfer.

The air velocity in a channel can be enhanced with bigger fans or better air leading from fans to channels. With higher velocity heat transfer is improved and the temperature variation in glass is reduced. High velocity ensures turbulent flow and in that case also the power of air-heating resistors should be scaled up.

REFERENCES

[1] http://en.wikipedia.org/wiki/Glass

[2] Keksinnöt kautta aikojen, Oy Valitut Palat-Reader's Digest Ab, 1982.

[3] http://en.wikipedia.org/wiki/Glass

[4] http://en.wikipedia.org/wiki/Glass_blowing

[5] http://en.wikipedia.org/wiki/Borosilicate_glass

[6] http://en.wikipedia.org/wiki/Float_glass

[7] Savaete, B., Milestones to better understand flat glass business (history – today – tomorrow), Glass Performance Days 2009, Tampere – Finland, Workshop 2 material.

[8] Barsoum, M., Fundamentals of ceramics, McGraw-Hill International Editions, Material Science Series, 1997.

[9] http://en.wikipedia.org/wiki/Float_glass

[10] The handbook of glass manufacture, vol. 2, New York, pp. 806-809, 1974.

[11] Gardon, R., Modelling annealing lehrs for flat glass, Journal of the American Ceramic Society, vol. 65, 8, pp. 372-379, 1982.

[12] Narayanaswamy, O.S., Optimum schedule for annealing flat glass, Journal of the American Ceramic Society, vol. 64, 2, pp. 109-104, 1981.

[13] Jones, A. C. and Hitchman, M. L., Chemical vapour deposition, precursors, processes and applications, ISBN (online): 978-1-84755-879-4, 2008.

[14] Hill, R. J., Nadel, S. J., Coated glass, applications and markets, BOC Coating Technology, 1999.

[15] Vuoristo, P. and Mäntylä, T., Basics of glass coating processes and coated glass, Glass Performance Days 2007, Tampere-Finland, workshop material, 2007.

[16] C4 Suomen rakentamismääräyskokoelma, lämmöneristys. Ohjeet 2003.

[17] http://en.wikipedia.org/wiki/Bolognesian_tear

[18] Gardon, R., Tempering glass with modulated cooling schedules, Journal of American Ceramic Society, vol. 71, 10, pp. 876-878, 1988.

[19] Schiavonato, M, Mognato, E. and Redner,A., Stress measurement, fragmentation and mechanical strength, Proceedings of Glass Performance Days 2015, Tampere-Finland, pp. 92-95, 2015.

[20] Uhlmann, D. R. and Kreidl, N. J., Elasticity and strength in glasses, vol.5, Academic Press, pp. 217-267, 1980.

[21] Akeyoshi, K. and Kanai, E., Mechanical properties of tempered glass, Proceedings of the VII:th Int. Glass Cong., Paper No. 80, 1965.

[22] Mognato, E., Barbieri, A., Schioavonato, M. and Pace, M., Thermally toughened safety glass: correlation between flexural strength, fragmentation and surface compression stress, Proceedings of Glass Performance Days 2011, Tampere-Finland, pp. 115-118, 2011.

[23] Lee, H., Cho, S., Yoon, K. and Lee, J., Glass thickness and fragmentation behavior in stressed glasses, New Journal of Glass and Ceramics, pp. 116-212, 2012.

[24] Nielsen, J. H., Tempered glass - Bolted connections and related problems, PhD thesis, Department of Civil Engineering, Technical University of Denmark, pp. 24, 2009.

[25] Boley, B.H. and Weiner, J.H., Theory of thermal stresses, Wiley, 1966.

[26] Karvinen, R. and Rantala, M., Heat transfer in tempering furnace, Proceedings of Glass Processing Days 1999, Tampere-Finland, pp. 52-55, 1999.

[27] Bartenev, G.M., Investigation of glass hardening (in Russian), Zh. Tekh. Fiz. 19, pp. 1423-1433, 1949.

[28] Narayanaswamy, O. S., Quantitative treatment of stress generation in tempered glass, Glass Processing Days 1999, short course material, Tampere, Finland, 1999.

[29] Schneider, J., Glass strength in the borehole area of annealed float glass and tempered float glass, Int. J. Forming Processes, vol. 7, 4, pp. 523-541, 2004.

[30] Carre, H. and Daudeville, L., Numerical simulation of soda-lime silicate tempering, Jou. De Physique IV, Colloque C1, Supplement au Journal de Physique III, vol. 6, pp. 175-185, 1996.

[31] Aronen, A., Modelling of deformations and stresses in glass tempering, publication 1036, PhD thesis, Tampere University of Technology, 2012.

[32] Aronen, A. and Karvinen, R., Tempering of thin glass, Engineered Transparency - International Conference at Glasstec, Dusseldorf-Germany, October 25-26, 2012.

[33] Narayanaswamy, O. S. and Gardon, R., Calculation of residual stresses in glass, Journal of American Ceramic Society, vol. 52, 10, pp. 375-380, 1969.

[34] Pincus, A. G. and Holmes, T.R., Annealing and strengthening in the glass industry, Second edition, Ashlee Publications Co., Inc., pp. 266, 1987.

[35] Pesonen, T., Combination convection/radiation –views on optimizing the production parameters in glass tempering, Proceedings of Glass Processing Days 1999, Tampere-Finland, pp. 46-51, 1999.

[36] United States patents US8618442 (Glaston Services Ltd. Oy, 2013) and US7448232 (Glassrobots Oy, 2008)

[37] Jalkanen, E., The high performance low-e tempering process, Proceedings of Glass Performance Days 2007, Tampere-Finland, pp. 675-678, 2007.

[38] European patent EP1491509 (Uniglass Engineering Oy, 2007)

[39] Rantala, M,. Lasin lämmitys karkaisu-uunissa, Master thesis, Tampereen Teknillinen Korkeakoulu, Konetekniikan osasto, 1998.

[40] Sözbir, N. and Yao, S-C., Experimental investigation of water mist cooling for glass tempering, Atomization and Sprays, vol. 14, pp. 191-210, 2004.

[41] German patent applications, DE102008046044, DE102008062359 and DE102008062362 (Technische Universität Bergakademie Freiberg, 2008)

[42] United States patents US3293015 (Pittsburgh Plate Glass Company, 1966) and US3338697 (Permanent Glass Inc., 1967)

[43] United States patent US7000433 (Technopat AG, 2006)

[44] United States patent US5951743 (TGL Tempering Systems Inc., 1997)

[45] Jalkanen, E., Processing factors for high-speed and large glass sizes, Proceedings of Glass Processing Days 2005, Tampere-Finland, pp 79-83, 2005.

[46] European patent EP0968970 (Tamglass Ltd. Oy, 1999)

[47] Vitkala, J., Low-e tempering – The latest results, Proceedings of Glass Processing Days 1999, Tampere-Finland, pp. 56-62, 1999.

[48] Vitkala, J., Tempering quality and case of large glass sizes, Proceedings of Glass Processing Days 2001, Tampere-Finland, pp. 242-246, 2001.

[49] Hecht, E., Optics. Fourth edition, Addison Wesley, San Francisco, pp. 66, 2002.

[50] European patent application EP2159199 (Arcon-dur Sicherheitsglas GmbH & Co. KG, 2009)

[51] Nicolau, V. and Fernando, P., Determination of radiative properties of commercial glass, PLEA 2001 - The 18th Conference on Passive and Low Energy Architecture, Florianópolis – BRAZIL, 2001, http://www.lmpt.ufsc.br/publicacao/130.pdf

[52] Aronen, A. and Karvinen, R., Explanation for edge bending of glass in tempering furnace, Proceedings of Glass Performance Days 2009, Tampere-Finland, pp. 575-579, 2009.

[53] European patent EP1184346 (Glaston Services Ltd. Oy, 2001)

[54] Glass in building – Thermally toughened soda-lime silicate safety glass – Part: Definition and description, European standard, Revision of N 294 prEN 12150-1 (E) 2008-06-25.

[55] Standard test method for measurement of roll wave optical distortion in heat-treated flat glass, ASTM Subcommittee C14.11, Work Item WK7898, 2007.

[56] Standard test method for measuring optical distortion in flat glass products using digital photography of grids, ASTM International, Designation C1652/C1652M-06.

[57] Pilkinton technology datasheet, Shaping and strengthening, http://www.pilkington.com/resources/datasheet6shapingandstrengthening.pdf

[58] Trosifol, Manual, Kuraray Europe GmbH, Druckerei Oskar Berg, Germany, 4th edition, 2007.

[59] United States patents US7476284 (Gyrotron Technology Inc., 2009), US8097107 (Bond Brothers Contracting Pty. Ltd, 2012), and US7143800 (Cardinal LG Company, 2006).

[60] Modest, M. F., Radiative heat transfer, McGraw-Hill International Editions, 1993.

[61] Siegel, R. and Howell, J. R., Thermal radiation heat transfer, Third Edition, Taylor & Francis Ltd., 1992.

[62] Edwards D. K., Radiation heat transfer notes, Hemisphere Publishing Corporation, pp. 4-7, 1981.

[63] Rubin, M., Optical properties of soda lime silica glasses, Solar Energy Materials 12, pp. 275-288, 1985.

[64] Gardon, R., The emissivity of transparent materials, Journal of American Ceramic Society, vol. 39, 6, pp. 278-288, 1956.

[65] Rantala, M. and Karvinen, R., Treatment of transient radiative heat transfer in glass tempering process. International Symposium on Radiative Transfer III. Poster abstracts, 2001.

[66] Field, R. E. and Viskanta, R., Measurement and prediction of the dynamic temperature distributions in soda-lime glass plates, Journal of American Ceramic Society, vol. 73, 7, pp. 2047-2053, 1990.

[67] Gardon, R., Calculation of temperature distribution in glass plates undergoing heat treatment, Journal of American Ceramic Society, vol. 41, 6, pp. 200-209, 1958.

[68] Siedow, N., Lochegnies, D., Grosan, T. and Romero, E., Application of a New Method for Radiative Heat Transfer to Flat Glass Tempering, Journal of American Ceramic Society, vol. 88, 8, pp. 2181-2187, 2005.

[69] Sharp, D. E., and Ginther, L. B., Effect of composition and temperature on the specific heat of glass, Journal of American Ceramic Society, vol. 34, pp. 260-271, 1951.

[70] Proceedings of the Colloquium on modelling of glass forming processes - Euromech 388, Valenciennes, France, 1998.

[71] Data given by float glass manufacturer (permission to publish it is given without the company name), 2005.

[72] Collins, R. E., Zhang, Q-C., Simko, T.M., Dey, C.J. and Turner, G.M., The measurement and calculation of radiative heat transfer between uncoated and doped tin oxide coated glass surfaces, Int. J. Heat Mass Transfer, vol. 40, 1, pp. 61-71, 1997.

[73] Sparrow, E.M., Goldstein, R.J. and Rout, M.A., Effect of nozzle surface separation distance on impingement heat transfer for a jet in a cross flow, J. Heat Transfer, vol. 97, pp. 528-533, 1975.

[74] Martin, H., Heat and mass transfer between impinging gas jets and solid surfaces, Advances in Heat Transfer (edited by Hartnett and Irvine), vol. 13, pp. 1-60, Academic Press, New York, 1977.

[75] Goldstein, R.J. and Behbahani, A.I., Impingement of a circular jet with and without cross flow, Int. J. Heat Mass Transfer, vol. 9, pp. 1377-1382, 1982.

[76] Hrycak, P., Heat transfer from round impinging jets to a flat plate, Int. J. Heat Mass Transfer, vol. 12, pp. 1857-1865, 1983.

[77] Lee, J. and Lee, S., The effect of nozzle configuration on stagnation region heat transfer enhancement of axisymmetric jet impingement, Int. J. Heat Mass Transfer, vol. 43, pp. 3497-3509, 2000.

[78] Hofmann, H. M, Kind M. and Martin H., Measurement on steady state heat transfer and flow structure and new correlations for heat and mass transfer in submerged impinging jets, Int. J. Heat and Mass Transfer, vol. 50, pp. 3957-3965, 2007.

[79] Zuckerman, N. and Lior, N., Jet impingement heat transfer: Physics, correlations, and numerical modelling, Advances in Heat Transfer, vol. 39, pp. 565-631, 2006.

[80] Florschuetz. L.W, Metzger, D.E. and Truman C.R., Jet array impingement with crossflow – correlation for streamwise resolved flow and heat transfer distributions, Nasa Contraction Report 3373, 1981.

[81] Deventer, C., Evrard, P., Feldheim, V., Lybaert, B. and Muller, J., Cooling a plate by an array of round jets: experimental and numerical study, 4th European Thermal Sciences Conference, Proceedings CD, Session 13, 2004.

[82] Hanjalic, K., Turbulent convection at high Re and Ra numbers: at the crossroads of Rans and Les, Advances in heat transfer engineering, 4th Baltic Heat Transfer Conference, pp. 30-42, 2003.

[83] Craft, T.J., Gant, S.E, Gerasimov, A.V., Iacovides, H. and Launder, B.E., Advances in practical near-wall turbulence modelling, 4th European Thermal Sciences Conference, Proceedings CD, Lecture 3, 2004.

[84] Chougele, N.K., Parishwad, G.V., Gore, P.R., Pagnis, S. and Sapali, S.N., CFD Analysis of multi-jet air impingement of flat plate, Proceedings of the World Congress on Engineering, July 6-8 2011, London, U.K., 5p.

[85] Rantala, M. and Karvinen, R., Heat tranfers under an impinging jet at long nozzle-to-surface distances, Proceedings of 13th International Heat Transfer Conference, Sydney/Australia, 2006, 12p.

[86] Crocker, M.E., Piping handbook, The Maple Press Company, York, 1945.

[87] Kayser, J.C. and Shambaugh, R. L., Discharge coefficients for compressible flow through small diameter orifices and convergent nozzles, Chemical Engineering Science, vol 46, 7, pp. 1697-1711, 1991.

[88] Lienhard, J.H. and Lienhard, J.H., Velocity coefficients for free jets from sharp-edged orifices, Journal of Fluids Engineering, vol.106/13, March 1984.

[89] White, F.M., Viscous fluid flow, Second Edition, McGraw-Hill, Boston, 1991.

[90] Chapman, A.J. and Walker, W.F., Introductory Gas Dynamics, Holt, New York, 1971.

[91] Oosthuizen, P.H. and Carscallen, W.E., Compressible fluid flow, McGraw-Hill Companies Inc, 1997.

[92] Cirillo, F. and Isopi, G.M., Glass tempering heat transfer coefficient evaluation and air jets parameter optimization, Appl. Therm. Eng., 2008. doi;10.1016/j.applthermaleng.2008.06.005

[93] Kuumola, V., Karkaistavan lasin konvektiivinen lämmönsiirto, Master thesis, Tampereen Teknillinen Korkeakoulu, 1987.

[94] Madhusana, C.V., Thermal contact conductance, Mechanical Engineering Series, 1996.

[95] Gelder, D., Instabilities in roller conveyors used in flat glass manufacture, Proceedings of the Sixth European Conference on Mathematics in Industry, Limerick 1991, pp. 31-40.

[96] Uusitalo, M., Lasin karkaisu-uunin lämmönsiirto, Master thesis, Tampereen Teknillinen Korkeakoulu, 1996.

[97] Kaspar, A., Fundamentals of spontaneous breakage mechanism caused by nickel sulfide, Proceedings of Glass Processing Days 2003, Tampere-Finland, pp. 696-698, 2003.

[98] European standard EN 14179-1, Glass in building, Heat soaked thermally toughened soda lime silicate safety glass, Part 1: Definition and description, 2005.

[99] Kays, W., Crawford, M. and Weigand, B., Convective heat and mass transfer, Third Edition, McGraw-Hill, 1993.

[100] Jakob M., Heat transfer, John Wiley & Sons, vol.2, 1959.

[101] Saastamoinen J., Heat transfer in unidirectional regenerators, Acta Polytechnica Scandinavica, PhD thesis, TKK, 1980.

[102] Shah R.K., London A.L., Laminar flow forced convection in ducts, Academic Press, 1978.

[103] Hrenya C., Miller S., Mallo T., and Sinclair J., Comparison of low Reynolds number k-ε turbulence models in predicting heat transfer rates for pipe flow, Int. J. Heat Mass Transfer, vol. 41, 11, pp. 1543-1547, 1998.

[104] Leontiev A.I., Petrikevich B.B., and Vyrodov O.G., Turbulent gas flow heat transfer and friction in channels of different cross-sections, Int. J.Heat Mass Transfer, vol. 33, 6, pp. 1047-1055, 1990.

[105] Karvinen R., Transient conjugated heat transfer to laminar flow in a tube or channel, Int. J. Heat Mass Transfer, vol. 31, 6, pp. 1326-1328, 1988.

[106] Nguyen T.V., Maclaine-Cross.I.L., Simultaneously developing laminar flow, forced convection in the entrance region of parallel plates, J. Heat Transfer, vol. 113, pp. 837-842, 1991.

[107] Endrys J. and Turkiz D., Die temperaturverteilung in glas bei stationärem zustand, Internationale Baustoff- und Silikattagung Weimar, Sektion 5, Hochschule für Architektur und Bauwesen, Weimar, pp. 35-40, 1985.

[108] In-house research reports, not made by Rantala M., Tamglass Engineering Ltd. Oy or Glaston Finland Oy, 1999-2012. Permission to publish is given.

[109] In-house or marketing material, not made or photographed by Rantala M., Tamglass Engineering Oy or Glaston Finland Oy, 1999-2012. Permission to publish is given.

APPENDIX A

Material properties of soda-lime float glass at room temperature (24˚C)

[Values are taken from the technical bulletin of NSG Group,

http://www.pilkington.com/resources/ats129propertiesofglass20130114.pdf]

Density, ρ = 2530 kg/m^3

Specific heat, c_p = 880 J/(kgK)

Thermal conductivity, k = 0.937 W/(mK)

Modulus on elasticity, $E = 72\times10^9$ Pa

Poisson's ratio, $\nu = 0.23$

Coefficient of linear expansion, $\alpha = 8.3\times10^{-6}$ K^{-1}

E,ν and α are are quite independent of temperature up to 480˚C.

Temperature dependence of specific heat and thermal conductivity of soda-lime float glass

For temperature dependence of specific heat the following is proposed

$$c_p(T) = \frac{0.00146aT^2 + 2aT + c_{p0}}{(0.00146T + 1)^2} \qquad \text{Cal/(g˚C)}$$

1 Cal/(g˚C) = 4187 J/(kgK)

where T in˚C [69]. The factors a and c_{p0} depends to some extent on the float glass composition. For the typical float glass composition defined in Sec. 2.1 a = 0.00051 and c_{p0} = 0.1745. For instance, c_p(600˚C) = 1255 J/(kgK). Note that the equation gives c_p(24˚C) = *779* J/(kgK), which differs quite substantially from the value above.

Ref. [68] uses $c_p(T) = 893 + 0.4T^2 - 1.8\times10^7/T^2$ J/(kgK), when T < 551°C

$c_p(T) = 1433 + 6.5\times10^{-3}T$, when T > 551°C

For temperature dependence of thermal conductivity the following is proposed

$$k(T) = 0.7222 + 0.001583T \qquad \text{W/(mK)}$$

where T in˚C [107]. For instance, k(600˚C) = 1.67 W/(mK). Note that the equation gives k(24˚C) = 0.76 W/(mK), which differs substantially from the value above.

Ref. [68] uses $k(T) = 0.975 + 8.58\times10^{-4}(T - 273)$ W/(mK)

Tampereen teknillinen yliopisto
PL 527
33101 Tampere

Tampere University of Technology
P.O.B. 527
FI-33101 Tampere, Finland

ISBN 978-952-15-3646-5
ISSN 1459-2045